INSTITUT FÜR WASSERCHEMIE UND CHEMISCHE BALNEOLOGIE
LEHRSTUHL FÜR HYDROGEOLOGIE, HYDROCHEMIE UND UMWELTANALYTIK
DER
TECHNISCHEN UNIVERSITÄT MÜNCHEN

Spectrochemical Analysis of Solid Samples by Laser-induced Plasma Spectroscopy

Igor Radivojevic

Vollständiger Abdruck der von der Fakultät für Chemie der Technischen Universität München zur Erlangung des akademischen Grades eines

Doktors der Naturwissenschaften (Dr. rer. nat.)

genehmigten Dissertation.

Vorsitzender:		Univ.-Prof. Dr. M. Schuster
Prüfer der Dissertation:	1.	Univ.-Prof. Dr. R. Nießner
	2.	Univ.-Prof. Dr. A. Laubereau

Die Dissertation wurde am 07. 02. 2004. bei der Technischen Universität München eingereicht und durch die Fakultät für Chemie am 26. 07. 2004. angenommen.

The major parts of this work are already published in different scientific journals:

I. Radivojevic, C. Haisch, R. Niessner, S. Florek, H. Becker-Ross, U. Panne, Microanalysis by Laser-induced Plasma Spectroscopy (LIPS) in Vacuum Ultraviolet, *Analytical Chemistry*, 76, 1648-1656*,* 2004.

I. Radivojevic, C. Haisch, R. Niessner, S. Florek, H. Becker-Ross, U. Panne, Detection of Bromine in Thermoplasts from Consumer Electronics by Laser-induced Plasma Spectroscopy (LIPS), *Spectrochimica Acta Part B,* 59*,* 335-343, 2004.

Et ignotas animum dimittit in artes.
OVIDIUS, METHAMORPHOSES, VIII, I88

And he sent forth his spirit
among the unknown arts.
OVID, METHAMORPHOSES, VIII, I88

to Anna and Katarina

Acknowledgments

The experimental work of this disertation was carried out in the time span from August 2000 till November 2003 at the institute of Hydrochemistry and Chemical Balneology, Technical University Munich under the supervision of o. Univ. Prof. Dr. Reinhard Niessner.

First of all, i would like to thank to Prof. Dr. Niessner for provision of technical and financial funds neccessary for this work, his scientific supervision, freedom in organization and realization of experiments, and most of all for his trust in me and my former education at the very begining of this work.

My special thanks is dedicated to PD Dr. Ulrich Panne for all his help and suggestions in performing the experiments, preparing the lectures, nad writhing the publications and, finally, my thesis. Besides that I am very grateful to him for many plesent conversations about all kind of subjects, his unlimited understandig, nice company and thime spent together, and, last but not the least, for not feeling an „alien" for a single moment.

Thanks to Dr. Christoph Haisch for help in constructing my set-ups, very useful everyday comments, and for an introduction in real German parsimonious spirit.

To Dr. Herbert Fink I would like to thank for the first steps towards LIPS, and his help in my first experiments.

Thanks to Dr. Thomas Schmid and Dr. Harald Prestel (Tom & Harry) for enjoyable company during long days in the lab, everyday lunch, and one conference (ANAKON 2003).

Thanks to Christine Sternkopf for all those chemical-technical stuffs, lots of reference analyses, and for her always-happy face.

Chiara Vallebona thanks for successfull cooperation, more than plesent friendship, and for the glimpse at the authentic Italian culture and life-style.

I would also like to thank to all my practical students (Eugenia, Martina, Reiner, Peter, Martin, Benjamin etc.) for great help, and for all boring work thay had to do instead of me.

At the end I wont to thank to my mother Biljana and my wife Katarina for all their support and understanding.

Content

1 Introduction

Soon after the first report of laser action in ruby in 1960 [1,2], it was generally recognized that an intense laser light beam could be used to excite material into a state of optical emission. The first published report about the analytical use of a laser-induced plasma was a meeting abstract by BRECH and CROSS [3]. MAKER, TERHUNE, and SAVAGE [4] reported the first observation on optically-induced breakdown in gases. In the same year, RUNGE, MINCK, and BRYAN [5] reported on the use of a pulsed ruby laser for direct spark excitation of metals. In 1966 YOUNG, HERCHER, and YU in [6] described the characteristics of laser-induced air sparks. In 1972, FELSKE, HAGENAH, and LAQUA [7] studied the analysis of steel by means of a Q-switched ruby laser. During the 1970s, development continued in several countries. Even commercial systems were available for a short time in the early 70ties. For spectrochemists, direct ablation, excitation, and observation of the spark on surfaces became a promising analytical method. On the other hand, laser-induced plasma spectroscopy (LIPS, or laser-induced breakdown spectroscopy, LIBS) was often used by physicists for fundamental studies on breakdown in gases.

In the early 80ties a renewed interest in applications of LIPS was driven by its unique advantages for spectrochemical analysis [8,11]. However, real applications were still hampered by the rather bulky instruments. In the 90ties the applications turned to very practical problems, such as monitoring environmental contaminations, control of material processing, and sorting of materials. As a result the analytical work was more concentrated on developing rugged and mobile instrumentation. Optical fibers were integrated into LIPS systems, primarily for carrying the plasma emission to the spectrometer, occasionally for the delivering of laser pulse as well.

With the new millennium, the two conferences: LIBS 2000 in Pisa, Italy [12], and LIBS 2002 in Orlando, USA, provided an excellent snapshot of the status of LIPS research, development, and, commercialization. In particular, many papers dealt with various categories of instrumentation development, from laboratory devices all the way to commercial systems. Clearly, the field is moved beyond the science and engineering laboratory to include the world of applications and sales as well. A search through the web site of US Patent Office [13] showed, for example, 37 relevant patents mentioning LIPS since 1976.

1.1. Spectroscopic Analysis in the Vacuum Ultraviolet (VUV)

Spectrochemical analysis in the vacuum ultraviolet (VUV, $\lambda < 200$ nm) was first attempted in 1936 by HARRISON [14], who determined sulfur using the lines at 180.7 nm, 182.0 nm, and 182.6 nm. Other authors at that time tried to avoid this spectral region because of experimental difficulties, shortage of stable sources, and lack of simple and convenient spectrometers for this region.
In 1947 MCNALLY, HARRISON, and ROWE [15] made a determination of fluorine from lines in the VUV region, but the utilized vacuum arc was unstable and the analytical procedure was rather lengthy, so that the authors had to develop a technique for fluorine determination using the visible spectrum of this element excited in a hollow cathode.
Analyses of gases and non-metals in the VUV in the vacuum ultraviolet are treated in detail by VODAR and co-workers [16-20], who worked with the creeping spark. The spectra were recorded both photograhically and photoelectrically. In 1960, the elemental emission lines in the VUV have been tabulated by ZAIDEL et al. [21-23]. In these tabulation line intensities are taken from sources like arcs, sparks, and various gas discharge tubes. KIRBRIGHT et al. [24,25] was the first to report detection limits in the determination of various non-metals using lines from VUV. They purged the monochromator and optical part between a plasma torch and the entrance slit with nitrogen. More recently various studies for argon- or nitrogen-purged and vacuum systems have been published. These publications include also discussions of spectral interferences [26, 27, 29]. In 1987 LA FRENIERE et al. [30] used a helium-purged direct plasma spectrometer and reported a list of prominent lines of Al, As, B, Bi, Br, Cl, Ga, Ge, I, In, P, Pb, S, Sb, Se, Si, Sn, Te, and Tl.
LIPS analysis in VUV was mostly devoted to the non-metals in steel and is basically connected with the works of GONZALES, SATTMAN, HEMMERLIN, KHATER and other. A short overview of present VUV-LIPS applications will be given in chapter 4 of this work, together with the main design principles and instrumentation for VUV spectroscopy in general.

1.2. Microanalysis by LIPS

Micro-analytical methods for determination of elemental composition of heterogeneous samples become more and more important in modern analysis. Especially advances in material science, for example, surface coating and modification technologies, are realized with structures and layers with variable composition in the range between 100 μm and 1 mm. Knowledge about the distribution of elements, phases, or grain boundaries are of essential importance for understanding of macroscopical properties of some material. Besides that, in many geochemical and mineralogical applications (like analysis of mineral phases or fluidic inclusions) a fast local characterization in μm range is needed. Micoanalytical tasks within environmental analysis are, for example, chemical characterization of aerosols or analysis of fine grained soils. Despite of the multiplicity of today's micro analytical methods a method for fast elemental mapping of surfaces with spatial resolution of few microns without any complex sample preparation is still missing.

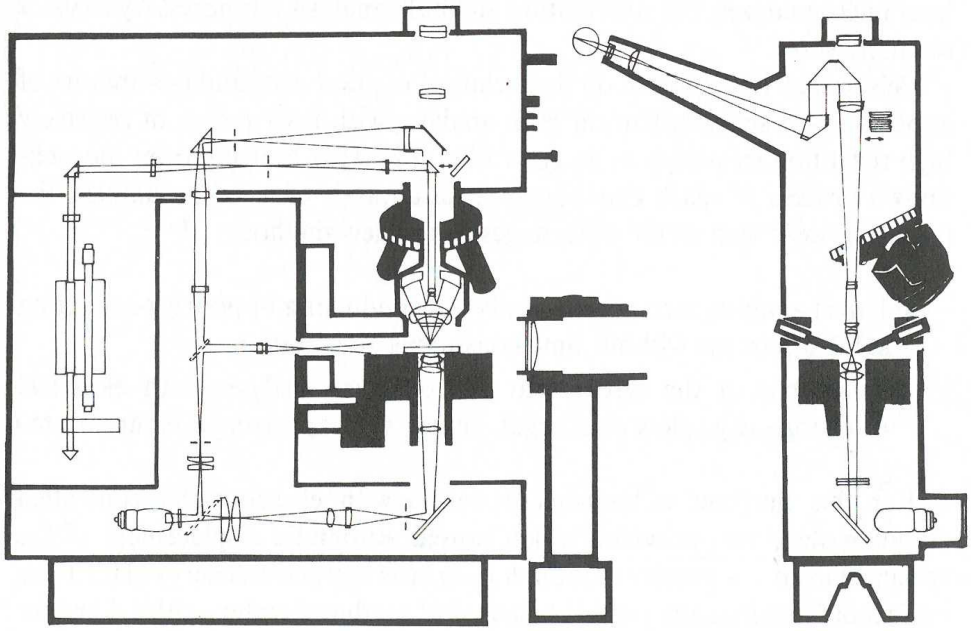

Fig. 1-1: *The schematic view of laser microanalyzer LMA10, Carl Zeiss, GDR (adopted from [32]).*

The idea of using a laser plasma for microanalysis is as old as the idea of spectrochemical application of laser-induced plasmas itselves and was inspired by the development of microprobe in the early 60ties. VILNAT et al.[31] reported the first application of LIPS for spatially-resolved analysis of surfaces. Most experimental set-ups for microanalysis by LIPS are based on microscopic optics for plasma generation and observation. Simultaneously the sample is imaged through a microscope so that the elemental composition can be related to the position on the surface. The first commercial microanalyzer, realized about 1970, was the LMA 10 by Carl Zeiss (see Fig.1.1). It was based on a ruby laser and was able to determine over 60 elements with limits of detection between 10 and 100 ppm and spatial resolution between 10 and 250 μm [32]. Due to technical problems, the commercial systems of the early 70ties were not produced

for long and scientific efforts shifted to laser ablation as a sampling method in combination with other plasma-source systems.
Recent efforts on the field of LIPS microanalysis are connected with work of LASERNA et. al. [33-37], GERTSEEN et al. [38,39] and FABRE et al. [40,41]. A detailed overview of methods and instrumentation for laser microanalysis can be found for example in [32] .

1.3. Objective of this Work

The objective of this work was to extend the range of elements, which can be analyzed by LIPS, via observation of atomic emission in the VUV while, simultaniously allowing a microanalysis. This permits not only a multielement analysis of metals, but also access to emission lines of non-metals and metalloids such as S, P, N,O, C, and As. Applying an appropriate beam shaping („micro focusing"), LIPS can provide a fast spatially resolved elemental characterization of surfaces with a typical resolution of about 10 μm. Using a UV laser beam (λ = 266 nm) for plasma ignition, fractionization effects can be minimized and a quantitative analysis can be performed. Analysis of the spectra from single pulses permit a depth- and spatially resolved investigation of a sample.
Two experimental set-ups for VUV-LIPS had to be developed. A set-up for bulk analysis based on conventional Czerny-Turner vacuum monochromator and a new echelle spectrograph for high spectral resolution ($\lambda/\Delta\lambda$> 10 000) in the spectral range between 150 and 300 nm. First applications in microanalysis should reveal the analytical figures of merit for geological samples with highly irregular distribution of certain elements. The general influence of sample heterogeneity on a LIPS analysis had to be investigated. Coal samples, available from earlier studies by LA-ICP-MS, could be utilized for this purpose. To counter problems of sampling statistics a single laser pulse sampling approach in combination with robust statistic had to be investigated. Single pulse analysis also demands for improved detection limits. Hence, the possibilities of using two laser pulses separated by short time interval instead of one in order to separately control and optimize processes of ablation and excitation of the ablated material was also investigated.

2 Theoretical Background

2.1. Plasma Fundamentals

2.1.1. Nature of Plasmas

Plasmas are found in nature in various forms and are characterized normally by their electron density n_e and electron temperature T_e. On earth they exist in the ionosphere in heights of 70-500 km (density $n_e = 10^{12}\ m^{-3}$, $T_e = 2300$ K*)*. Solar wind is another „natural" plasma originating from the sun with $n_e = 10^6\ m^{-3}$ and $T_e = 10^5$ K. The corona which extends around the sun has an electron density $n_e = 10^{14}\ m^{-3}$ and electron temperature is $T_e = 10^6$ K. Finally, white dwarfs, the final state of stellar evolution, have a n_e of $10^{36}\ m^{-3}$. To illustrate these various plasma domains, Fig. 2-1 displays the electron density n_e (m^{-3}) vs. the electron temperature $k_B T_e$ (eV). As the temperature of material is raised, its state changes from solid to liquid and then to gas. If the temperature is elevated further, an appreciable number of gas atoms are ionized and enter a high temperature gaseous state in which the charge numbers of ions and electrons are almost the same and charge neutrality is satisfied in a macroscopic scale.
When the ions and electrons move collectively, these charged particles interact via Coulomb forces which are long-range forces and decay with the inverse square of the distance r between charged particles. The resultant current flows due to the motion of the charged particles and Lorentz interaction . Therefore, many charged particles interact with each other by long range forces rather then through short range collision process like in a „common" gas. This results in different kinds of collective phenomena such as plasma instabilities and wave

phenomena. Hence, the word „plasma“ is used in physics to designate the high temperature ionized gaseous state with charge neutrality and collective interaction between the charged particles and waves [43].

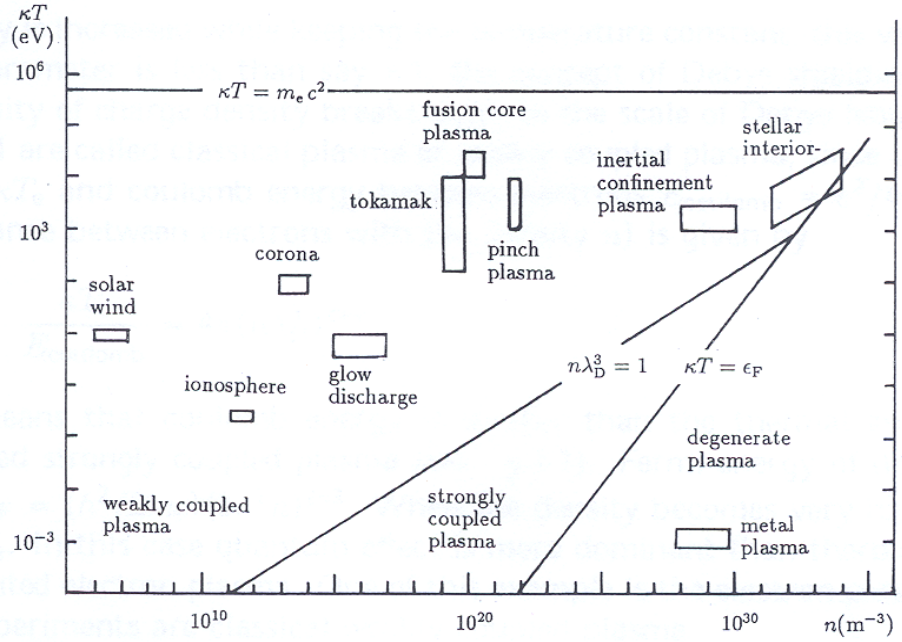

Fig. 2-1: *Plasma domains in a n_e-kT diagram (adopted from [43]).*

2.1.2. The Local Thermodynamic Equilibrium (LTE) Model of Plasma

In the local thermodynamic equilibrium (LTE) model it is assumed that the distribution of population densities of the electrons is determined exclusively through collisional processes and that they have sufficient rate constants so that the distribution responds instantaneously to any change in the plasma conditions. In such circumstances each process is accompanied by its inverse and these pairs of processes occur at equal rates by the principle of detailed balance. Thus, the distribution of population densities of the electrons energy levels is the same as it would be in the system in complete thermodynamic equilibrium. The population distribution is determined by the statistical mechanical law of equipartition among energy levels and does not require knowledge of atomic cross sections for its calculation. Thus, although the plasma density and temperature may vary in space and time, the distribution of population densities at any instant and point in space depends entirely on local values of density, temperature, and chemical composition of plasma. If the free electrons are distributed among the energy levels available for them, their velocities have a Maxwellian distribution

$$dn_v = n_e 4\pi\left(\frac{m_e}{2\pi k_B T_e}\right)^{\frac{3}{2}} \exp\left(-\frac{m_e v^2}{2k_B T_e}\right) v^2 dv \,. \tag{2.1}$$

For the bound levels the distributions of population densities of neutrals and ions are given by the Boltzmann (2.2) and Saha (2.3) equations

$$\frac{n(i)}{n(j)} = \frac{\omega(i)}{\omega(j)} \exp\left(\frac{\Delta E(i,j)}{k_B T_e}\right) \quad , \tag{2.2}$$

$$\frac{n(z+1,k)n_e}{n(z,k)} = \frac{\omega(z+1,k)}{\omega(z,k)} 2\left(\frac{2\pi m k_B T_e}{h^2}\right)^{\frac{3}{2}} \exp\left(\frac{\chi(z,k)}{k_B T_e}\right) \quad , \tag{2.3}$$

where n(i), n(j), n(z+1,k) and n(z,k) are the population densities of various levels designated by their quantum numbers i, j, and k (the last for the ground level) and ionic charge z and z+1. The term $\omega(z, i)$ is the statistical weight of the designated level, $\Delta E(i,j)$ is the energy difference between levels i and j and χ (z, k) is the ionization potential of the ion of charge z in its ground level k. The last three equations, 2.1-2.3, describe the state of the electrons in an LTE plasma.
For complete LTE of the populations of all levels, including the ground state, a necessary condition is that electron collisional rates for a given transition exceed the corresponding radiative rates by about an order of magnitude [44]. This condition gives a criterion [45] for the critical electron density of the level with Energy E

$$n_{e,\,crit} \geq \frac{5}{8\sqrt{\pi}}\left(\frac{\alpha}{a_0}\right)^3 z^7 \left(\frac{E}{z^2 E_H}\right)^3 \left(\frac{k_B T_e}{z^2 E_H}\right)^{\frac{1}{2}}, \tag{2.4}$$

where α is fine-structure parameter, a_0 is Bohr radius, and E_H is the hydrogen ionization potential.
Many plasmas of particulate interest do not come close to complete LTE, but can be considered to be only in partial thermodynamic equilibrium (PLTE) in the sense that the population of sufficiently highly excited levels are related to the next ion's ground state population by Saha-Boltzmann relations, respectively to the total population in all fine-structure levels of the ground state configuration [44]. For any atom or ion with simple Rydberg level structure, various criteria were advanced for the minimum principal quantum number n_{cr} for the lowest level, often called thermal or collision limit, for which PLTE remains valid to within 10%. One criterion with quite general validity is given by Griem [45]:

$$n_{cr} \approx \left[\frac{10}{2\sqrt{\pi}}\frac{z^7}{N_e}\left(\frac{\alpha}{a_0}\right)^3\right]^{\frac{2}{17}}\left(\frac{k_B T_e}{z^2 E_H}\right)^{\frac{1}{17}} . \quad (2.5)$$

2.1.3. Elements of Plasma Spectroscopy

In contrast to conventional spectroscopy, where one is mainly concerned with the structure of an isolated atom and molecule, the radiation from the plasma also depends on the properties of the plasma in the intermediate environment of the atomic or molecular radiator. This dependence is a consequence of the long-range Coulumb potential effects which dominate the interactions of ions and electrons with each other and with existing neutral particles. These interactions are reflected in the characteristic radiations in several ways. They can control population densities of the discrete atomic states, spectral shift and broadening by Stark effect, lower the ionization potentials of the atomic species, cause continuum radiation emissions and emission of normally forbidden lines. Generally, the radiation emitted from a self-luminous plasma can be divided into bound-bound (b-b), bound-free (b-f), and free-free (f-f) transitions.

Line Radiation

Line radiation from plasma occurs for electron transitions between the discrete or bound energy levels in atoms or ions. If the plasma is optically thin [46], then the intensity I_{ij} of a spectral line arising from a transition between bound levels i and j is given by

$$I_{ij} = \frac{1}{4\pi}\int n_i A_{ij} h\nu_{ij} ds , \quad (2.6)$$

where n_i is the population density of the level i, $h\nu_{ij}$ is the photon energy (energy difference between levels i and j), and A_{ij} is the spontaneous transition probability or Einstein coefficient. The integration is taken over a depth of plasma viewed by the detector, and the intensity of radiation is measured in units of power per unit area per unit solid angle.

Transition probabilities can be sometimes expressed via the oscillator strength f_{ij}. This is defined as the ratio of the number of classical oscillators to the number of lower state atoms required to give the same line-integrated absorption [47]. Its relationship to the Einstein coefficient is

$$f_{ji} = \frac{4\pi\varepsilon_0}{e^2}\frac{m_e c^3}{8\pi^2\nu_{ij}}\frac{g_i}{g_j}A_{ij} . \quad (2.7)$$

g_i and g_j are degenerations (multiplicities) of levels i and j. The usefulness of f_{ij} is that it is dimensionless, describing just the relative strength of the transition.

The detailed values of A_{ij} , g_i, and g_j can be obtained from reference compilations or from electronic databases, i.e by NIST [48].

Continuum Radiation

The origins of continuum radiation are both bound-free and free-free transitions. The absorption of radiation from a discrete atomic state, such that the photon has enough energy to extend above the next ionization threshold, results in a release of an electron and gives rise to the process of photoionization. The reverse process of recombination occurs when an ion and an electron recombine with emission of a photon to form an ion in the next lowest ionic state (or in the neutral atomic state). Since the upper state is continuous, the emitted or absorbed radiation in both processes is also continuous.
Transitions between two free energy levels can occur in plasmas increasing the energy exchanges of charged particles. Classically, this takes place because a moving charge radiates when it is a accelerated or retarded. For most cases of practical importance, these free-free transitions are classified as bremsstrahlung or cyclotron spectra. In bremsstrahlung, the acceleration of charged particle takes place via the Coulomb field of charged particles. In cyclotron radiation, the acceleration is due to the gyration of charged particles in a magnetic field.
The total continuum radiation at any particular frequency $I(\nu)$ is the sum of the contributions from all such processes having components at the specified frequency. Thus:

$$I(\nu)d\nu = \frac{1}{4\pi}\int n_e \sum_i n(i)\left\{\gamma(i, T_e, \nu) + \sum_p \alpha(i, p, T_e, \nu)\right\} h\nu \, ds \, d\nu \quad , \quad (2.8)$$

where $\gamma(i, T_e, \nu)$ is the atomic probability of a photon of frequency ν being produced in the field of an atom or ion (specified by i) by an electron of mean kinetic temperature T_e making free-free transition; $\alpha(i, p, T_e, \nu)$ is the corresponding probability where the electron makes a free-bond transition into a level p. As before, the integration is taken over the plasma depth s.

Line Broadening

It has been recognized for a long time that the broadening of spectral lines is influenced by the environment of the radiating atoms or ions, and depends notably on the pressure and temperature. The fundamental broadening of a spectral line is that which occurs for an atom which is completely isolated from its neighbours, is in a motionless state and is shielded from electric and magnetic fields. Under these conditions, the discrete transition is found to have the natural line width. An excited state of an isolated atom has a natural lifetime τ_{ij} which is dependent on the probability of spontaneous decay.

$$\tau_{ij} = A_{ij}^{-1} . \quad (2.9.)$$

According to the Heisenberg uncertainty principle, this leads to an energy uncertainty given by

$$\tau_{ij}\Delta E_{ij} \approx \frac{h}{2\pi}. \tag{2.10.}$$

Transitions between excited states will involve energy uncertainties of the two states

$$\Delta E = \Delta E_{ij} + \Delta E_{kj} . \tag{2.11.}$$

The natural spectral line width is therefore denoted by

$$\Delta\nu_N = \frac{\Delta E}{h} \approx \frac{1}{2\pi}[\sum A_{ij} + \sum A_{kj}] . \tag{2.12.}$$

The line shape function $F^N(\nu-\nu_0)$ in this case can be written as

$$F^N(\nu-\nu_0) = \frac{1}{\pi}\frac{\Delta\nu_N}{2(\nu-\nu_0)^2 + \frac{1}{2}\Delta\nu_N^2} , \tag{2.13}$$

which corresponds to a pure Lorentzian profile. If a source of monochromatic light of frequency ν_0 is moving with a velocity whose component in the line of sight is v, the frequency appears to be shifted by an amount $\nu_0 v/c$ compared with the frequency ν_0 of the source. The random motion of the atoms in the source cause the spectral lines to be broadened. This kind of line broadening is the so called Doppler broadening The intensity distribution in this case is determined by Maxwellian distribution of velocities. Introducing this, the shape function due to Doppler shifted components becomes

$$F^D(\nu-\nu_0) = \frac{c}{\nu_0}\left(\frac{m_a}{2\pi kT}\right)^{\frac{1}{2}} \exp\left(-\frac{m_a c^2}{2kT}\frac{(\nu-\nu_0)^2}{\nu_0^2}\right) , \tag{2.14.}$$

where M_a is the mass of the atom. This kind of shape factor implies a Gaussian profile. The half-width for Doppler broadening is given by

$$\Delta\nu_D = \frac{2\nu_0}{c}\sqrt{\frac{2kT\ln 2}{M_a}} . \tag{2.15.}$$

Collisional broadening arises from the influence of nearby particles upon the emitting atom. There are two main approaches to calculate the broadening, starting from opposite extremes. The collisional approach developed initial from LORENTZ supposes that for most of the time the atom radiates undisturbed, but occasionally collisions occur that interrupt the wave train. The quasistatic approach developed by HOLTZMARK assumes that an atom radiates in an environment that is effectively quasistatic during the period of emission. Any

individual radiator thus experiences an instantaneous shift in wavelength and the average possible perturbations gives the line width and shape.
The most important perturbing effect is generally the electric field of nearby particles. The atomic energy levels of an atom in an electric field are perturbed by the alternation of the potential energy. States near the continuum are more strongly perturbed. The shift in a spectral line due to electric fields is called the Stark shift; hence the name Stark broadening. Detailed calculations of Stark broadening are extremely complicated and have been done in detail only for few atoms [49,50]. Although, the simplified approach (often called nearest neighbour treatment) does not give a full picture of the complexity of the problem, it does quite accurately give the electron density dependence of the line width and its dependence of the electron temperature for lines which upper state has an even principal quantum number, n. Full scale calculations give the width as [47]

$$\Delta\lambda_{1/2} = 0.54\alpha_{1/2}n_{20}^{2/3}[\mathrm{nm}], \qquad (2.16.)$$

where n_{20} is the ion density in units of 10^{20} m^{-3} and the parameter $\alpha_{1/2}$ is tabulated from several authors [51,52].
The overall profile of most atomic lines are neither purely Gaussian nor purely Lorentzian, but rather a combination known as Voigt profile. Assuming that pressure and Doppler broadening are independent processes, the combined line profile is a convolution of normalized Lorentzian and Gaussian profiles. The numerical procedure for calculation of a Voigt profile is described by several authors (for example, see [53])

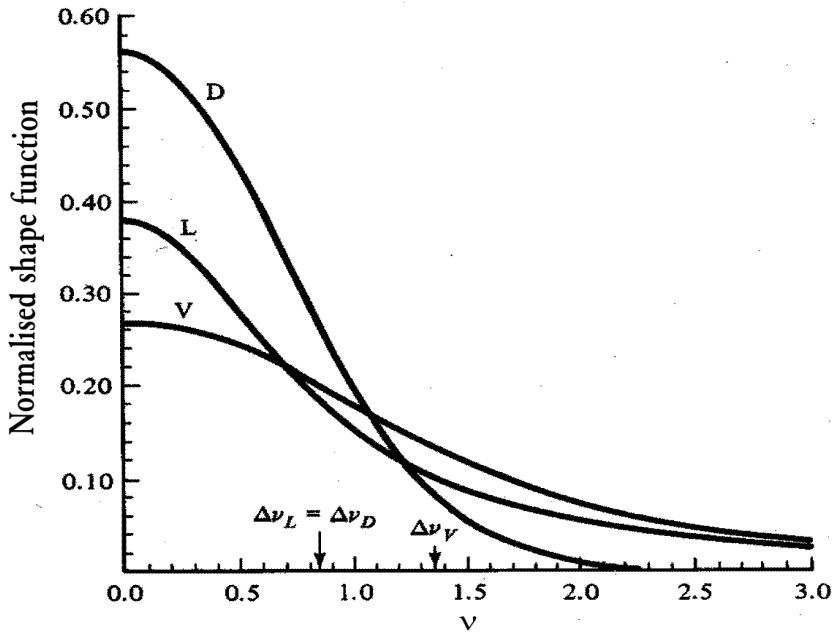

Fig. 2-2: *Normalized spectral profiles vs. relative frequency for pure Doppler (D), pure Lorentzian(L) and Voigt (V) distributions(addopted from [53].*

Spectroscopic Determination of the Electron Density

The most powerful spectroscopic technique for determination of the electron density n_e comes from the measurement of the Stark broadening of optical lines. As already mentioned, the perturbation of radiating particles arise from microscopic electric fields of the ambient ions and electrons. In this method absolute photon intensities are not required, merely relative line widths and shapes. And since for densities $n_e > 10^{15}\,cm^{-3}$ the broadening is usually appreciable, conventional spectrometers and monochromators often suffice. Once the spectral line has been determined, the density is extracted by matching the width (or the entire shape) to the theoretical prediction.
Stark broadening of well-isolated lines in neutral atoms and singly ionized non-hydrogenic ions is predominately from electrons [44,52]. Therefore, the half-width of these lines can be computed with the electron impact approximation and corrected for the relatively unimportant quasistatic ion broadening [54]. In addition to the broadening, there is also shift (usually toward increasing wavelengths) of the line center away from the position it has in the limit $n_e = 0$. A fairly good approximation (20-30%) of the $\Delta\lambda_{1/2}$ and the line shift $\Delta\lambda_{shift}$ are given by Griem [49,52]:

$$\Delta\lambda_{1/2} = 2W\left(\frac{n_e}{10^{16}}\right) + 3.5A\left(\frac{n_e}{10^{16}}\right)^{\frac{1}{4}}\left[1 - \frac{3}{4}N_D^{-\frac{1}{3}}\right]W\left(\frac{n_e}{10^{16}}\right), \qquad (2.17.)$$

$$\Delta\lambda_{shift} = 2D\left(\frac{n_e}{10^{16}}\right) \mp 2A\left(\frac{n_e}{10^{16}}\right)^{\frac{1}{4}}\left[1 - \frac{3}{4}N_D^{-\frac{1}{3}}\right]W\left(\frac{n_e}{10^{16}}\right). \qquad (2.18.)$$

The first term in both equations represent the electron contribution while the second term gives the ion correction. Here, the width and shift are in Angstroms and the electron density in cm^{-3}. The parameter N_D represents the number of particles in the Debye sphere. The coefficients W, A, and D are independent from n_e and are slowly varying functions of the electron temperature T_e. The two formulas can be applied to lines from neutral atoms. To make them applicable also for singly ionized ions, the numerical coefficient 1/4 is replaced by 1.2. A comprehensive list of width and shift parameters W, A, and D is given by Griem [52].

Spectroscopic Determination of the Electron Temperature

In an optical thin plasma of length l along the line of sight, the integrated emission line intensity is given by

$$I_{ij} = \frac{hc}{\lambda_{ij}}A_{ij}\int_0^l n_i dx = \frac{hc}{\lambda_{ij}}A_{ij}N_i l \quad . \qquad (2.19.)$$

For PLTE, as already discussed, down to the upper levels m and p of two lines of the same atom or ion, the electron populations are distributed according to Boltzmann and the ratio of intensities of two lines is given by

$$\frac{I_{nm}}{I_{qp}} = \frac{\lambda_{pq}}{\lambda_{mn}}\frac{A_{nm}g_m}{A_{qp}g_p}\exp\left(-\frac{E_m - E_p}{k_B T_e}\right)$$

or

$$k_B T_e = \frac{E_p - E_m}{\ln\left(\frac{\lambda_{pq}}{\lambda_{mn}} \frac{A_{nm} g_m}{A_{qp} g_p} \frac{I_{nm}}{I_{qp}}\right)} . \qquad (2.20.)$$

The practical procedure is based on taking a set of lines from the same element and same ionization state. A plot of the values under the natural algorithm versus the differences of energies of upper levels for a combination of each two lines should result in a linear relation. The slope of such curve, α, can be used for determination of electron temperature T_e via

$$T = \frac{1}{\alpha k_B} . \qquad (2.21.)$$

This method is so called Boltzmann-plot method and it is used for determination of electron temperature in most cases. Beside this approach there are several other methods based on: (i) relative intensities of subsequent ionization stages of the same element, (ii) relative line to continuum intensity, (iii) frequency spectrum of the continuum or line reversal methods. A systematic overview of all these methods can be found for example in [44] or [54].

2.2. Laser-induced Plasma Spectroscopy

When a high power laser pulse is focused onto a solid sample, the irradiance can lead to rapid local heating, intense evaporation, and ablation of material. The ablated material compresses the surrounding gas and leads to formation of a shock wave. As for nanosecond laser pulses incident laser radiation interacts with the partially ionized material vapor and the material clusters embedded therein, the characteristics of the laser affects the efficiency and quality of the ablation. Factors, such as pulse width, spatial and temporal fluctuations of the pulse, and power variations can influence the ablation. The mechanical, physical, and chemical properties of the sample also determine the ablation process. As for LIPS mainly nanosecond-laser pulses are utilized, the discussion here will be limited to this time scale. For ns pulses (pulse width between 1-30 ns), the laser matter interaction can be treated separately from the adiabatic expansion of the plasma into a buffer gas or vacuum

Chronologically, the laser-ablation process can be divided roughly in three phases (Fig. 2-3): (i) primary laser-matter interaction (heating and evaporation), (ii) plasma generation and, in the case of ns pulses, laser plasma interaction (laser-induced breakdown), (iii) adiabatic expansion of the plasma. Although linearly depicted in Fig. 2-3, the phenomena are temporally overlapping during laser ablation

2.2.1. Theoretical Modelling of Laser-induced Plasmas

Laser-induced breakdown can be defined as the generation of an ionized gas (plasma) by a laser pulse [55]. There are two main mechanisms for the electron generation and growth. The first mechanism involves absorption of laser radiation by electrons when they collide with neutrals. If the electrons gain sufficient energy, they can ionize neutrals through the collisional process

$$e^- + M \rightarrow 2e^- + M^+$$

It is obviously that this reaction will lead to cascade breakdown, i.e. the electron concentration will increase exponentially with time. However two preconditions are necessary: (i) an initial electron in the focal volume and (ii) the electrons acquire an energy above the ionization threshold of the gas (or band gap for solids).
The second ionization mechanism, multiphoton ionization (MPI), involves the simultaneous absorption of a several photons by an atom or molecule. MPI is generally described by

$$M + mh\nu \rightarrow M^+ + e^-$$

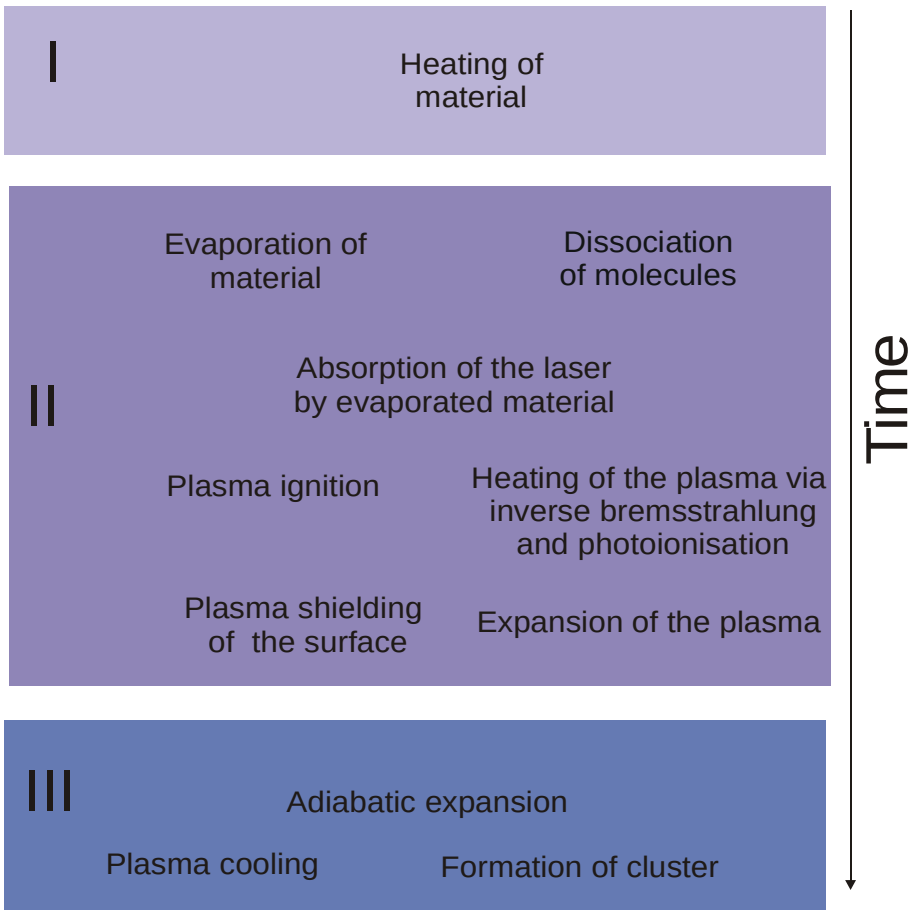

Fig. 2-3: *Chronology of a laser ablation.*

The number of photons m for ionization is determined via

$$m > \frac{E_I}{h\nu} + 1 , \tag{2.22.}$$

where E_I is the ionization potential. The ionization rate in a laser beam of intensity I is proportional to I^m and the electron density. MPI is important only at short wavelengths ($\lambda < 1\ \mu m$). For longer wavelengths, simultaneous absorption of m > 10 photons is necessary which is highly improbable.
The thresholds for breakdown of solids are usually significantly lower than breakdown threshold of gases or liquids. It is useful to separate solids into transparent and absorptive insofar as they interact with laser radiation. A transparent material has a neglectable absorption at low irradiances at the laser wavelength so that high irradiances are needed to invoke a nonlinear absorption mechanism and subsequent breakdown. Breakdown will occur when electrons are generated by MPI and their density grows by electron impact of neutrals in the lattice.
If breakdown is due to electron avalanche, then one can use the wavelength scaling relation based on the heating rate Q [55]

$$Q(t) = \frac{4\pi}{c}\frac{e^2}{m_e}\frac{\nu_m}{\frac{4\pi^2}{\lambda_L^2} + \nu_m^2} I . \tag{2.23.}$$

Here, ν_m is momentum-transfer collision frequency of electrons with neutrals, λ_L the laser wavelength, and I the laser intensity. The phenomenology of laser-induced breakdown of dielectrics is similar to that of gases, the band gap ε_p corresponding to the ionization potential. In order to obtain quantitative results that adequately model, one requires an understanding of the source of initial electrons and a knowledge of the electron-photon-phonon interaction. The materials most studied both experimentally and theoretically have been the alkali halides and SiO_2. Prominent experimental and theoretical work has been done by EPIFANOV [56,57], GORSHKOV [58], YABLONOVICH and BLOEMBERGEN [59] and several others.
If a dielectric material has significant absorption coefficient α at the laser wavelength, then the layer of thickens α^{-1} is heated and will subsequently vaporize assuming that a sufficient energy per unit volume is deposited. At high temperature the vapor layer can be partially ionized. Subsequent absorption of the laser energy by inverse bremsstrahlung may eventually lead to breakdown in the hot vapor through further impact ionization. The vapor, can support a strong shock wave into the surrounding air. Absorption in the shocked air that is partially ionized may eventually lead to breakdown [60]. Further details on laser-induced heating and vaporization of surfaces were described by READY [61].
The energy deposited per unit surface of the sample by a irradiance E is $E\tau_L$, where τ_L is the duration of the laser pulse. For evaporation to occur, the energy deposited in the layer of thickens α^{-1} must exceed the latent heat of vaporization of the sample, L_v. Thus, the following threshold condition is obtained for

the minimum absorbed irradiance (E_{min}) below which no evaporation will occur [62].

$$E_{min} = \rho L_v \sqrt{\frac{a}{\tau_l}} \quad , \tag{2.24.}$$

where a is the thermal diffusivity of the sample. From the above relation follows that the vaporization threshold is dependent upon the duration of the laser pulse. A considerable difference in the ablation is a observed for a nanosecond compared with femtosecond laser pulse. Typically E_{min} is in the region of 10^{12} Wm^{-2} for a nanosecond pulse [63]. For, a typical absorptive material, the surface is raised to the vaporization temperature (boiling point) in a very short time τ_v, which is given by READY [61] as

$$\tau_v = \frac{\pi k \rho C (T_v - T_0)^2}{4\Phi^2} \quad . \tag{2.25.}$$

Here, T_v and T_0 are the temperature of vaporization and the initial temperature of material and ρ, C, and k are the density, specific heat, and thermal conductivity of the material, respectively.
The overall breakdown time is now given by the sum of the time required for vaporization of the material and the time required to breakdown the vapor.

$$\tau_{br} = \tau_v + \tau_{vbr} \quad . \tag{2.26.}$$

Time τ_{vbr} can be found from [55]

$$\tau_{vbr} = \frac{(\rho C_p)_v (T_v - T_0)}{K n_e n I (1 + R)} \quad . \tag{2.27.}$$

K is the electron-neutral inverse bremsstrahlung cross section, n_e and n are concentrations of electrons and atoms respectively which can be calculated from the Saha equation (Eq. 2.3.), I is the intensity of the laser and R the reflectivity of the sample.
In metals, absorption of nanosecond laser pulse occurs within a typical skin depth measured in nm. Unless the laser pulse is extremely short, the thermal diffusion length will be much larger then the skin depth.
The generation of substantial n_e between 10^{13} and 10^{15} cm^{-3} above the surface due to thermionic emission before and during the vaporization has often been considered as the starting point for plasma ignition. The plasma sheath that one calculates for such a high densities is, however so thin, that electron leave the surface, reflect off the edge of the sheath, and return to the surface before they make any collision with the vapor atoms. A more likely mechanism that can explain the threshold is absorption by thermally generated electrons in the vapor [64].
Further absorption of laser radiation by the ignited plasma generally commences via electron-neutral inverse bremsstrahlung, but when sufficient electrons are generated, the dominant laser absorption mechanism makes a

transition to electron-ion inverse bremsstrahlung. Photoionization of excited states can also contribute for short laser wavelengths (λ_L < 400 nm).
Such plasmas interact with the surrounding atmosphere in the two ways: (i) the expansion of plasma drives a shock wave into the atmosphere, and (ii) energy is transferred to the atmosphere by a combination of thermal conduction and radiative transfer. The relative importance of these processes in determining the subsequent plasma evolution depends on the irradiance, size of the plasma, sample vapor composition, ambient gas composition and pressure, respective thre laser wavelength. At low irradiance, conduction dominates the early stages of plasma development in the surrounding gas; the plasma is too thin, spatially and optically, to transport energy efficiently by radiation, at higher irradiances, shock wave dominates the transfer processes.

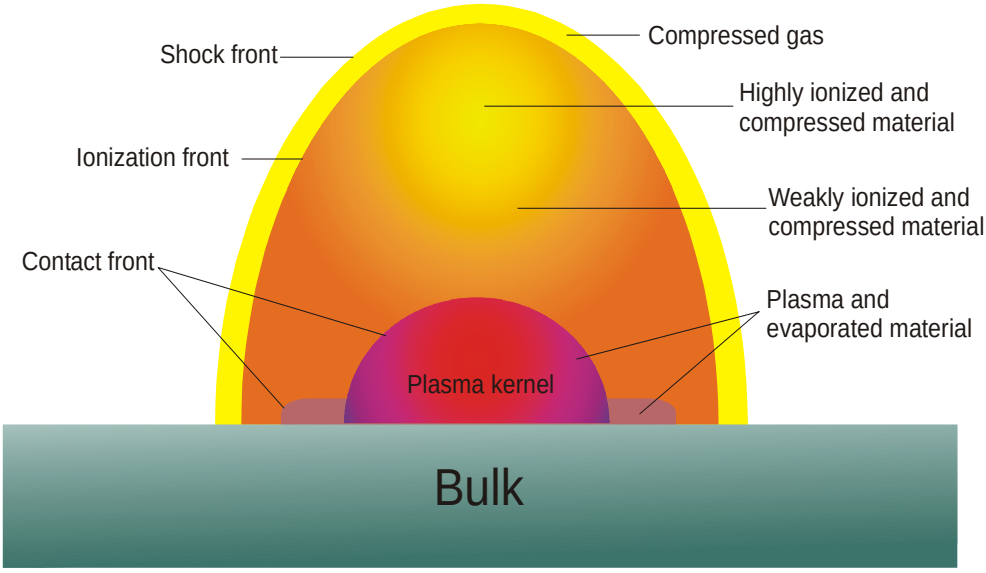

Fig. 2-4: *Plasma expansion and formation of a shock wave after plasma ignition.*

Regardless to the details of the plasma initiation, the atmosphere adjacent to the vapor plasma is heated. Gases, which were initially transparent to the laser radiation when cold, start to absorb the laser radiation. Once a critical number of electrons are generated, the heated gas layer absorbs strongly and rapidly heats to plasma conditions. As the atmosphere begins to absorb a significant fraction of the laser energy, a self-perturbing absorption process commences that results in plasma propagation into the surrounding atmosphere; subsequent layers of gas experiences the same ignition process, heating initially by energy transfer from the plasma until laser absorption is initiated in the gas, then rapidly heating by laser absorption to produce a strongly absorbing plasma. By creating absorbing gas layers in front of it, the plasma changes from its initial confined vapor state to fully developed propagating absorption wave in the gas. The plasma propagates up to the laser beam until the irradiation is either terminated or reduced to irradiance levels that can no longer support an absorption wave. The plasma up to the end of the laser pulse is optically thick throughout the entire UV to IR spectral range and, consequently, the observable spectrum is characterized by the surface temperature of the plasma, which is in the order of 10^4 K. This fuels the expansion and sustains the luminosity of the plasma for a

long time after the expiration of the laser pulse. Depending upon the ambient gases and other factors the post pulse plasma lifetimes may vary between 300 ns and more than 40 μs. A vertical cross-section of the propagating plasma is shown schematically in Fig. 2-4. More details about laser ablation can be for example found in several monographs [32, 55, 65-69].

2.2.2. Analytical Use of Laser-induced Plasma

The principles of laser-induced plasma analysis are similar to those of conventional plasma-based methods of atomic emission spectroscopy (AES) [53, 70]. The latter use the inductively-coupled (ICP), microwave-induced (MIP), and direct-current plasma (DCP) or plasmas produced by sparks or arcs. The sample to be analyzed is introduced into the plasma where it is vaporized, atomized, and electronically excited. The plasma radiation is spectrally resolved to identify emitting species. A measurement involves integration of signals from a line or set of lines of the elements of interest over a certain time period. The amount of an element present is determined by constructing calibration curves of signal vs. concentration by introducing samples of known composition into the source.

In LIPS the source of excited species is a micro plasma formed by focusing a sufficiently powerful laser beam in or on the sample to be analyzed. This distinguishes LIPS from the other conventional AES sources: There is no need for the sample to be dissolved and in that form to be transported to the source. The plasma can be formed in or on the sample in situ. In addition, because the plasma is formed by optical radiation, the method can be used to analyze gases, liquids, and solids without or with only minor sample preparation. Also, no physical contact of the sample to form the spark is needed, thereby preventing contamination.

As pointed out earlier, the laser pulse energies required to ignite a plasma depend on mode quality, wavelength, pulse length. Normally, properties of the material such reflectivity at the laser wavelength (solids) and density (gases) determine the breakdown threshold, too. Typically, irradiances between 0.5 and 10 $GWcm^{-2}$ are sufficient to generate plasma for most types of analyses [55].

Because the laser-induced plasma is transient, its excitation characteristics are a function of time. Fig. 2-5 shows the typical temporal sequence of laser-induced plasma and Fig. 2-6 shows evolution of a typical laser-induced plasma spectrum. Due to the dominating emission from free-free (ff) transitions (bremsstrahlung) and free-bound transitions (fb) transitions (recombination), the early phase of plasma emission can not be used for atomic spectroscopy. Only after a certain delay, relative to the plasma ignition, the atomic and ionic emission can be integrated for a defined time and utilized for analytical purposes. Typically electron densities are between 10^{16} -10^{18} cm^{-3} and temperatures of 6000-23000 K are observed after 1-5 μs at 1 atm in air. Both parameters, delay time and integration time, have to be optimized via optimization of signal-to-noise ratio for one or several prominent lines of an analyte. Several

optimization procedures have been developed [71, 72], and some of them will be described later.

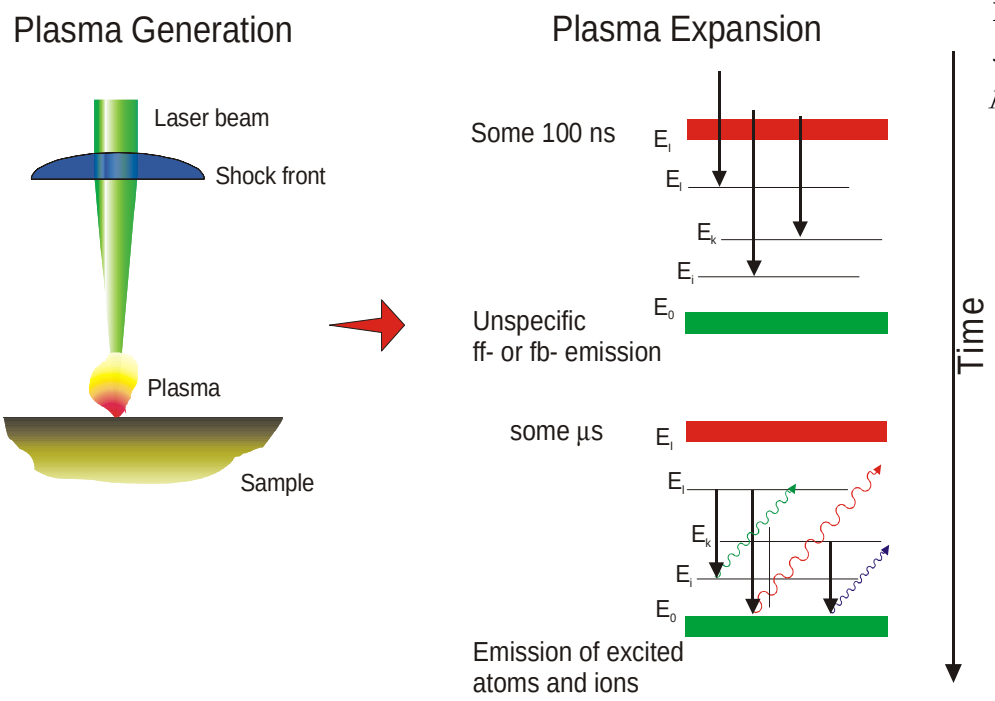

Fig. 2-5: *Temporal sequence of a laser-induced plasma.*

Quantitative Analysis

Determination of the elemental composition of a sample by LIPS requires the measurement of the intensities of those spectral lines that are characteristic of the individual species present in the sample. The intensities must then be related to the concentrations of the species present in the plasma. A quantitative LIPS analysis is based on the assumption of existence of local thermodynamic equilibrium (LTE), and on the assumption of an optically thin plasma. For LTE, the characteristic times to establish the corresponding equilibrium is essential. Macroscopic deviations are observed when the excitation and deexcitation are locally not compensated, i.e. either recombining or ionizing plasma conditions are found. Further, non-equilibrium situations can arise during the expansion of the plasma due to transport phenomena. In this case, n_e and T_e decrease faster than the corresponding ionization and population of excited states. In a transient plasma, the characteristic time τ_{plasma} for a change in the temperature or electron density

$$\tau_{plasma} = \min\left(\frac{n_e}{\frac{\partial n_e}{\partial t}}, \frac{T_e}{\frac{\partial T_e}{\partial t}}\right), \qquad (2.28.)$$

should be significantly larger then the time τ_a

$$\tau_a = \frac{1}{n_e \langle \sigma v \rangle}, \qquad (2.29.)$$

of an atomic process such as excitation or recombination.

The σ denotes here the cross section for the most frequent process and v is the electron velocity given through the Maxwell distribution and related thereby to T_e. If $\tau_{plasma} >> \tau_a$, a LTE can be safely assumed even in an transient plasma. For a delay time relative to the plasma ignition of 1-3 μs, a focal diameter (typically, d_{laser} is about 100 μm), and an expansion velocity of the plasma ($v_{exp} = 5\times10^4$ cm s^{-1}), τ_{plasma} can be estimated via d_{laser} / v_{exp} (~ 5×10^{-6} s). Although with τ_a in the order of ~ 5×10^{-7} s, the LTE assumption seems to be verified. The difference of only one order of magnitude indicates, however, that deviations from LTE in form of recombining plasma can still occur in practice.

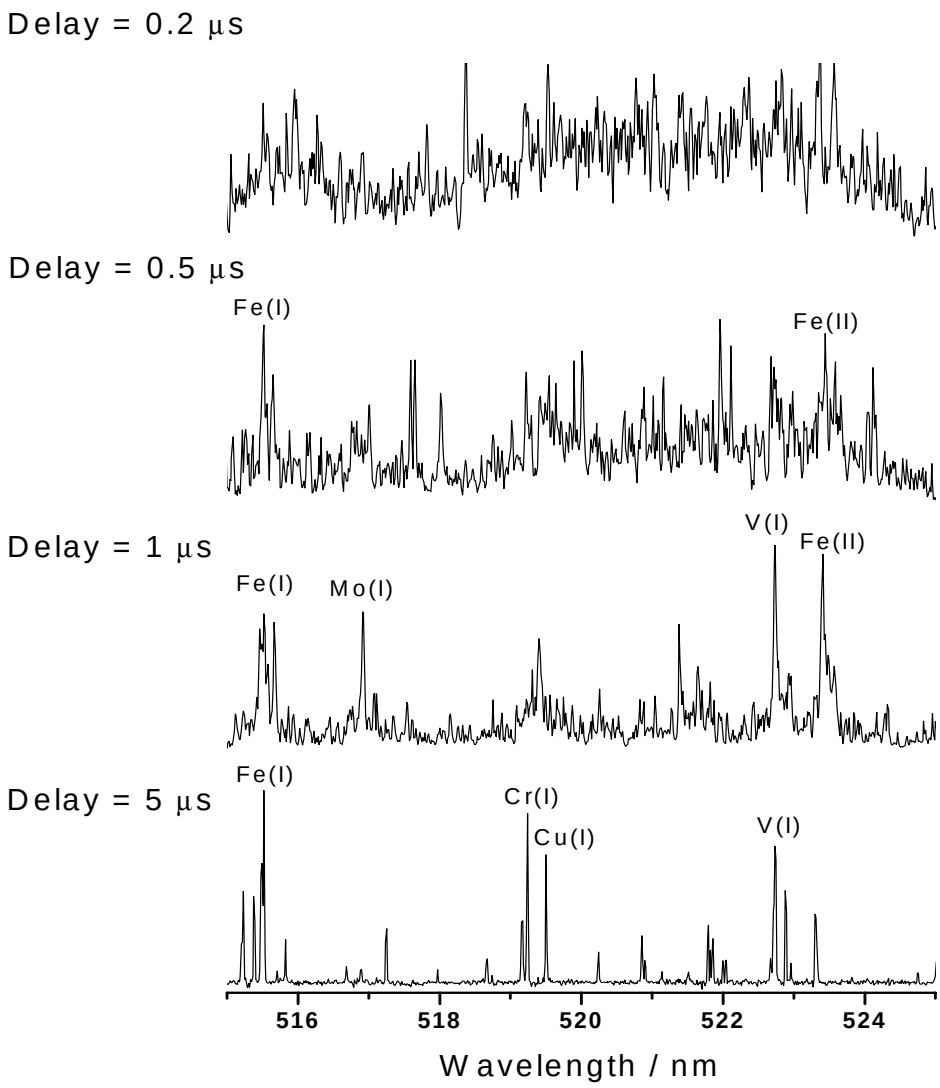

Fig. 2-6: *Temporal change of the spectrum of laser-induced plasma in a steel sample (low alloy steel SS402, Bureau of Analyzed Samples, Ltd.).*

The specific intensity of an emission line at the frequency ν is defined as the energy emitted from the plasma per unit time, unit surface area, unit solid angle, and unit frequency. Integrated specific intensity for a plasma of depth d could be obtained as

$$I(\nu) = B(\nu, T_e)[1 - \exp(-K(\nu)d)] \,. \tag{2.30.}$$

Here $B(\nu,T)$ is the Planck blackbody function and $K(\nu)$ is the absorption coefficient of the plasma which is the linear function of the number density n_i of radiators in the lower of two energy levels between which the radiative transition take place. The complete forms of $B(\nu, T_e)$ and $K(\nu)$ can be found in the literature [44, 55]. The product $K(\nu)D$ is a measure of the optical thickness of the plasma; the plasma is considered optically thin if this product is small compared to unity. If $K(\nu)D$ grows infinitely large, the specific intensity is given entirely by the blackbody function reducing, the plasma to a blackbody surface radiator at a temperature T_e.
The integrated intensity of whole spectral line with central frequency ν_0 can be defined by

$$I = \int_{(\nu - \infty)}^{(\nu + \infty)} I(\nu)d\nu \,. \tag{2.31.}$$

With Eq. 1.30 it becomes

$$I = B(\nu_0, T_e) \int_{(\nu - \infty)}^{(\nu_0 + \infty)} [1 - \exp(-K(\nu)D)]d\nu \,. \tag{2.32.}$$

The integrated intensity as given by Eq. 2.32 grows with concentration of the species in the plasma through the number density of the species, as contained in $K(\nu)$. The concentration dependence of the integrated intensity is in general nonlinear. This is because the optical depth of the plasma decreases effectively with increasing concentration, reducing the number of radiators participating in the observable emission intensity below the actual available number. In the low concentration limit, where the plasma becomes optically thin, the integrated intensity grows linear with the number density. In this limit, the integral in the Eq. 1.32 can be expanded in a Taylor series and the integral evaluated by keeping only the first-order. Assuming a Boltzmann distribution for species number densities [55] the following equation holds

$$I = \frac{hf_0 D A_{ji} g_j n_0 \exp\left(-\frac{E_j}{kT_e}\right)}{\sum_s g_s \exp\left(-\frac{E_s}{kT_e}\right)} \,. \tag{2.33.}$$

When the intensity is measured and all other properties are known, the number density of the species can be determined. The ease and accuracy of such a deter-

mination depends on the extent to which the plasma is optically thin and if the plasma properties are known through other measurements. It is quite evident that a successful analysis depends on the selection of a favorable region in time and space of the plasma for quantitative spectroscopic measurements. This has been verified experimentally as well [73-75].

The oldest and frequently used approach for quantitative analysis is based on the line ratio of the analyte and an internal standard (usually a main component) of constant concentration and similar chemical properties. The energy levels of the upper states for the observed lines and ionization potentials of the analyte and the standard should be comparable (see for example [76]).

However, as this a priori knowledge of the sample is not always available, it seems more sensible to use simultaneously recorded plasma characteristics for normalization. One of the well established methods is so-called temperature normalization. From the Eq. 2.33 the intensity ratio of two emission lines from two different species a and b is:

$$\frac{I_a}{I_b} = \frac{(f_0 A_{ji} g_j)_a}{(f_0 A_{ji} g_j)_b} \frac{Q_a}{Q_b} \frac{n_a}{n_b} \exp\left(\frac{E_{bj} - E_{aj}}{kT_e}\right). \qquad (2.34.)$$

The Q_a and Q_b are the canonical partition functions for species a and b which can be accurately calculated. Once the plasma temperature is established (usually through Boltzmann plot, see chapter 1.1.3), Eq. 2.34 can be routinely applied to measure the elemental abundance of element a in relationship to b. It follows that for multi-elemental analysis, it is desirable to choose the most abundant element as a reference. The error for this approach is mainly connected to error of determination of T_e from Boltzmann plot which lies between 10 and 40%.

A promising approach was described by PALESCCHI et al. [77] based on the hypothesis that for every element only a single line and T_e and n_e have to be known to determine the concentration of species. The method assumes that all major elements in the sample are detected which automatically gives an error in the order of the concentration of the non-detected elements. Further calibration methods described in the literature are rather phenomenological, e.g. the normalization to the acoustic signal from plasma ignition [78,79].

Problems in LIPS Analysis

It has been already shown that a linear relation between an elemental emission line and concentration of the element in a sample can be established. In practical applications this dependence can be disturbed through several factors. The most influent are: self-absorption and self-reversal of a line, non-stochiometric ablation, and fluctuation of plasma parameters such as n_e and T_e.

The radiation emitted from the relaxation of an excited species in the plasma can be absorbed by another specie, most probably, from the same element in the lower energy state of the corresponding transition. This process is named self-absorption [80,81]. Through this effect the measured line intensity in a certain time interval will be decreased. The probability for self-absorption

depends on the number of particles in the lower energy level of the transition and the transition probability. Therefore, most influenced will be the resonant transitions of the main components. Self-absorption can be diagnosed by comparison of measured and theoretical intensity ratio of two lines with different lower energy levels [44]. The second indicator is a departure from linearity of calibration curve for higher analyte concentrations [82]. Self-absorption can lead to self-reversal if the emission from the hot, inner region of the plasma is absorbed in the cooler region near the plasma surface. Because the line widths of emission and absorption are temperature dependent, the emitted line is broader than the absorption profile and observed line shows a local minimum in the center of the line.

LIPS analysis of a solid sample assumes always that the composition of the ablated gaseous material corresponds ideally to the composition of the sample itself (stohiometric ablation). Through some other methods utilizing laser ablation for a sample introduction (LA-ICP-MS and LA-ICP-OES) it has been realized that a fractionation can occur. Fractionation is related to thermal effects, i.e. components with lower melting point are preferable ablated [83,84]. Fractionation makes an accurate quantification difficult because it destroys the linearity between the LIPS signal and element concentration. It is difficult to say if the fractionation has to be expected in an unknown sample. By calibration with the set of samples which have similar physical and chemical properties, and normalization to an internal standard or some plasma parameter fractionization can be compensated [85,86].

The fluctuation of plasma parameters can not be avoided because even modern solid state laser have intensity instability in order of 5-10%. Due to the localized sampling, micro-heterogeneity of the sample can also play an important role.

LIPS as an Analytical Method

Advantages and disadvantages of LIPS can be discussed only having a concrete analytical application in mind. LIPS primary use is in the direct elemental analysis of solids, liquids, gases, and aerosols with a minimal sample preparation for on-line and in-situ analysis. On the other side, due to the detection limits in ppm range and precision of 5-10%, LIPS is not comparable with well established analytical methods such as AAS or ICP-MS. The main advantages and disadvantages are listed in the Table 2-1.

Tab. 2-1: *Advantages and disadvantages of LIPS.*

Advantages	Disadvantages
Simple and rapid analysis, sampling and excitation are carried out in a single step	Considerable interferences, including matrix and particle size effects. Bulk analysis is only possible for homogeneous samples
Possibility of simultaneous multi-element analysis	Difficulty in obtaining suitable standards

Tab. 2-1: *Advantages and disadvantages of LIPS.*

Advantages	Disadvantages
No or little preparation is necessary, resulting in increased throughput and reduction of tedious and time-consuming preparation procedures which can lead to contamination	Detection limits in the order of 5-10%
Versatile sampling of all media, non-conducting as well as conducting materials	
Very small amount of sample is vaporized, i.e.quasi non-destructive method	
Ability to analyze extremely hard materials which are difficult to digest or dissolve	
Spatially resolved analysis with resolution of a few µm	

2.2.3. LIPS Instrumentation

The experimental LIPS set-up is relatively simple and compact. Figure 2-7 shows a schematic diagram of a typical LIPS experimental set-up.

Laser Systems

Most present LIPS systems use Q-switched Nd:YAG lasers for plasma ignition. It is a 4-level laser system and its energy diagram is shown in the Fig. 2-8. The lasing material is a neodymium doped yttrium-aluminium-garnet crystal. When the neodymium ion absorbs light at wavelengths shorter than 900 nm, the ion is raised to the $^4F_{3/2}$ level or one of the higher-lying levels shown in Fig. 2-8.Those levels are rather closely spaced, so the energy gaps between them are comparable to the energy of lattice vibration and the excitation cascades rapidly down to the $^4F_{3/2}$ upper laser level. The laser emission is generated by the transition from $^4F_{3/2}$ to $^4I_{11/2}$. The $^4I_{11/2}$ level has a small energy gap to the sublevels of the $^4I_{9/2}$ ground state of the atom, so ions in the lower laser level relax very rapidly to the lower levels, emptying the lower laser level and maintaining the population inversion.

Because the upper level of the transition has a long lifetime, a large population of excited Nd ions can be stored in YAG rod. By Q-switching, energy is stored in the amplifying medium by optical pumping while the quality factor Q of the cavity is lowered to prevent onset of laser emission. This allows short, highly energetic pulses to be produced. The Nd:YAG has been usually pumped by a Xe-arc flash lamp, but diode lasers are becoming more popular. As already mentioned, the fundamental wavelength from this laser is 1064 nm but with frequency doubling it can easily convert it to visible emission at 532 nm. In addition, 355 nm emission can be generated by frequency mixing between 1064

nm and 532 nm. Emission of 266 nm is generated by frequency doubling of the 532 nm laser emission.

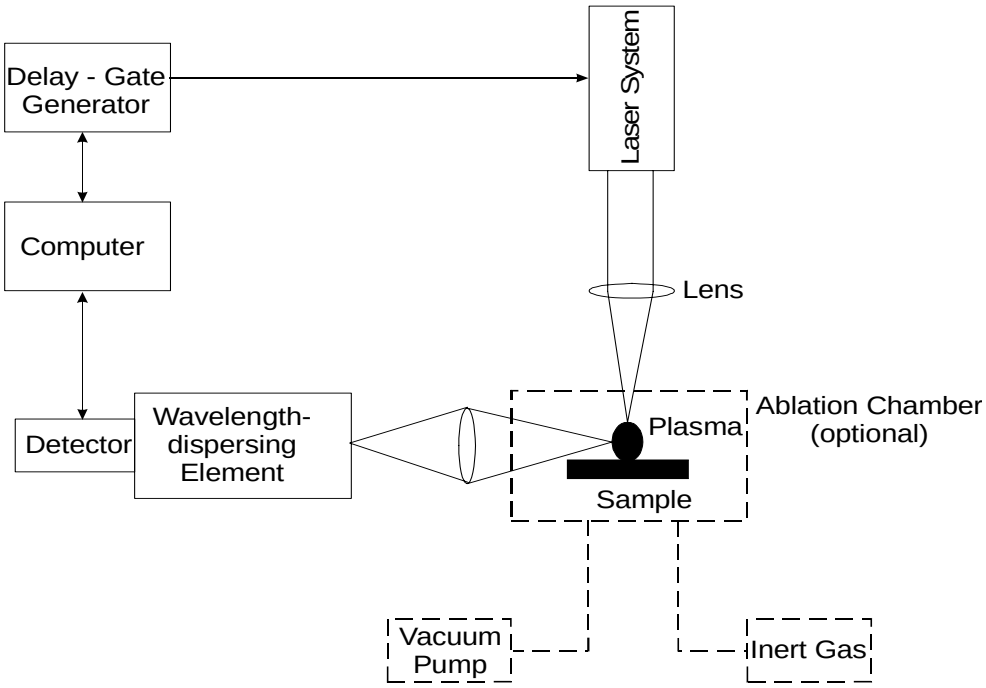

Fig. 2-7: *Block diagram of a typical-LIPS experimental set-up.*

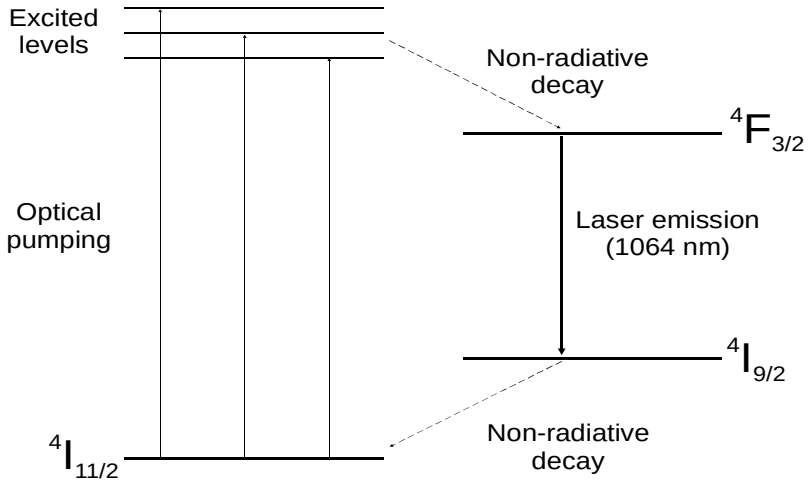

Fig. 2-8: *Energy level diagram for Nd:YAG laser system.*

The second type of laser fairly often used for plasma ignition is the excimer laser [81,87,94, 95]. The main advantage of a solid state Nd:YAG laser is its stability (1-3% precision at 1064 nm), low maintenance, and minimum infra-structure needed. In addition, the small dimensions of modern Nd:YAG's permit the construction of transportable LIPS systems.

Wavelength Dispersing Elements

Wavelength dispersing elements used for LIPS generally have to fulfill two contrary requests: (i) need for high resolving power $\lambda/\Delta\lambda$ because of highly pronounced spectral interferences in atomic emission spectroscopy (see Fig. 2-9). For example, Fe has an average of five lines per nanometer in the UV-Visible range. (ii) For multielemental analysis with single laser pulse the wide spectral region should be covered.

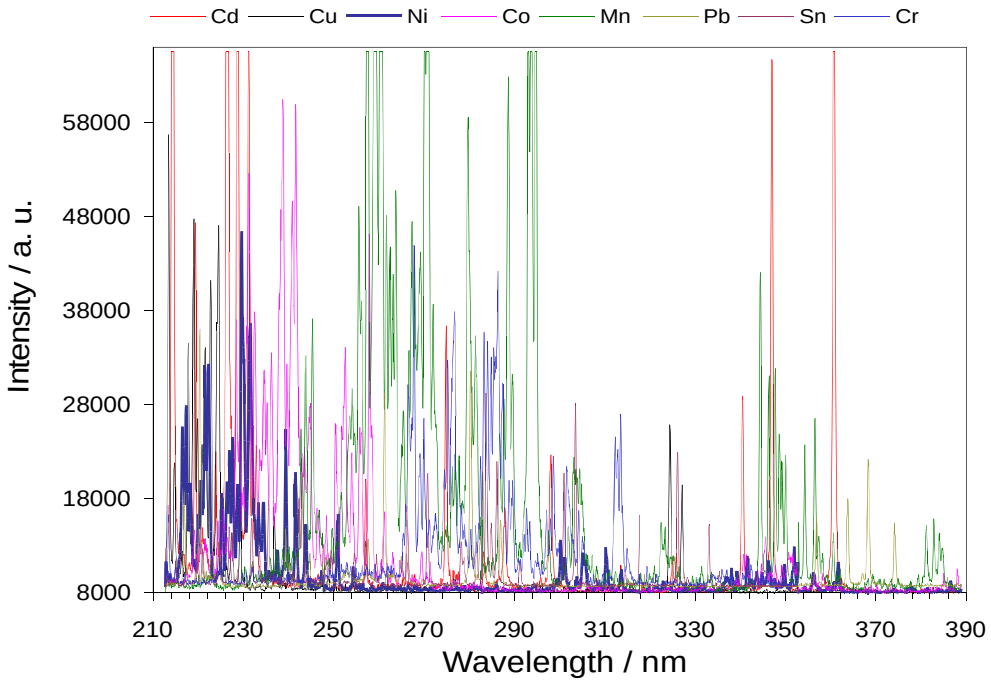

Fig. 2-9: *Spectral interferences of emission for some typical heavy metal analytes (0.3-m-Czerny-Turner spectrograph, 1200 l mm^{-1} grating).*

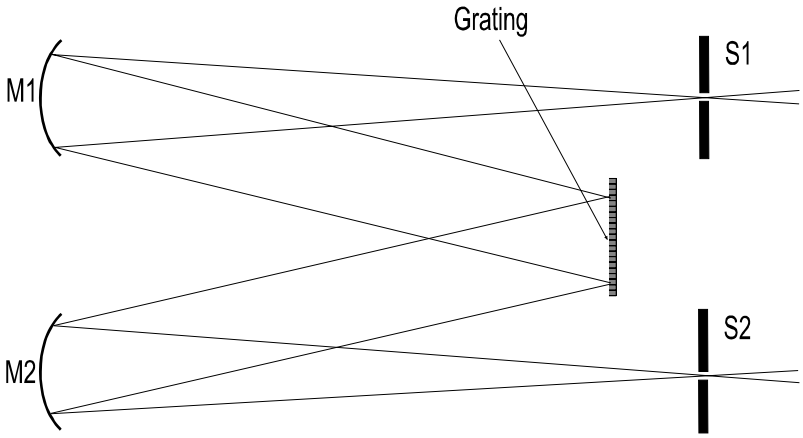

Fig. 2-10: *Czerny-Turner plane grating monochromator.*

Today, usually, four different spectrograph mountings are mainly in use for OES: Czerny-Turner, Echelle, Rowland and Paschen-Runge. Here, only the first two systems will be described, descriptions of Rowland and Paschen-Runge spectrographs can be found for example in [96].

A Czerny-Turner mount using a plane grating is shown in the Fig. 2-10. The incident radiation passes through the entrance slit S1 and strikes the parabolic collimating mirror M1. This mirror produces a collimated light beam reflected onto the grating, which spatially disperses the spectral components of the incident radiation. Collimated rays of diffracted radiation strikes the parabolic focusing mirror M2. The dispersed radiation is focused in the focal plane producing the entrance slit images in that plane. Because the parallel rays of a given wavelength are incident on the focusing element at a specific angle, each wavelength is focused to a slit image at a different center position on the focal plane. The exit slit S2 isolates a particular wavelength interval.

For simultaneous detection of multiple lines over a large spectral range, echelle spectrographs are the systems of choice. They offer the necessary spectral

coverage and spectral resolving power for minimizing spectral interferences in complex matrices. An echelle spectrograph employs two dispersing elements, an echelle grating and an, orthogonally placed, prism. The echelle grating, which was first described by HARRISON in 1949, provides higher dispersion and higher resolution than a common (echellete) grating (Fig. 2-11 a and b) of the same size [70].

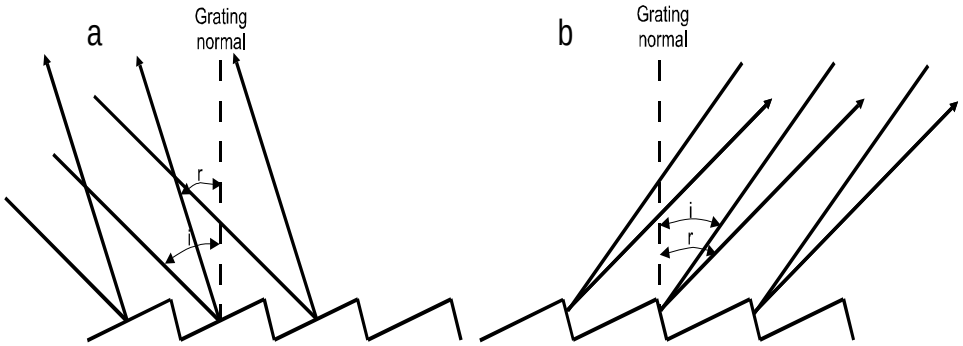

Fig. 2-11: *Mechanism of diffraction for an echellete (a) and an echelle (b) grating.*

To achieve a high angle of incidence, the blaze angle of an echelle grating is significantly larger (typically 63°-76°) than of a conventional one (10°-38°), and the short side of the blaze is used rather then the long. Furthermore, the grating is relatively coarse, having typically 300 or fewer grooves per millimeter for UV-Visible radiation. Note, that the angle of refraction r is much higher in the echelle grating than the echellete and approaches the angle of incidence i ($i \approx r = \beta$). Under these circumstances the condition for a constructive interference

$$n\lambda = d(\sin i + \sin r) \tag{2.35.}$$

becomes

$$n\lambda = 2d\sin\beta \ . \tag{2.36.}$$

With a normal echellete grating, high dispersion, or low reciprocal dispersion, is obtained by making the groove width d small and the focal length f large. A large focal length reduces light gathering and results in monochromators of large dimensions. In contrast, the echelle grating achieves high dispersion by making both the angle β and the order of diffraction n large. The reciprocal dispersion for an echelle grating can be obtained via

$$D^{-1} = \frac{2d\cos\beta}{nf}. \tag{2.37.}$$

The linear dispersion at the high orders of refraction for an echelle grating is so extended that to cover a reasonably broad spectral range it is necessary to use many successive orders. As these orders inevitably overlap, it is essential that another dispersing element is employed. This is usually an orthogonally placed low-dispersion prism. In this way, a two dimensional spectrum is generated, as shown in Fig. 2-12.

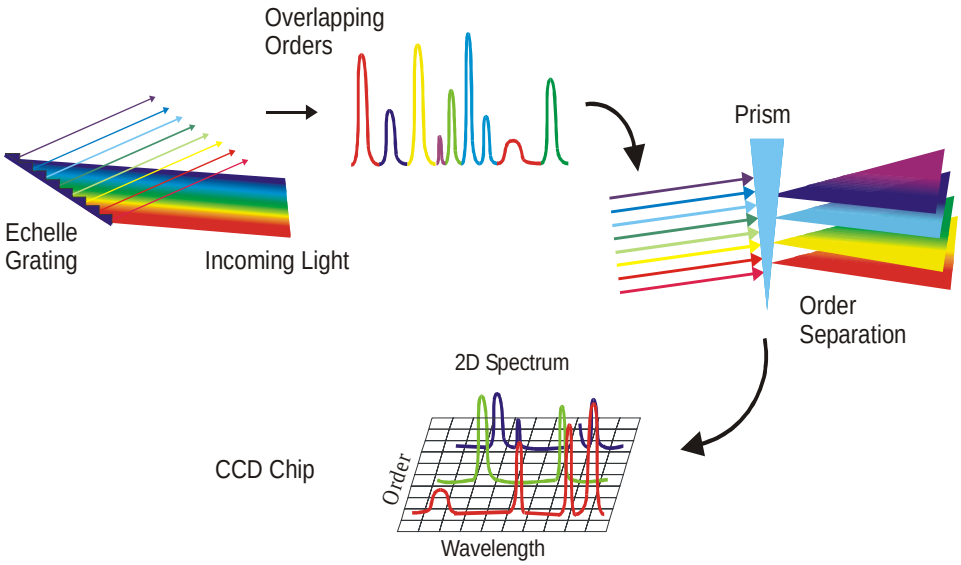

Fig. 2-12: *Operation principal of an echelle spectrograph.*

Detectors

For the detection of plasma emissions in LIPS experiments, photomultipliers (PMT), charge-coupled and intensified charge coupled devices (CCD and ICCD) and optical multichannel analyzers (OMA) can be utilized depending on the type of spectrometer. More general information about optical multichannel analyzers can be found in [53,70,97].

A photomultiplier tube (PMT) consists of the photo-emissive cathode, several dynodes, and an anode. When the radiation hits the chatted electrons are generated. A high voltage across the dynodes leads to further multiplication of these photoelectrons (typically 10^6-10^8 electrons for each incident photoelectron). A PMT is relatively inexpensive and very sensitive detector, which allows recording of time-integrated plasma emission signals (see Fig. 2-13). It requires, however, a scanning mode monochromator to obtain full spectral information about an emission line. Therefore, the PMT is not convenient for multielement analysis with a single laser pulse or when fast scan results are required.

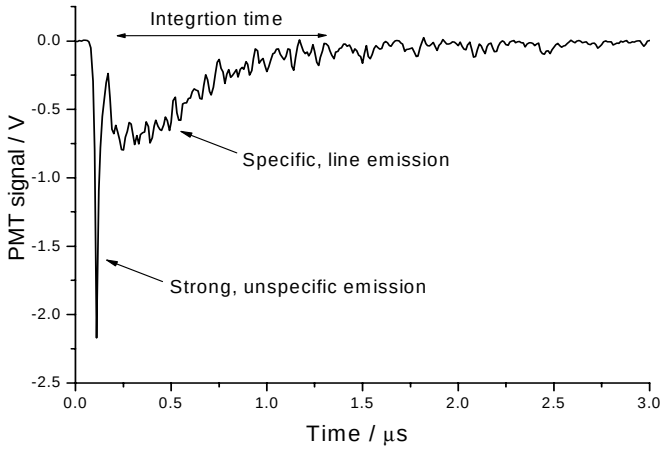

Fig. 2-13: *Typical plasma emission signal recorded with a PMT.*

The charge coupled devices (CCDs) are made up of a two-dimensional array of semiconductor capacitors (pixels) that have been formed on a single silicon chip. Commercially available CCD chips usually consisted of 512×512 or 1024×1024 pixels. Performance characteristics of these instruments with respect to sensitivity, dynamic range, and signal-to-noise ratio appear to approach those of PMT's in addition to having the multichannel advantage.
A CCD system can be equipped with an intensifier (microchannel plate, MCP) which allows high photonics gain (about than 10^6 electron/photoelectron) and possibility of electronic gating which is of essential importance for time-resolved LIPS measurements.Special advantage arises from the combination of an ICCD camera with an echelle spectrometer. With this system it is possible to record an emission spectrum simultaneously as shown on the Fig. 2-14. For more information about principles and application of CCDs and ICCD's see [98,102].

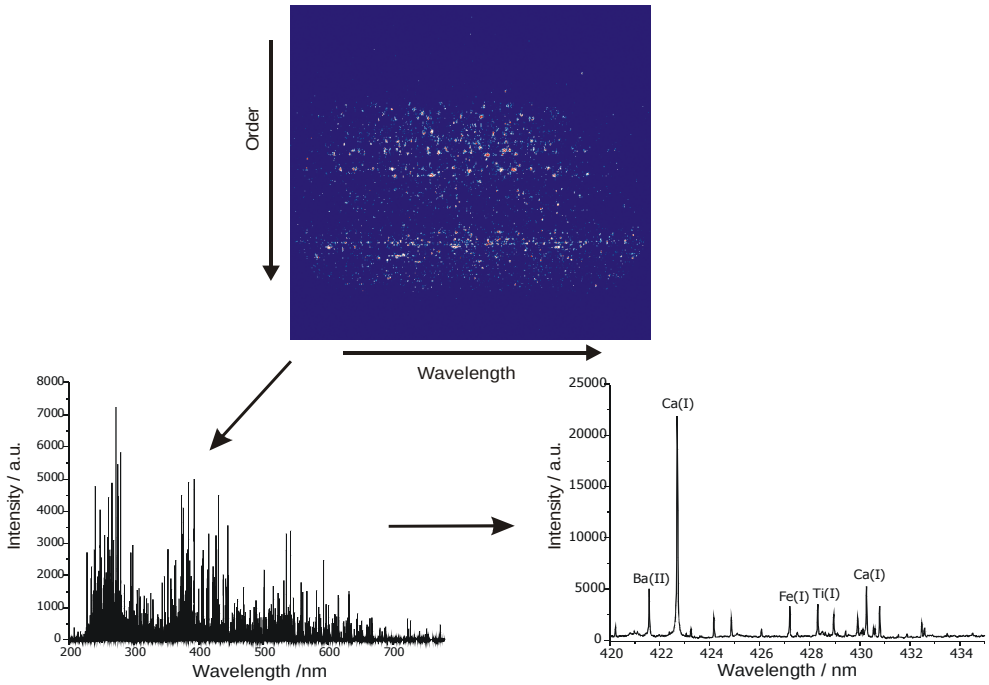

Fig. 2-14: *A 2D and 1D LIPS spectrum (200-780 nm) of an coal sample made recorded with an Echelle spectrometer coupled to an ICCD camera.*

2.3. Vacuum Ultraviolet Spectroscopy

The vacuum or the far ultraviolet designates the spectral region which extends between 1 and 200 nm. The long-wave limit of this region is fairly defined, as it is near 200 nm where the region of continuous absorption of oxygen begins. The shortwave limit is much less defined. Here, the vacuum ultraviolet (VUV) overlaps with the soft x-ray spectrum. The difference between these two regions is simply that ultraviolet or optical radiation corresponds to energy changes of outer (optical) electrons of an atom or ion, while x-ray corresponds to energy changes of the inner electrons. The optical radiation in the overlapping region is generally produced from highly ionised atoms. The shortest

optical emission line presently observed is a line from Fe (XXII) at 0.9 nm [48]. Various names have been given to the wavelength region below 200 nm. However, because of opacity of air between about 0.2 and 200 nm and the consequent need to evacuate spectrographs, this region is usually addressed as vacuum ultraviolet. Responsible for the opacity of air in this region is molecular oxygen (O_2). The absorption bands between 175 and 200 nm corresponds to the $B^3\Sigma^-_u$ - $X^3\Sigma^-_g$ transitions [103] and are called Schumann-Runge system (Fig. 2-15 a). The region 130 to 175 nm is continuous, i.e. the Schumann-Runge continuum (Fig. 2-15 b). Below 130 nm numerous Rydberg transitions are observed (Fig. 2-15 c). The second important absorber in VUV is water. Below 124 nm sharp rotational structures have been observed and assigned to the $^1B_1$-$^1A_1$ transitions [103]. The absorption coefficient of water in VUV has been measured by WATANABE et al. [104,105] and is shown in Fig. 2-16.

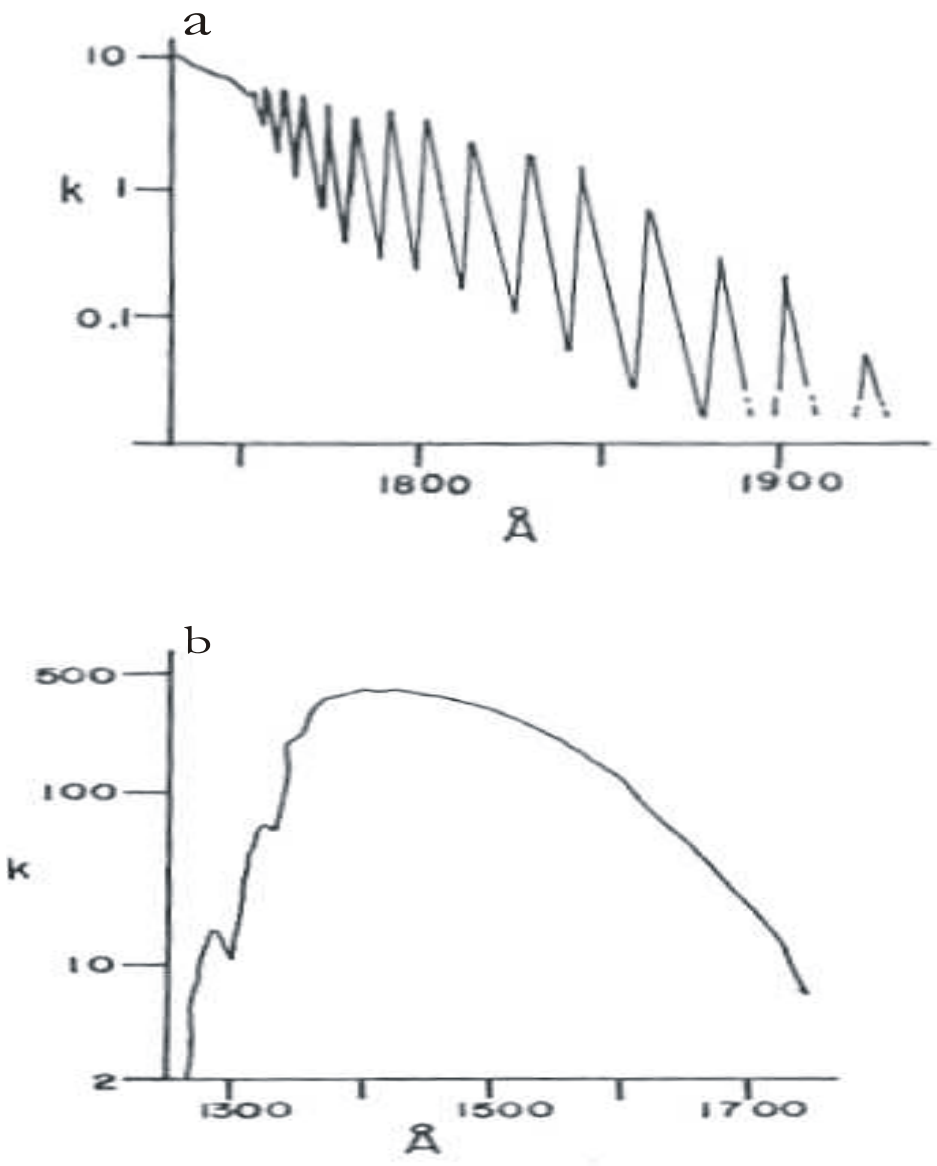

Fig. 2-15 a-c: *Absorption coefficient of O_2 in the region 110 to 200 nm. k is in units of atm^{-1} cm^{-1} (addopted from [107]).*

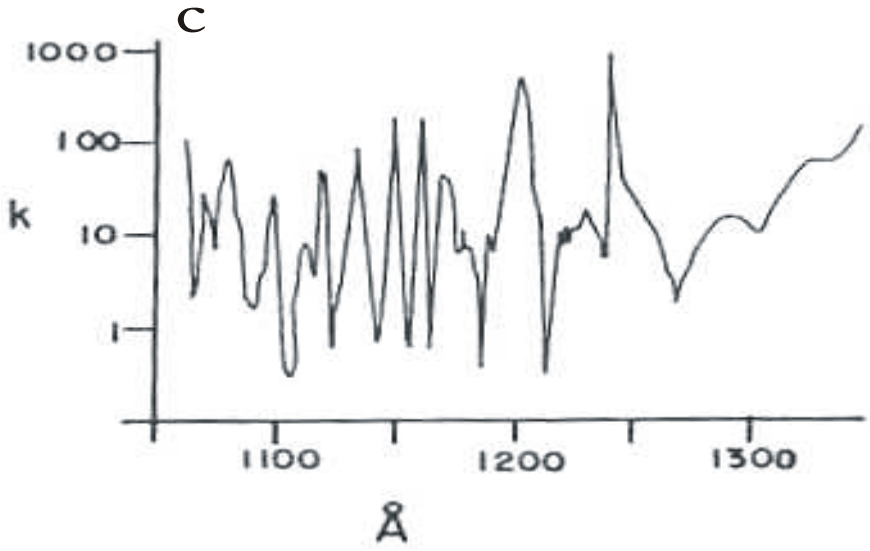

2.3.1 Instrumentation for VUV spectroscopy

Historically, VUV spectroscopy began with SCHUMANN (1841-1913) who build the first vacuum spectrograph in 1893 and made investigations in this region. He employed a fluorite prism as dispersing element, but because the dispersion of fluorite was unknown, he was unable to determine the wavelengths of the dispersed radiation. Nevertheless, he was able to show that air and, in particular, oxygen was responsible for the absorption below 200 nm. LYMAN, using a vacuum spectrograph equipped with a concave diffraction grating, was the first to measure exact wavelengths in the VUV. He found that Schumann's spectrum had a short wavelength limit of about 125 nm, the limit due to the transmission characteristics of fluorite. The region between 125 and 200 nm is now known as the Schumann region (Fig. 2-17).

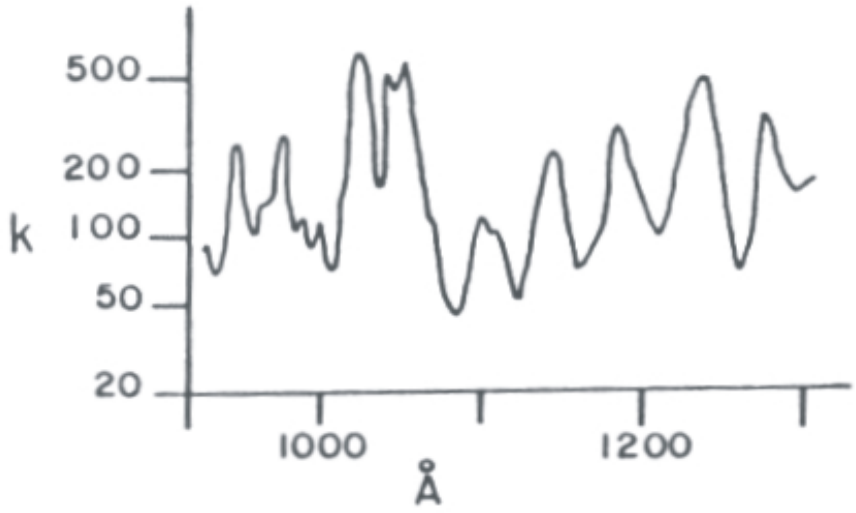

Fig. 2-16: *Absorption coefficient of H_2O in VUV region. k is in units of atm^{-1} cm^{-1} (addopted from [107]).*

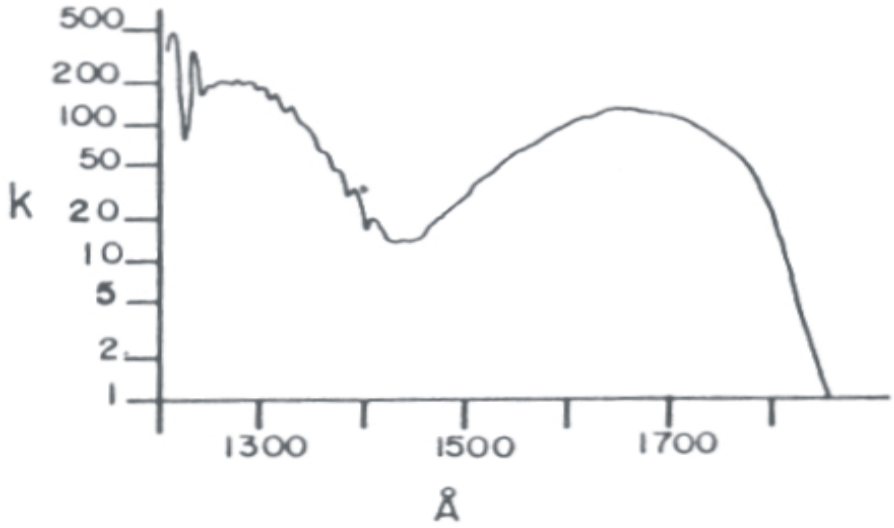

The VUV can be also divided in different spectral subregions due to the nature of the optical instruments used. For example, below 100 nm, transparent materials can not be used, and below about 30 nm the low reflectance of grating necessitates the use of a grazing incidence spectrographs. Additionally, the use of different light sources tends to establish separate regions for the experimenter. The H_2 glow-discharge lamp provides useful radiation for investigations in Schumann region. At shorter wavelengths sources based on high voltage condensed spark discharge type have to be used. This is the region of extreme ultraviolet. Since this region includes the soft x-ray region it has been named XUV.

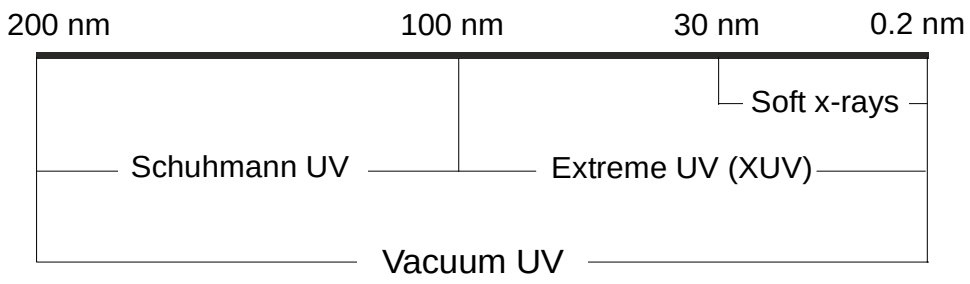

Fig. 2-17: *The wavelength range and nomenclature used in vacuum ultraviolet.*

Optical Materials

In addition to fundamental requirements of transparency and reflectance in the VUV, the optical materials should also meet a number of other specifications: they should be homogeneous, easily machined, readily accessible, and their properties should be immune to the effects of radiation at the relevant wavelengths.

Going deeper into the VUV, the range of suitable optical material diminishes, and in fact no single bulky solid is transparent below 100 nm.

The crystals of CaF_2, MgF_2, BaF_2, LiF, and sapphire (α–Al_2O_3) are transparent in the vacuum ultraviolet. Minor impurities, however, may substantially lower their transmittance especially in the short-wave region. Considerable reduction of transmittance in the short-wave region is mostly associated with the absorption of radiation by a thin surface film, and not by the crystal bulk property.

This harmful film may be a reaction production of some active medium which attacked the crystal during the storage or normal service life.
For the manufacturing of prisms, CaF_2 is usually used and for lenses CaF_2 and MgF_2. Transmittance characteristics of CaF_2 and MgF_2 are summarized in the Fig. 2-18. The absence of sufficiently transparent materials in extreme ultraviolet leads to an ever growing use of reflection optics. The reflection coefficient is highly sensitive to the incidence angle of radiation and this is particularly noticeable at the wavelengths below 100 nm.

.

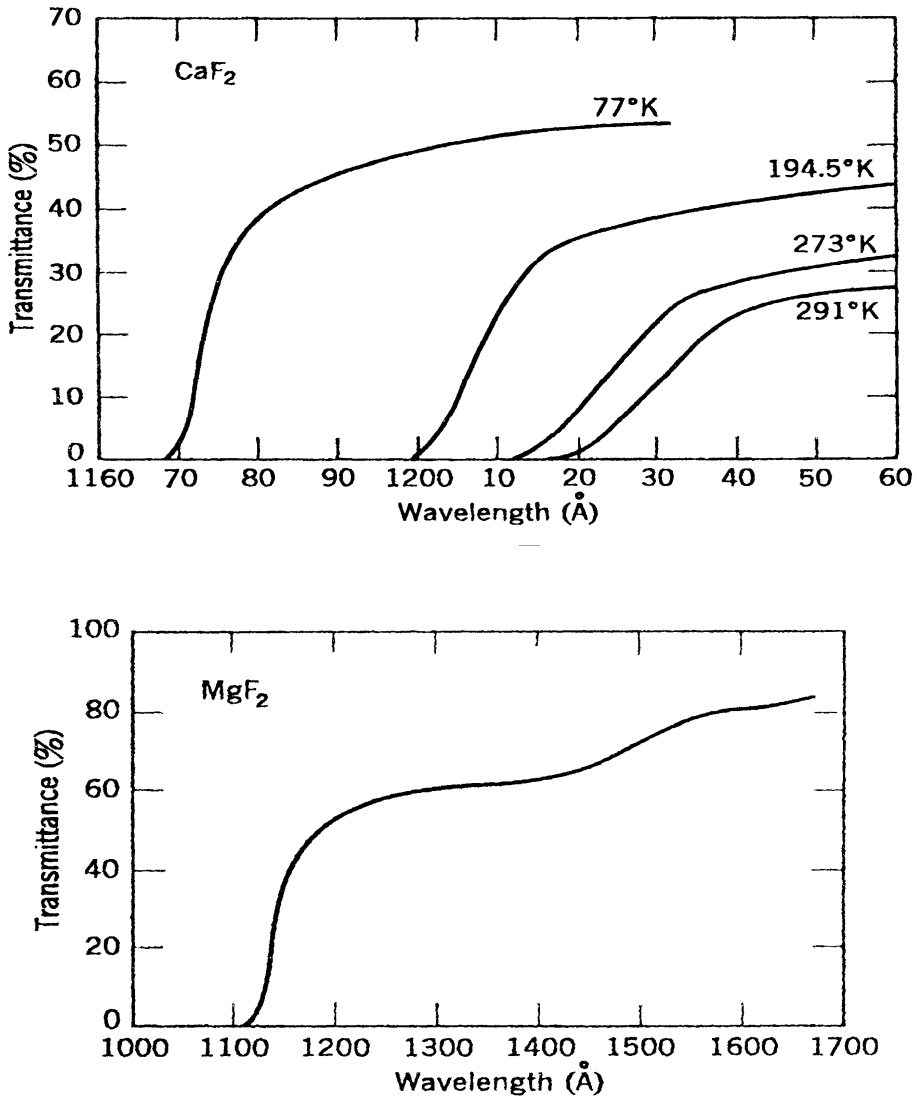

Fig. 2-18: *Transmittance of CaF_2 (up) and MgF_2 (down) in the VUV. Values for CaF_2 are given for the different values of crystal temperature (addopted from [106]).*

As reflecting materials mainly aluminium is employed to coat mirrors and diffraction gratings. The reflection coefficient is of aluminium is highest for the normal incidence at the wavelengths above 100 nm. Reflection coefficient of aluminium layer soon after deposition is fairly constant between 100 and 200 nm reaching over 85% and decrease with time which is associated with the oxidation of aluminium. (Fig. 2-19).
To prevent the formation of the oxide film the aluminium surface may be coated with an MgF_2 film which protects the metal against oxidation. If the film thickness is appropriately chosen, constructive interference will enhance the

reflection coefficient. Beside aluminium, as reflective materials, platinum group elements (Pt, Rh, Au) and several kind of multilayered films are in use [106]

Spectrometer

The range of spectral instruments for the vacuum ultraviolet is substantially more limited than for the other spectral regions. Researchers often have to use instruments of their own design, custom built in their laboratories. Commercial instruments are only of the newer date.

The difficulties in manufacturing spectral instruments for the short-wave region arise from the exact precision requirements to be met by the optical and the mechanical components intended to use at short wavelengths, as well as from the overall decrease in transmission and reflection coefficients of most materials in the VUV. The sharpness of the image depends on the relative deviation of the actual surfaces from the ideal theoretical profiles, measured in the number of wavelengths. Therefore, in the long-wavelength region (say, IR) fairly crudely finished gratings and lenses are quite acceptable, whereas the optical components in the VUV are expected to meet much higher precision standards.

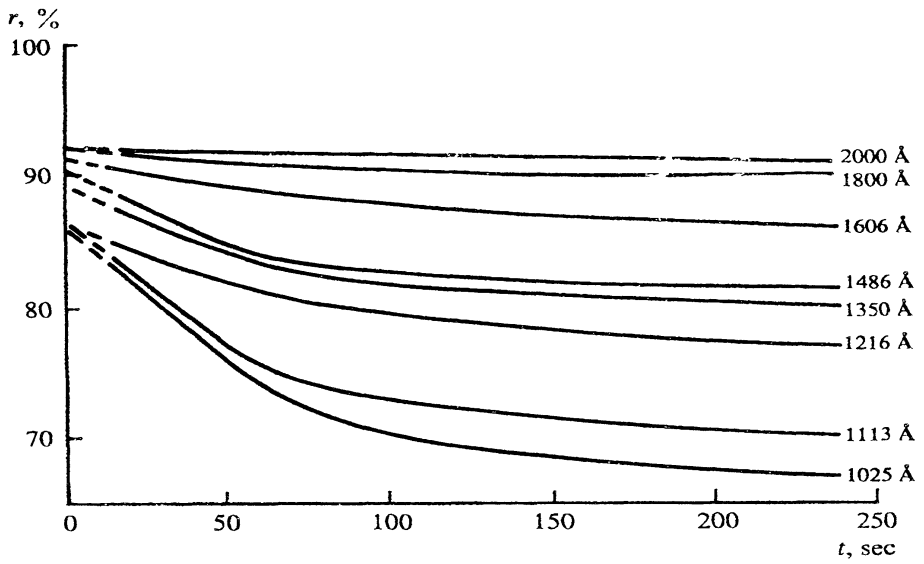

Fig. 2-19: *Effect of aging on reflection coefficient of aluminium film (addopted from [106]).*

An additional difficulty is associated with the vacuum conditions that have to be maintained. This not only places definite restriction on the design of the body of the instrument, but also substantially complicates various routine operations such as instrument adjustment and source alignment. It is relatively difficult to create a sufficiently high vacuum in a large volume. To avoid the tedious pump down stage, it is possible to fill the instrument with a gas that is transparent at the relevant wavelengths, such as Ar, He, or N_2. However, to eliminate the effect of residual gases, the instrument had first to be evacuated.

At wavelengths shorter than 50 nm, the angle of incidence of light is generally greater than 80°. This is the only way to ensure sufficient energy in the diffracted beam. The corresponding instruments are known as grazing-incidence instruments. At wavelengths above 100 nm, small incidence angles are generally used (0-30°). These are so called normal incidence instruments.

Between 50 and 100 nm, instruments of the both kinds can be used, depending on the particular problem.
Spectral dispersing instruments in the VUV usually employ both concave and plane grating. Plane gratings have unique advantage to produce a strictly stigmatic image. These grating, however, require concave focusing mirrors, and additional light losses severely limit their uses. Several kind of well known grating mountings are in use in VUV: Paschen-Runge, Rowland, and Czerny-Turner, etc.. Detailed theoretical consideration about concave and plane grating as well as overview of grating mountings for VUV is given in two books about VUV spectroscopy from ZAIDEL and SHREIDER [106] and SAMSON [107].

Detectors

A wide range of detectors, originally developed for other spectral regions, have adequate response and sensitivity in the vacuum ultraviolet. Alongside with these, there are detectors which are used exclusively in the vacuum ultraviolet, since they are virtually insensitive to photons with energies less then 6-7 eV (ionization chambers, some photocathodes etc.).
Photomultipliers for VUV are generally divided into closed and open types. In closed-type detectors, the photocathode is protected by a special screen which converts the short-wave ultraviolet radiation into longer wavelengths. In open-type detectors, the photocathode is directly exposed to the incident radiation.
Phosphors, when exposed to the VUV emit, light which readily passes through the glass windows of photocells and photomultipliers. The spectral composition of the emission of most phosphors is independent of the wavelength of the exciting radiation. The phosphor layer in detectors is applied either directly on the photomultiplier window or on special screen mounted in front of the window. Observation can be made via the transmitted and reflected radiation; the latter mode often reduces the scattering component. The most common phosphor is saturated solution of sodium salicylate. Its fluorescent spectrum has a maximum at 420 nm (see Fig. 2-20). A freshly prepared layer of sodium salicylate has a constant quantum efficiency (within 10%) between 40 and 340 nm. At wavelengths shorter than 160 nm the quantum yield decrease rapidly with the age of the layer [107].
Other fluorescent materials in use are: diphenylstilbene (DPS), tetraphenyl butadiene (TPB), anthracene, and several kinds of plastic and liquid phosphors and inorganic crystals [107]. Sensitive photocathodes for open-type photomultipliers use the volume photo-effect, whose quantum efficiency in metals is higher then that of surface photo-effect. Pure metals can be used for the corresponding photocathode (Ni, Pt, W, Cu, Ag). The quantum efficiency of pure metals around 100 nm is about 10%. Various photomultipliers use binary compound photocathodes with sufficiently high quantum yield (BeCu, CuI, CsTe, CsSb, RbTe, CsI, etc.). At wavelengths around 10 nm, CsI and SrF_2 photocathodes are particularly effective, their quantum efficiency reaches 10 - 40% [106].

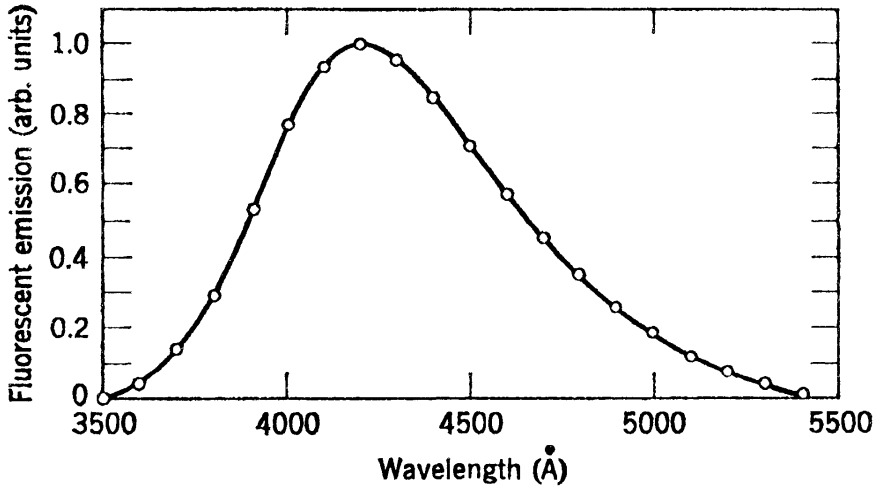

Fig. 2-20: *Fluorescent emission spectrum of sodium saliciyate (adopted from [106]).*

Direct illuminated CCDs are not commonly used in the VUV because of the poor quantum efficiency obtainable with commercially available CCDs. The 1/e attenuation length of silicon is less then 10 nm for the wavelengths between 90 and 360 nm [108] and photons are absorbed in the CCD gate structure or in the surface dead layers.

These problems can be minimized by coating the CCD with some phosphor [109] to convert the UV wavelength to a more penetrating visible photon or to illuminate the backside of the CCD after the silicon substrate has been thinned to expose the active epitaxial layer [109]. Use of these techniques can provide acceptable (30-40%) quantum efficiencies in the range 100 - 200 nm. ICCDs for VUV appeared also recently on the market. Generally the performance of the ICCD is determined by the intensifier (MCP).

Vacuum Techniques

The degree of vacuum necessary in a spectrograph to prevent any appreciable attenuation of the radiation from the source depends on the wavelength and the path length from the source to the detector via the diffraction grating. The amount of attenuation of the radiation is given by the Lambert-Beer law, namely,

$$I = I_0 \exp(-k(\lambda) p D d) \ , \qquad (2.38.)$$

where I_0 is the intensity of the source, I is the intensity reaching the detector, d is path length, p is the pressure and $k(\lambda)$ is the molar absorption coefficient in units of $mbar^{-1}m^{-1}$. The absorption coefficient of gases is a function of wavelength (e.g. energy) and generally larger at wavelengths shorter than the first ionization potential. Since the first ionization potential of most gases is located below 110 nm, and no window materials exists below 104 nm, the minimum vacuum requirements are divided naturally into two regions above and below 110 nm. The region below 110 nm not only requires a better vacuum than the region above 110 nm, but it also requires higher pumping speeds to remove the gas, which continually diffuses in through the entrance slit from the radiation source.

Figure 1-22 shows amount of absorption vs. path length for pure O_2 at the 150 nm (maximum of absorption coefficient) calculated from Lambert-Beer law. For a pressure below 10^{-4} mbar there is practically no absorption and this value can be taken as the upper limit for VUV spectroscopy. A common pumping system used for spectroscopic measurements above 110 nm consists of a high speed turbo molecular pump with a mechanical pump (rotary vane or piston) as a pre-pump [108]. Pumping capacity and speed of the system has to be chosen for a concrete experiment depending of recipient volume and leak rate. For the end pressure measurement, a ionization gauge is usually employed Further details about designing a vacuum environment can be found, for example, in the very concise book about vacuum technique from O'HANLON [110].

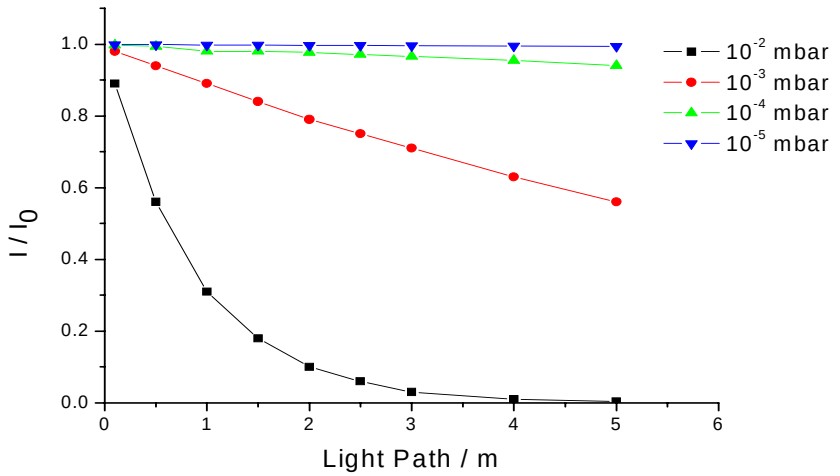

Fig. 2-21: *Amount of O_2 absorption at 150 nm calculated from Lamber-Ber law.*

2.3.2. Spectrochemical Analysis in VUV

The resonance lines of numerous elements (some 20%) fall in the vacuum ultra-violet. These include the resonance lines of the inert gases, halogens, and most other non-metals. The sensitivity of determination of these elements by VUV spectroscopy is higher than by spectroscopic analysis in the near UV or visible range. Table 2-2 gives a list of resonance lines of several elements which lie below 200 nm.

Tab. 2-2: *Resonance lines below 200 nm.*

Element	λ / nm	Element	λ / nm	Element	λ / nm
H	102.6; 121.6	P	177.5; 178.3	Br	148.9; 157.6
He	58.4; 53.7	S	180.7; 190.0	Kr	116.5; 123.6
C	156.1; 165.7	Cl	134.7; 138.0	I	183.0
N	113.5; 135.6	Ar	104.8; 106.7	Xe	129.6; 147.0
O	130.2; 135.6	As	189.0; 193.8	Hg	184.9

Tab. 2-2: *Resonance lines below 200 nm.*

Element	λ / nm	Element	λ / nm	Element	λ / nm
F	95.2; 95.5	Se	196.1	Rn	145.2; 178.6
Ne	73.6; 74.4				

In general the analytical sensitivity is higher for elements with relatively simple spectra (i.e. for systems with a single optical electron). Hence it follows that carbon can be determined with higher sensitivity using the C(IV) lines than the C(I) lines. This conclusion is only valid if the concentration of the corresponding ions in the discharge is comparable with the concentration of normal atoms; this condition can be met by using a sufficiently hot source for sample excitation.

LIPS in the VUV

Almost all VUV-LIPS investigations are concentrated on analysis of non-metals (at the first place C, N, O, P, S) in steel matrix and possible applications for process analysis in steel industry where typical LIPS advantages like speed and absence of sample preparation have significant importance.

In 1991, CARLHOFF et al. [111] demonstrated a LIPS system for the analysis of carbon concentration directly on a steel melt in a converter. The limit of detection (LOD) for C was about 200 ppm. In 1995, GONZALES at al. [112] used LIPS for determination of the sulphur concentration in referenced steel samples using the S(I) lines from the VUV. They applied an 1-m vacuum Czerny-Turner monochromator and an optical multichannel analyzer as a detection system. Both, monochromator and sample chamber were filled with N_2 to 1000 mbar. A LOD of 70 ppm and precision of 7% were reported. In the same year, SATTMAN et al. [113] used multiple Q-switched Nd:YAG laser for plasma ignition on steel samples. They used two different detection systems: A Czerny-Turner spectrometer with an intensified photo-diode array and a Paschen-Runge spectrometer with several PMT's. Material ablation is found to increase with multiple pulses compared to single pulses as well as electron temperature and densities. They reported an improved precision and lower LODs, i.e. 6 ppm and 90 ppm for boron and carbon, respectively. In an extension of this work, STURM et al. [114] used again multiple laser pulses for excitation and reported excellent LOD's bellow 10 ppm for S, P and C.

KHATER et al. [115] used time-integrated, space-resolved laser-induced plasma spectroscopy (TISR-LIPS) for the quantitative determination of carbon content in steel. They used a 1-m normal incidence vacuum spectrometer coupled with microchannel plate photo-diode array and observed several C(II) and C(III) lines from the XUV. A lower limit of detection (87 ppm) was obtained for the C(III) 97.7 nm line. HEMMERLIN et al. [116] described the development of an industrial prototype with the ability to use either a spark or laser source for excitation on the same optical mounting to directly compare the performances of both sources. Similar LOD's for C, N, S, and P between 2 and 100 ppm were reported.

Most recently, KHATER et al. [117] made a detailed optimization study of the parameters important for laser produced steel plasmas such as: laser focusing lens type, laser wavelength and energy, ambient atmosphere and pressure as well as spatial distribution of emitting species. In this way, an improved LOD for carbon in steel of 1.2 ppm was reported.

3 Double-Pulse LIPS

3.1. Introduction

Two main advantages of LIPS, it's speed and reduced sample preparation, stem from the fact that sampling, atomization, and excitation of the sample is made in a single step. However, the processes of ablation, laser-plasma interaction, and excitation of the ablated material are already very complicated, and can not be controlled and optimized separately. This condition often leads to poor precision and detection limits inferior to comparable methods, such as spark spectroscopy. To address these problems, the use of two laser pulses separated by a short time interval has been proposed by several authors [92,118,127] Earlier studies claimed an enhanced ablation, an improved S/N ratio and consequently lower detection limits.

Double-pulse LIPS experiments are usually performed in two geometries: (i) A collinear geometry where both laser beams are incident onto the same spot on the sample surface (Fig. 3-1a). (ii) An orthogonal geometry where one laser beam is aligned perpendicular to the sample and focused on the sample surface (ablation laser), while the second laser beam is aligned parallel to the sample surface and focused slightly above it (Fig. 3-1 b). Considering the timing between the two pulses in the orthogonal geometry, it is possible to define two modes: reheating and pre-ablation. In the reheating regime, the second laser pulse is used to reheat the already decaying ablation plasma. The main idea behind this approach is that during the time after impact of ablation pulse droplets and clusters from the sample enter the hot plasma just above the sample surface where they are further vaporized and atomized. However, the initially very hot plasma is considerably cooled down by the process of atomization and therefore line emission is almost ceased after a delay of 10 μs or more. There-

fore, it is sensible to try to reexcite the sample atoms by reheating the plasma with the second laser pulse.A similar approach was already applied in an early commercial LIPS system, the LMA10 which utilized an electrical spark for reheating [32]. In the pre-ablation mode, the first laser pulse, parallel to the sample surface, generates an air plasma slightly above the sample. Although the plasma generated by this pulse heats the sample, it is sufficiently removed from the surface to cause no ablation. Atomic and ionic lines are observed only in the plasma created with the second pulse. In this way, an enhanced ablation and S/N ratio for the line emission can be achieved. The reason for this phenomenon is still not totally clear and will be explained to some extent in this work.

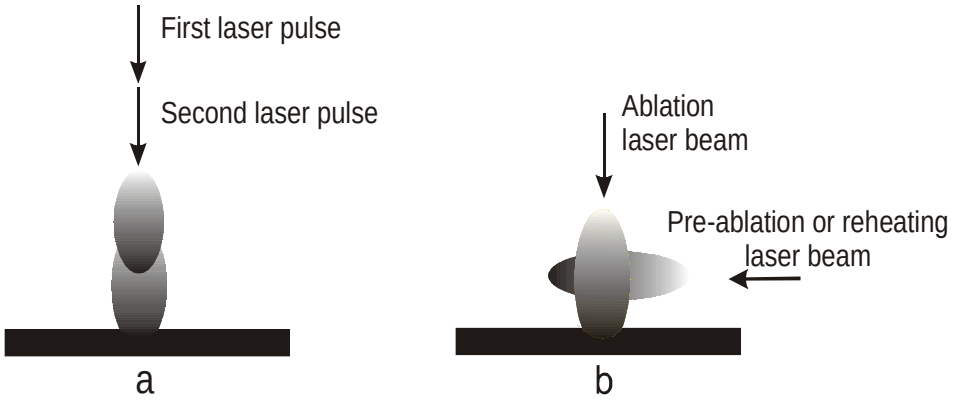

Fig. 3-1: *Collinear (a) and orthogonal (b) double-pulse geometry.*

Historically, the double-pulse approach was first shown to facilitate the bulk analysis of transparent liquids [128]. Later studies were devoted to the analysis of solids immersed in liquids [92,127]. Here, the double-pulse technique in the collinear geometry enables an expanding gaseous cavity to be formed inside the liquid. The analysis itself is carried out by excitation of this gas using the second pulse. The main objective in this case is to modify the surroundings in such way that the plasma can expand into a gas phase. The emission is then much stronger than in the aqueous matrix [129].

UEBBING et al. [130] used a double-pulse scheme in the reheating mode for LIPS analysis of glass and steel. They observed significantly enhanced intensities for Al and Mn lines in steel and Mg and Mn lines in glass. SATTMAN et al. [113] used a single Nd:YAG laser modified to operate in a double-pulse mode. In this case, both pulses were incident on the (steel) target and could lead to ablation. They reported that the volume of a plasma generated with double-pulse mode was twice as large as formed with a single pulse of equal energy. Their experiments also revealed an increase of ablated mass when going from the single to double-pulse mode, which they explained by a smaller plasma shielding effect compared to a single pulse. ST-ONGE et al. [131] also used multiple Q-switched Nd:YAG for investigation of aluminium alloys. It was found that the Al(II) line at 281.6 nm is considerably enhanced when using the double-pulse burst instead of a single pulse of similar energy. However, the electron density was found to be approximately the same in both cases with the plasma temperature about 10% higher in the double-pulse burst. The line enhancement is rather explained by the formation of a larger volume of plasma.

This, in turn can be linked to a greater ablated mass, as well as to the presence of a „pre-plasma" into which the second laser pulse is absorbed. COLAO et al. [125] employed a multiple Q-switched Nd:YAG and performed detailed investigation and comparison of important LIPS parameters, i.e. pulse energy, plasma temperature and electron number density, dimension of ablation crater, etc. in both, single and double-pulse, mode. STRATIS et al. [118,120,124] concentrated on the pre-ablation effect in the orthogonal geometry and reported enhancements in signal intensity and ablated mass. They also performed detailed plasma diagnostic and research on several other important factors, but unfortunately did not succeed to totally explain the pre-ablation phenomenon.
The objective here was the investigation of the orthogonal double-pulse geometry in both pre-ablation and reheating regime on a non-conducting matrix, glass and a conducting matrix, steel. Comparison with a single pulse was carried out at a constant total pulse energy. Additionally, the influence of the ablation wavelength has been studied with 266 nm/1064 nm and 1064 nm/1064 nm combinations of ablation and pre-ablation (e.g. reheating) laser beams (using the UV and IR pulses of the same irradiance). Time-resolved measurements of the plasma electron number density via Stark broadening and electron temperature via the Boltzmann plot method were also done. Calibration curves for several elements in the steel matrix were constructed in order to investigate possible improvement in the analytical figures of merit in the double-pulse regime.

3.2. Experimental Set-up

The experimental set-up is shown in Fig. 3-2. Two Q-switched Nd:YAG lasers were used: The first laser (Surelite I-10, Continuum, Darmstadt, FRG) with a repetition rate of 10 Hz and pulse width 5-7 ns (FWHM) was used for ablation. It was aligned orthogonally to the sample surface and focused 1-2 mm inside the sample with single plano-convex lens (f = 100 mm). By mounting second and fourth harmonic crystals in front of the output laser mirror and separation box with proper dichroic mirrors (HR266HT532+1064/45/AR, Laser Components, Germany) it was possible to operate the laser at 266 nm. Irradiance on the sample was adjusted by a beam attenuation system (Newport, USA). The pulse stability of the laser was monitored via a beam splitter and a pulse energy meter (Powerlite C5100, Continuum, USA).
The second laser (Quanta-Ray DCR-11, Spectra-Physics, USA), had a repetition rate of 10 Hz, a pulse width of 8-9 ns (FWHM) and was operating at 1064 nm. The laser was, by means of reflecting prisms and single plano-convex lens (f = 100 mm), aligned parallel to sample surface and focused a few millimeter above sample surface. The pulse energies of the both lasers were hold constant, namely, 60 mJ/pulse for the pre-ablation/reheating laser and 18 mJ/pulse for the ablation laser, on both 266 and 1064 nm wavelengths. A detailed investigation of the influence of laser pulse energy was beyond the scope of this work. Samples were placed on a motorized xyz-translation stage (CTC290, Micos,

Germany). The stage was controlled via an in-house programed LabView (National Instruments, USA) software. This system enabled automatic ablation of different sample spots as well as precise positioning of the sample surface. Observation of the ablation plasma was perpendicular („head-on“).

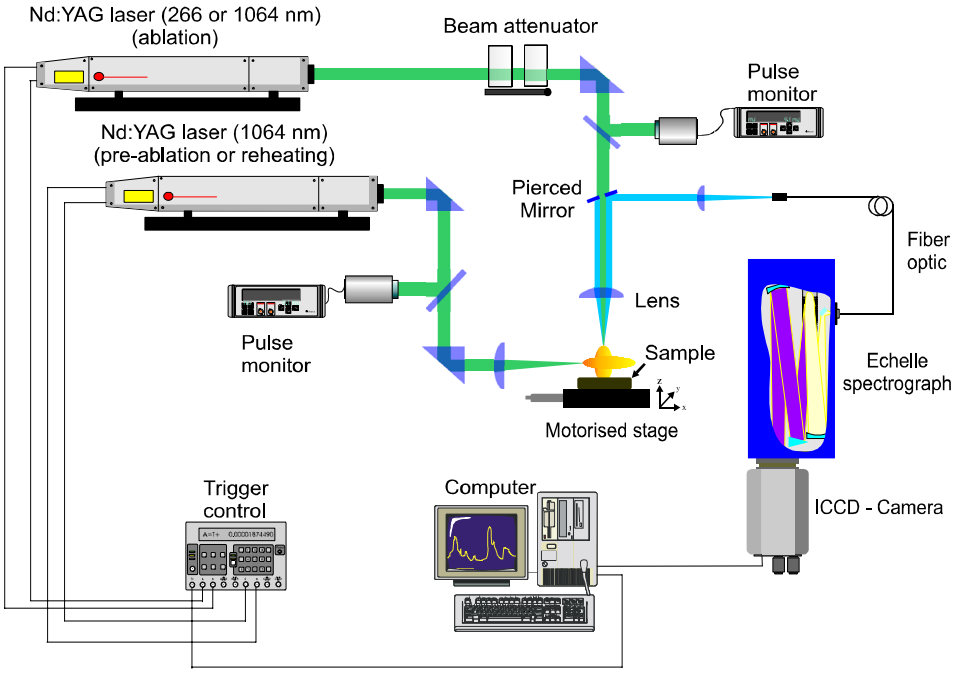

Fig. 3-2: *Experimental setup for double-pulse experiments.*

The plasma emission was collimated with the focusing lens, and by means of an pierced mirror, an achromatic lens system (f = 100 mm) and quartz optic fiber (d =550 µm) introduced into the detection system. The spectrograph with an ICCD camera (ESA3000, LLA, Germany) with resolution power, $\Delta\lambda/\lambda = 10000$ (at 250 nm) and wavelength range between 200 and 780 nm. The ICCD-camera (1024 × 1024 pixel) had the maximum of quantum efficiency of about 20% at 460 nm.

The delay between the laser pulses is an essential parameter in double-pulse experiments. The timing was achieved by independent external triggering of the respective flash lamps of both lasers via a delay generator (DG535, Stanford Research Systems, USA). A TTL signal from the ICCD-camera was used as a master trigger for the delay generator. Flash lamp-Q-Switch (FL-QS) times are fixed for the both lasers, i.e. 183 µs for the first laser and 270 µs for the second laser. If the trigger signal for the flash lamp of the second laser was adjusted to be coincident with the master trigger ($\Delta t_1 = 0$) by shifting the delay between the master trigger and the trigger signal for the flash lamp of the first laser (Δt_2) it is possible to shift the delay between two laser pulses, $\Delta\tau$ (see Fig. 3-3) according to

$$\Delta\tau = (183 - 270) + \Delta t = -87 + \Delta t[\mu s]. \qquad (3.1.)$$

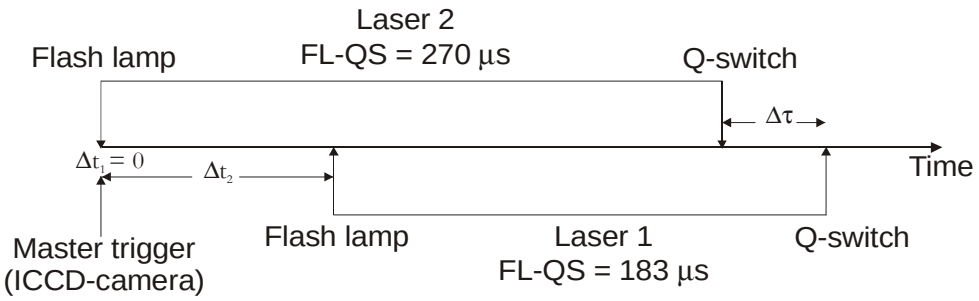

Fig. 3-3: *Timing for the double-pulse experiments.*

In this way, negative values for the $\Delta\tau$ correspond to pre-ablation regime, and positive values (ablation pulse comes first) to the reheating regime. For analysis a set of 9 reference steel samples (Bureau of Analysed Samples, Ltd. SS401 - SS409) and 5 reference glass samples (NIST 610, 612, 614, 1412 and 1830) were used without further sample preparation.

3.3. Results and Discussion

One of the main assumptions for the double-pulse experiments in the orthogonal geometry is that the laser parallel to sample surface is focused well above the surface and does not ablate the sample. To confirm this first in a series of preliminary experiments only the plasma produced by the pre-ablation (resp. reheating) laser was investigated. The laser beam was focused approximately two millimeter above the surface of the sample.

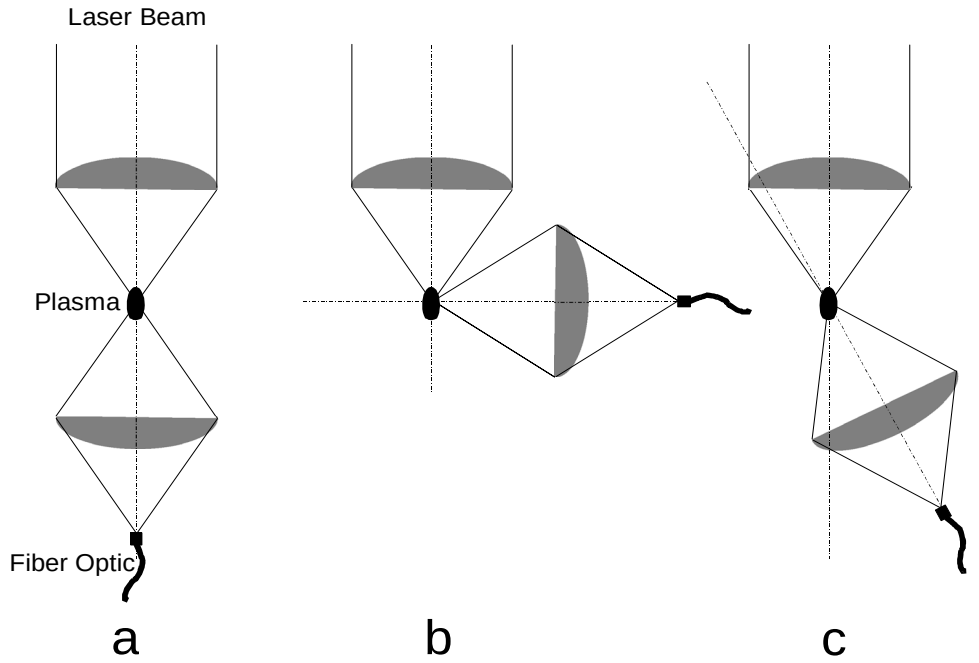

Fig. 3-4: *Observation geometries of air plasma: head-on (a), side-on (b), and angled (c) observation.*

The plasma produced in air with this kind of irradiance (~ 1 GW cm^{-2}) has the shape of elongated ellipsoid with the longest axis, in the direction of laser beam, and a characteristic size of a few millimeters. Side-on observation (Fig. 3-4b) leads to a poor collection of emission on the entrance of the fiber optic because

of reduced solid angle of observation. On the other side, head-on observation in the direction of the laser beam propagation (Fig. 3-4a) brings danger of the destruction of the fiber optic due to the breakdown caused by the portion of the laser beam passed through the plasma and focused with the imaging lens. Therefore, an angled observation (approx. 15°) has been chosen (Fig. 3-4c). The detection was delayed for 500 ns after the plasma ignition and integration time (gate) of 10 μs was utilized. This corresponds to nearly time integrated measurement of the plasma emission. A comprehensive LIPS spectrum (200-780 nm) is shown in Fig. 3-5. Several ionic oxygen lines between 400 and 450 nm and very intensive atomic lines of oxygen between 740 and 780 nm were observed. No emission of typical elements from the steel matrix were detected. So it can be safely assumed that no ablation of the sample took place.

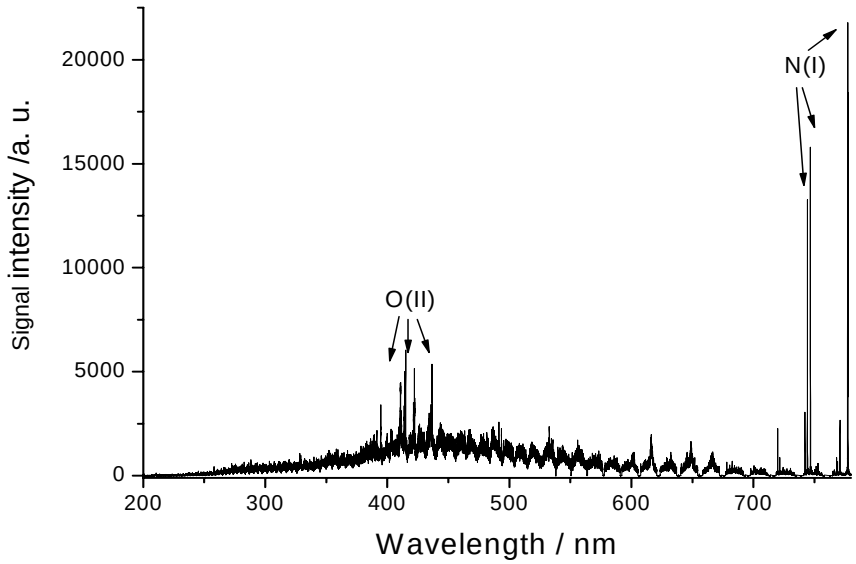

Fig. 3-5: *Spectrum of the plasma formed in air above the sample.*

The effect of timing between laser pulses was investigated over a wide range of $\Delta\tau$ for both ablation wavelengths and both matrices (Fig. 3-6 a-d). The intensities of several lines from different elements were plotted against the delay between laser pulses. As already mentioned, negative delays correspond to the pre-ablation and positive to reheating regime.

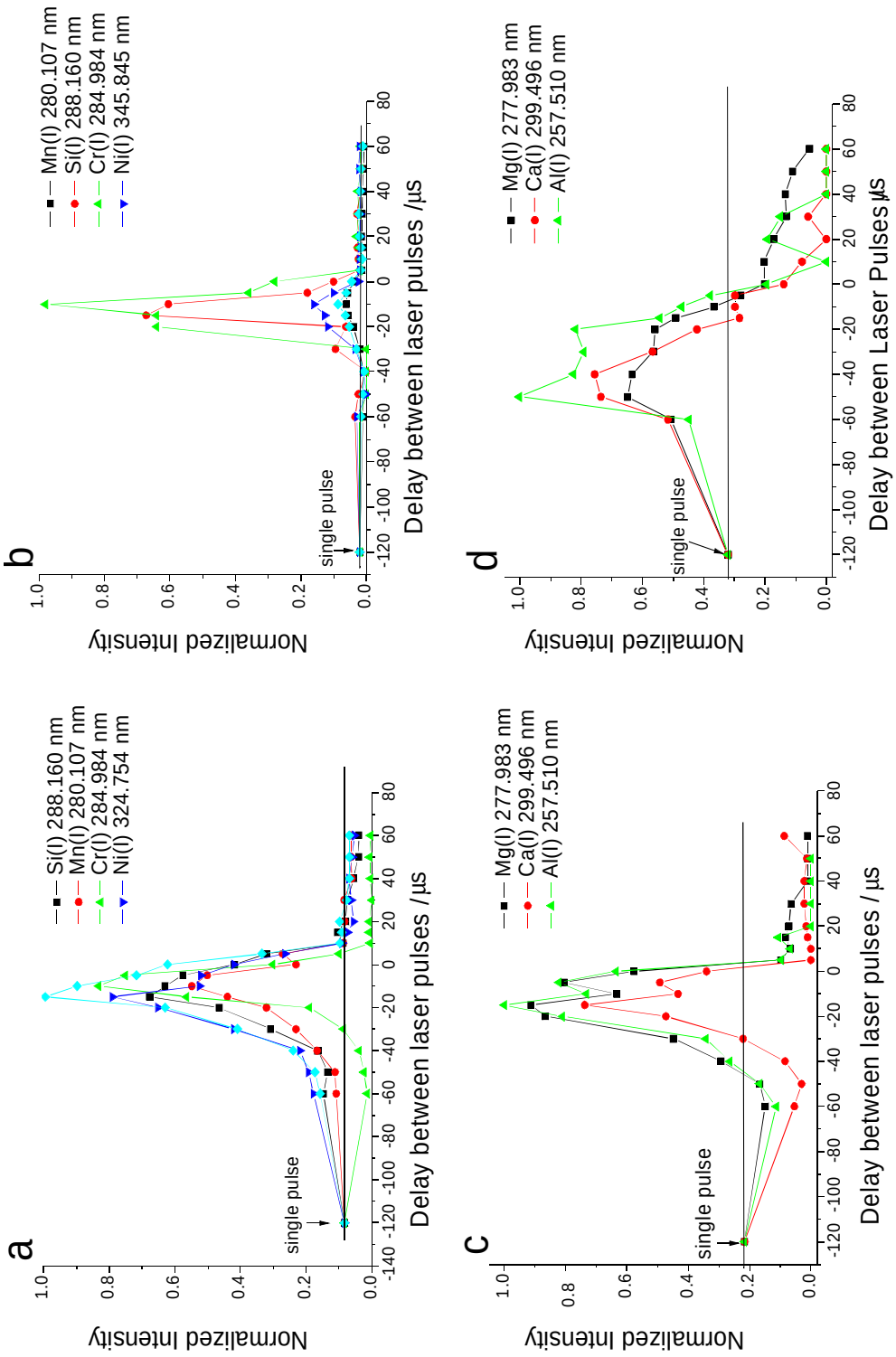

Fig. 3-6: *Normalized line intensities from several elements vs. time between the two laser pulses for (a) steel matrix and UV ablation, (b) steel matrix and IR ablation, (c) glass matrix and UV ablation, and glass matrix and IR ablation (d).*

Note, that $\Delta\tau$ = -120 µs corresponds to a single pulse experiment.The intensities of all lines were normalized to the single pulse intensity. The enhancement of intensities are present only for pre-ablation, no enhancement was detected for reheating. For the later even a significant decrease in intensities for the glass matrix were observed compared to the single pulse experiment. All lines under investigation exhibited similar trends. The enhancement had a single maximum for all lines. This delay is characteristic of the matrix and was found to be 10 µs for steel and between 20 and 40 µs for glass. The relative signal enhancement was depended upon the element, the ablation wavelength and the matrix. Overall enhancements are higher for the steel matrix than for the UV ablation than IR ablation. The maximal increase found was, a 50fold enhancement for the Cr(I) line at 284.984 nm in steel.

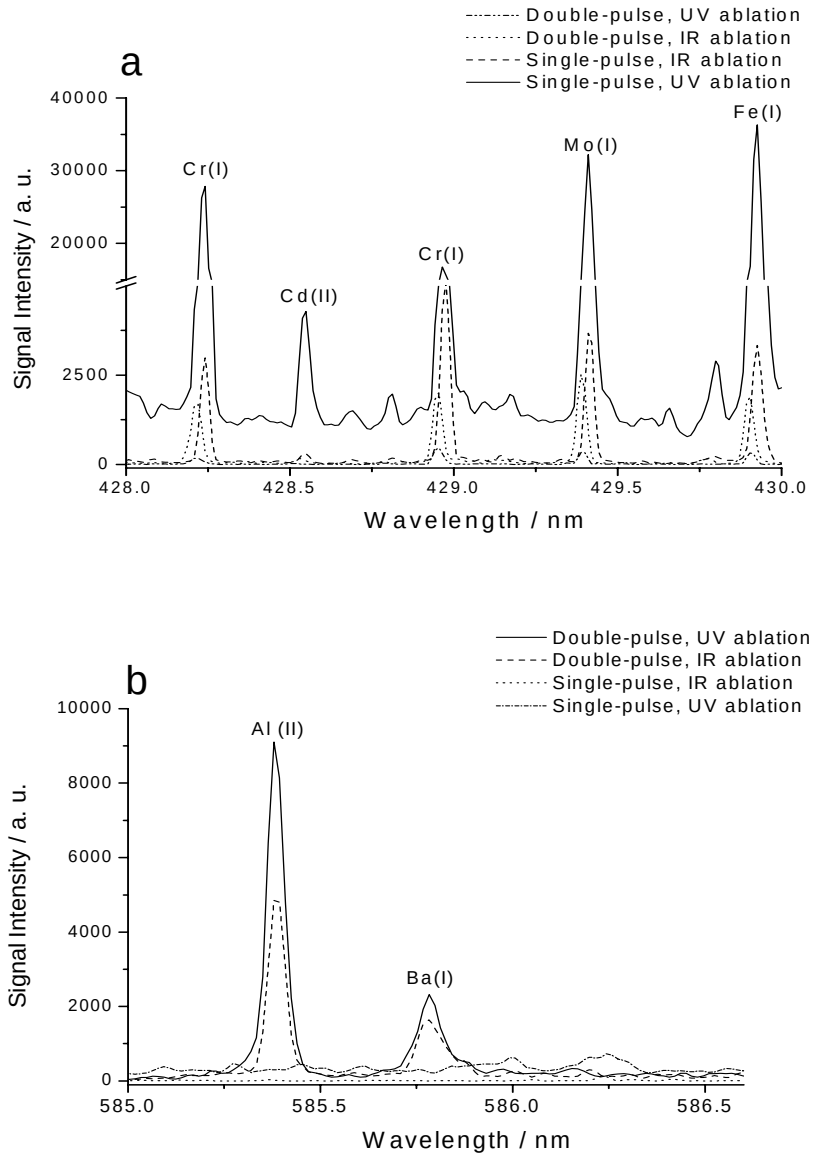

Fig. 3-7: *Spectra of a steel (a) and a glass (b) sample made with single- and double-pulse technique and two different ablation wavelengths.*

Figure 3-7a, reveals the spectra from a steel sample made with a single and double-pulse of $\Delta\tau$ = -10 µs (maximum enhancement). Significant enhance-

ment of line emission is obvious with only a slight increase of background radiation. The spectra from the glass matrix (see Fig. 3-7b) recorded in pre-ablation mode ($\Delta\tau = -20$ µs for UV ablation and -40 µs for IR ablation) showed also a line enhancement but less pronounced. The detection timing was the same for the single pulse and double pulse measurements. (delay = 3 µs, gate = 1 µs for steel and delay = 1 µs, gate = 2 µs for glass).

Figures 3-8 a and b show the time-resolved intensities of the Cu(I) 324.754 nm line from a steel sample (a) and the Al(I) 305.754 nm line from a glass sample (b). The measurements are made over the first 10 µs after plasma ignition. The gate was held constant (1 µs) throughout all experiments. After 10 µs the single-pulse lines almost diminishes to zero while double pulse lines have still significant intensities. Intensities of double pulse lines are also higher over the whole plasma duration.

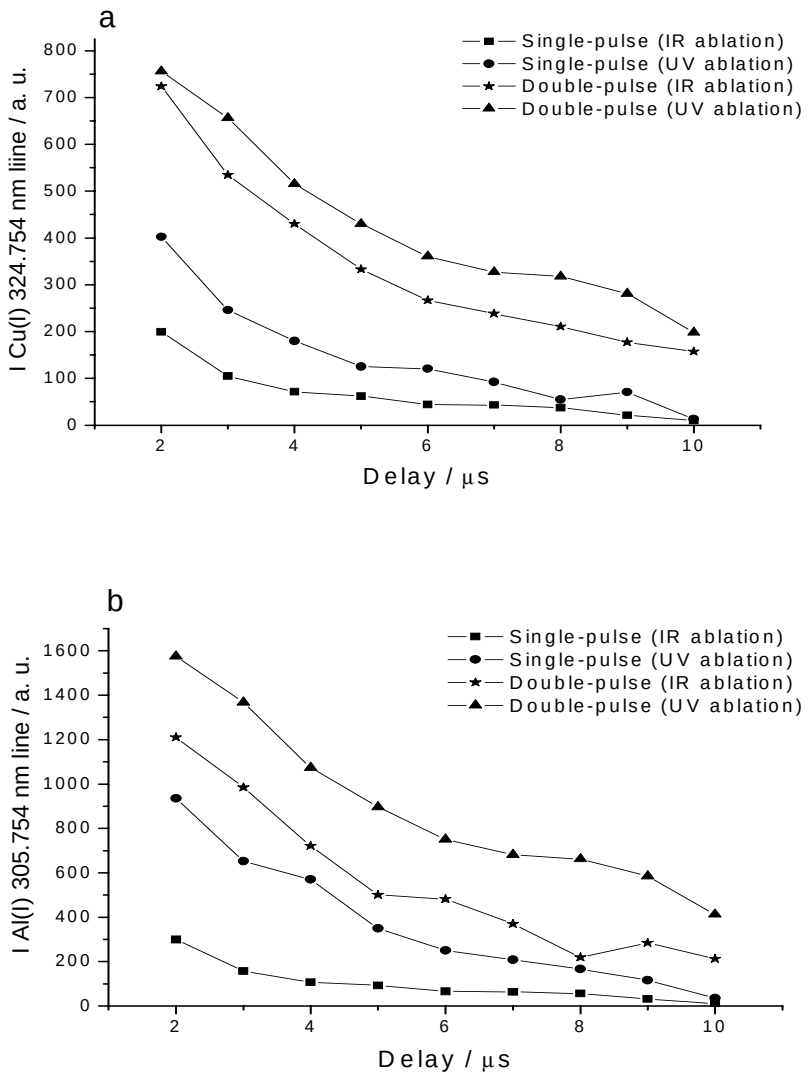

Fig. 3-8: *Time-resolved intensity of Cu(I) 324.754 nm line in a steel matrix (a) and Pb(I) 368.346 nm line in a glass matrix (b).*

The background radiation in double pulse experiments was not significantly increased compared to single pulse experiment (see Fig. 3-7 a and b) and, therefore, time-resolved signal-to-background ratios showed similar trends like pure line intensities (see Fig. 3-8)

Electron temperature and density were estimated by means of spectroscopic methods. In the first approximation, the PLTE can be assumed for the laser-induced plasma, in both single and double-pulse experiments [125]. For the determination of the electron temperature the Boltzman plot method was used (see chapter 2.1.3). For the steel matrix four atomic iron lines were used (see Table 3-1) and for the glass four atomic calcium lines (see Table 3-2). All lines under study have relatively high „lower energy levels" which allowed assuming PLTE for those levels.

Tab. 3-1: *Iron lines used for electron temperature determinations in the steel matrix [48].*

Line	A / 10^7 s^{-1}	E_{lower} / eV	E_{upper} / eV	g_{upper}
Fe(I) 326.562 nm	3.776	2.176	5.972	5
Fe(I) 328.026 nm	5.379	3.302	7.080	11
Fe(I) 337.078 nm	3.289	2.693	6.369	11
Fe(I) 341.313 nm	3.568	2.198	5.828	7

Tab. 3-2: *Calcium lines used for electron temperature determinations in the glass matrix [48].*

Line	A / 10^7 s^{-1}	E_{lower} / eV	E_{upper} / eV	g_{upper}
Ca(I) 300.921 nm	4.264	1.899	6.018	3
Ca(I) 431.865 nm	7.380	1.899	4.765	3
Ca(I) 585.745 nm	6.599	2.993	5.041	5
Ca(I) 647.166 nm	0.845	2.526	4.441	7

Figure 3-9 demonstrates the Boltzmann plot for a single pulse experiment with a steel sample for two different delays.

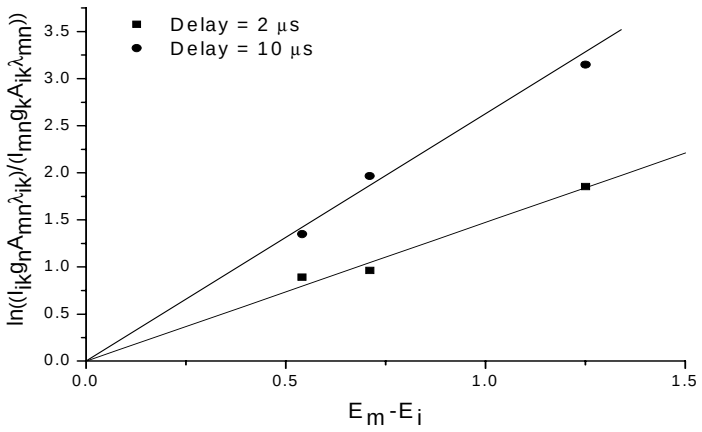

Fig. 3-9: *Boltzmann plot for single-pulse plasma for two different delays of detection.*

The temporal evaluation of plasma electron temperature in steel and glass is given in Figure 3-10.

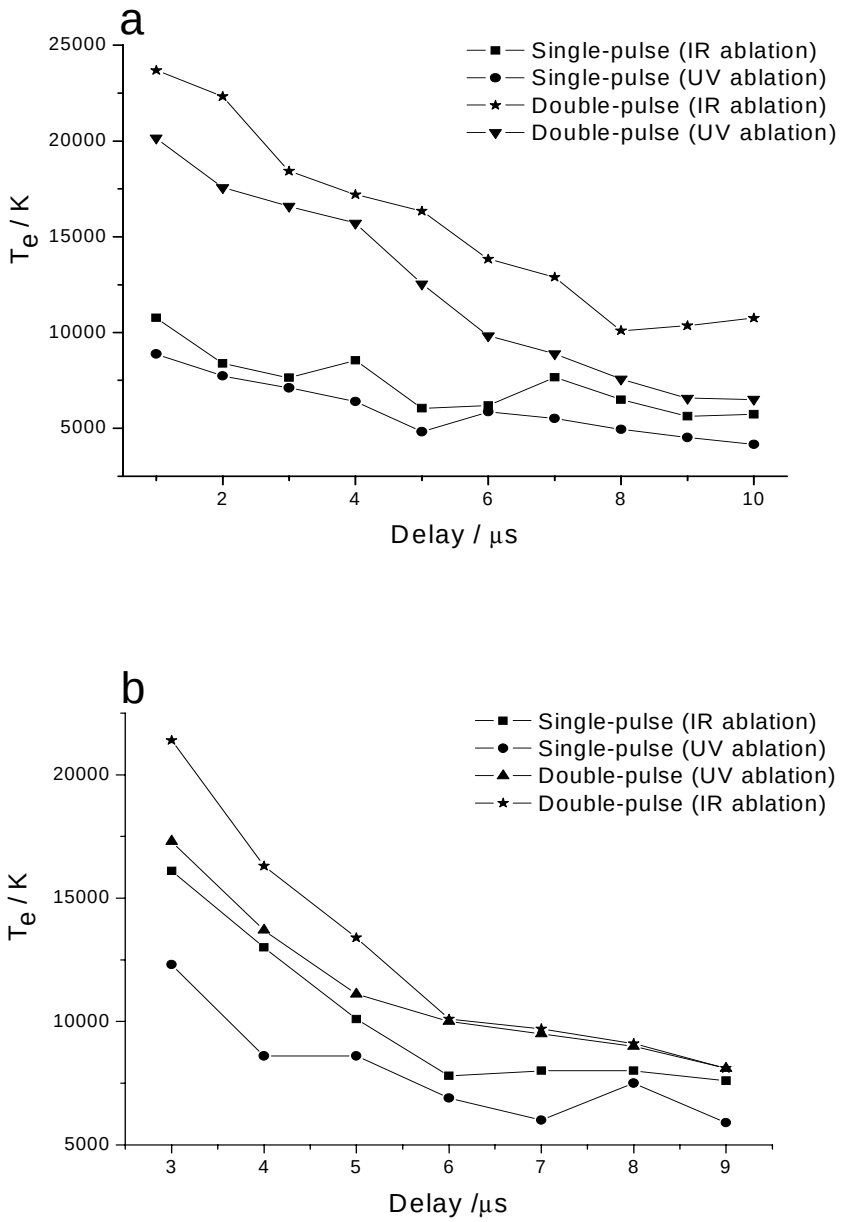

Fig. 3-10: *Temporal evaluation of the plasma temperature for the steel (a) and glass (b) matrix.*

A significant enhancement in the electron temperature for the double-pulse experiment was observed for the steel sample while only a slight increase for the glass was found. For the determination of the electron number density an approximation of „Stark broadening" method suggested from DETALLE et al. [132] was applied. The electron density n_e can be estimated to an accuracy of 20-30% via:

$$\Delta\lambda_{st} = 2 \cdot \lambda_{st}^{ref} \cdot \frac{n_e}{n_e^{ref}} \quad , \tag{3.2.}$$

where $\Delta\lambda_{st}$ is the FWHM of the observed Stark (e.g. Lorentz) line profile and $\Delta\lambda_{st}^{ref}$ is the same value for the known value of electron number density n_e^{ref}.

From this relationships, it is easy to calculate the desired number electron density according to

$$N_e = n_e^{ref} \cdot \frac{\Delta\lambda_{st}}{\Delta\lambda_{st}^{ref}} \quad . \tag{3.3.}$$

Some additional approximations have to be made: (i) The doppler effect should be neglected and a pure lorentzian line shape can be used. Pure Stark broadening can be calculated according to [54]

$$\Delta\lambda_{st} = \Delta\lambda_{lor} - \Delta\lambda_{inst} \quad , \tag{3.4}$$

where $\Delta\lambda_{inst}$ is the contribution from the instrumental broadening. DETALLE et al. suggested that $\Delta\lambda_{inst}$ can be approximated with the observed line profile $\Delta\lambda^{long}$ for longer delays after plasma ignition, when n_e becomes constant and relatively low. In this case, we can assume that $\Delta\lambda_{st} = 0$ (see Fig. 3-11) and $\Delta\lambda_{lor} = \Delta\lambda_{inst}$

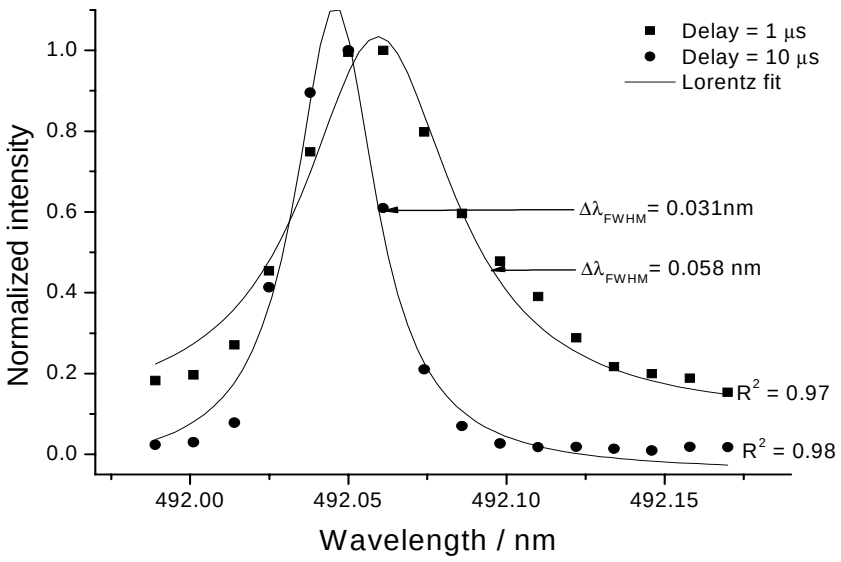

Fig. 3-11: *Normalized line profile of the Fe(I) 492.050 nm line, 1 µs and 10 µs after plasma ignition.*

For the determination of n_e for steel, the Fe(I) 492.050 nm line is used and for glass the Al(I) 394.401 nm line. The lines under study were the „most sensitive" available lines to the Stark effect. Values for n_e^{ref} and $\Delta\lambda_{st}^{ref}$ were taken from KONJEVIC [133] and are listed in the Table 3-3.

Tab. 3.3: *Reference values for n_e and $\Delta\lambda_{stark}$ for the lines used for determination of electron number density.*

Line	N^{ref}_e / 10^{17} cm^{-3}	$\Delta\lambda_{stark}^{ref}$ / nm
Fe(I) 492.050 nm	0.1	0.0107
Al(I) 394.401 nm	0.1	0.0370

An enhancement in the electron number density is observed only at early times for steel samples (Fig. 3-12). Note, that the described approximation method becomes highly inaccurate for longer delays.

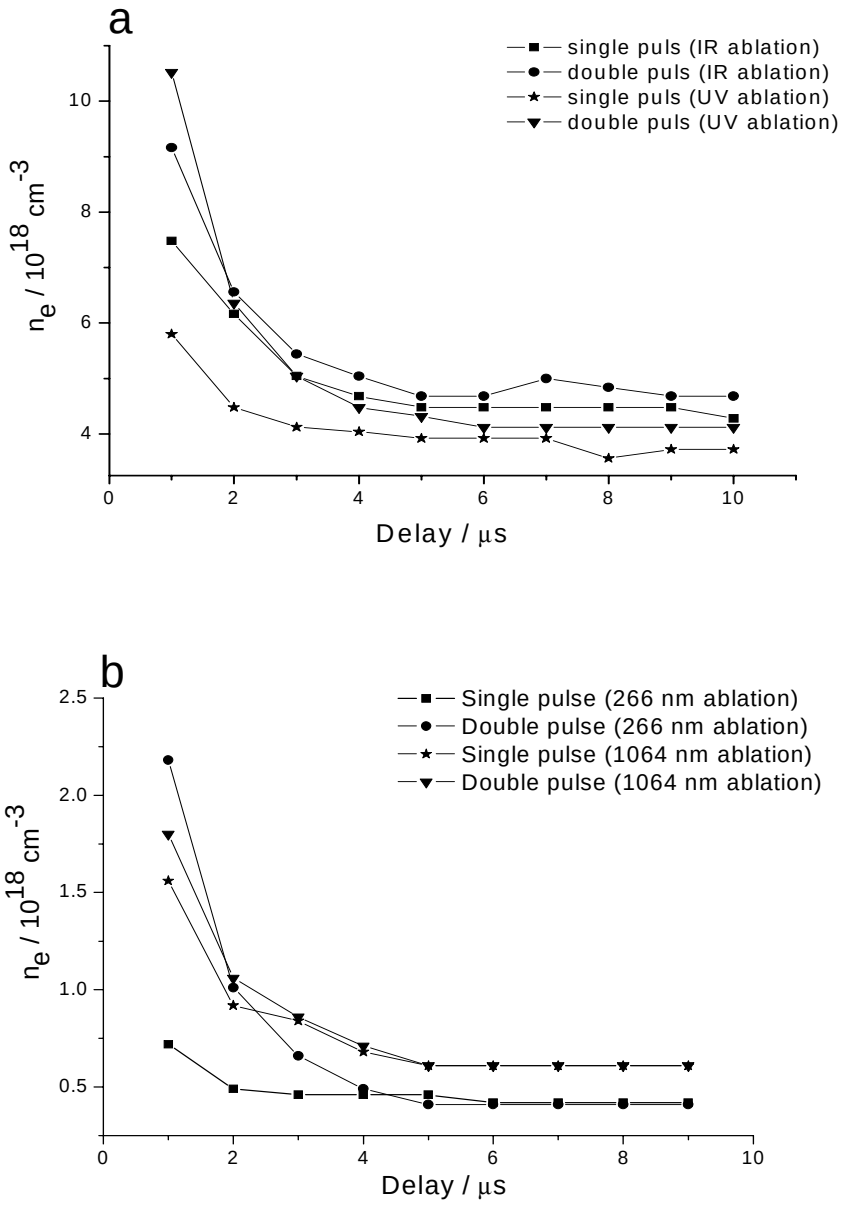

Fig. 3-12: *Electron number density for a steel (a) and glass (b) sample.*

Fig. 3-13. show calibration curves for Si, Mn, Ni, and Cr in steel. For this purpose, a set of 8 referenced samples have been measured. Each sample has been probed with 100 laser pulses, with a delay = 1 µs and gate = 2 µs. Hundered spectra were averaged and the average spectrum was background corrected and smoothed using the Sawitzky-Golay polynomial [134]. All lines used have relatively high upper energy levels and lower energy levels different

from zero (see Table 3-4) which allows assumption of PLTE and no self-absorption.

Tab. 3-4: *Lines used for construction of calibration curves for steel*

Line	E_{lower} / eV	E_{upper} / eV
Si(I) 288.160 nm	0.780	7.799
Mn(I) 280.107 nm	3.132	7.558
Ni(I) 345.845 nm	3.480	5.082
Cr(I) 284.584 nm	3.450	7.064

Enhancement of line intensities with pre-ablation pulse directly leads to an increasment of calibration sensitivity and lower limit of detection especially in the case of UV ablation. Table 3-5 gives the results of the sensitivity for all four elements.

Tab. 3-5: *Calibration sensitivity for steel*

Element	Sensitivity /%$^{-1}$			
	Single pulse IR ablation	Single pulse UV ablation	Double pulse IR ablation	Double pulse UV ablation
Si	6.29	49.77	271.72	542.05
Mn	3.61	33.82	119.84	298.13
Ni	1.74	13.29	130.76	381.69
Cr	0.90	13.66	183.95	532.94

For the purpose of better understanding of pre-ablation phenomenon, time resolved measurement of intensity and electron number density of pre-ablation plasma have been performed. The line used was very intensive and especially good resolved N(I) 746.831 nm line. For the determination of the electron number density, the already described methods were used. Stark width parameters have been also taken from KONJEVIC et. al. [133].

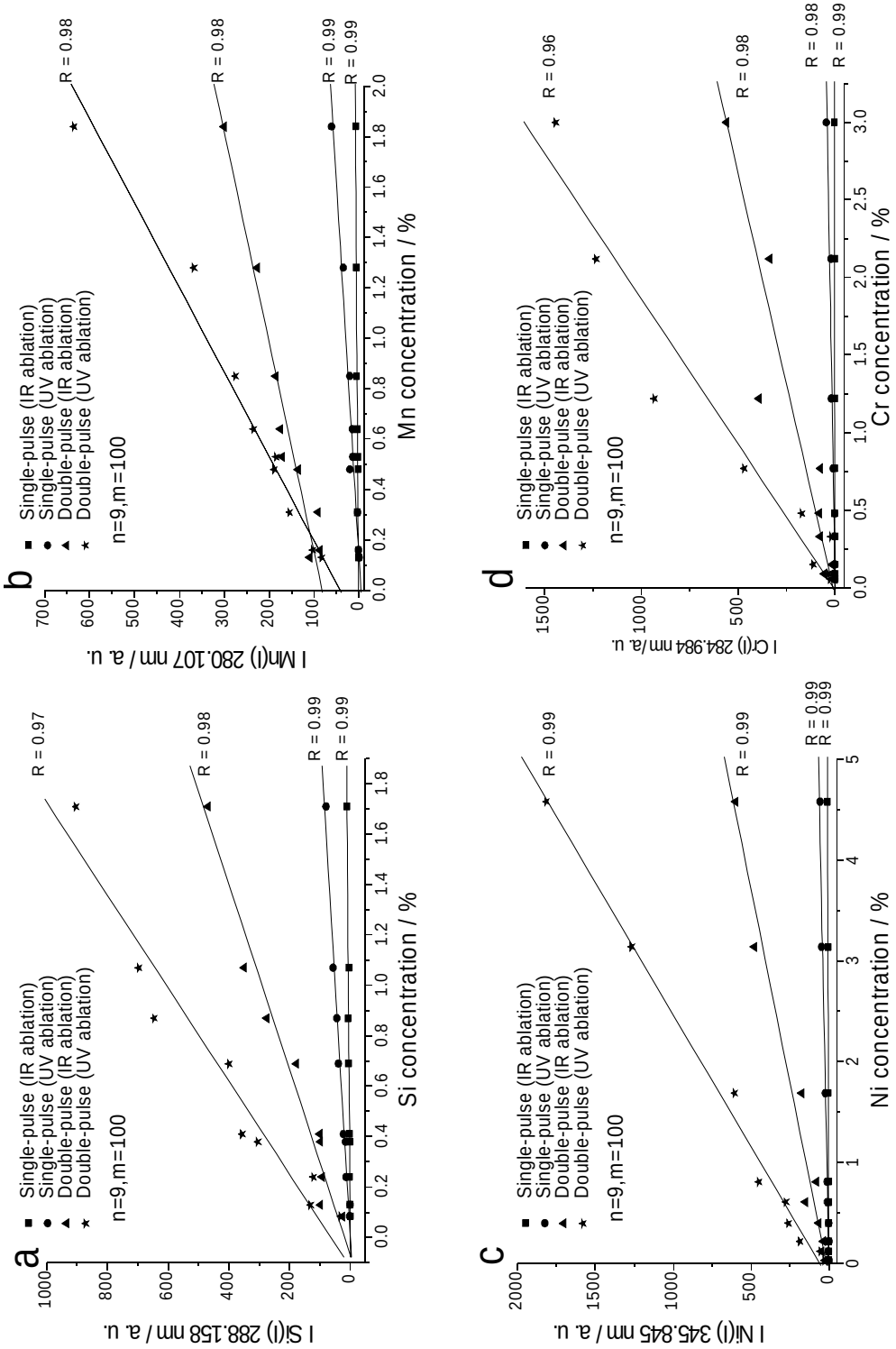

Fig. 3.-13: *Calibration curves for Si (a), Mn (b), Ni (c), and Cr (d) in steel.*

The measurement was done over the first 40 µs after plasma ignition in order to investigate what is happening in the pre-ablation plasma during the ablation pulse. Fig. 3-14 and 3-15 show time-resolved electron temperature and electron number density in the pre-ablation plasma.

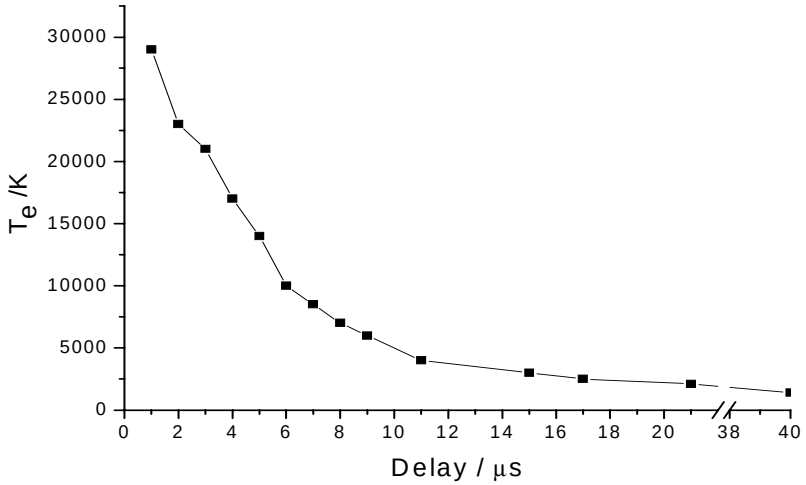

Fig. 3-14: *Time-resolved electron temperature in ablation plasma*

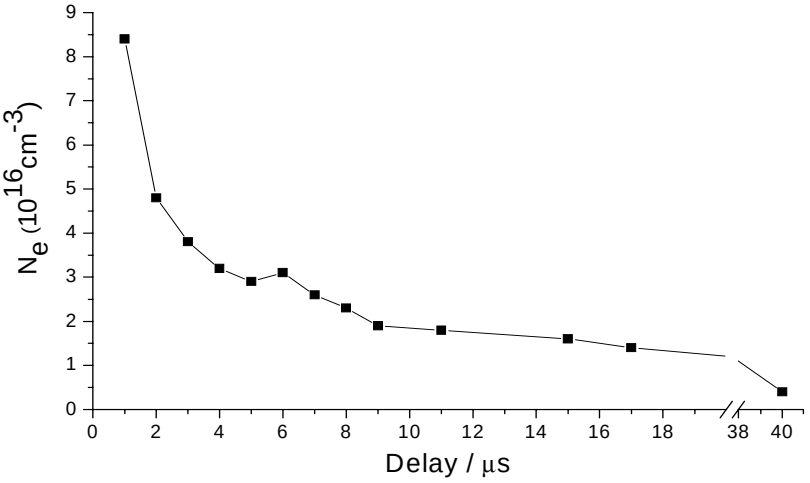

Fig. 3-15: *Time-resolved electron number density in pre-ablation plasma*

The mechanism that leads to pre-ablation enhancement is not yet totally understood. It seems possible that the pre-ablation plasma heats the sample, causing changes in its optical properties, which results in an increased coupling of the ablation pulse to the surface. Sufficiently high temperatures above the sample in the moment of the ablation laser pulse (see Fig. 3-14) contribute to this assumption. An increase in crater diameter and ablated mass was observed by STRATIS et al. [118,120] and confirmed this. However, since the laser pulse timing is critical to the magnitude of signal enhancement, it is clear that the pre-ablation effect must be transient in nature. The observed shorter delay times for a maximum enhancement in steel (higher thermal conductivity) than for the glass

point to thermal effects. Different enhancements for different ablation wavelengths and absence of enhancement effect for delays between laser pulses around the $\Delta\tau = 0$ are possibly due to the shielding effect of the pre-ablation plasma.

Further, it seems reasonable that pre-ablation spark creates free electrons in the atmosphere above sample, which aid the formation and propagation of the ablation plasma. Sufficient number of free electrons in the pre-ablation spark even after 40 μs (see Fig. 3-15) makes this hypothesis feasible. Another hypothesis is that the expanding shock wave from pre-ablation breakdown creates a lower pressure environment into which the ablation plasma is formed, which could result in larger and better formed plasmas [120,124]. Most probably the pre-ablation effect is a combination of all the indicated effects and further work should be devoted to a more detailed investigation and optimization of each of them.

4 LIPS in UV-Vis

4.1. Experimental Set-up

The experimental set-up for LIPS analysis in the UV/Vis region is depicted in Fig. 4-1. A Q-switched Nd:YAG laser (SL282G, Spectron Laser Systems, England) is employed for plasma generation. The main operating parameters of the laser are given in the Table 4-1.

Tab. 4-1: *Operating parameters of the Spectron, SL282G laser*

Parameter	Value
Max. pulse energy	200 mJ (1064 nm), 100 mJ (532 nm), 25 mJ (266 nm)
Pulse duration (FWHM)	< 6 ns
Beam divergence $1/e^2$	0.5 mrad
Beam diameter	6 mm
Pulse repetition rate	10 Hz

To maintain a constant temporal beam profile, the beam energy was adjusted by means of a variable attenuator (Newport, Irvine, USA). Monitoring of laser pulse energy was possible by means of a beam splitter and an pulse energy meter (Powerlite C5100, Continuum, Santa Clara, USA). Through a pierced mirror, the beam of the Nd:YAG laser (see Fig. 4-1) was focused with a single plano-convex lens (f = 100 mm) on the sample surface.

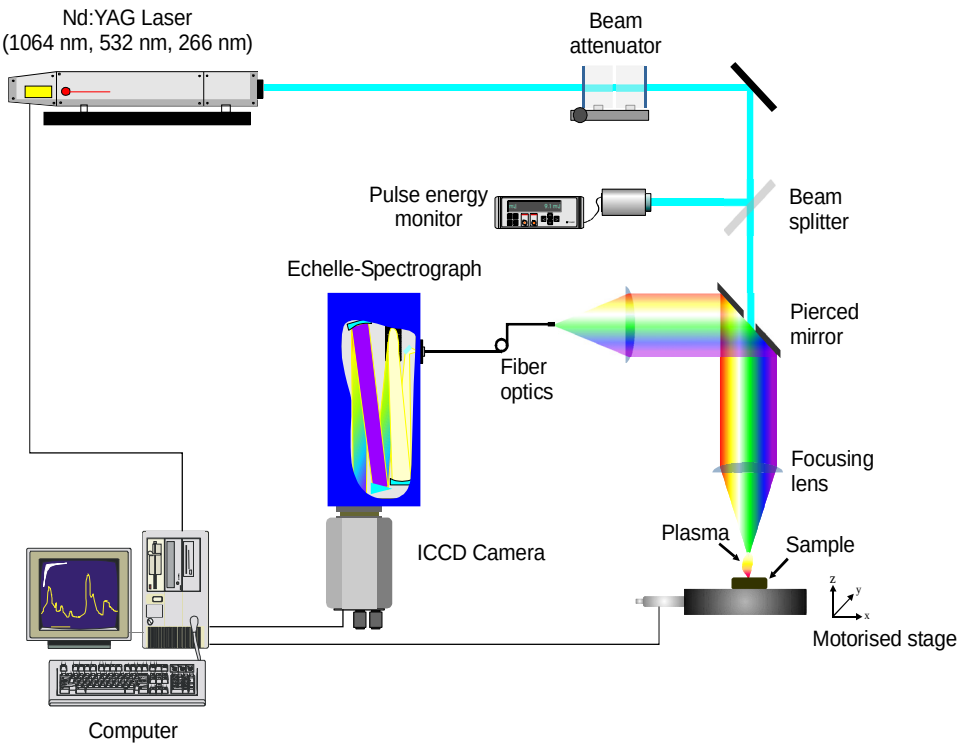

Fig. 4-1: *Experimental set-up for LIPS analysis in UV-Vis spectral region*

The stage control was performed with an in-house written LabView (National instruments, USA) routine. The plasma emission was collimated with the same lens, and focused by an achromatic lens system (f = 100 mm) on a fiber optic coupled to the spectrometer entrance slit. The detection system was based on an Echelle spectrograph (ESA3000, LLA, Germany) with spectral range: 200-780 nm and resolving power ($\Delta\lambda/\lambda$) of 10 000 integrated with an intensified CCD camera with an UV-Vis optimized photocathode.

4.2. Optimizated Detection in LIPS

Due to the transient nature of the laser-induced plasma, the detection has to be time-optimized for each matrix separately. The average duration of a laser-induced plasma is between several hundreds of nanosecond and several tenths of microsecond. Directly after the laser pulse, the plasma is characterized by unspecific emission from free-free and free-bond transitions. The emission near the end of plasma duration, from the other side, is weak and the signal-to-noise ratio is low. Earlier work [135,140] showed that with a proper optimization timing parameters it is possible to improve significantly the sensitivity and the limit of detection.

Basically, two parameters have to be optimized: the delay, which is the time after plasma ignition when the signal integration starts and the gate, which is the actual integration time. The optimization method used here is based on the work of VOIGTMAN [71] and assumes that the dominant noise is stationary and white and that the signal-to-noise ratio has a gaussian distribution. In this case Voigtman defined an optimum integration area which lies within $\pm 1.4\sigma$, which

is the area for which the signal-to-noise ratio is higher than 37.5% of the maximum value. The practical procedure implies shifting of a small, constant gate along the time axis relative to the plasma ignition. For each delay, a sufficient numbers of signals are recorded and the signal-to-noise is calculated and plotted against the delays. The obtained curve is fitted by a gaussian function, and the optimal timing parameters can be extracted by intersecting this function at 0.375 of the maximum. Figure 3-2 shows the result of such procedure for the carbon line C(I) at 247.931 nm in a standard steel sample (SS402, Bureau of Analysed Samples Ltd.). The exact parameters are: gate=2.6 μs and delay=4.3 μs.

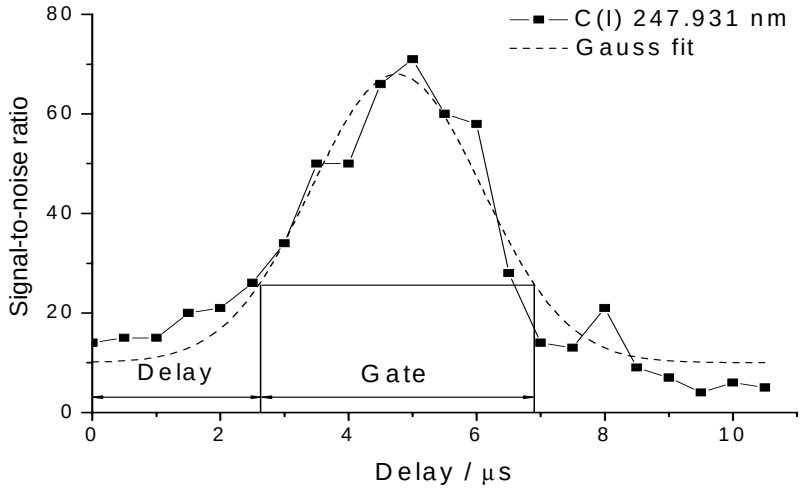

Fig. 4-2: *Signal-to-noise ratio vs. delay after plasma ignition (C(I) 247.931 nm line in a standard steel sample).*

4.3. The Internal Standard Method in LIPS

An internal standard is a substance that is added in a constant amounts to all samples, blanks, and calibration standards in an analysis [70]. Alternatively, it may be a major constituent of all samples that is present in a large enough amount that its concentration can be assumed to be constant in all cases. Calibration then involves plotting the ratio of the analyte signal to the internal standard signal as a function of the analyte concentration. An internal standard, if properly chosen and used, can compensate for a several types of both random and systematic errors. Thus, if the analyte and internal standard signals respond proportionally to random instrumental and method fluctuations, the ratio of these signals is independent of these fluctuations. If the two signals are influenced in the same way by matrix effects, compensation of these effect also occurs. The internal standard method was first introduced in atomic emission spectroscopy by GERLACH [141] and is today most prominent standardization method for quantitative analysis.

An internal standard for LIPS has to fulfill several requests: (i) the analyte and internal standard have to have similar optical (absorptivity, reflectivity) and physical (melting and evaporation point) properties in order to avoid possible non-stochiometric ablation (see chapter 1.2.5), (ii) the emission line of the analyte and

the internal standard have to be close to each other in the spectrum that a simultaneous detection is possible with similar instrumental spectral response, (iii) the excitation energies of the upper levels of both transitions have to be in the same range, and (iv) the lower level of internal standard have to be different from zero (non-resonant line) and sufficiently high to avoid self-absorption and neglect thermal population [142].
Exemplary, the internal standard method in LIPS is demonstrated for analysis of steel. Two elements, Mn and Cr were investigated. A set of nine standard steel samples (Bureau of Analysed Samples Ltd.) was measured with 100 single laser pulse pro sample. The laser was operating at $\lambda = 1064$ nm wavelength producing irradiance of about 2.5 $MWcm^{-2}$. Detection parameter were: delay = 1 μs and gate = 3 μs. The standardization was performed using iron as an internal standard. Two pairs of ionic lines which satisfy the criteria discussed above have been chosen (see Table 4-2).

Tab. 4-2: *Line pairs used for internal standardization*

Line	E^{lower} (eV)	E^{upper} (eV)
Mn(II) 259.563 nm	0	4.78
Fe(II) 258.588 nm	1.076	4.79
Cr(II) 284.984 nm	1.506	5.855
Fe(II) 256.693 nm	1.076	5.904

Figure 4-3 shows a clear improvement in the linearity of calibration curves using the Fe lines as an internal standard.

4.4. Analysis of Coal

Coal is an organic sediment containing also inorganic constituents and minerals [143]. It is not a uniquely defined material, but a class of substances having both similarities and differences in the physico-chemical properties. Generally, according to chemical composition and heating value coals can be divided in four categories: lignite, subbituminous, bituminous and anthracite (see. Fig. 4-4). Coal is extensively utilized for power generation by combustion. While the inorganic fraction contributes little if anything to the value of the coal, most problems associated with coal use (abrasion, corrosion, environmental relevant emissions) arise from this fraction [144]. To optimize the overall efficiency, various parameters, e.g. water content, ash content, or volatile matter content, have been explored for different coal types [145]. An analysis must be performed prior or during the utilization of coal, which calls for efficient methods suitable for on-line analysis and process control.

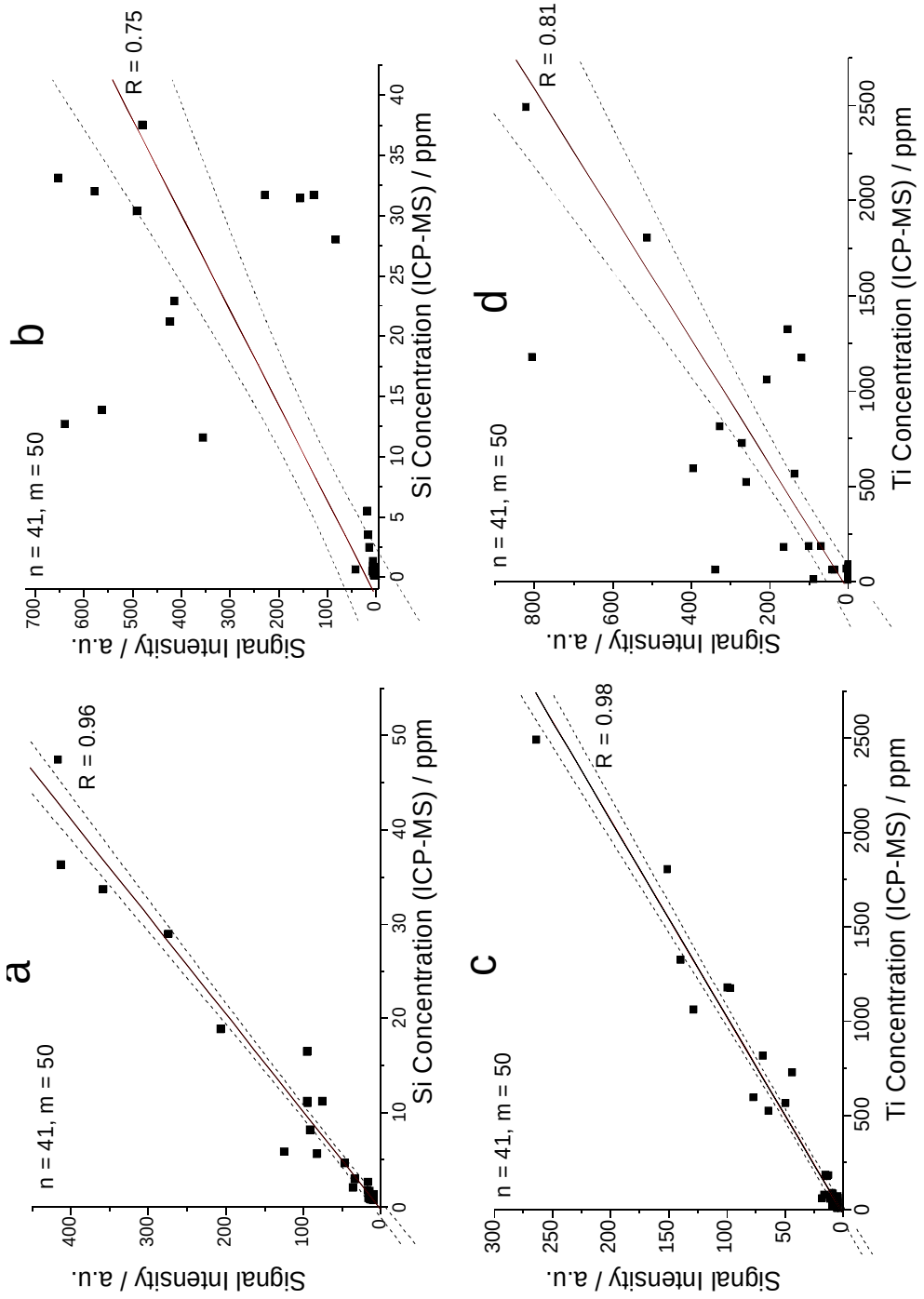

Fig. 4-3: *Calibration curves for Mn and Cr in steel wthout (a,c) and with (b,d) iron as an internal standard (dashed lines represents the 95% confidence inetrval for regression).*

The ash content is specifically important for the thermal efficiency of the boilers and closely linked to the inorganic composition of the coal. The elemental analysis of a coal sample includes the determination of both major components (Si, Al, Fe, Na, Ca, and S), minor components (Mg, K, Ti, and P), and can also demand a determination of about 50 trace elements (e.g. Cr, Ni, Cu, Mn, Zn, Hg, and As) [143].

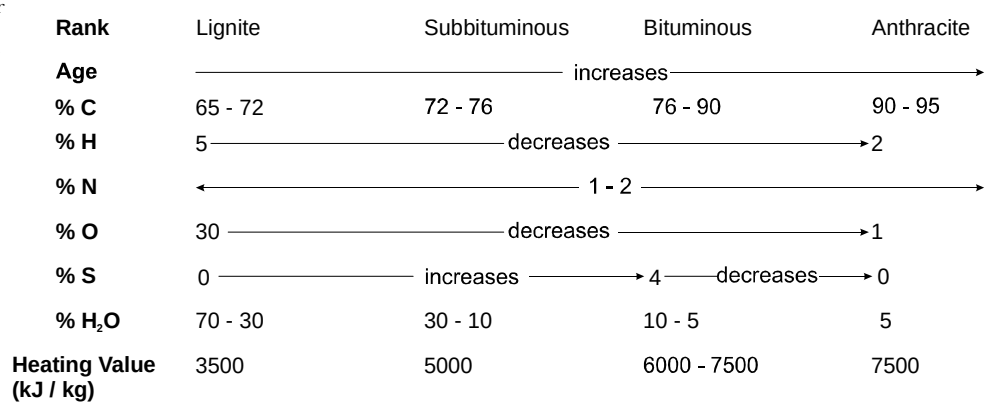

Fig. 4-4: *Variation of selected coal properties with coal rank.*

Today's systems for a fast characterization of coal are mainly based on X-ray fluorescence (XRF) [146] and prompt-gamma neutron activation analysis (PGNAA) [147]. However, both techniques have serious shortcomings for a rapid elemental process analysis of coal [145,148]. The XRF approach shows the most potential but is still hampered by the lack of sensitivity for the lighter elements. To overcome this situation, several attempts have been made to evaluate the potential of other spectroscopic methods of inorganic analysis for coal characterization. To assess the relevant parameters of the combustion, it is sufficient in practice to determine the inorganic composition of coals within a certain range of concentration. Methods such as atomic absorption spectroscopy (AAS), inductively coupled plasma atomic emission spectroscopy (ICP-AES), and inductively coupled plasma mass spectroscopy (ICP-MS) have been described in the literature, but are not suitable for process analysis as they all imply a tedious sample preparation procedure, i.e. digestion of the coal [149,151].
The prospect of a highly automated and contactless analysis with no or minor sample preparation makes LIPS a very attractive alternative to XRF. Furthermore, the data are instantly available in digital form and can be used for an online process control. Earlier work on coal samples demonstrated the potential of LIPS for set of lignites [155,156], whereas this study is based on a larger set of 40 very different samples and the NIST standard 1635 (trace elements in subbituminous coal). We focused mainly on elements important for the assessment of the ash content (Mg, Si, Ca, Al, Fe, Ti) and the merits of different sample conditioning.

4.4.1. Experimental

In order to investigate the application of LIPS for analysis of coal of different type and origin an extensive set of 41 coal samples was studied. The set consisted of 36 lignite coal samples from two different mining regions in Rheinland, Germany, and 5 mineral coal samples from one mining place in Ruhrgebit, Germany. The samples were originally in the form of granulates with diameter between 1 and 5 mm.
The reference analysis was based ICP-MS of the digested samples. The procedure was based on some already published methods [149,150] and adapted to the

available instrumentation. First 5 g of each sample was dried at 75°C for 24 hours. The dried samples were than ground with a laboratory grinder (Mühle A10, IKA-Werke, Germany) down to grain size of less than 1 mm. From each such prepared sample 100 mg has been put in a digestion vessel and mixed with an acid mixture of 4.9 ml HNO_3 (65%), 1 ml H_2O_2 (30%) and 0.1 µl HF (40%). In each vessel 50 µl of a Rh standard solution (c = 10 mg/l) was added as an internal standard. Such mixtures were digested in a microwave accelerated reaction system (MWS 1, Berghof-Maassen, Germany) using an optimized temperature program (first step: heating at 180°C, 5°/s and holding for 5 min; second step: holding the temperature of 180°C for 15 min). For the measurement with ICP-MS (Elan 6100, Perkin-Elemer, Germany), 0.75 ml of the solution has been taken, mixed with 0.5 ml Be Standard solution and diluted to 100 ml (total dilution 1:8000). Calibration was made with external standards (multielemental standards Merck IV and Merck V) for the range of concentrations between 0.2-1.2 µg/l. For the main componets such as Si, K, Na, Fe, and Ti, a calibration was made for concentrations between 0.2-1.2 mg/l. The instrumental parameters are given in the Table 4-3. The relative error of analysis was estimated to be 10%. The complete results of ICP-MS analysis of coal samples are given in the appendix.
The LIPS measurements implied some minor sample preparation. As for the reference analysis a few grams of each samples were dried and ground. The samples were then pressed under 10 t pressure into solid pellets with an even smooth analytical surface. Additonally, one set of totally unprepared samples was also studied.

Tab. 4-3: *Instrumental parameters for ICP-MS analysis of coal*

Parameter	Value
Generator power	1100 W
Peak-hopping	2 s
Argon flow-rate	0.8 - 1 ml / min
Measured masses	^{23}Na, ^{24}Mg, ^{27}Al, ^{30}Si, ^{43}Ca, ^{49}Ti,^{51}V, ^{55}Mn,^{87}Sr, ^{138}Ba
Additional option	Auto-lens correction, dual-detector modus

The experimental set-up for LIPS analysis in UV-Vis was already described in chapter 3.1. The laser was operating on fundamental wavelength (1064 nm) with energy of 30 mJ/pulse, which corresponded to irradiance of 1.1 GW cm^{-2}.

4.4.2. Results and Discussion

As already said, coal samples were investigated in this study either as raw samples or as pellets pressed from the ground coal. For the coal pellets, the lens-to-sample distance was optimized via the intensity of a magnesium line (Mg(II) 279.535 nm). The highest intensity was achieved by focusing 2 mm inside the sample (see Fig. 4-5).

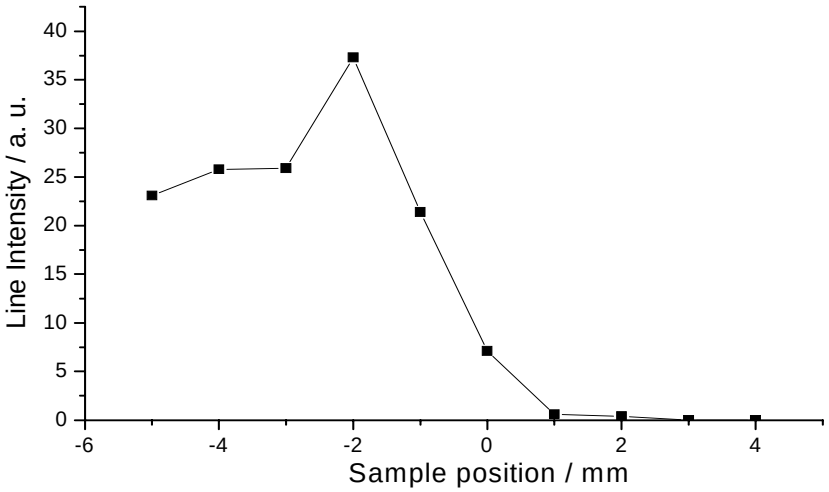

Fig. 4-5: *Intensity of Mg(II) 279.535 nm line for different lens-to-sample distances (zero position corresponds to lens focal point).*

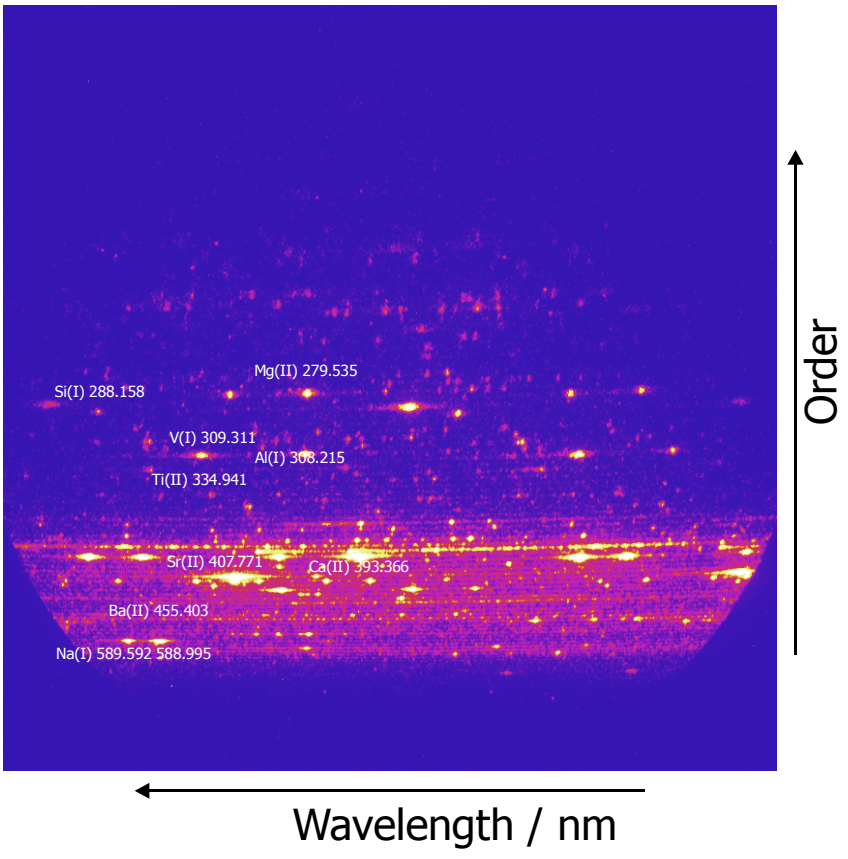

Fig. 4-6: *Typical echelle image from a lignite coal sample.*

The consistency of the pellets prepared from the ground coals varied from compact to brittle due to their density (0.9-1.2 g cm^{-3}), which lead also to a different ablation characteristic. At an irradiance of 1.1 GW cm^{-2} which was used throughout all experiments, the typical crater diameter was about 400 µm on lignite samples and slightly smaller on bituminous coal. Further, the signal-to-noise ratio (SNR) for Mg, Al, and Si was optimized for the delay to the plasma

ignition (here 1 μs) and the total integration time (here 3 μs). The echelle image in Fig. 4-6 illustrates the potential of LIPS for a rather comprehensive elemental analysis of major and minor elements in coal with this kind of instrumentation. The choice of emission lines (see Table 4-4) was, however, limited by the objective to analyze major and minor components with a sufficient dynamic range and in a rather short time. Similar compromises had to be made for the optimum delay and integration parameters. To compensate the obvious heterogeneity of the samples, two sampling procedures were compared in a preliminary experiment. From different locations on the pellet were acquired either: (i) 50 spectra of ten successive laser pulses (taken at a single location) integrated on the ICCD or (ii) 50 spectra of a single laser pulse; for both sampling procedures a total average was compute from all spectra.

Figure 4-7 reveals that the single pulse approach yielded a significant better linearity, hence analytical figure of merits. Theoretically, the better SNR [158] of the first approach should also improve the linearity, this was, however, not the case here. To investigate this effect further, we compared the recorded signal intensities from 50 single pulses at different locations and 50 subsequent single pulses at one location on the sample. Fig. 4-8 shows that the emission intensities of single pulses at different locations on the sample follow a gaussian distribution (RSD 29%), whereas in-depth sampling leads to a skewed distribution due to several low intensity events (RSD 69%). Evidently, this effect distorts the calculated total average.

Although the emission intensities are expected to decrease with the changing aspect ratio of in-depth sampling, surprisingly not all low intensity events were observed at late times during this sampling approach. This points to a considerable heterogeneity of the sample, which influenced the single pulse approach less. Similar effects were already observed for particulate matrices by other authors [159,160].

Figure 4-9 a-i show the calibration curves and Table 4-3 summarize the limits of detection (LOD) for the investigated elements utilizing the single pulse approach. To improve the RSD, 100 single pulses were evaluated instead of 50, which resulted in RSD's between 8% and 17% and total analysis time of 30 s. The LODs were calculated according to the 3s-criteria, no internal standardization was required. The determined LODs and reproducibility are sufficient to qualify LIPS for a process analysis of coal samples. The necessary sample preparation (drying and pressing) can be easily done automatically even with a process stream on conveyor belts.

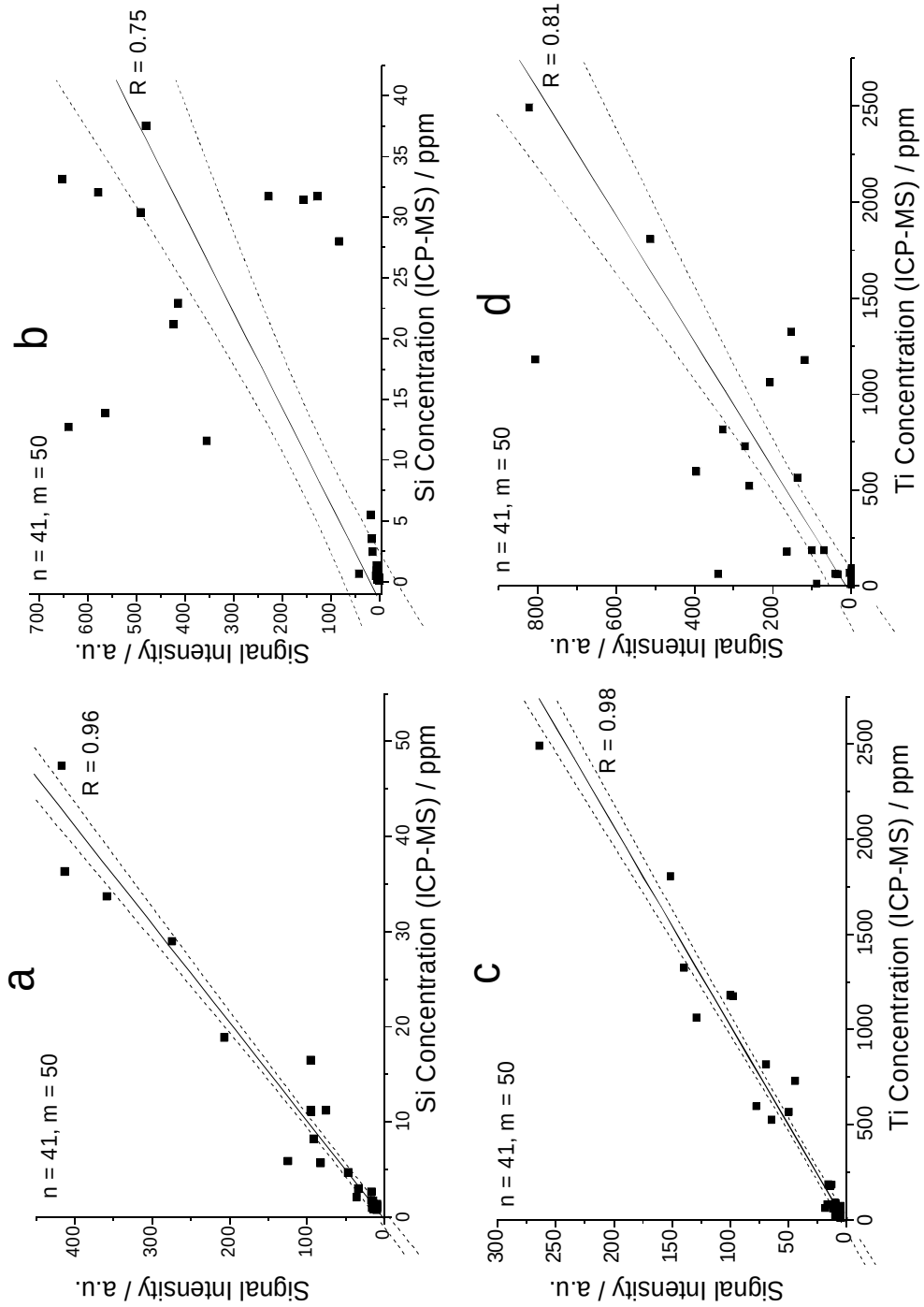

Fig. 4-7: *Comparison of the linearity achieved for different sampling procedures (a,b: Si(I) 288.158 nm; c,d: Ti(II) 334.941 nm; dashed line: 95% confidence interval of regression line, no of samples: 41; a, c: 50 single pulses at different locations on the sample; b, d: 10 pulses averages at 50 different locations on the sample).*

To explore the possibilities for LIPS analysis of raw samples, the original sample set were classified according to their inorganic composition established by reference analysis. To cover the main elemental variance of the sample set, the classes were established via cluster analysis with a centroid linkage procedure [161]. For analysis, the ground samples were outspread and flattened on a glass dish and then sampled directly by single pulses from different locations. Preliminary work

showed that the emission intensities varied significantly in this approach due to the strong variations of the surface height and roughness. An optimization of the lens-to-sample distance was not possible in this way.

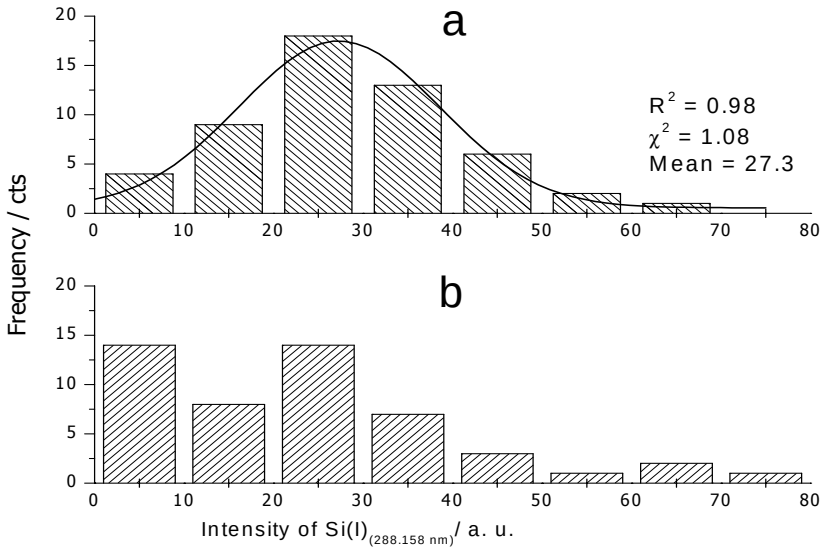

Fig. 4-8: *Distribution of emission intensities for 50 single pulses at different locations on the sample (a) and 50 subsequent single pulse on a single location (b). (Si(I) 288.158 nm, solid line: least square fit to a gaussian distribution, sample: NIST 1635 reference material).*

For a more detailed investigation of single-pulse sampling of raw coal samples, the NIST 1635 reference material as pellet and ground raw sample with 500 single pulses has been sampled. For the pellet, the frequency of the recorded pulse intensities follow already with 50 pulses a gaussian distribution ($R^2 = 0.95$), while with 500 pulses a very reproducible signal is observed ($R^2 = 0.98$). For the raw sample, a gaussian distribution was observed after 100-500 pulses, e.g. for aluminium in Fig.4-10, but not for all elements, e.g. magnesium in Fig. 4-11. Characteristic for all distributions (compare Fig. 3-11 and 3-12) were high frequency counts of low intensities, which is probably due to the mismatch between the focal plane and the raw sample height. Note, that in Fig. 4-10 also fairly high intensities occur with a significant frequency. Both observations indicate an incorrect sampling of the raw coal for some elements which could be caused by particle size dependent elemental distribution ([162] and references therein).

The variables in Fig. 4-12 are regrouped by similarity and the scale (color) gives the value of correlation coefficient R for each variable pair. As the most abundant minerals in coal are clays including kaolinite, illite, montmorillonite, and illite-montmorillonite mixed layer clays, Si, Al, and Ti have a high correlation in Fig. 4-12. Carbonates are the next most common minerals, mainly siderite, ankerite, calcite, and dolomite, but Mg and Ca have only a low correlation with the first group. This indicates different minerals but supports also our hypothesis of the incorrect sampling of certain size fractions (see Fig. 4-11) as Mg and Ca could not be determined in the raw coal.

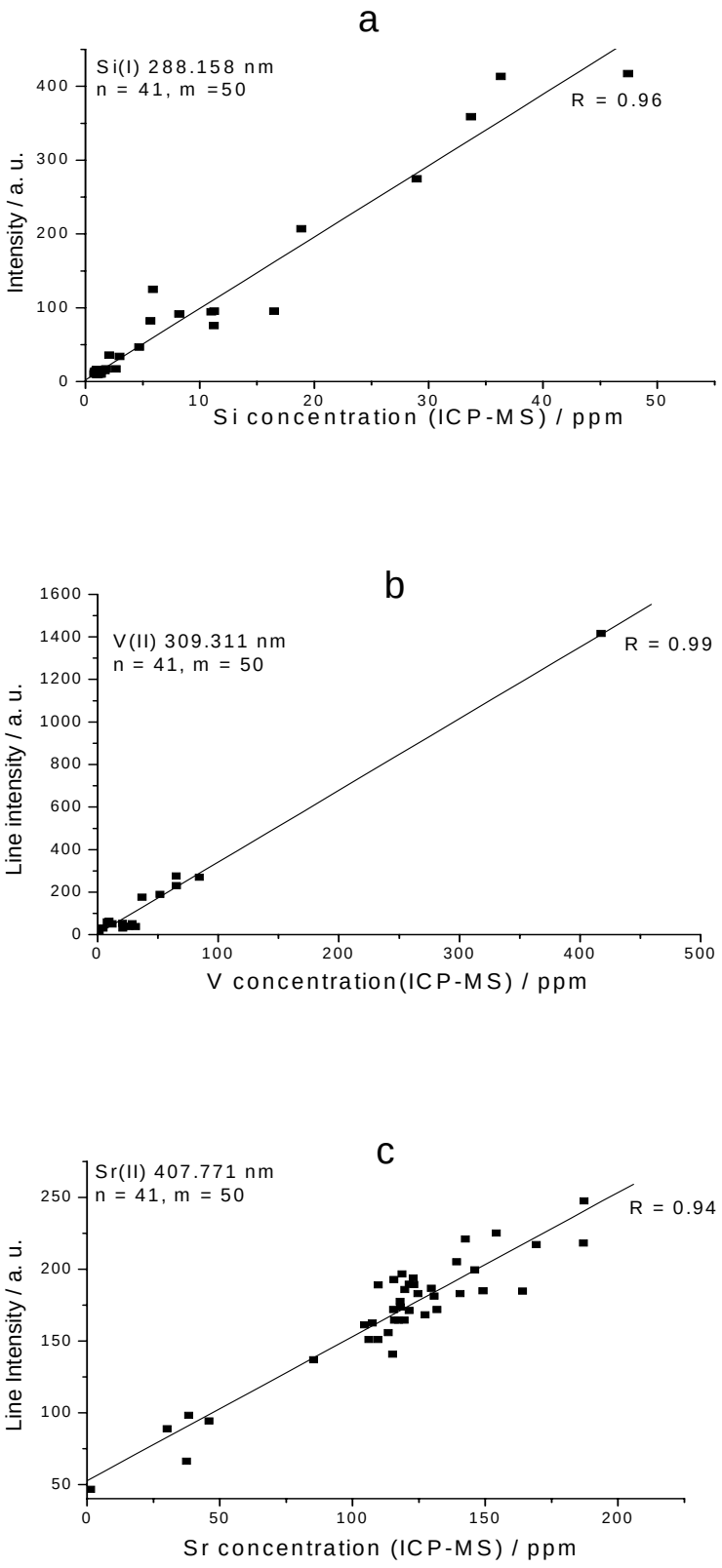

Fig. 4-9: *Calibration curves for Si (a), V (b), Sr (c), Ba, (d), Mg (e), Ti (f), Al (g), Ca (h), and Na (i) in coal.*

d

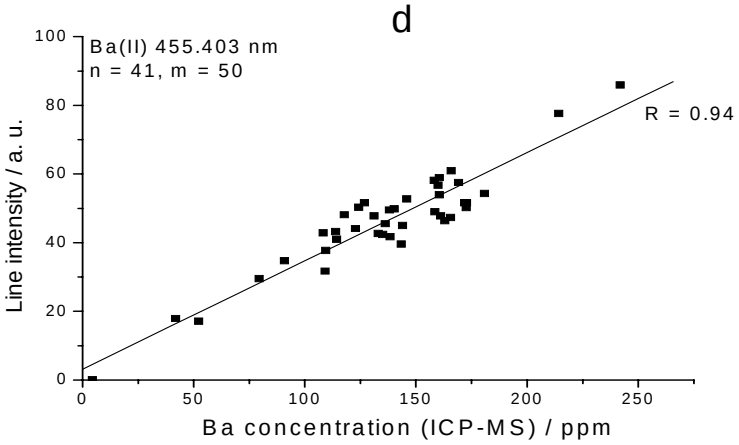
Ba(II) 455.403 nm
n = 41, m = 50
R = 0.94
Line intensity / a. u.
Ba concentration (ICP-MS) / ppm
0
20
40
60
80
100
0
50
100
150
200
250

e

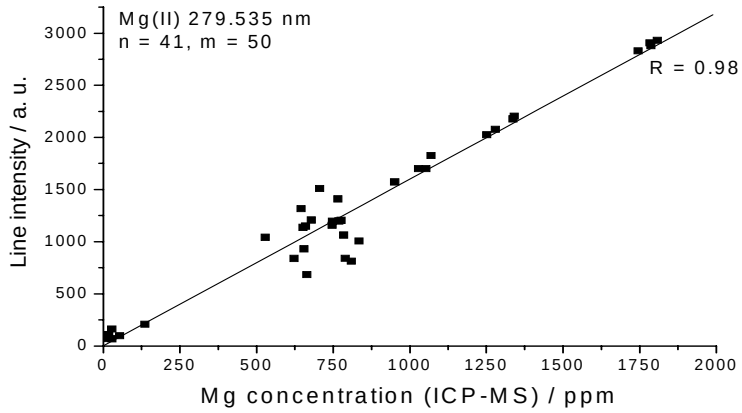
Mg(II) 279.535 nm
n = 41, m = 50
R = 0.98
Line intensity / a. u.
Mg concentration (ICP-MS) / ppm
0
500
1000
1500
2000
2500
3000
0
250
500
750
1000
1250
1500
1750
2000

f

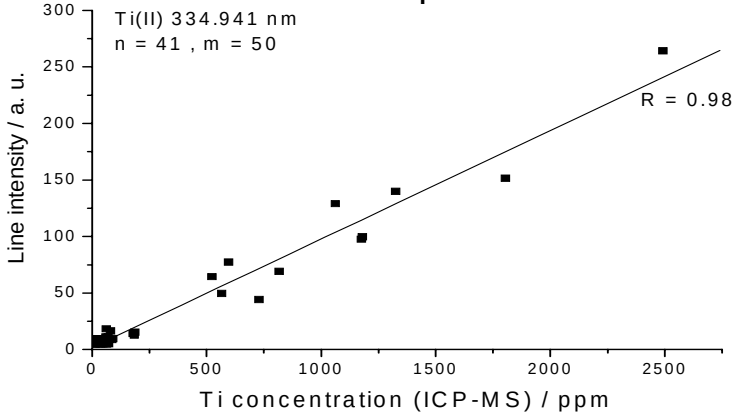
Ti(II) 334.941 nm
n = 41 , m = 50
R = 0.98
Line intensity / a. u.
Ti concentration (ICP-MS) / ppm
0
50
100
150
200
250
300
0
500
1000
1500
2000
2500

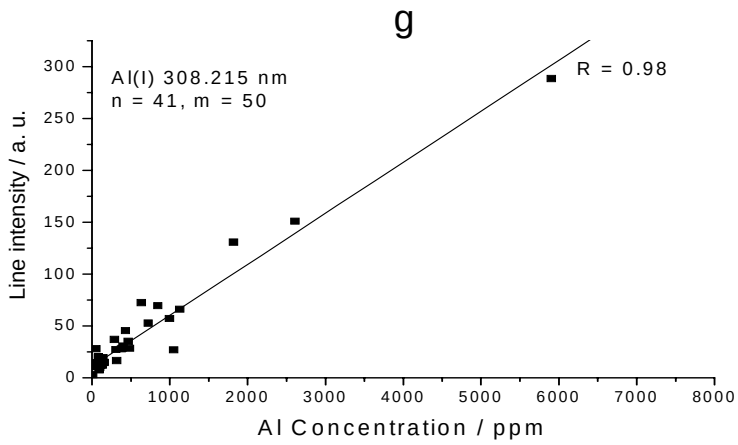
g
Al(I) 308.215 nm
n = 41, m = 50
R = 0.98
Line intensity / a. u.
Al Concentration / ppm

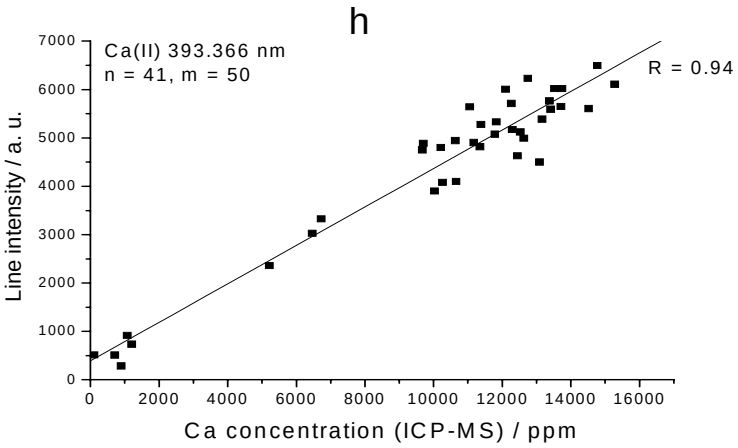
h
Ca(II) 393.366 nm
n = 41, m = 50
R = 0.94
Line intensity / a. u.
Ca concentration (ICP-MS) / ppm

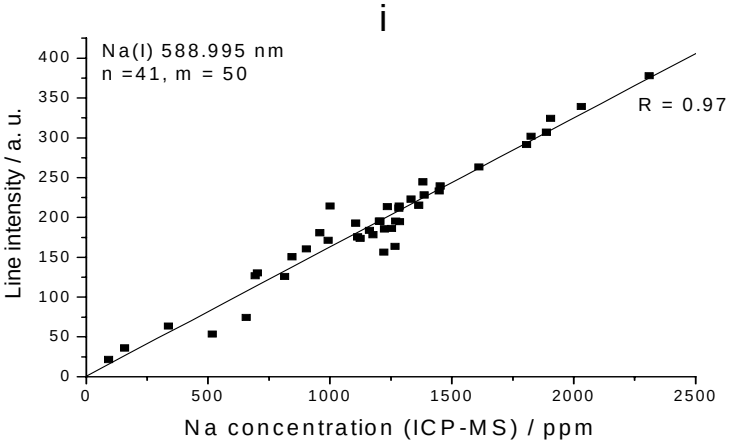
i
Na(I) 588.995 nm
n =41, m = 50
R = 0.97
Line intensity / a. u.
Na concentration (ICP-MS) / ppm

Tab. 4-4: *Limits of detection for inorganic elements in coal,*

Element & Analytical Line	R	n	LOD / ppm
Si(I) 288.158 nm	0.98 / 0.98*	41	2 / 10*
V(II) 309.311 nm	0.99	41	4
Sr(II) 407.771 nm	0.94	41	22
Ba(II) 455.403 nm	0.94	41	26
Ti(II) 334.941 nm	0.98 / 0.98*	41	56 / 161*
Mg(II) 279.535 nm	0.97	41	111
Al(I) 308.215 nm	0.98 / 0.98*	41	120 / 341*
Ca(II) 393.366 nm	0.97	41	139
Na(I) 588.995 nm	0.97	41	141

** denote values for Si, Ti, and Al for raw coal samples*

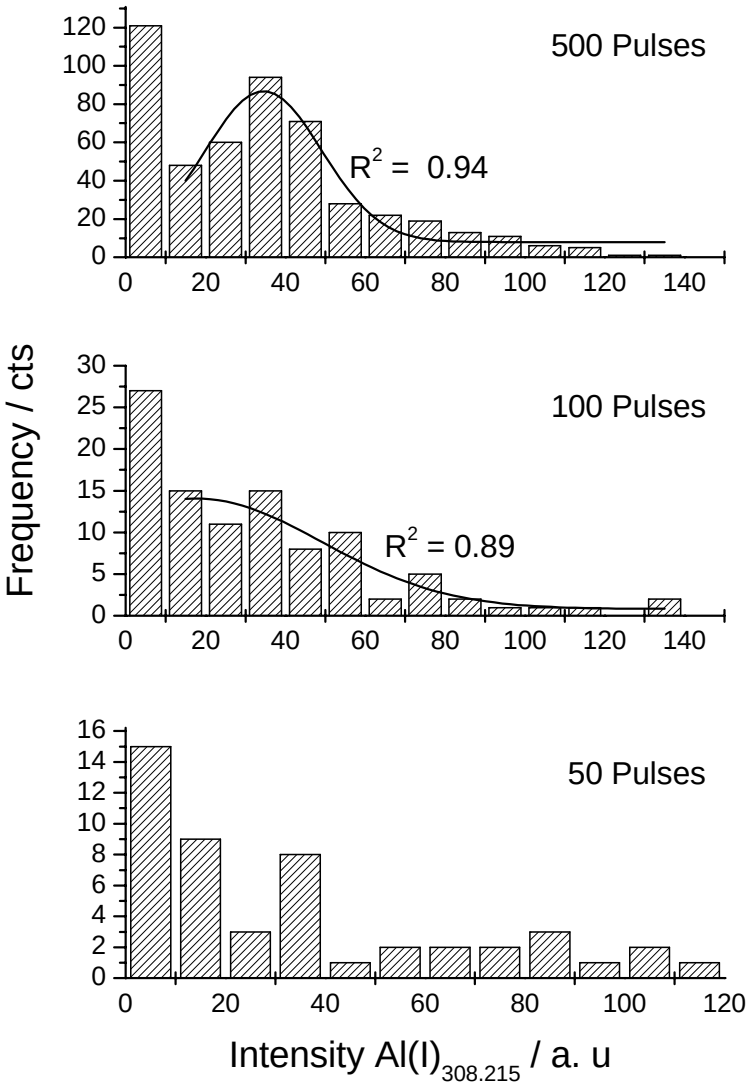

Fig. 4-10: *Distribution of the emission intensities of the Al(I) line at 308.215 nm for a different number of single pulses on a raw coal sample (NIST 1635 reference material).*

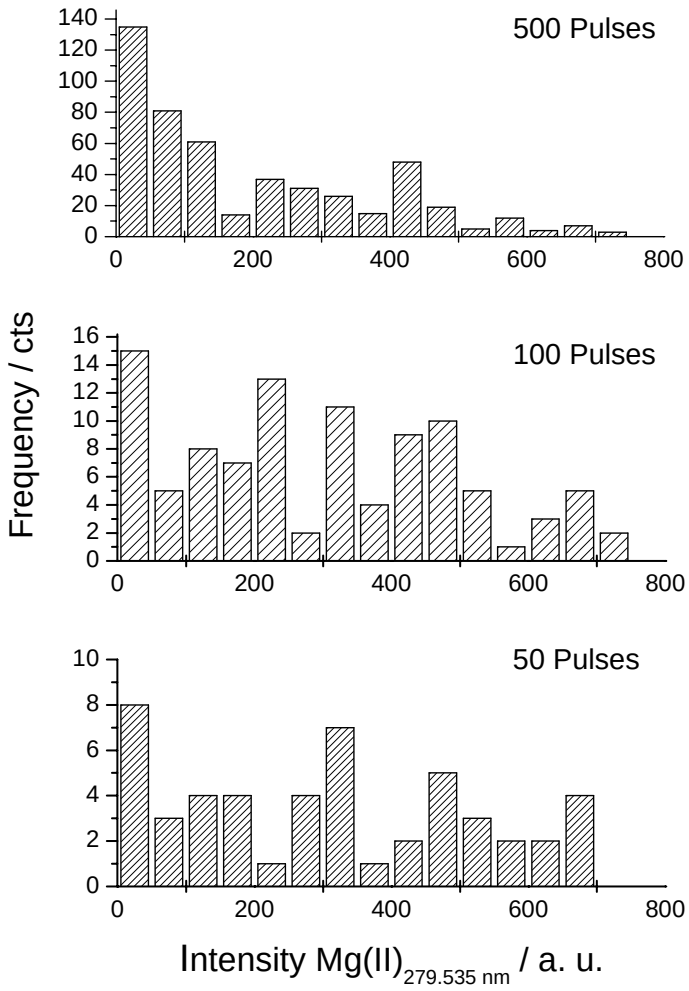

Fig.4-11: *Distribution of the emission intensities of the Mg(II) line at 279.535 nm for a different number of single pulses on a raw coal sample (NIST 1635 reference material).*

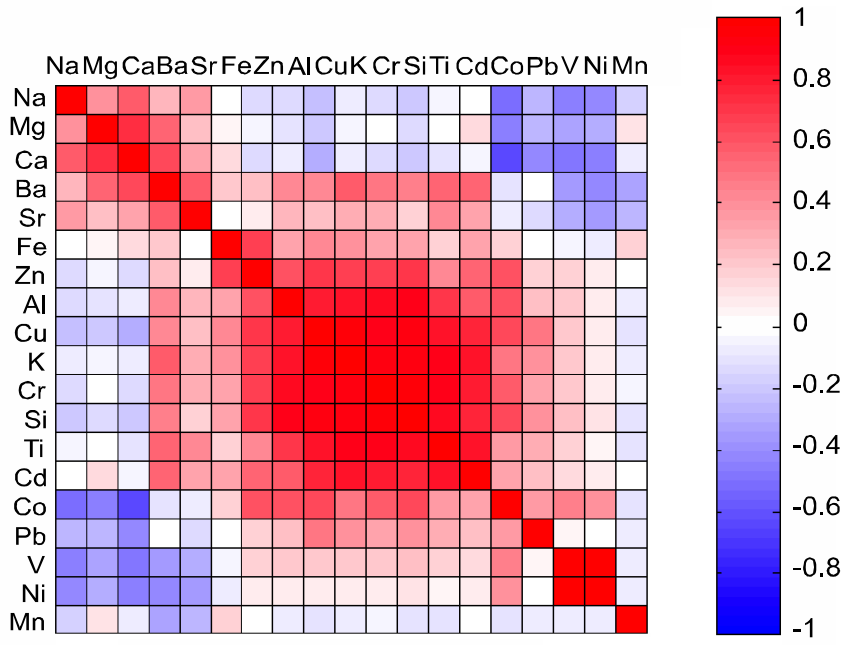

Fig. 4-11: *Correlation map of the major and minor elements found by ICP-MS reference analysis in the investigated 41 coal samples*

4.5. Analysis of Clay

4.5.1. Introduction

Clay is a classical sediment which belongs to class of pelites. A typical clay consists mainly of the clay minerals, quartz, some other phylosilicates (e.g. mica), and divers carbonate minerals [164]. Often also sulfides (e.g. pyrite), iron oxides and hydroxides and organic substances (e.g. plants residuals) are included in clay. In ordinary brown or yellow clays variable amounts of Fe, Mn, Mg, Ti, P, N, and other trace elements that are either chemically bound, or adsorbed on small particles. Generally said, the composition of a typical clay material can be described with: SiO_2 (65-80%), Al_2O_3 (15-30%), K_2O (2-3%), TiO_2 (~2%), and Fe_2O_3 (2-3%). The clay constituent are almost exclusively in crystalline form. Amorphous substances are either not present or present in negligible concentrations.
Clay is an important raw material in production of all kinds of bricks, technical and household porcelain, ceramic plates, terracotta and fire-resistant materials. Pure clays like such from attapulgit or betonit are used as carriers for catalysators. The development of both structural and functional ceramics for modern industrial applications and electronic devices necessitates a fundamental study of the relations of their properties to the chemical composition of the basic and raw materials as well as to the microstructure in these materials. Therefore, powerful analytical methods and strategies are required to determine the main elements and the impurities especially in the raw materials. From these requirements, developments in atomic spectrometric methods have resulted. At the first place there is ICP-AES (Inductively-Coupled Plasma Atomic Emission Spectroscopy) which was found to be most versatile method for major, minor and trace element determination in geochemical analysis [165-167]. Several other authors reported successful applications of XRF (X-ray Fluorescence) and XRPD (X-ray Powder Diffraction) [168, 169]. Several other reports discuss the spectrochemical examination of clay minerals and terracotta samples using a simple complexometric method [170] or Mössbauer spectroscopy [171]. In the context of fast analysis of raw materials such as coal we extended here the work to another important raw material, i.e. clay.

4.5.2. Experimental

Five different clay samples provided by company G&S GmbH & Co. KG (Siershahn, Germany) have been used. Aim of the experiment was quantitative LIPS analysis of metalic components. Similar to analysis of coal samples (see chapter 3.4), a reference analysis based on ICP-MS system was made. Microwave supported total digestion of the samples have been performed according to the method described in the literature [172]. All 5 samples were ground with a laboratory grinder (Mühle A10, IKA- Werke, Germany) and 5 g of each sample was left for drying during 24 hours at the temperature of 100 °C. 100 mg of such dried

sample was put in reaction vessel and mixed with 2 ml HNO_3 (65%), 3.5 ml HCl (30%) and 1.5 ml HF (40%). Such prepared vessels were introduced in microwave accelerated reaction system (MARS5, CEM corporation, USA). Digestion was performed using an optimized temperature program (first step: heating on 160 °C for 10 minutes and holding for 3 minutes; second step: heating for 5 minutes at 180°C and holding for 3 minutes and third step: heating for 5 minutes at 220°C and holding for 20 minutes). The digestion resulted in clear solutions without any residue. The results of ICP-MS analysis are given in appendix of this work.

For the LIPS analysis, 500 mg of powdered and dried samples were mixed with 250 mg KBr and 100 mg of graphite and pressed under the 10 t pressure into the flat solid pallets. Potassium bromide was used here because of its excellent binding properties. Additionally its atomic line emission in UV is extremely weak [173] and possible spectral interferences are minimized. The graphite was added as an internal standard. The experimental set-up used was described in chapter 4.1. The laser was frequency quadrupled, operating at $\lambda = 266$ nm with a sample irradiance of about 1 $GWcm^{-2}$.

4.5.3. Results and Discussion

Figure 3-13 shows a cut-out of a baseline corrected and smoothed spectrum of a clay sample. A good resolved and intensive iron atomic line at 297.323 nm has been used for optimization of delay and gate. The parameters used here were: delay =1.2 μs and gate = 2 μs.

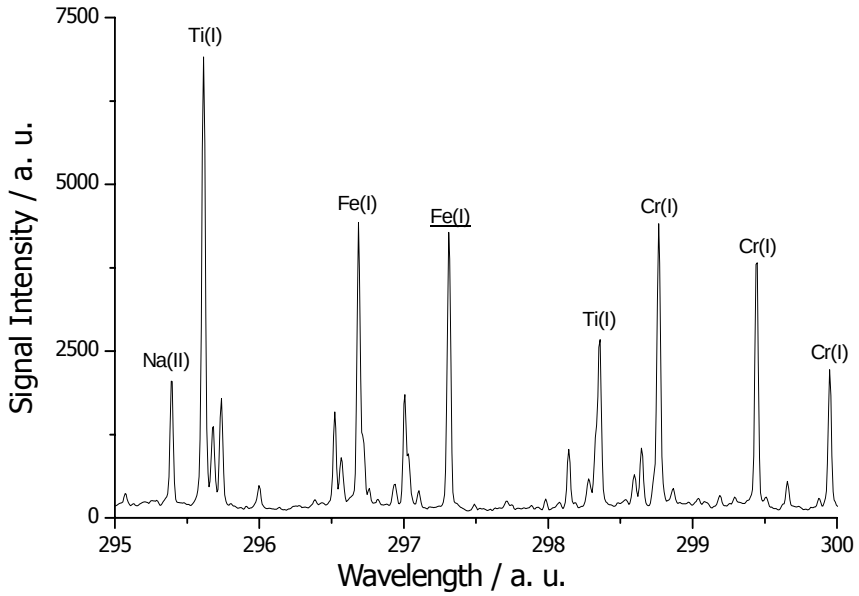

Fig. 4-12: *Cut-out of baseline-corrected and smoothed spectrum of an clay sample (Sample T1724, Delay = 1.2 μs, Gate = 2 μs).*

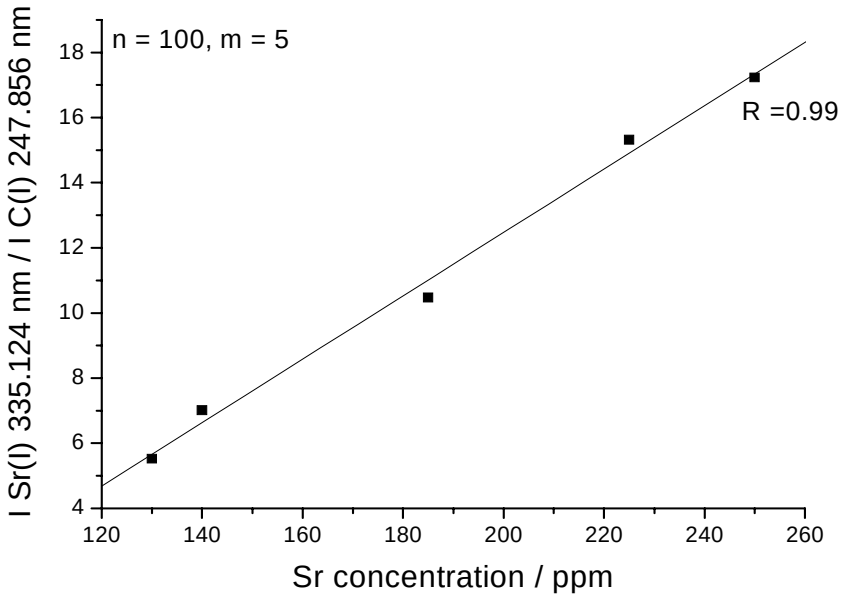

Fig. 4-13: *Calibration curve for Sr in clay.*

All five samples have been measured with 100 single laser pulses focused on different sample spots. All lines used for quantitative analysis were good resolved prominent lines of certain element. Second request was the similarity of upper energy levels with the C(I) 247.856 nm line which was used for internal standardization (see Table 4-5). Figure 4-14 shows calibration curve for strontium in clay using the added carbon as the internal standard. Table 4-5 gives the used lines, energy levels and LOD's for all analysed elements.

Tab. 4-5: *The used lines, corresponding energy levels and limits of detection for analysed elements.*

Element and used line	E^{lower} / eV	E^{upper} / eV	LOD / ppm
Li (I) 214.391 nm	0	5.11	8
Cu (I) 222.778 nm	1.642	7.206	12
Ni (I) 214.391 nm	0.423	6.204	13
Ba (I) 244.462 nm	0	5.071	28
Sr (I) 335.124 nm	1.847	5.546	31
Mg (I) 383.827 nm	4.436	7.575	45
Fe (I) 297.323 nm	0.051	4.220	63
C (I) 245.856 nm	2.680	7.685	int. standard

5 LIPS in the VUV

5.1. Experimental Set-up

The experimental set-up for the LIPS analysis in VUV region is depicted in Fig. 5-1. For plasma ignition, a Q-switched Nd:YAG laser (Surelite I, Continuum, USA) with a maximum pulse energy of 430 mJ (λ = 1064 nm) was utilized at a 10 Hz repetition rate (FWHM: 7 ns). The pulse energy was regulated by a variable attenuator (Newport, Irvine, USA) instead of the Q-switch delay to ensure a constant spatial and temporal profile of the laser beam. In addition, the pulse energy was monitored via a beam splitter and a pulse energy meter (Powerlite C5100, Continuum, USA). The laser beam was focused on the sample surface inside a vacuum chamber with a single plano-convex lens (f = 200 mm). The sample is placed inside vacuum chamber (V = 11 l) on a rotation stage, which allows an ablation of different, pristine sites on the sample. Rotation of the stage is achieved by a mechanical feed-through and a simple electric motor outside the chamber. The chamber has several additional ports for observation and connection of a manometer, the pumping system, a hot ion gauge, and a buffer gas supply. The pumping system consisted of a turbo molecular pump (Turbovac 50, Leybold, Germany) with a dual-stage rotary vane pre-pump (Trivac D 25 BCS, Leybold, Germany). This system achieves a vacuum about 10^{-5} mbar inside the chamber within 15 min. The actual pressure inside the chamber was controlled through a hot ion gauge (Ionvac ITR90, Leybold, Germany).

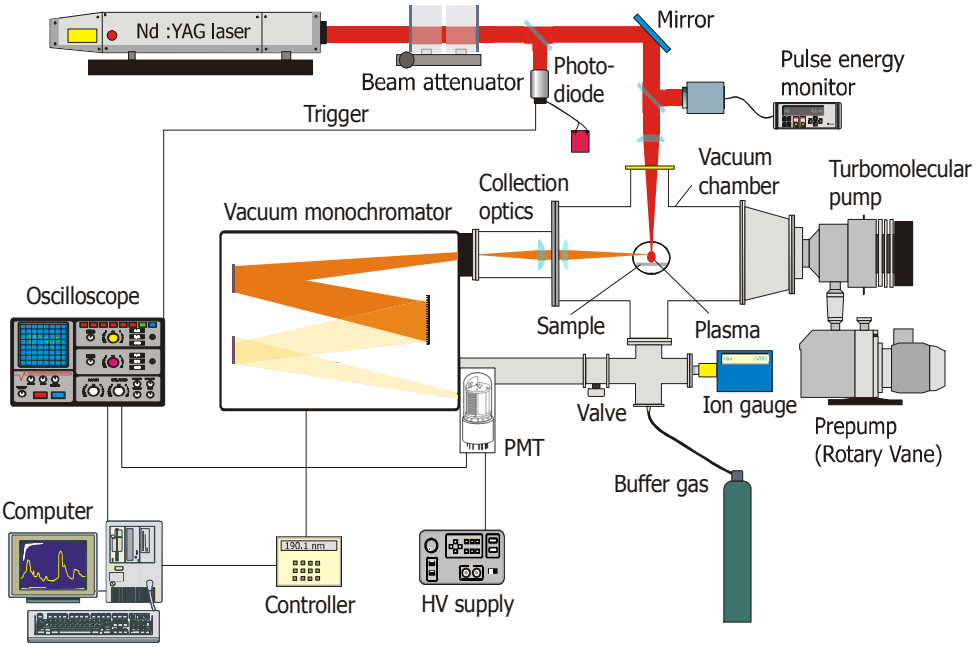

Fig. 5-1: *The experimental set-up for LIPS in the VUV.*

As displayed in Fig. 5-2, the plasma emission was collected perpendicular to the incoming laser beam (side-on observation) and focused on the monochromator entrance slit by means of two plano-convex lenses (MgF_2, f = 100 mm). This side-on observation geometry restricted the set-up to flat samples and made a precise adjustment of the sample necessary to ensure that always the same section of the expanding plasma is imaged on the entrance slit.

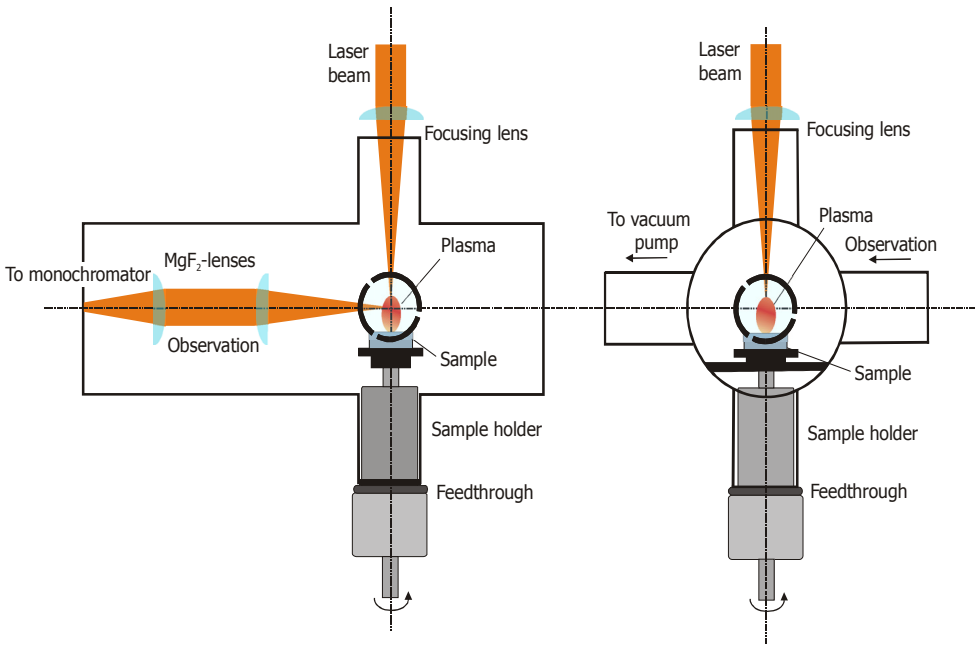

Fig. 5-2: *Detailed view of the focusing and observation geometry inside the vacuum chamber (see Fig. 5-1).*

The chamber is directly coupled to a 0.39-m-vacuum monochromator with a Czerny-Turner mounting (VM-504, Acton Research Corporation, Acton, USA) equipped with a 1200-g/mm-grating. This allows a spectral resolution of 0.06 nm (at 200 nm). For detection of emission lines in the VUV region, a head-on photomultiplier (52 mm diameter, Type 9635B, Electron tubes Inc., USA) with

an sodium salicylate ($NaC_7H_5O_3$) coated window was employed, the signal from the PMT was directly fed into a digitizing oscilloscope (TDS620A, Tektronix, USA). The experiment was triggered via a fast photodiode (BPX65, Laser Components) illuminated by the laser beam through a beam splitter. The overall system was controlled via an in-house made LabVIEW (National Instruments, USA) software. Argon was used as buffer gas for all VUV experiments and had a purity of 99.999%.

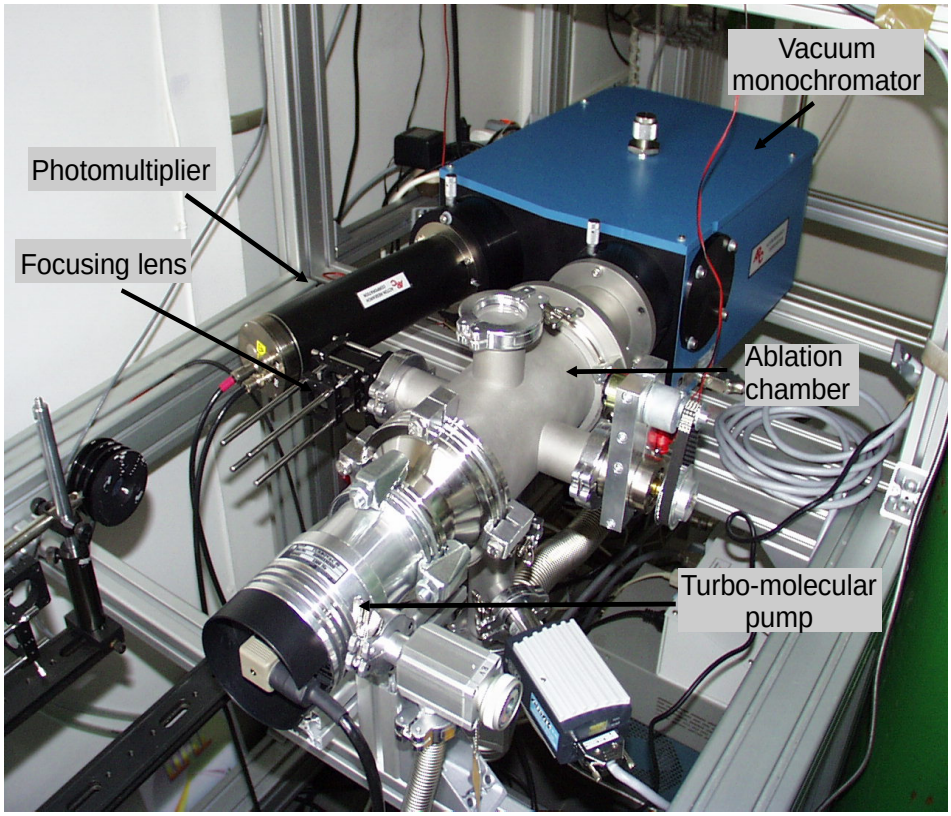

Fig. 5-3: *Photograph of the laboratory experimental set-up for LIPS experiments in VUV (Nd:YAG laser is not shown).*

5.2. Characterization of a VUV Monochromator

The slits of monochromator play an important role in determining the monochromator's performance characteristics and quality. The entrance slit of monochromator serves as a radiation source; its image is ultimately focused on the focal plane that contains the exit slit. The effective bandwidth $\Delta\lambda_{eff}$ the range of wavelengths that exit the monochromators at a given wavelength settings. The effective bandwidth can be related to reciprocal linear dispersion D^{-1} according to [70]

$$\Delta\lambda_{eff} = wD^{-1}, \tag{5.1.}$$

where w is the slit width. A complete resolution of two lines is feasible only if the slit width is adjusted so that effective bandwidth of the monochromator is equal to one half the wavelength difference of the lines. The use of the minimal slit width is desirable when resolution of narrow bands is needed. On the other

hand, a marked decrease in the available radiant power accompanies a narrowing of slits, and accurate measurements of this power becomes more difficult. Thus, wider slit widths may be used for quantitative analysis rather than for qualitative work, where spectral detail is important.

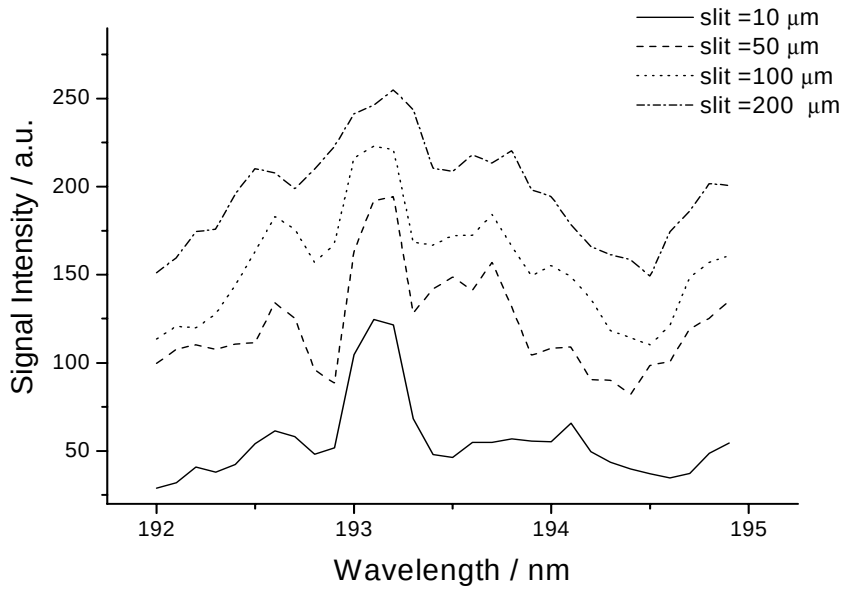

Fig. 5-4: *Profiles of C(I) 193.1 nm line in steel for different monochromator entrance slit widths.*

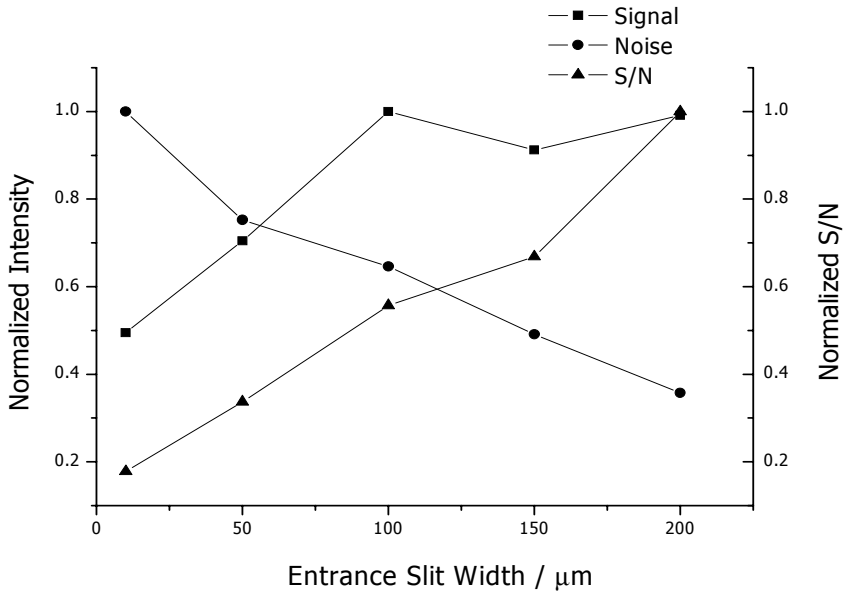

Fig. 5-5: *Signal, noise, and signal-to-noise ratio of C(I) 193.091 nm line for different entrance slit widths (values are determined from statistic of 100 repetitive signals).*

Figure 5-4 shows the line profile of C(I) 193.091 nm line in one steel sample for different widths of the entrance slit of the vacuum monochromator. The exit slit width was constant, i.e. 100 μm. Increasing the entrance slit width increase line intensity but leads also to a significant increase of background. The line is also broadened and for the width > 100μm no meaningful spectral resolution was achieved. On the other side noise for the line maximum decreases and signal-to-noise ratio is preferable for wider input slits (see Fig. 5-5).

Increasing the exit slit width leads to an increased line intensity but only to the width of about 100 μm. After that the line maximum remains constant and line is only broadened (compare Fig. 5-4). Consenquently, signal-to-noise ratio of the line maximum signal increases rapidly to the width of 100 μm and than remain more or less constant (Fig. 5-5). In this experiment, entrance slith was held constant at the minimum width of 10 μm.
In all further experiments the exit slit width was held always at 100 μm, and entrance slit was shifted from 10 μm for the purpose of identification of emission lines and qualitative analysis to 100 μm for quantitative measurements

.

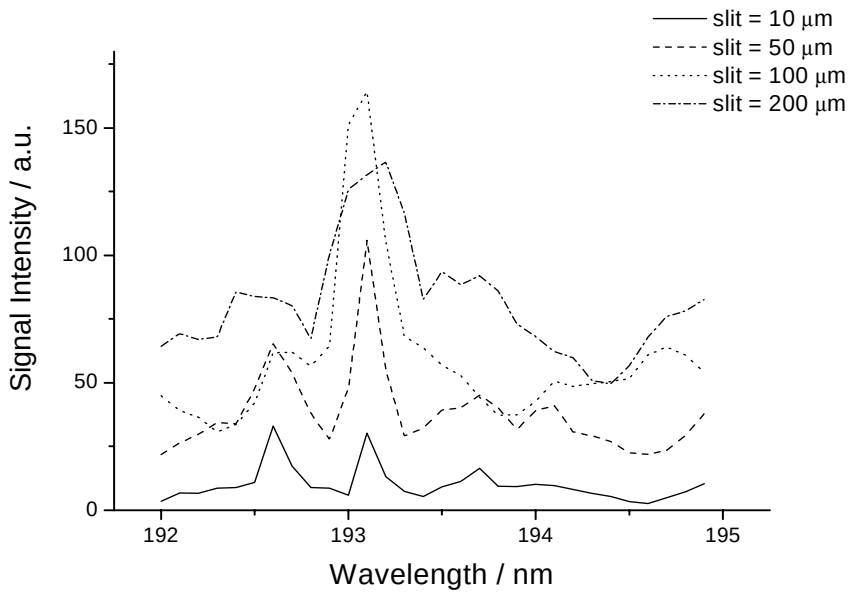

Fig. 5-6: *The profiles of C(I) 193.1 nm line in steel for different monochromator exit slit widths.*

.

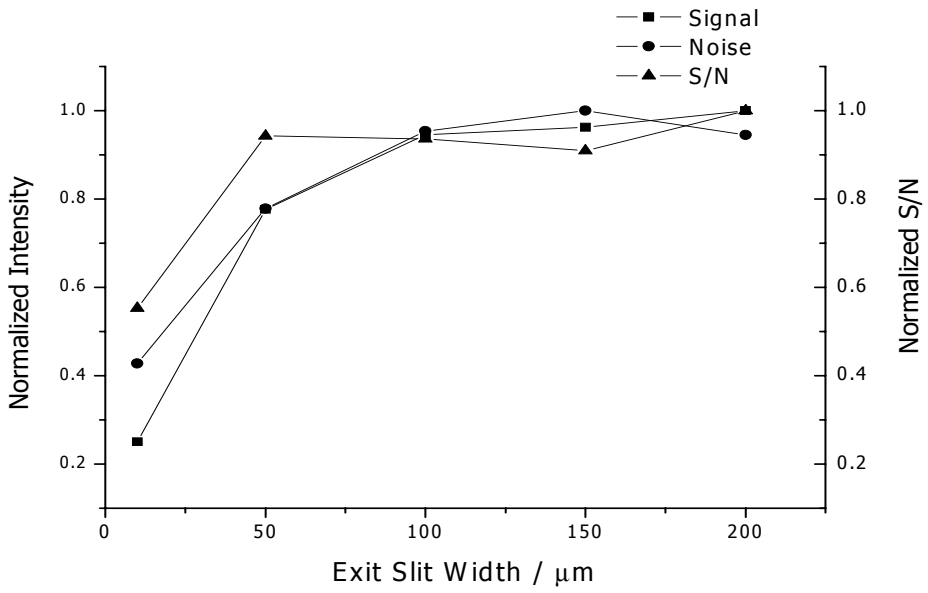

Fig. 5-7: *Signal, noise, and signal-to-noise ratio of C(I) 193.091 nm line for different exit slit widths (values are determined from statistic of 100 repetitive signals).*

5.3. Analysis of Non-Metals in Steel

5.3.1. Introduction

Nowdays the term steel is understood to include not only all forgeable iron-based materials, but also all highly alloyed metallic materials in which the element iron is an important component, but which are not necessarily forgeable [174]. The versatility of steel is due to polymorphism of the iron crystal and its ability to alloy with other elements, forming solid solutions or compounds. The microstructure of steel in a finished component can be adjusted by via the chemical composition, the forming conditions and a wide variety of possible heat treatments.

.

Tab. 5-1: *Chemical composition of different steels*

Type	Properties	Added elements
Alloyed, refined steel	High strength and toughens.	Ni, Cr, V, Mo, W
Durable steel	Higher durability	Mn, sometimes Cr or Mo
Stainless steel	Resistant to rust and acid	Extra Cr, Ni, Mo, Ti
Heat resistant steel	Resistant to high temperatures. Suitable for exhaust pipes of motors.	Cr or Cr and Ni, possibly Ti
Alloyed tool steel	Loses toughness above 600°C	

Many different types of steel exist of which a number are summarized in Table 5-1. Even small differences in concentration of added elements can make a large difference in the properties of the final product

An increasing demand for better quality control exists within the steel industry [175]. The quality of production and the efficiency of the production process depend on fast and accurate control. Due to an ever increasing demand for high quality steel, the field of process analytical chemistry in steel industry has been characterized by a series of technological advances over the last decade. As a result, standards in process analytical measurements are high for steel and other metal industries [176].

In the past, wet chemical analysis methods were the only tool for process analytical measurements at steel plants. These methods needed extensive sample pretreatment and were therefore not suitable for fast process control. Methods such as XRF (X-ray fluorescence) and OES (optical emission spectroscopy) enable fast process analytical measurements. For quality control, still methods such as AAS (atomic emission spectroscopy) and ICP-OES (inductively-coupled plasma optical emission spectroscopy) are in common use but those methods are too time consuming to be used for control of the steel making process. Today, the commonly used method, spark OES, is still the best

method available for process control in the steel production. Especially, due to the increase in production of high performance steels and scrap recycling, an improvement in the precision, accuracy, and response time of OES is vital.
In the last 15 years several experimental techniques, most of them based on emission and/or mass spectroscopy combined with direct solid sampling, have been used for the quantitative determination of trace and minor elements in steel alloys [112, 177-182]. These techniques include, among others: laser-ablation-ICP-MS [183,184], spark-ablation-ICP-MS [185,188], laser-ablation inductively-coupled and/or microwave-induced plasma atomic emission spectroscopy (LA-ICP/MIP-AES [189,191] direct current and radio frequency glow discharge source-atomic emission spectroscopy (GD-AES) [192].
Around 1990 some groups started to investigate possibilities of using LIPS for a fast on-line analysis of steel. CARLHOF [111] first described a LIPS system suitable for on-line analysis of molten materials in a steel converter. The system was primarily developed for analysis of carbon but also other elements as silicon, manganese, chromium or nickel could be determined. They used the C(I) 193.1 nm line and the Fe(I) 193.2 nm line for internal standardization and achieved a LOD of 200 ppm. AGUILERA et al [181] applied LIPS for the quantitative determination of carbon content in solid steel samples. The emitting plasma was imaged on the entrance slit of a 1-m nitrogen purged spectrograph, which was equipped with a time gated OMA detection system. The spectral range of the spectrometer was 185-700 nm with a typical resolution of 0.03 nm. Excellent values for precision and detection limits (1.6% and 65 ppm respectively), which can be favorably compared with the most accurate direct emission techniques, were obtained. Sulfur analysis in steel was reported by GONZALEZ et al [112]. Calibrations in the 0.008-0.28% concentration range was reported, with a detection limit of 70 ppm. ARAGON et al [193] reported C, Si, Cr, and Ni analysis in steel. Calibrations in the range of 0.005-1.5% are presented, with LODs of 80 ppm for C and Si. In STURM et al. [114] calibrations of C, S, and P in the 1-1800 ppm range were described, with limits of detection of 7-9 ppm for these elements. KHATER et al [115] applied time-integrated LIPS in the vacuum ultraviolet for the characterization of steel alloys. They used a 1-m normal incidence vacuum spectrometer, equipped with a concave grating and a micro-channel plate/photodiode array detector combination. A particular interesting feature of this work is the demonstration that VUV spectroscopy allows lines from higher ionic states to be used. In this sense, the lowest detection limit for carbon (87 ppm) was obtained from the C(III) 97.70 nm line. HEMMERLIN et al [116] reported the development of an industrial prototype with the ability to operate either a spark or a laser source on the same optical mounting in order to directly compare the performances of both sources. Similar sensitivities between LIPS and spark-OES could be obtained for low alloying elements (Mn, Cr, Ni, Mo, etc., in the range of 1 -1200 ppm) as well as for traces of C, N, S, and P between 2 and 100 ppm. Recently, KHATER et al. [117] made detailed optimization study of the parameters important for LIPS analysis of steel. Laser focusing, laser wavelength and energy, ambient atmosphere and pressure as well as spatial distribution of emitting species was showed. In that way, an excellent LOD for carbon in steel of 1.2 ppm was achieved.

In this work, application of our VUV-LIPS system for detection of relevant non-metals in steel (C, S, P, and N) has been investigated. A series of optimization studies of important LIPS parameters such as delay and gate of detection, type and pressure of buffer gas, laser wavelength and pulse energy of laser beam have been performed. The final objective would be a dedicated VUV-LIPS system for on-line steel analysis, similar to the approach of CARLHOF [111]

5.3.2. Experimental

The experimental set-up was already described in detail in Chapter 4.1. Three different laser wavelengths have been used: 1064 nm, 532 nm, and 266 nm. The latter two were produced by mounting second harmonic (SLD) and fourth harmonics (SLF) frequency doubling crystals in front of the resonator cavity in combination with adequate dichroic mirrors. The pulse energy of the laser beam was in this case also adjusted by a variable attenuator. Two different buffer gases, argon and helium were used, both with purity of 99.999%.

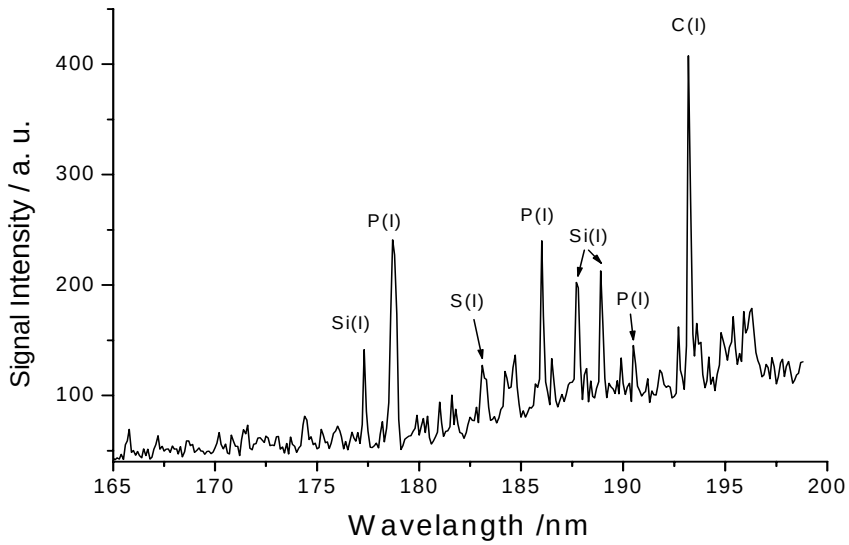

Fig. 5-8: *VUV spectrum of the SS402 referenced low alloy steel sample (laser: 1064 nm, irradiance = 1 GWcm^{-2}, buffer gas: Ar 5.0, p=1000 mbar).*

For the optimization of the experimental parameters and determination of the analytical figures of merit, a set of nine reference steel samples (Low Alloy Steel SS401-SS409, Bureau of Analysed Samples Ltd.) was used. Additionally sets of 18 samples with known P concentrations and 9 samples with known N concentrations were supplied from an actual steel production (by Ferrotron Technologies GmbH, Moers, Germany). The reference analysis in this case was made with a conventional spark-OES analyzer. All samples were in the form of roughly polished pieces and no additional sample preparation was performed.
Figure 5-8 shows a typical VUV spectrum of a steel sample, between 165 and 200 nm. Because of the relatively weak resolving power of monochromator ($\lambda/\Delta\lambda$~2000) and highly pronounced spectral interferences typical for steel matrix,

intensity of the signal at a peak wavelength rather then the peak area was used as spectral information of interest [114].

5.3.3. Results and Discussion

Figure 5-9. shows the photomultiplier signals from 193.1 nm (C(I) emission line) and at 192.5 nm. It is obvious that at early times after the plasma ignition both signals are decaying very fast and there is no significant difference in the intensity between those two signals (unspecific emission). At later times, a difference is observed due to the specific line emission.
This result shows the necessity of time optimization of the detection. In this case, time integration of the signal is not done via hardware, but via software, i.e. integrating the time-integrated plasma emission signal from the PMT in a defined time window. The optimization itself was performed here according to procedure described in Chapter 3.2. for the determination of carbon at the 193.1 nm. Five hundred repetitive signals were recorded, averaged, and integrated in 500 ns steps. The signal-to-noise ratio for each of those steps was calculated, and obtained dependance was fitted with a gaussian function.

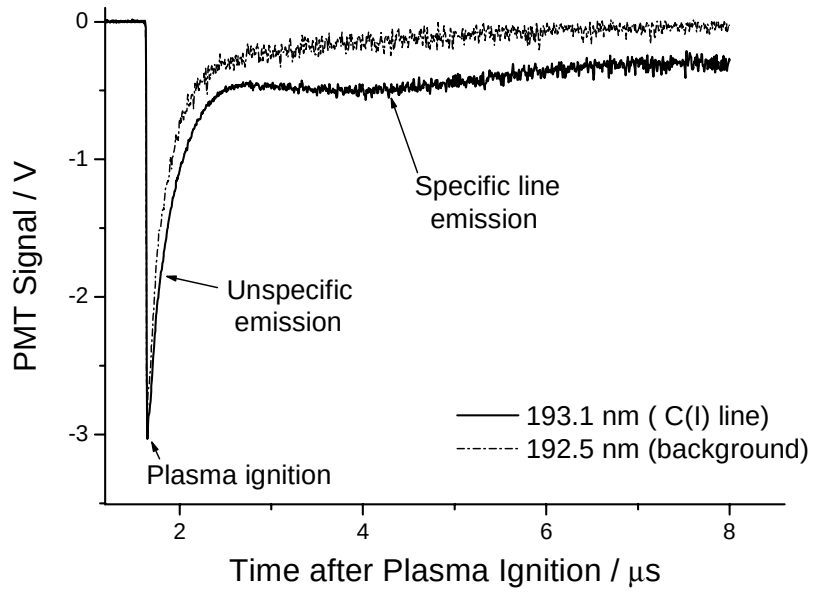

Fig. 5-9: *Plasma emission signal from PMT for two different wavelengths in VUV.*

The optimal timing parameters have been determined by intersecting the function at the 0.37 of the full maximum and found to be: delay = 4.9 μs and gate (integration time) = 4 μs. Those two values have been applied in all further evaluations.

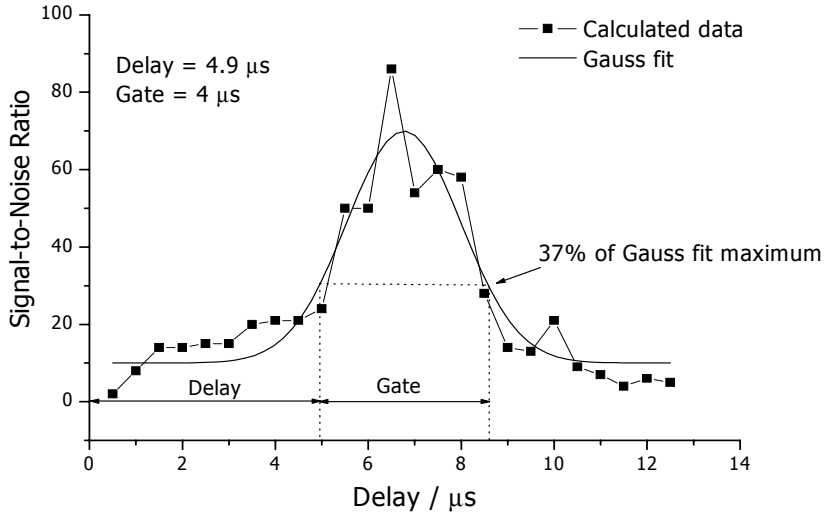

Fig. 5-10: *Signal-to-noise ratio vs. delay after plasma ignition for the C(I) 193.1 nm line in a steel sample.*

The type and pressure of a buffer gas strongly affects the plasma ignition and characteristics [194, 195]. Generally, noble gases should be used to avoid possible reactions of the gas with the plasma components. Heavier and denser gases produce hotter and denser plasmas which directly improve atomization and excitation processes but also can lead to plasma shielding [195]. The price plays also important role in process analysis and usually the cheapest noble gas, argon, is used.

In this work, the influence of two noble gases, argon and helium, both with purity of 99.999% was studied. Pressure within monochromator was held constant at 1000 mbar while the pressure in the sample chamber was varied between 50 and 1000 mbar for both gases. Additionally, emission signal in under vacuum conditions (~10^{-5} mbar) have been recorded. The signal intensity and signal-to-background ratio from the C (I) 193.1 nm line was exemplary investigated. The measurements have been performed with a laser wavelength of 1064 nm and an irradiance of 1 GWcm^{-2} (see Fig. 5-4 and 5-5).

Much higher intensities were observed in the case of argon as a buffer gas (see Fig. 5-11a). A decrease of pressure leads to a decrease of line intensities as well as the background (see Fig. 5-12), but the overall signal-to-background ratio was most favorable in the case of 1000 mbar argon (see Fig. 5-11b).

Investigations of a dynamic buffer gas atmosphere were also performed. For this purpose the chamber was steadily flashed with argon under several flow rates. The line intensities from three different elements have been observed. Results showed that there is no significant difference in the intensities of the lines in the case of dynamic and static argon atmosphere (Fig. 5-13). This indicates the possibilities of VUV-LIPS system for real on-line analysis.

The absorption characteristics of the sample varies with the wavelength of the laser. Therefore, the mass ablated in the single shot can vary with the wavelength as well [196]. Also other processes involved in laser-induced breakdown

and laser-plasma interaction depend strongly upon wavelength and irradiance by the laser beam [32,55,69,197,198].
The raw signal intensity and signal-to-noise ratio of the C (I) 193.1 nm line has been investigated for different irradiances and three available wavelengths (266, 532 and 1064 nm).Throughout all experiments, the atmosphere in the chamber was held constant at 1000 mbar of Ar.
Despite the fact that all three wavelengths produce similar signal intensities for same irradiances (see Fig. 5-14a), signal-to-noise ratio for 532 nm and 266 nm beams were significantly better (see Fig. 5-14b). This is mainly due to the improved relative standard deviation for 266 nm and 532 nm (~1%) compared with 3.14% for the 1064 nm beam. A possible explanation for this are the reduced fractionation and plasma shielding effects for shorter laser wavelengths (see chapter 3.3.2. and also [32,55,69,154]). The similar signal-to-noise ratios for 266 nm and 532 nm wavelength come from the inherent pulse energy variation of the 266 nm laser beam.

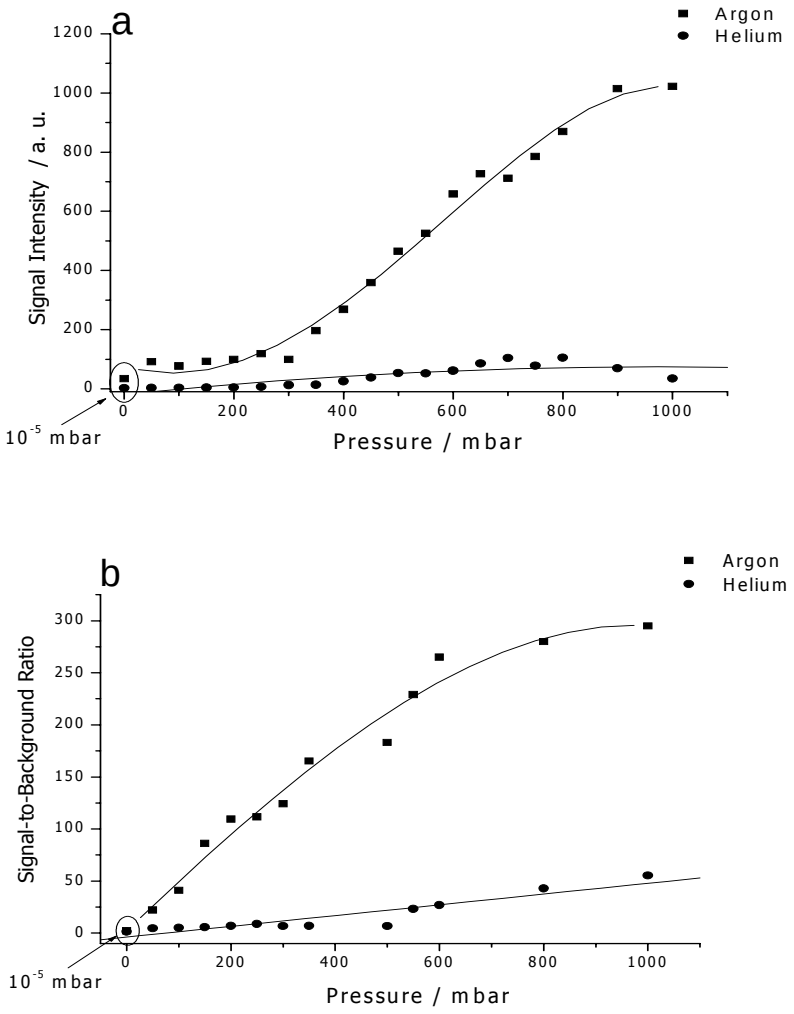

Fig. 5-11: *Intensity (a) and line-to-background ratio (b) of C(I) 193.1 nm line for different buffer gas conditions in the vacuum chamber.*

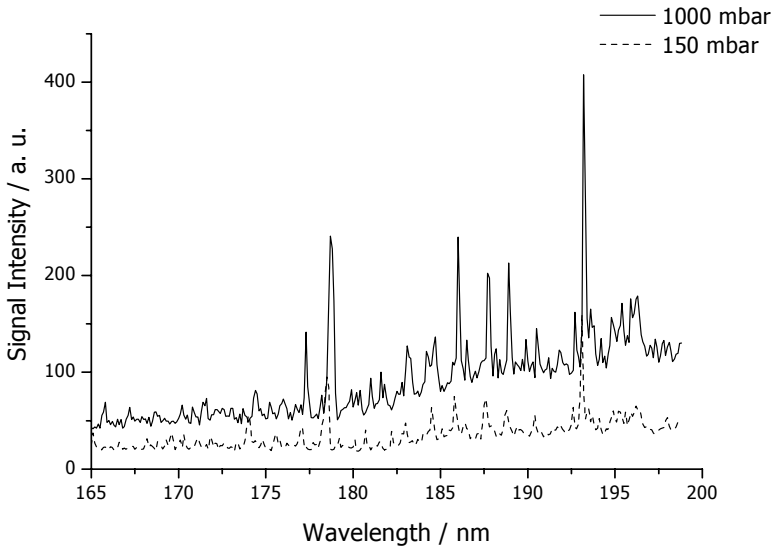

Fig. 5-12: *VUV spectrum of one steel sample for the two different argon pressures in ablation chamber*

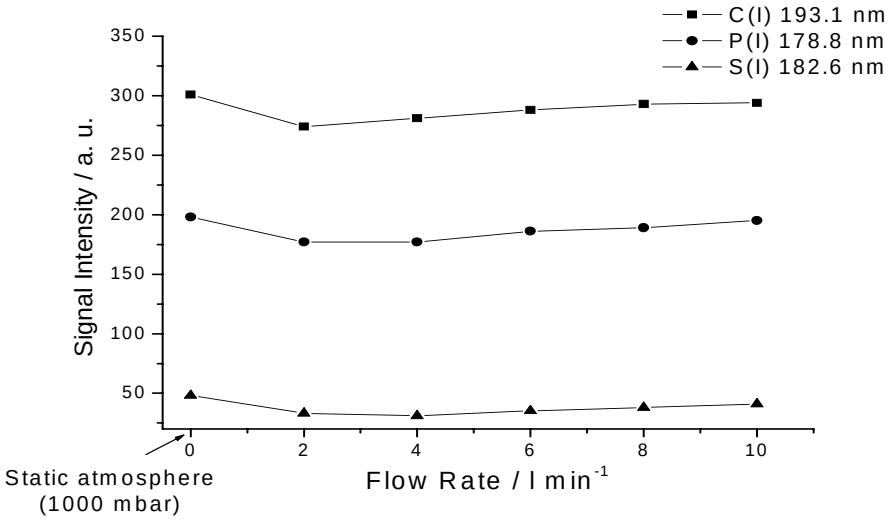

Fig. 5-13: *Intensities of three atomic lines from C, P and S for the different argon flow rates through the ablation chamber*

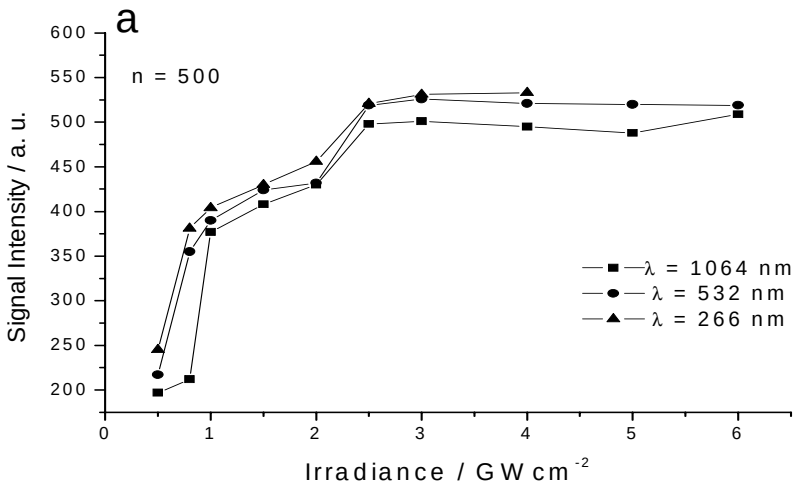

Fig. 5-14: *Signal intensity (a) and signal-to-noise ratio (b) of C(I) 193.1 nm line vs. irradiance of laser beam laser energies and 3 different laser wavelengths.*

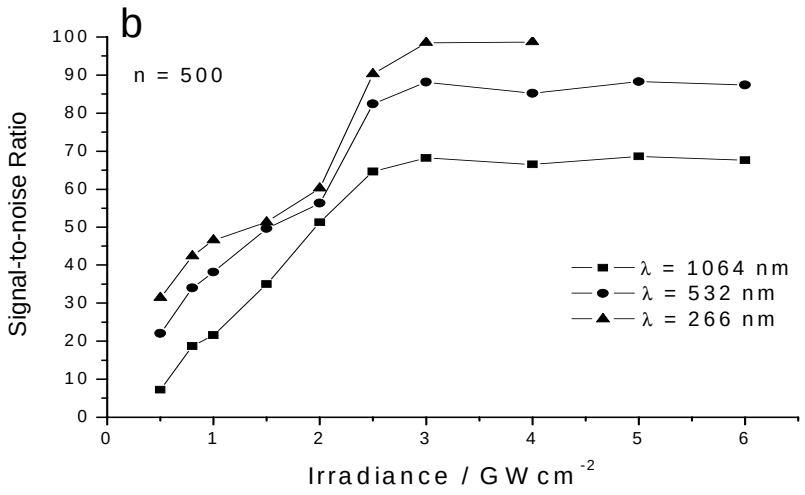

Another interesting result is the saturation of the signal (see Fig. 5-14a) for irradiances higher than 3 GWcm^{-2}. The reason for this could be a pronounced shielding effect of the plasma for higher irradiances. A direct comparison of signals for two samples with different concentrations of carbon produced at different laser wavelengths (here shown only for 532 nm and 1064 nm) demonstrates another advantage of using laser beams with shorter wavelengths (Fig. 5-15 and 5-16). Regardless the fact that the signal at 532 nm was just slightly more intensive than at 1064 nm (see Fig. 5-15), analysis at 532 nm is much more sensitive i.e. exhibits bigger difference for different carbon concentrations (Fig. 5-16 a and b). This fact in combination with lower noise directly leads to the bigger slope of the calibration curve (i.e. higher sensitivity) and lower limit of detection in the case of using the 532 nm (or 266 nm) laser wavelengths (Fig. 5-17 a, b, and c). Limits of detection and precision for S, P, and C and all laser wavelengths are given in Table 5-2.

Tab. 5-2: *Limits of detection and precision for S, P, and C in steel for three different laser wavelengths*

Element and line	LOD / precision λ = **266 nm**	LOD / precision λ = **532 nm**	LOD / precision λ = **1064 nm**
S(I) 182.6 nm	130 ppm / 14%	65 ppm / 9%	45 ppm / 7%
P(I) 178.8 nm	52 ppm / 8%	27 ppm / 4%	16 ppm / 2%
C(I) 193.1 nm	31 ppm / 12%	11 ppm / 3%	6 ppm / 2%

In a further study in collaboration with Ferrotron Technologies GmbH (Moers, Germany) the focus was placed on the quantitative analysis of phosphor and nitrogen. There, 18 steel samples with referenced phosphorus and 9 samples with referenced nitrogen concentrations were investigated. Reference analysis was made with a conventional spark-OES analyzer. Figure 7-18 shows VUV spectrum of a sample with 80 ppm of P.

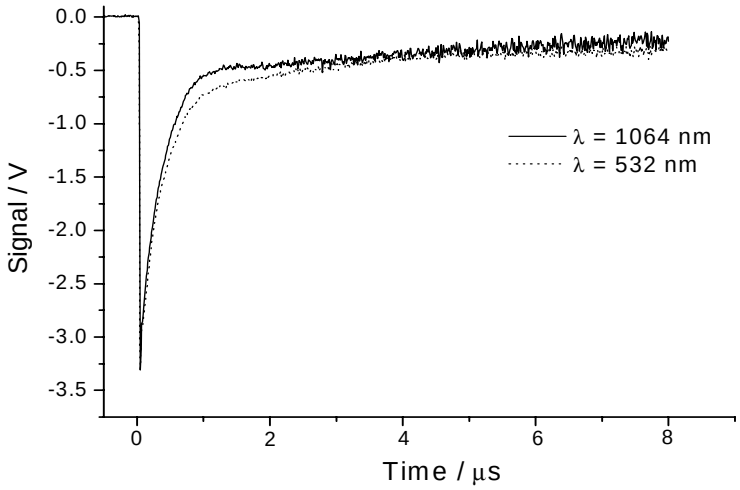

Fig. 5-15: *Plasma emission signal at 193.1 nm (C(I) line) in a steel sample with 1.06% of carbon.*

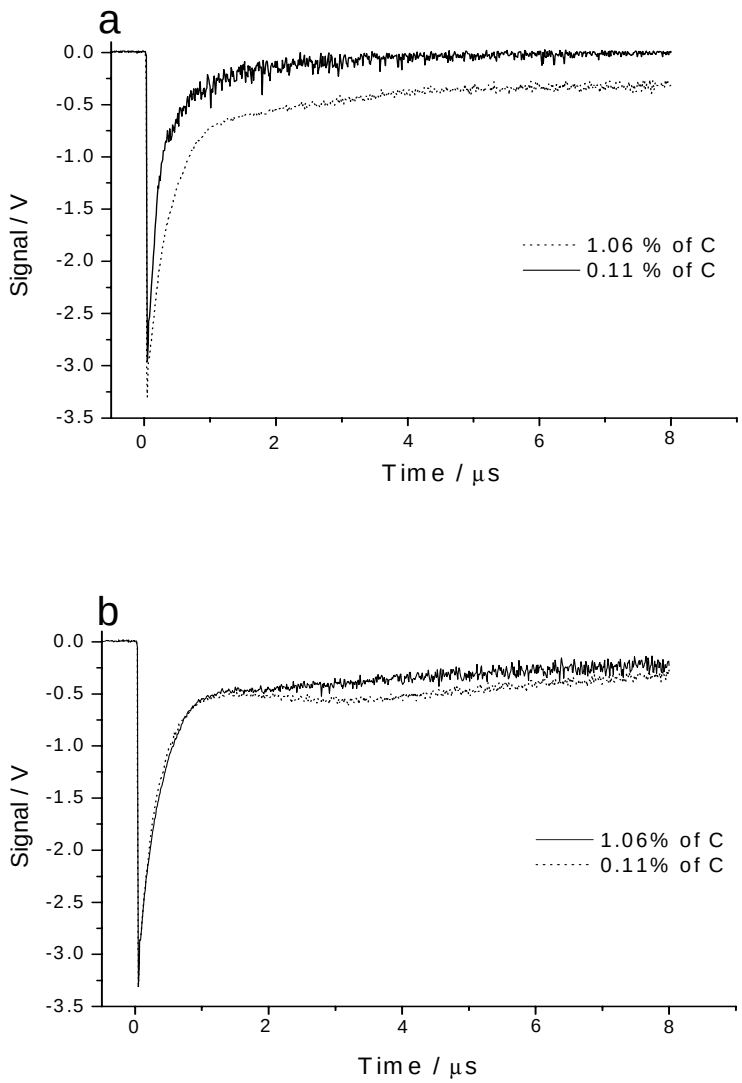

Fig. 5-16: *Signals from C(I) 193.1 nm line in two steel samples with 0.11% and 1.06% of carbon (532 nm (a) and 1064 nm (b) wavelength)*

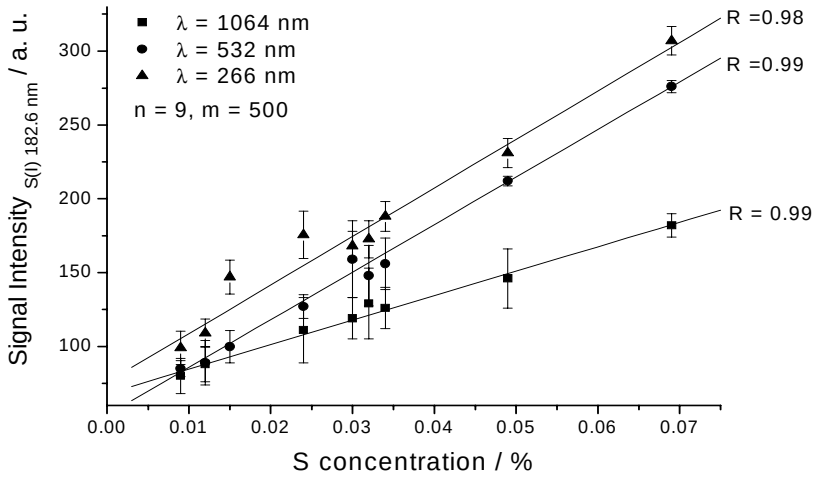

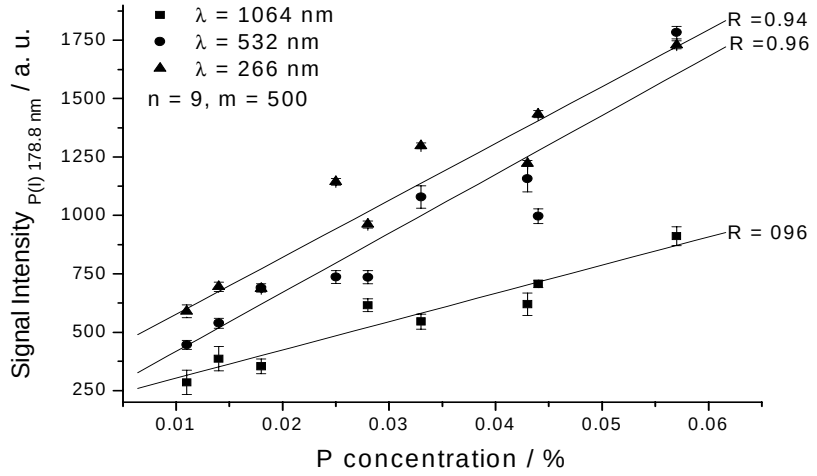

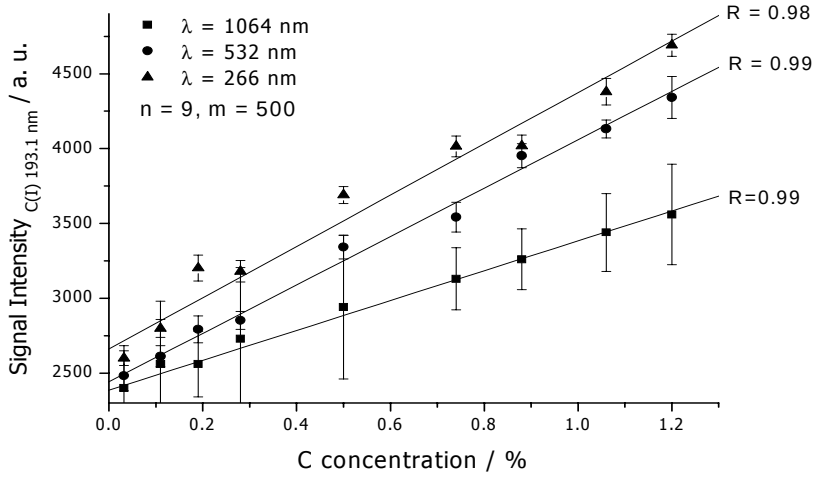

Fig. 5-17: *Calibration curves for sulfur, phosphorus, and carbon in steel (n =9 samples, 500 pulses per sample, buffer gas: p(Ar) =1000 mbar, delay: 4.9 μs, integration time: 4 μs).*

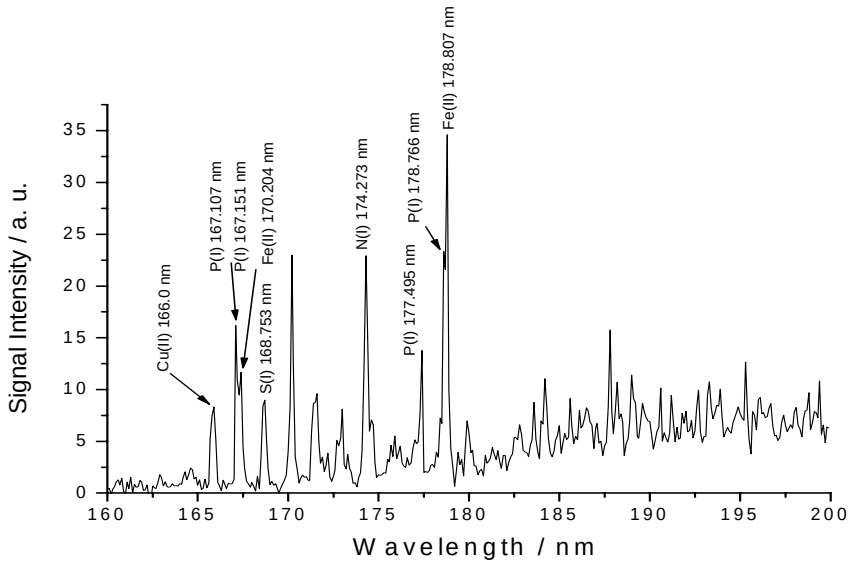

Fig. 5-18: *The spectrum of a sample from real steel production containing 80 ppm of P; laser λ=532 nm, irradiance of 3 GWcm^{-2}, p(Ar)=1000 mbar.*

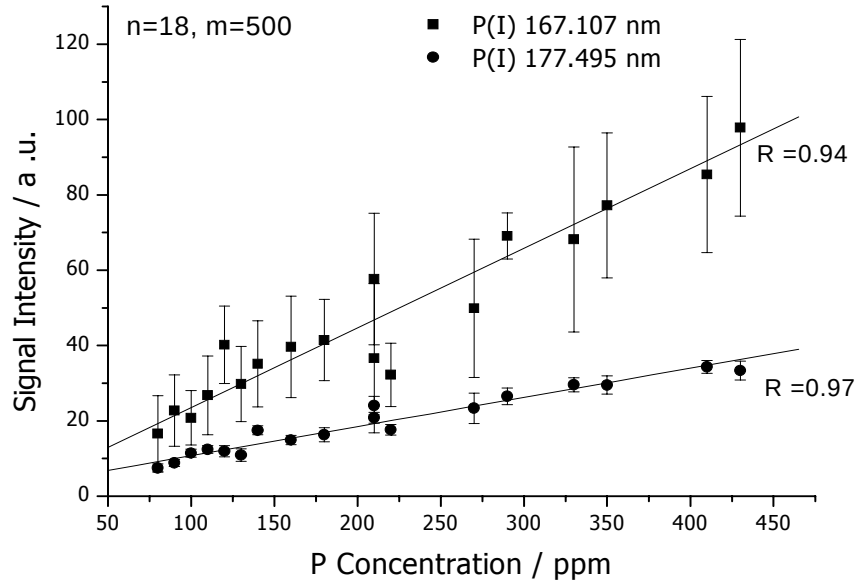

Fig.5-19: *The calibration curve for phosphorus in real samples from steel production.*

All 18 samples were measured with 500 laser pulses using the optimized experimental parameters, i.e. laser wavelength 532 nm, irradiance of 3GWcm^{-2}, buffer gas atmosphere of 1000 mbar of Ar (purity of 99.999%), delay = 4.9 μs, gate 4 μs. The 532 nm laser wavelength was chosen because of its much better pulse energy stability compared with 266 nm which is of the essential importance for possible applications directly at the production line. Two atomic phosphorus lines have been measured and used for calibration curves: P(I) 167.107 nm and P(I) 177.495 nm (see Fig. 5-19).

Lower LOD and much improved precision was achieved with the P(I) line at 177.495 nm (see Table 5-3). This is due to the fact that P(I) 166.107 nm line interfere strongly with other phosphorus line, P(I) 167.151 nm (see Fig 5-18),

which certainly influences the pulse-to-pulse reproducibility of the measured line intensity.

Tab. 5-2: *LOD and precision for two measured phosphorus line in real steel sampled*

Elemental line	LOD / ppm	Precision /%
P(I) 167.107 nm	80	33
P(I) 177.495 nm	30	9

Figure 5-20 shows the VUV spectrum of a steel sample containing 410 ppm of nitrogen. The N(I) 149.263 nm, which is usually used in spark-OES analysis of steel [199-201], was strongly interfered from Cu lines between 148 and 150 nm due to the one order of magnitude higher concentration of copper. This negatively influenced the LOD and precision in the case of using this line (see Table 5-3).The N(I) 166.388 nm line exhibited much higher signal-to-noise ratio and allowed lower LOD and better precision (see Table 5-4). In this case plotting pure line intensity versus concentration did not provide sufficient linearity. Therefore, Fe(I) 195.259 nm line was used for internal standardization (see Fig. 5-21)

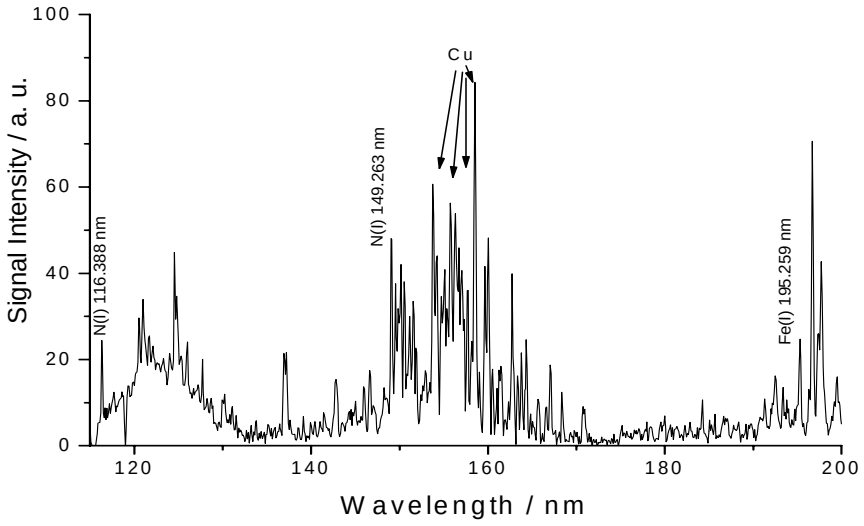

Fig. 5-20: *The VUV spectrum of a steel sample containing 410 ppm of nitrogen (laser λ=532 nm, irradiance = 3 GW/cm^2, p(Ar) = 1000 mbar.*

Tab. 5-3: *Limit of detection and precision for two investigated nitrogen lines*

Line	LOD / ppm	Precision /%
N(I) 116.388 nm	150	6
N(I) 149.263 nm	292	28

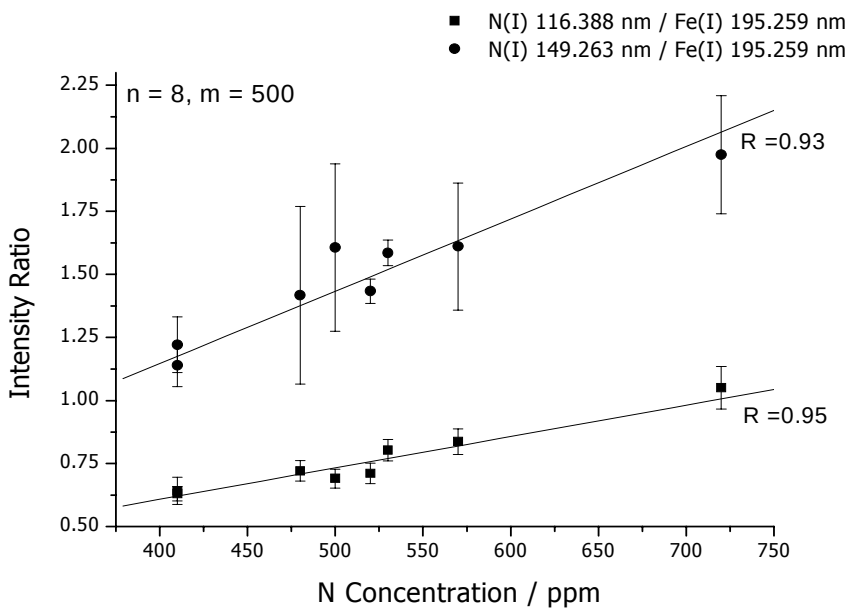

Fig. 5-21: *Calibration plots for two different nitrogen atomic emission lines.*

5.2. Detection of Bromine in Thermoplasts from Consumer Electronics

5.2.1. Introduction

Thermoplastic polymers are widely utilized in many of today's industrial designs. The chemical and mechanical properties can be altered by a large variety of additives. Among these are several inorganic compounds (TiO_2, ZnO, Fe_2O_3, and soot), flame retardants such as Sb_2O_3 - often combined with brominated organic compounds and numerous thermal and photochemical stabilizers. The actual mass concentration of the additives varies from a few mg kg^{-1} to several mass percentages corresponding to the intended modification of the polymer [202-204]. The extensive use of the rather expensive thermoplasts in short-lived consumer electronic products necessitates an efficient recycling. Process analysis of simple polymers from household waste is easily achieved by molecular spectroscopy (e.g. NIR spectroscopy). However, the multitude of additives in thermoplasts requires both, elemental analysis of inorganic materials and assessment of the bulk material via molecular spectroscopy. For an economic sensible recycling, only fast analytical methods with on-line and high-throughput capability qualify for this kind of process analysis.
Earlier work [205,206] reported the successful application of LIPS for on-line elemental characterization of recycled thermoplasts from consumer electronics.

Future legislation of the European Union demands also that thermoplasts with any kind of brominated flame retardants are identified and/or eliminated from the recycling process due to their potential health hazard [207,208].
Brominated flame retardants are a structurally diverse group of compounds including aromatics, cyclic aliphatic, phenolic derivatives, aliphatic and phthalic anhydride derivatives. The most common are tetrabromobisphenol A (TBBPA), polybrominated diphenyl ethers (PBDEs), hexabromocyclododecane (HBCD), and polybrominated biphenyls (PBB). Flame retardants can be either covalently bound to the polymer or simply mixed with the polymer during the extrusion process.
The determination of elemental bromine by atomic emission spectroscopy is generally hampered by the high excitation energy of the emitting states, with the consequence that the atomic resonance transitions are located in the vacuum ultraviolet region. In principle, transitions in the Vis/NIR region are far more amenable to current detector technology. However, these transitions are several eVs above the ground state and consequently often result in a poor analytical sensitivity.
Until now, reports on analysis of polymers by LIPS were limited to laboratory investigations of rather pure polymers [209-211]. While Br could be detected in the gas phase via LIPS [212], only recently Br and other halogens were analyzed in solid organic samples [213]. However, the later study was limited to pure substances and determination of the elemental ratios. Another study could only estimated the Br content in thermoplasts indirectly through the correlation with the synergistic Sb [214], which is, however, not always correlated to brominated compounds.

5.2.2 Experimental

The experimental set-up for measurements in VUV region is already described in chapter 7-1. The set-up for Vis/NIR region is similar to other work in UV/ Vis region and is described in chapter 4.1. For the studies in NIR region an alternative detection system was based on a 0.3-m monochromator (SpectraPro-300i, ARC, Acton, USA; 1200 g/mm grating with blaze 500 nm, spectral bandpass 0.07 nm, 50 μm slit width) equipped with an ICCD camera (Dynamight, LaVision, Göttingen, Germany; Vis/NIR optimized photocathode). The typical irradiance on the sample realized for both set-ups was about 20 GW cm^{-2}.
For preliminary studies, a sample lot, comprising 96 different shreddered thermoplasts (acrylonitrile butadiene styrene (ABS), polyamide (PA), polycarbonate (PC), polystyrene (PS), styrene butadiene (SB), polyphenylene oxide (PPO), thermoplastic polyester (TPO), polyvinyl chloride (PVC) and commingled mixtures of them such as PPO/PS) from consumer electronics (i.e. TVs, computers etc.), was analyzed. Reference analysis was performed by total X-ray florescence analysis (TXRF) after dissolution of small amounts of the samples in suitable organic solvents, and alternatively, by instrumental neutron activa-

tion analysis (INAA), the procedure was described in detail elsewhere [215]. To cover the main variance of bromine in this sample set, a sub-set of 10 samples was established via cluster analysis with a centroid linkage procedure [161].
The studied model compound, 2-bromo-4,6-dinitroaniline (99% purity, Merck, Darmstadt, Germany), was ground and pressed to pellets with a hydraulic laboratory press (PW 30, Paul Weber Apparate, Germany) and appropriate pressing tools (LOT-Oriel, Germany). For all pellets, a pressure of 75 MPa was applied for a period of 300 s.

5.2.3. Results and Discussion

VUV Region

Bromine exhibits several intensive atomic lines in the region between 130 nm and 160 nm. Most prominent are the Br(I) lines at 148.85 nm, 153.17 nm, 157.48 nm, and 163.34 nm. Fig. 5-22 displays the LIPS spectrum of a recycled ABS thermoplast sample with 7.3% (m/m) bromine between 130 nm and 170 nm under a buffer gas flow of argon (2 l min^{-1}) through the chamber, respectively a static argon atmosphere (1000 mbar)

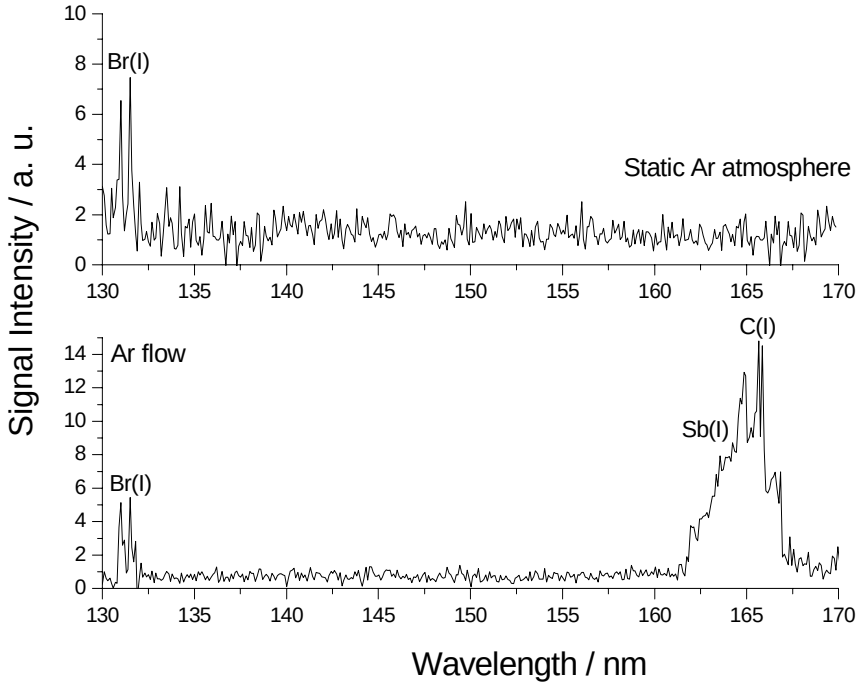

Fig. 5-22: *LIPS spectrum of an ABS thermoplast polymer sample with Br- and Sb-containing flame retardants under a static argon atmosphere (1000 mbar), respectively a continuous argon flow (2 l min^{-1}; delay: 1 µs, integration time: 4 µs).*

In both spectra, the atomic Br(I) lines at 130.99 nm and the unresolved triplet (131.67 nm, 131.74 nm, and 131.77 nm) are readily recognized. Under a static atmosphere other emissions were not observed in this wavelength region. With a continuous argon flow through the chamber, several overlapping lines between 161 nm and 167 nm can be found in addition. The most prominent lines are due to antimony, here utilized as synergistic flame retardant (4.89%), and carbon from the bulk material. The spectrum did not change with an

increase of the argon flow up to 15 l min^{-1}. Note, that in both spectra none of the expected strong atomic bromine lines between 140-160 nm can be found. In addition, the signal-to-noise ratio determined for the atomic Br(I) lines around 130 nm are similar.

To investigate this effect further, the C(I) line at 165.70 nm was monitored for 1000 pulses, which corresponds considering the acquisition time to about 3 min, under a static atmosphere and a steady argon flow. Figure. 5-23 reveals that only under a constant argon flow the emission intensity of the C(I) line remains fairly constant, while under a static argon atmosphere of 1000 mbar a continuous decrease in the LIPS signal can be seen. A feasible hypothesis is the absorption of the characteristic plasma emission by molecular oxygen in the Schumann-Runge system (175-200 nm, $B^3\Sigma_u^- - X_3\Sigma_g^-$) and the Schumann-Runge continuum (130-175 nm). In the spectral region between 130 and 160 nm the absorption coefficient of molecular oxygen [103] increases most strongly (× 00), which corresponds to our observation of diminished emission lines under both experimental conditions, i.e. a static buffer gas atmosphere and a buffer gas flow through the chamber. Further, it was assumed that the molecular oxygen originates from the ablation process itself. This is supported by the trend in Fig. 5-23 and the fact that before the buffer gas was added after we achieved a sufficient vacuum (10^{-5} mbar) to ensure a neglectable absorption by the remaining molecular oxygen.

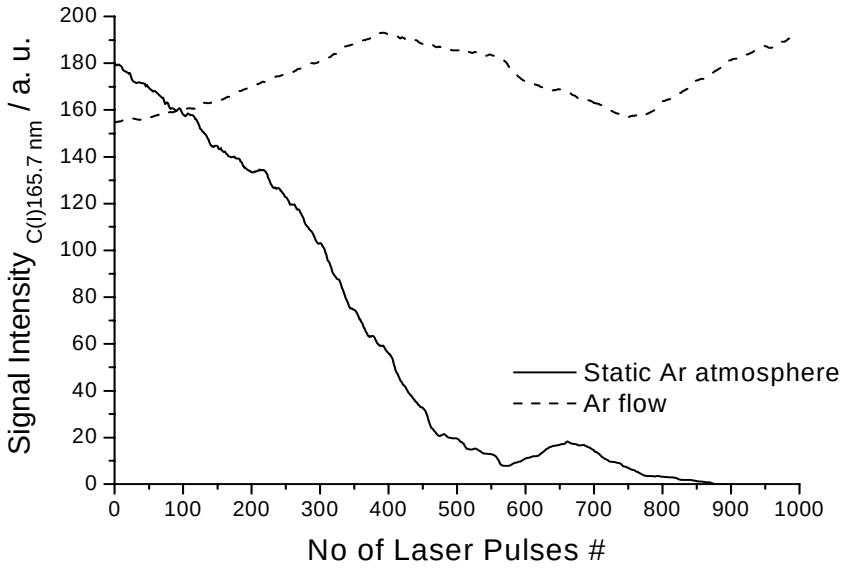

Fig. 5-23: *Time-resolved variation of the LIPS intensity of the C(I) line at 165.70 nm (sample and experimental conditions, see Fig. 3a) under a static argon atmosphere (1000 mbar), resp. a continuous argon flow (2 l min^{-1}).*

In addition, the initial intensity under a static argon atmosphere is comparable (for the first 100 pulses) to the relative intensity under an argon flow through the chamber. To understand this effect properly, a solid organic model compound, 2-bromo-4,6-dinitroaniline was used, instead of the more complex thermoplast. Figure 5-24 gives an overview of the corresponding spectra between 135 nm and 165 nm at different integration and delay times, while Fig. 5-26 focuses on the shaded areas in Fig. 5-25 in greater detail. Fig. 5-25a demonstrates that at early times after the plasma ignition several emission lines

can be observed even in the region of the Schumann-Runge continuum. The emission lines of O(I) in Fig. 5-25a and Fig. 5-26a indicate that at these times no significant amount of molecular oxygen is present. Strong Br(I) lines at 125 nm, 128 nm, 130 nm 157 nm, and 163 nm appear only at delay times around 0.5 μs (Fig. 5-24/5-25), but decrease at later delay times above 130 nm probably due to assumed formation of molecular oxygen (Fig. 5-25c,d and Fig. 5-26c,d). This is also supported by the fact that at longer delay times emission lines from atomic oxygen are no longer observed.

To explore the possibilities for a quantitative LIPS analysis of Br in thermoplasts we optimized the timing for the Br(I) lines at 130 nm via the SNR as described before [140]. For the calibration, a delay of 0.4 μs and an integration time of 0.9 μs were used. An additional variation of the buffer gas pressure revealed an increase of the SNR with increasing pressure, hence 1000 mbar of argon was used throughout all measurements.

Helium as buffer gas was utilized in preliminary experiments but yielded a lower SNR under comparable experimental conditions (for an extensive discussion of buffer gas influence on the plasma see [213,216]). From a representative sample sub-set, covering the complete observed concentration range of bromine in the investigated recycled thermoplasts, a calibration plot was constructed (Fig. 5-27) for the Br(I) line at 130.99 nm. Normalization to the C(I) line at 193.09 yielded an improved linearity as already demonstrated earlier [206], although in this case the C(I) emission was not detected simultaneously with the Br(I) emission but rather sequentially. The unresolved triplet at 131 nm resulted in an inferior linearity. Although the Br(I) line at 128.63 nm showed a higher intensity for the model compound (compare Fig. 5-26.), this apparent improved SNR was not found for the thermoplasts. Here, the intensity of the Br(I) line at 130.99 nm was about three times higher than the intensity of the line at 128.63 nm. The limit of detection (LOD) according to the 3s-criteria was found to be 473 mg kg^{-1}, the accuracy was in the order of 7-11%.

UV-Visible Region

Despite the fact that bromine has several strong atomic lines in the UV-Visible range, it was not possible to detect any of these lines with any of the thermoplast samples neither under normal conditions nor under a static atmosphere between 100 mbar and 1000 mbar of argon or a flow of argon (between1-15 l min^{-1}). Further qualitative experiments with gaseous molecular bromine in argon, which was pumped through our simple glass cell at 1 l min^{-1} and KBr pellets (67% (m/m) of Br) under an argon atmosphere between 100 mbar and 1000 mbar revealed only very weak atomic and ionic lines of Br around 440 and 450 nm, all of them in the order of the detection limit of experimental set-up employing an echelle spectrometer. Hence, the bromine detection in this wavelength region was not pursued further.

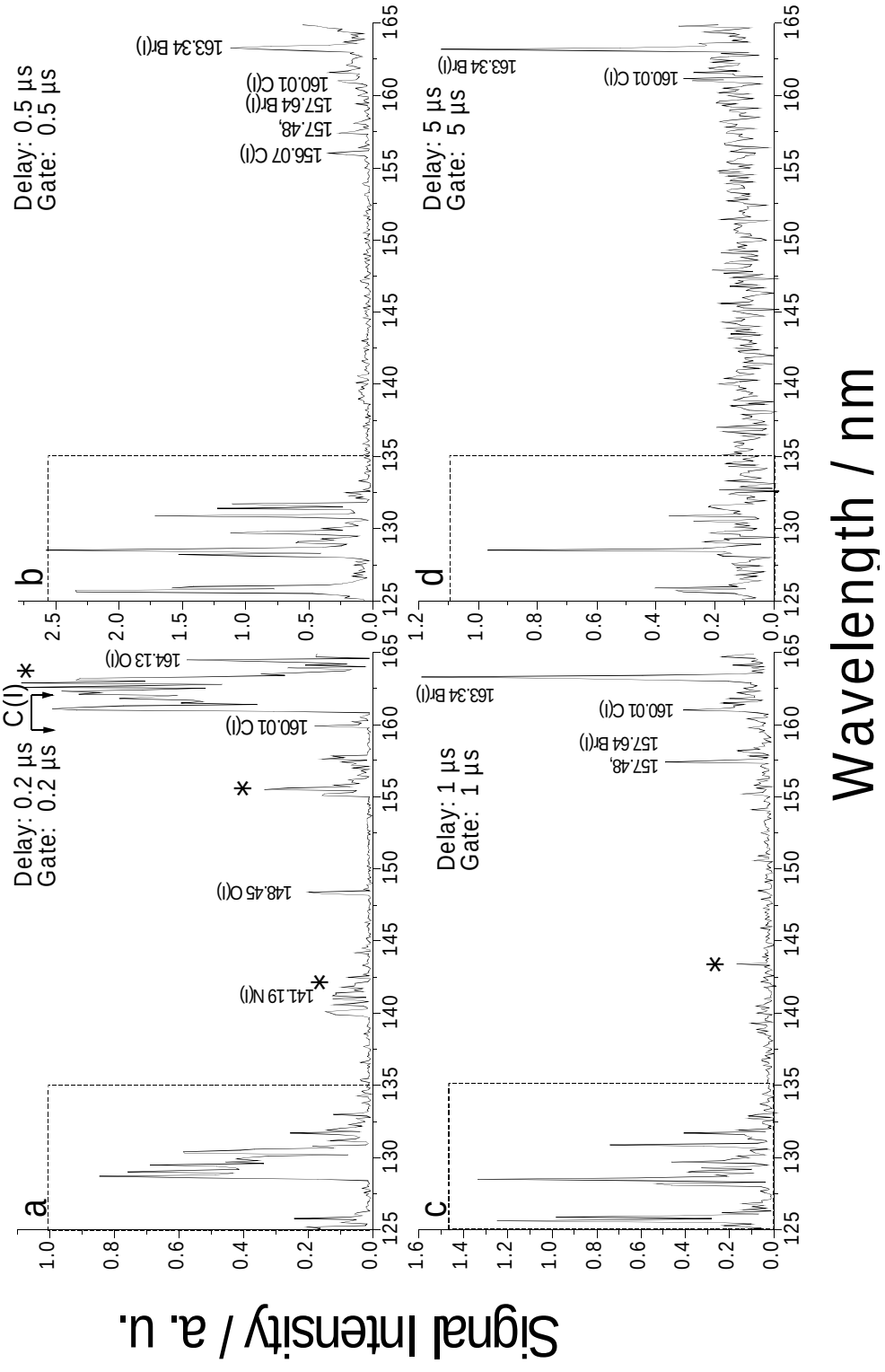

Fig. 5-24: *VUV-LIPS spectrum of the investigated model compound, 2-bromo-4,6-dinitroaniline, at different delay and integration times (* denotes emission lines, which were not identified; for the arreas within the squares, see Fig. 5-25).*

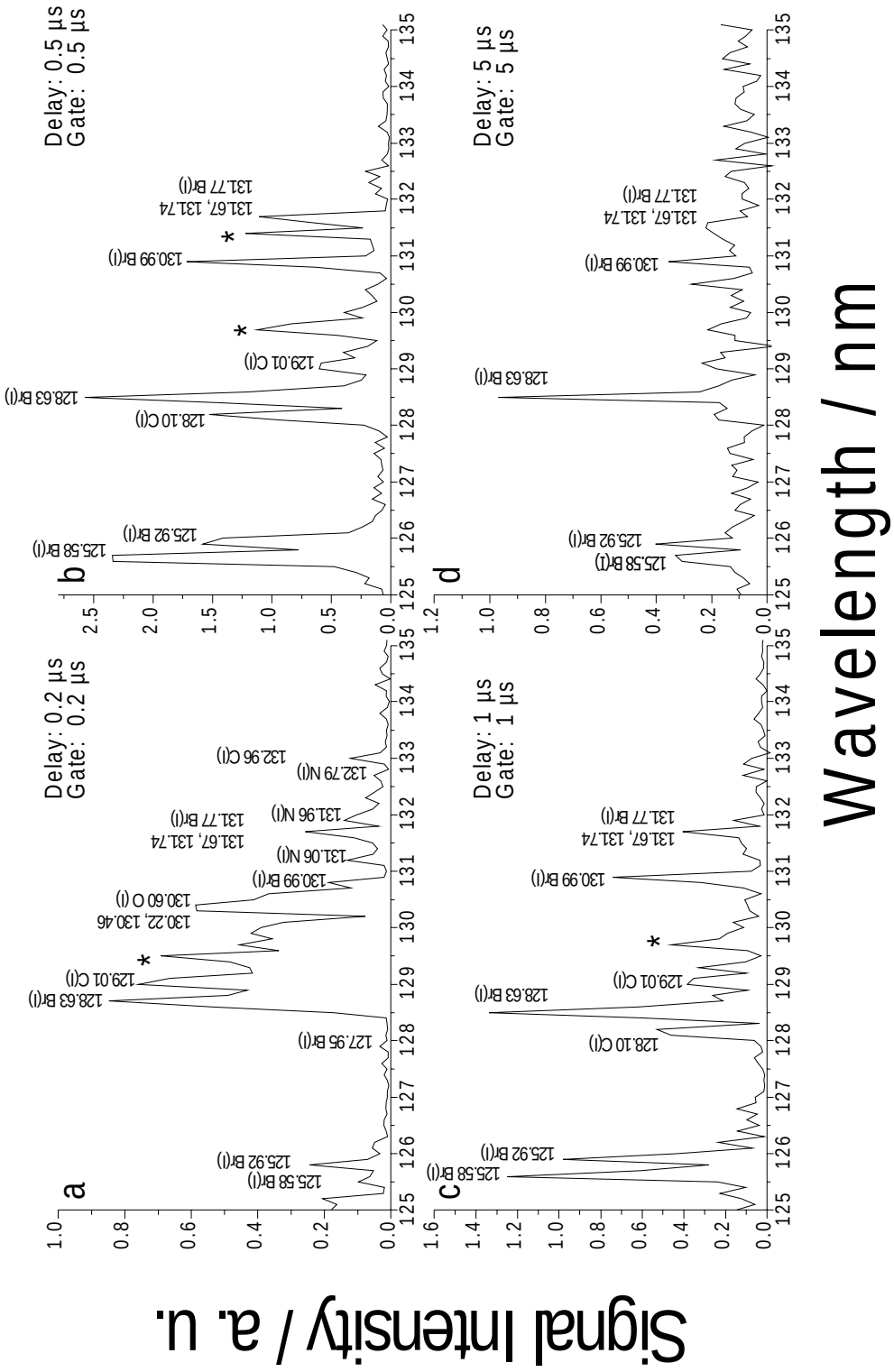

Fig. 5-25: *Detailed view of the VUV-LIPS spectrum (compare Fig. 1.5) of the investigated model compound, 2-bromo-4,6-dinitroaniline, at different delay and integration times (* denotes emission lines, which were not identified).*

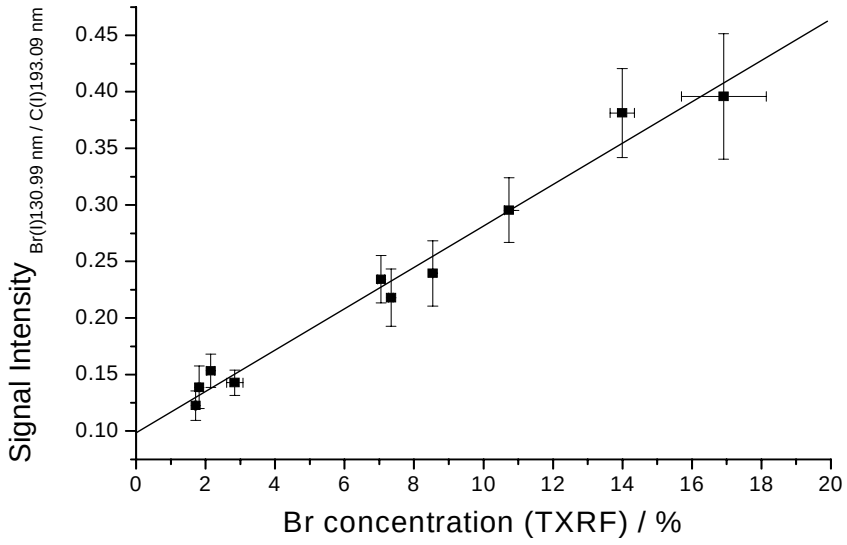

Fig. 5-26: *Calibration plot for bromine in recycled thermoplast samples utilizing the atomic Br(I) line at 130.99 nm normalized to the C(I) line at 193.09 nm (LOD = 473 mg kg-1, R = 0.98, n = 10 (500 pulses per sample), p (Ar) =1000 mbar, delay: 0.4 μs, integration time:0.9 μs.*

NIR region

For detection in the NIR region, a spectral window around 830 nm has been chosen, which is favorable both in the spectral sensitivity of the ICCD detector and occurrence of strong Br(I) lines. Fig. 5-28. reveals a comparison of spectra from an ABS thermoplast sample with 16.9% of Br in air and under a steady argon flow of 5 l min^{-1}. Although the strong Br(I) lines at 826.50 nm and 833.47 nm were overlapped by argon and carbon lines, the two lines were used for a calibration with the sample set described above, assuming a constant contribution of the other interfering elements.

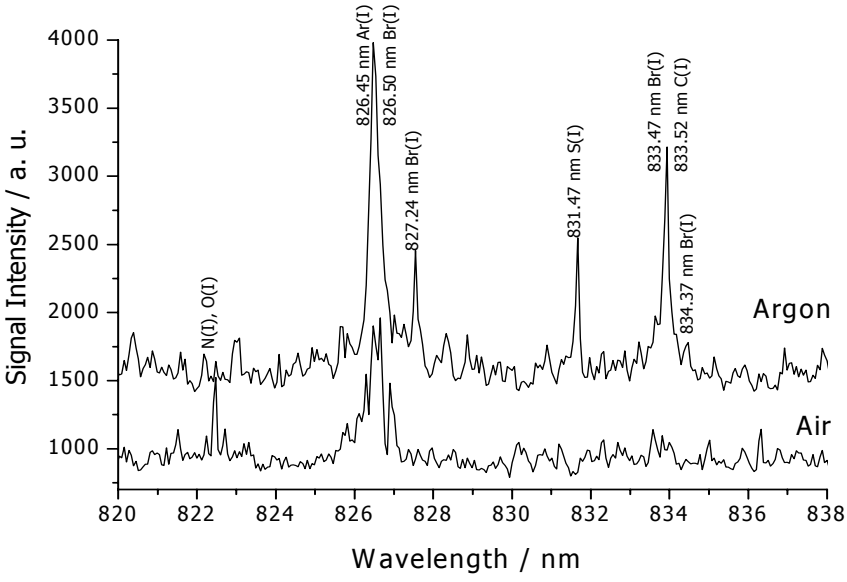

Fig. 5-27: *Comparison of the NIR-LIPS spectra from an ABS thermoplast sample with 16.9% (m/m) bromine in air and under a steady argon flow of 5 l min-1 (delay: 1 μs, integration time: 3 μs).*

An optimization of the timing was performed and yielded an optimum delay of 1 µs and an integration time of 3 µs. With a sequential normalization to the C(I) line at 247.86 nm a good linearity for both regression lines was achieved, although the sensitivity differed considerably. The determined detection limits of 37500 mg kg^{-1} and 11000 mg kg^{-1} are in good agreement with similar studies [213]. The limits of detection (based on 3s-criteria) are about 20- and 80- fold higher than for the calibration in the VUV region, while the accuracy was comparable to the calibration in the VUV range.

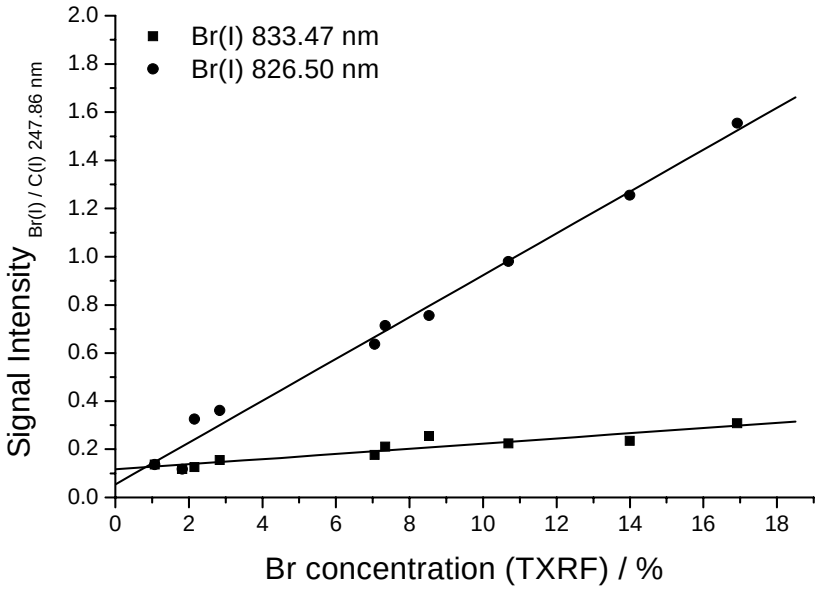

Fig. 5-28: *Calibration plot for bromine in recycled thermoplast samples utilizing two atomic Br(I) lines in the NIR normalized to the atomic C(I) line at 247.86 nm (n = 10 (50 pulses per sample)).*

5.3. Determination of C:H:O:N Atomic Ratios in Solid Organic Compounds

5.3.1. Introduction

The conventional technique, to determine organic elemental ratios, is combustion of the sample with an excess of oxygen, collecting the products from the combustion, including carbon dioxide (from carbon), water (from hydrogen) and nitrogen oxide (from nitrogen), and analyzing by means of a thermal conductivity detector [217]. Though the combustion is fully automated and runs without supervision, it does not provide on-line and real-time analysis. In addition, oxygen can not be analyzed directly, but is calculated from the molecular weight when the other elements are determined, or is determined through other methods such as radionuclear techniques. LIPS, on the other hand, is very simple and rapid technique and requires little sample preparation. Real-time analysis is also possible. One disadvantages of LIPS is the poorer precision

compared to commercial CHN analyzers, which have precision less than 1%. Recently, LIPS has been used to identify solid organic materials by correlating the LIPS spectrum of the unknown with library spectra [218]. Similarly, SATTMAN et al. [210] used LIPS to identify different polymers using artificial neural networks. MORRIS et al. [219] used LIPS as a sensitive detector for GC by measuring the C emission line at 247.9 nm. By measuring the ratios of several elements such as O, H, N, and C positive identification of eluting peaks was possible. TRAN et al. [213] determined F, Cl, and Br in solid organic samples by means of LIPS using the lines from NIR. Objective of this work was to investigate possibilities of using the resonance transitions of the C, H, O, and N located in VUV for the determination of C:H, C:O, and C:N atomic ratios in several organic compounds.

5.3.2. Experimental

The experimental set-up was based on the VUV monochromator and is described in the details in chapter 5.1. The laser was operating at 1064 nm providing an irradiance of about 1 GW cm^{-2}. All measurements were performed under a steady flow of argon (purity: 99.999%) through the ablation chamber with flow rate of 5 l min^{-1}. Ten organic compound in powdered form were chosen. The C:H, C:O, and C:N ratios for are displayed in Table 5-5.

Tab. 5-3: *Organic compounds used for determination of C:H, C:O and C:N ratios.*

Substance	Formula	C:H ratio	C:O ratio	C:N ratio
Glycine	$C_2H_5O_2N$	0.4	1	2
Cyanic acid	$C_3H_3O_3N_3$	1	1	1
Barbituric acid	$C_4H_4O_3N_2$	1	1.33	2
Methacrylamide	C_4H_7ON	0.57	4	4
Biuret	$C_2H_5O_3N_2$	0.7	0.67	1
N,N Metylendiacrylamide	$C_7H_{10}O_2N_2$	0.4	3.5	3.5
4-Aminoantipyrine	$C_{11}H_{13}ON_3$	0.84	11	3.67
1,1-Carbonyldimidazol	$C_7H_6O_{10}N_4$	1.17	7	1.75
Methionine	$C_5H_{11}O_2NS$	0.45	2.5	5
Chininsulfate	$C_{20}H_{30}O_8N_2S$	0.67	2.5	10

A few grams of each substance was ground in a laboratory mortar and pressed under the 10 T pressure into flat pellets. Each sample was analyzed with 100 laser pulses. Signals at the chosen line maximum were recorded, averaged, and

integrated with optimized time parameters (delay = 0.8 μs, gate = 2 μs); the lines under study are listed in Table 5-6.

Tab. 5-4: *The emission lines used for determinations of C:H, C:O, and C:N atomic ratios.*

Element	Line
C	C(I)193.1 nm
H	H(I)121.6 nm
O	O(I)130.2 nm; O(I)130.5 nm; O(I)130.6 nm;
N	N(I)141.2 nm; N(I)149.3 nm; N(I)149.7 nm; N(I)174.3 nm; N(I)174.5 nm

5.3.3. Results and Discussion

Figure 5-29 a-c show calibration plots for C:H, C:O and C:N atomic ratios. A very good linear response was obtained with correlation coefficients between 0.97 and 0.99. As mentioned earlier, one advantage of the LIPS over conventional combustion method is the possibility of the direct analysis of oxygen, not only as a relative (ratio) concentration but also as a an absolute concentration (atomic fraction). Therefore, the oxygen mole fraction was calculated in all used substances and intensity of oxygen line O(I) 130.2 nm was plotted against these calculated values (see Fig. 5-30). Once the oxygen atomic fraction was determined, the mole fraction of other elements could be calculated from their ratio with carbon. To determine accurancy of the whole approach one additional organic substance, N,N-diethyl-p-phenylendiaminsulfate was measured under the same conditions.

The values for atomic ratios were derived from calibration curves and compared with the actual ratio from the formula of the molecule. The accurancy of method is found to be around 5% (see Table. 5-7). To determine the sensitivity of our technique, the limits of detection for all four elements (in terms of mole fraction). For that purpose atomic fractions of C, H, O and N were calculated in all 10 samples and calibration plots were constructed (see Fig. 5-31 for oxygen). The LODs were then calculated according to the common 3σ–criterion (see Table 5-8)

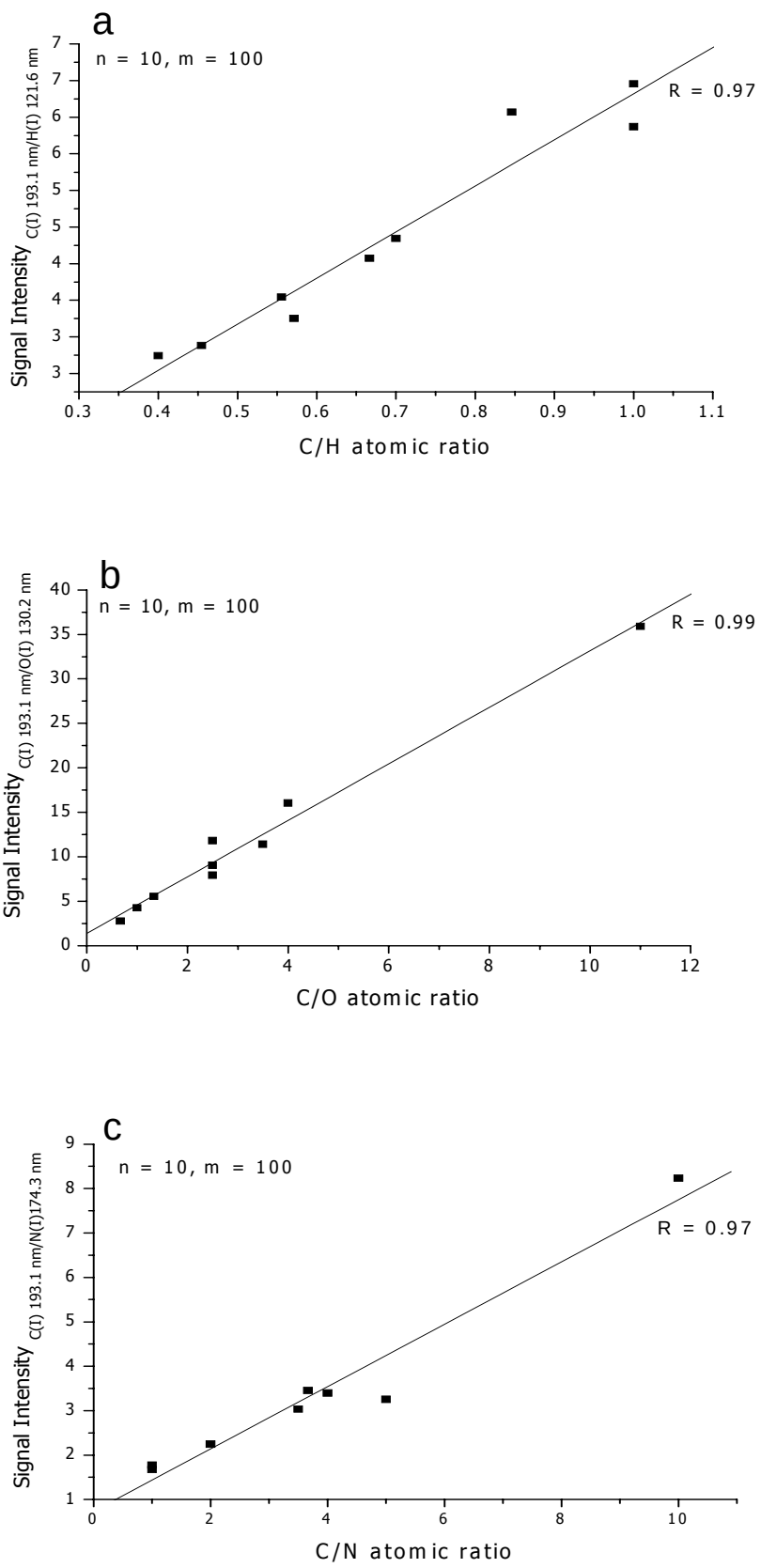

Fig. 5-29: *Calibration plots for C:H, C:O and C:N (laser: 1064 nm, irradiance = 1 GW cm^{-2}, delay = 0.8 µs, gate = 2 µs.*

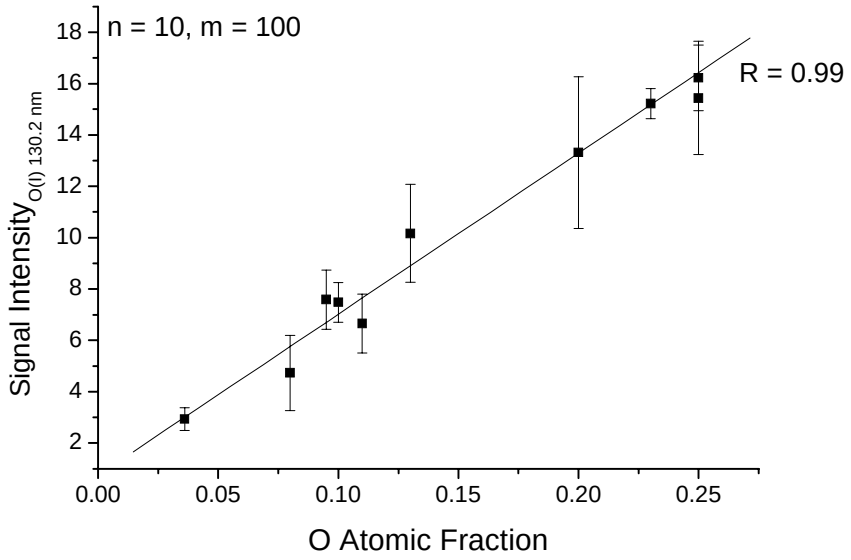

Fig. 5-30: *Intensity of O(I)130.2 nm line vs. oxygen mole fraction in the organic substances.*

Tab. 5-5: *Calculated and measured values of C, H, O, and N elemental ratios for N,N - diethyl-p-phenylendiaminsulfate (the fort column gives occurrences of applied method)*

Atomic ratio	From formula	From cal. plot	Accuracy /%
C:H	0.56	0.59	5.4
C:O	2.50	2.38	4.8
C:N	5.10	5.27	5.4

Tab. 5-6: *Limits of detection for C, H, O, and N mole fractions.*

Element	Used line	LOD (atomic fraction*)
C	C(I) 193.1 nm	0.0004
H	H(I) 121.6 nm	0.0015
O	O(I) 130.2 nm	0.00034
N	N(I) 174.3 nm	0.0011

** Atomic fraction is the number of analyte atoms divided by the total numbers of atoms in the molecule*

6 Microanalysis by LIPS

6.1. Introduction

Advancements in material science lead to increased demand of microanalytical techniques which allow a spatially and depth-resolved analysis of solid samples without an extensive sample preparation. This stems from the observation that the distribution of macroscopic inclusions, fibers, and grain boundaries can influence the macroscopic properties of solid materials in a rather subtle way. While a variety of conventional beam and particle techniques exist to analyze spatial features in the nm- to μm-range with high sensitivity, the necessary experimental conditions, such as high vacuum and extensive sample pre-treatment, limit these methods to specialized, personnel and cost intensive laboratory environments. On the other hand, many of today's production processes require fast information on spatiallyresolved elemental distributions on a μm-scale. This should be achieved with a minimum of sample preparation and if possible in an atline fashion to permit fast turnaround times. Similar application profiles can arise in geochemical and petrographic work.
Since the early days of laser spectroscopy, laser ablation (LA) in combination with optical emission spectroscopy (OES) or mass spectrometry (MS) has been utilized for spatially-resolved analysis. LIPS has been recognized early as potential tool for microanalysis. In contrast to other techniques such as electron probe micro analysis (EPMA), LIPS offers the prospect of a fast and highly automated at-line analysis without or only minor sample preparation. Not surprisingly, LIPS systems for microanalysis have been described very early and commercial systems (LMA 10 VEB CARL ZEISS, MARK III JARRELL-ASH, JLM 200 JEOL) have been realized in the early 70ties, but were discontinued by

the mid-70ties due to numerous experimental challenges [32]. The recent renaissance in LIPS [220, 221,153] led also to dedicated microanalytical systems: LASERNA et al. described in several communications [33-35,37] the potential of LIPS for chemical imaging and depth-resolved analysis of samples with industrial relevance. Earlier work was focused mainly on the detection of inclusions in metals, steel, and various alloys [32]. In all cases, the instrumentation was based on a conventional Czerny-Turner (CT) spectrograph with an intensified CCD (ICCD) detector, the spot size on the sample was typically in the order of 100 μm. GEERTSEN et al. demonstrated not only an improved lateral resolution in the order of 10 μm, but also illustrated the improved precision for UV laser ablation [38,39]. A very similar set-up was utilized by DUBESSY et al. for fluid inclusion analysis in minerals [40,41].

Present systems are still limited in their capability for simultaneous multi element analysis by the spectral range and resolution of the utilized spectrographs. The typically achieved spectral range of about 15 nm permits a resolution of $\lambda/\Delta\lambda$ of 5000-10000, which results in a small number of simultaneously detectable elements (3-8 in most applications). Due to the destructive nature of LIPS, this can be a rather sever limitation in the case of point-to-point scanning of unique samples. Further, problem arise in the limitation of current LIPS systems to metals, whereas non-metals and metalloids with strong resonance lines in the vacuum ultraviolet (VUV, 120-200 nm) are rarely analyzed via LIPS. In general, emission spectroscopy in this regime is hampered by the strong oxygen absorption which can be avoided only through the use of vacuum or buffer gases such as argon. The objective of this work was to design a dedicated system for microanalysis by LIPS with the following features:

1. A focal spot size below 30 μm at an ablation wavelength of $\lambda = 266$ nm (quadrupled Nd:YAG-laser)
2. Observation of elemental emissions between 150-300 nm to address non-metals such as S, C, P, Br, or N
3. Simultaneous detection of the complete LIPS spectrum over the whole spectral range with a resolving power $\lambda/\Delta\lambda > 10000$
4. Set-up of a system which permits fast sample change and qualifies for atline process analysis

6.2. Experimental

Apparatus

A capable VUV-LIPS system requires an integrated design of the ablation and detection modules. Due to strong absorption of molecular oxygen in the VUV range, the optical path must be held under vacuum conditions or a suitable buffer gas (see chapter 5). This leads to separated modules for ablation and the spectrometer. The vacuum system should achieve at least 10^{-5} mbar in all critical compartments and permit a sufficient pumping speed for a fast sample change. The sample must be positioned in xyz-direction in combination with an autofocus system.

Details of the experimental set-up are given in Fig. 6-1 - 6-3. The set-up is based on cylindrical vacuum chamber (total volume ~ 48 L) divided into separated modules. The ablation module houses a xyz-stage for the sample and several optical components, a large door facilitates a fast sample change. The spectrometer module contains the VUV echelle spectrograph. At present, both modules are simultaneously pumped through a dry compressing piston prepump (Ecodry M, Leybold Vakuum,Germany) and a turbomolecular pump (Turbovac 361, Leybold Vakuum, Germany). If the modules are isolated from each other through an optional MgF_2 window, the modules can be pumped also through separate flanges and gate valves. The system achieves a vacuum about 10^{-6} mbar inside both chamber within 12 min, if the spectrometer module is isolated from the ablation module the pumping time reduces to 6 min. Throughout all experiments argon was used as buffer gas and had a purity of 99.999%. The actual pressure inside the chamber was controlled through a pirani gauge (Ionvac ITR90, Leybold Vakuum, Germany). The ablation module has additional ports for the incoming laser beam, a Schwarzschild objective with a video camera for observation of the sample, and a view port for an additional lateral observation of the ablation.

Figure 6-1 reveals details of the ablation chamber and the focusing optics for the laser. A frequency-quadrupled (λ = 266 nm, pulse width 6 ns) Nd:YAG laser (Surelite I, Continuum, USA) with a repetition rate of 10 Hz was utilized for plasma generation. To ensure a constant spatial and temporal pulse profile, the pulse energy, monitored via a beam splitter and a pyroelectric probe (PHD25, Laser 2000, Germany), was adjusted by a variable attenuator (Newport, Irvine, USA). The laser beam waist was demagnified through a Galilean telescope (AR 266 nm, assembled from Microbank components, Linos Photonics, Germany) and focused onto the sample inside the ablation chamber through an aplantic lens system (AR 266 nm, CVI Laser Corp., USA). Although this long distance focusing arrangement limited the achievable spot size, i.e. spatial resolution, on the sample, this set-up simplifies the adjustment of the optical system outside of the ablation chamber, substantially. As it is not possible to observe simply through the focusing optics (see below), an increased lens-to-sample distance additionally permits a larger solid angle for observation of the plasma.

Further, the contamination of the focusing/observation optics through debris from the sample was avoided, respectively damage through the extending plasma. These general issues are a serious drawback for all systems based on a microscope objective. Note, that observation/excitation geometries based on dichroic mirrors or fiber optics, as described earlier [39], are principally not suitable for intended operation in the VUV range. A side-on observation was ruled out here, as it requires polished samples and limits intended scanning and mapping performance.

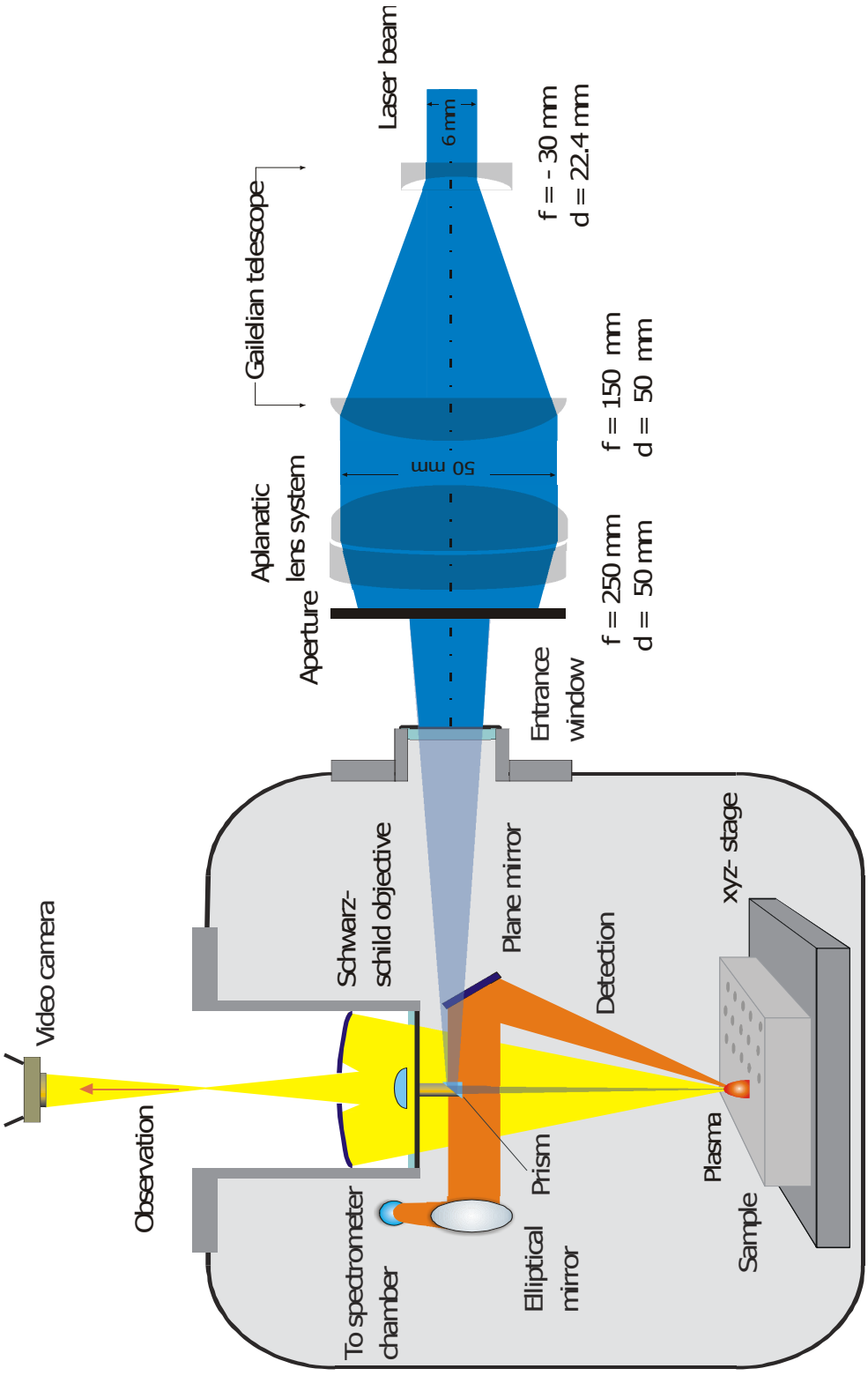

Fig. 6-1: *Set-up of the VUV-LIPS ablation module and the corresponding focusing optics.*

The emission from the plasma is folded through a plane mirror onto an ellipsoidal mirror which focuses the plasma with a 1:2 magnification ratio onto the entrance slit system through a aperture (d = 4 mm) between the ablation and spectrometer module. The use of mirror optics avoids chromatic aberrations

which is essential for a detection within a broad wavelength range. The sample is positioned on a xyz-translation stage (Limes 90, HVM 60, OWIS, Staufen, Germany) with a spatial resolution of 1 μm. A special designed long-distance Schwarzschild objective (primary concave mirror R = 100 mm, secondary convex mirror R = 38 mm, central bore d = 22 mm) was employed to observe a section of the sample with a magnification of 10 times by a video camera (resolution 1 pixel/μm, field of view ~ 500 × 500 μm, DFM 5303/P camera, DFG/LC1 frame grabber, The Imaging Source, Germany). Due to the orthogonal observation of the sample surface and the very low depth of focus, the objective can be utilized as an autofocus system, which is an essential feature for an imaging ablation system. The focus of the Schwarzschild objective, the focus of the ellipsoidal mirror, and the focused laser beam are aligned for a complete overlap. In this way, the sample is correctly aligned, i.e. in the focus of the observation and the ablation, if the video feed shows a sharp image. The focused laser beam is folded via a small quartz prism (6 mm edge length) attached to the Schwarzschild objective onto the sample instead of mirror. Thus, a change of the laser wavelength for ablation can be achieved simply by adjusting the exterior optics outside the ablation module. Further, the irradiance threshold and long-time stability for a quartz prism is favorable compared to a reflective mirror.

The spectrometer module is illustrated in Figure 6-2. The echelle spectrograph was interface to an intensified CCD (ICCD) camera suitable for the VUV range (ICCD MAX 512 VUV, Photometrics, Germany). A 18-mm-MCP with a MgF_2 window is fiber-optically coupled (1.27:1 demagnification) to 512 × 512 CCD with a pixel size of 19 μm, resulting in a total image area of 12.4 × 12.4 mm. The optical train of the echelle spectrograph is configured in a „double-Z" layout (see Fig. 6-2). Two spherical mirrors (f = 250 mm, f/# 10, Al/MgF_2-VUV coating) were chosen as collimator and camera mirror. Their positioning follows the Czerny-Turner-condition for compensation of the image broadening chromatic aberration, i.e. the wave front distortion generated by the collimator is compensated by the second mirror. The additional astigmatic image blur due to the off axis illumination of the spherical mirrors is suppressed by separating the entrance slit spatially along the optical axis into two components. the tangential component defines the slith in direction of cross dispersion, the sagittal one in direction of echelle dispersion. This artificially introduced astigmatism is compensated along the optical train, resulting in a sharp image both in the horizontal and the vertical direction in the focal plane. The echelle grating (75 l/mm, blaze angle 64°, size 30 × 60 mm, ELAN Ltd., Russia) is mounted in an off-plane configuration (3°) at its blaze maximum, so that the luminosity power of the grating is maximized and anamorphic effects of grating diffraction are avoided. The resulting rotation of the slit image is balanced by a corresponding tilt of the sagittal slit component. A back reflection CaF_2-prism (Littrow configuration, 9.5°, size 30 × 40 mm) with an Al coating is employed for order separation.

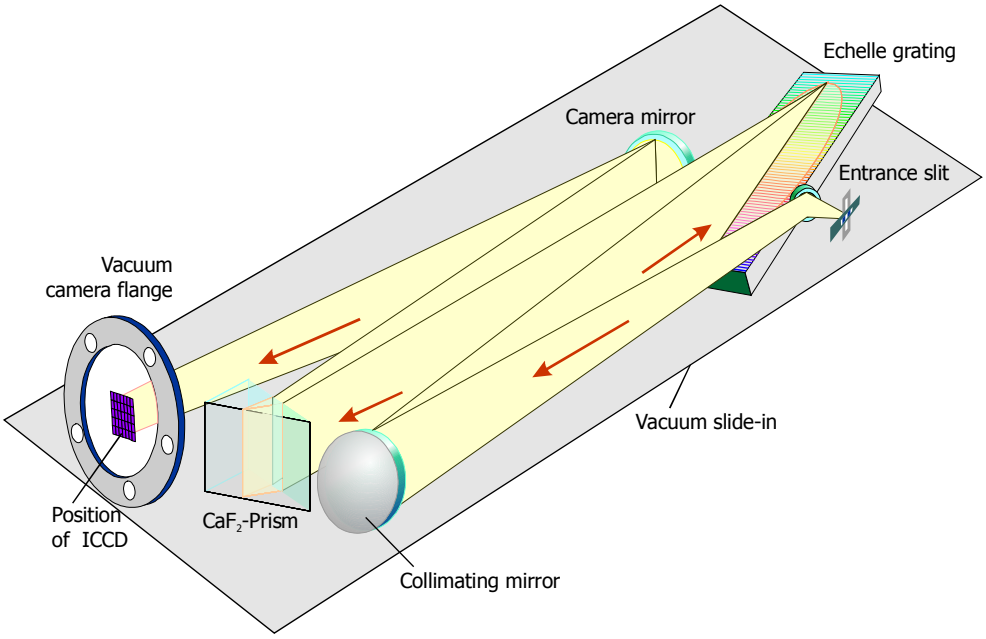

Fig. 6-2: *Optical train of the VUV echelle spectrograph.*

The design allows the imaging of about 75 separated orders on the available detector area in the spectral range of 150-300 nm. The free spectral range (FSR) of the lowest order, i.e. the geometrically longest one, at 300 nm is matched to the width of the detector area. At higher orders, i.e. shorter wavelengths, the detector width is not completely filled so that some spectral sections can be detected twice in adjacent orders (compare Fig. 6-8). Consequently, the spectra recorded above 300 nm have gaps. Further, at wavelengths about 400 nm the order lines cannot separated properly any longer due to decreasing dispersion of the CaF_2 prism. However, we observed characteristic distinct emission lines up to 560 nm in some cases. The optical design was optimized via ZEMAX 9.0 (Focus Software, Tucson, USA). Spectral calibration was done with a VUV deuterium continuum source (L1835, Hamamatsu, Herrsching, Germany). The echelle spectrograph was mounted on a removable slide-in perpendicular to the inlet of the spectrometer module (see Fig. 6-3), so that the spectrograph could be adjusted outside the main chamber and then simply inserted into the spectrometer module. The ICCD camera is located outside the chamber and can be easily removed from the module for maintenance. Figure 6-3 gives a side-view of the complete system and arrangement of all major components beside the vacuum system. The Figures 6-4 - 6-7 give the photos of the real system.

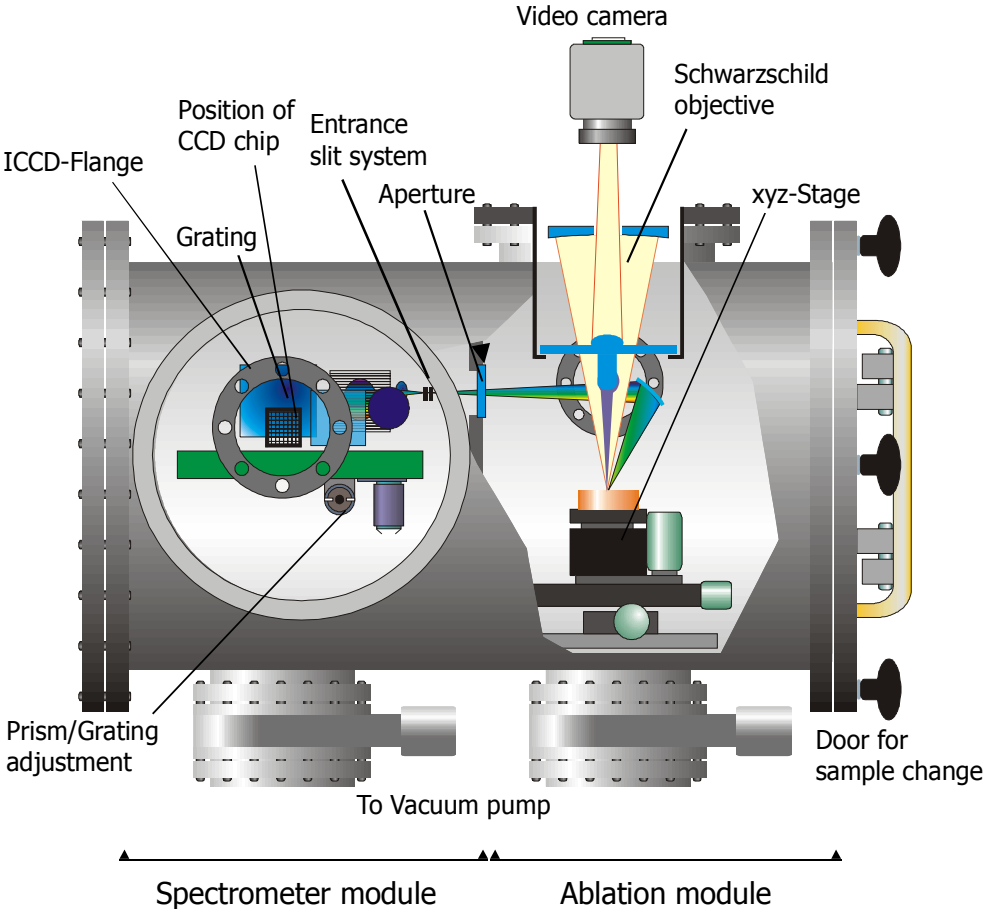

Fig. 6-3: *Side-view of the complete experimental set-up, i.e. spectrometer and ablation module, for LIPS microanalysis in the VUV (laser and vacuum pump system not shown).*

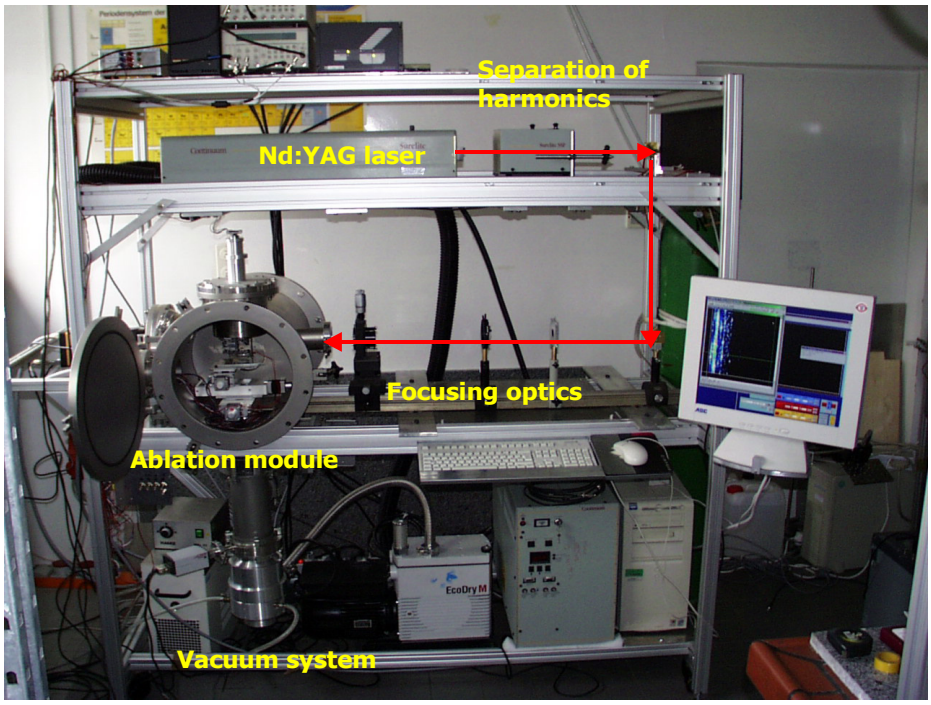

Fig. 6-4: *The complete Micro-LIPS set -up (arrows denote laser beam path).*

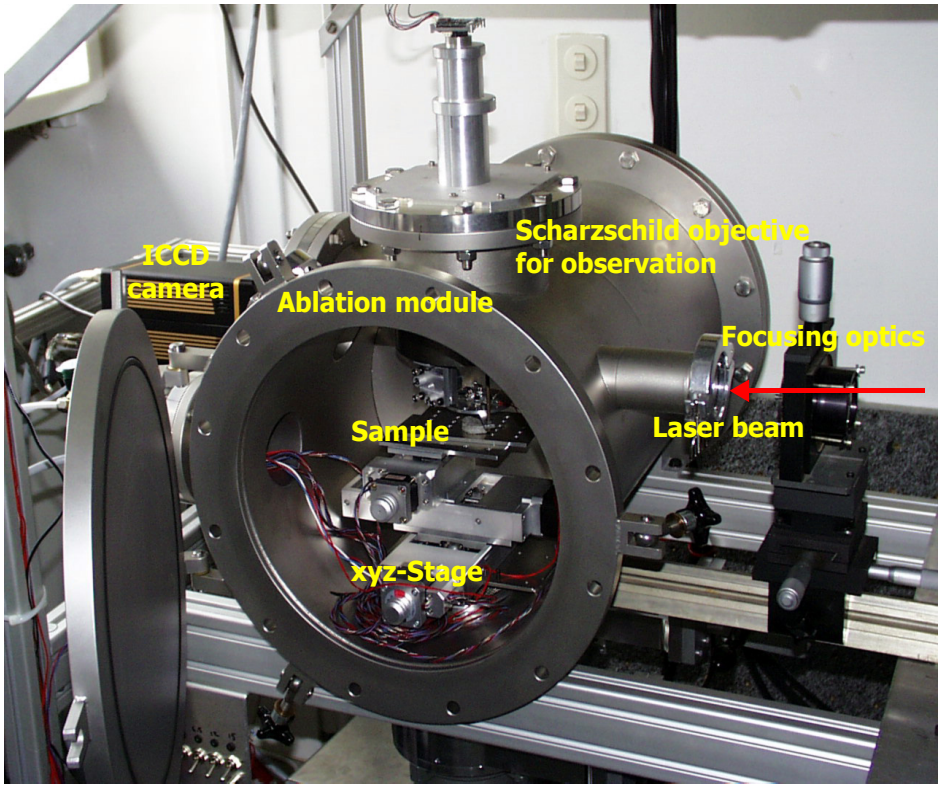

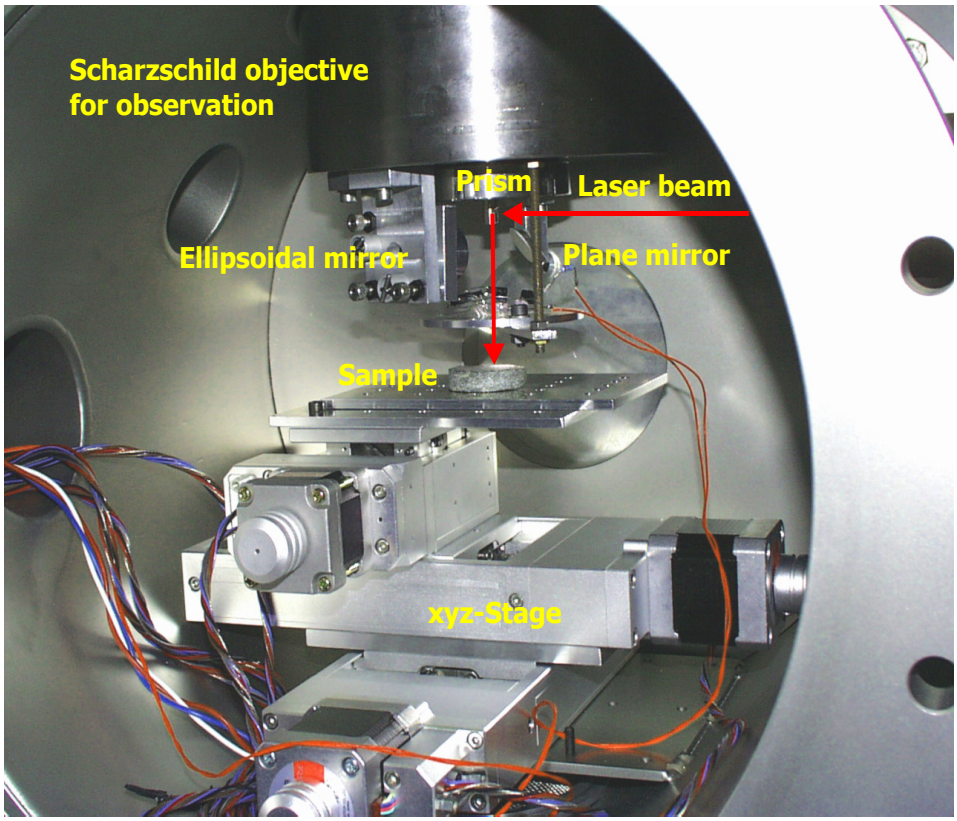

Fig. 6-5: *The photos of whole tank (up) and ablation module (down).*

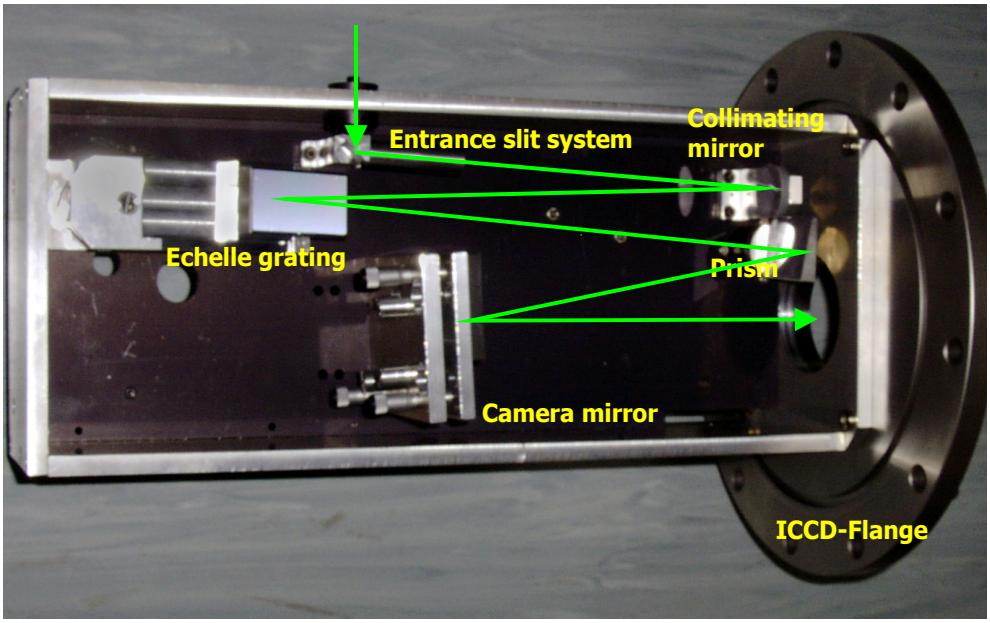

Fig. 6-6: *Photo of the echelle spectrometer module (arrow denotes plasma emission path).*

The LIPS experiment, i.e. delay to the laser pulse and integration time (gate width), was timed through a delay generator (DG 525, Stanford Research Systems, Sunnyvale, USA). The complete set-up was controlled through an in-house written Labview (National Instruments, Munich, Germany) program which controlled and integrated the main components of the experimental set-up.

Procedure

The set of steel samples was consisted of 9 standard reference materials (low alloy steels SS 401-409, NIST, Gaithersburg, USA) and 9 samples supplied from an actual steel production (supplied by Ferrotron, Moers, Germany). The later samples were delivered with reference analysis from a conventional spark-analyzer. The samples for mapping and imaging with LIPS were taken from a study of bottom ash from municipal waste incineration, see [222] for details of the sample preparation and embedding procedure. To image the chemical composition of samples and determine the ablation crater size, a scanning electron microscope (SEM, Cambridge S360, LEICA, Bensheim, Germany) equipped with an energy dispersive X-ray Si(Li) detector (EDX, RÖNTEC UHV Dewar Xflash detector system, EasyUse/EDR288 M, Berlin, Germany), and a back-scattered electron detector was employed. The working distance for microanalysis was 25 mm, an accelerating voltage of 25 kV and a beam current of about 1 nA (about 1300 cps) were used. Mapping was performed with a pixel size of 0.65 µm and a integration time of 5 s per pixel, usually five replicate EDX mappings were averaged.

6.3. Results and Discussion

To evaluate the spectrometer performance, light from a VUV deuterium continuum source was imaged onto the entrance slit system of the echelle spec-

trograph under vacuum conditions (10^{-6} mbar). Figure 6-7 shows the different orders along the horizontal direction, while the wavelength is increasing along the vertical direction. Obviously, the orders are not parallel and slightly curved. The overall spectrum follows the well-known continuum spectrum of a deuterium lamp in the UV and the characteristic line spectra in the Vis and VUV region [223]. In the VUV range between 150 nm and 180 nm the orders are well separated, i.e. a single order line is 7 pixel wide and the inter-order distance is about 3 pixel. Above 180 nm the order separation degrades to a width of 3 pixel and an inter-order distance of 1-2 pixel. At even higher wavelengths the full spectrum coverage is lost (i.e. > 300 nm) due to the detector size (see above) and the observed part of the order lines are merged. Due to the blaze function of the echelle grating, the intensity within a single order line (see Fig. 6-7) decreases to the edges of the order. These effects can be eliminated with a proper calibration as described in more detail in [224].

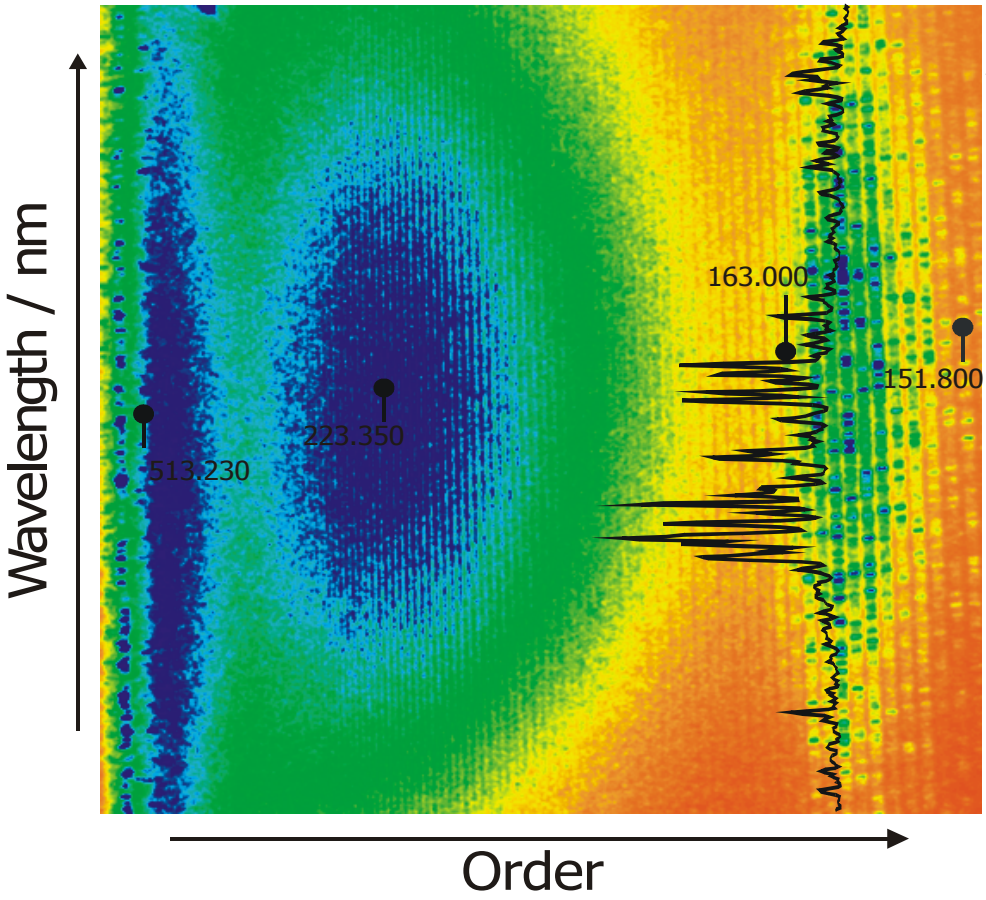

Fig. 6-7: *Echelle image from a VUV deuterium lamp under vacuum conditions (insert: order line 152 from 158.270-159.300 nm; wavelength markers for orientation).*

To determine the spectral resolution a mercury calibration lamp under atmospheric conditions was utilized. Figure 6-8 shows the corresponding echelle image. Clearly, spectral lines can be utilized even above 300 nm in the visible range with this echelle if the lines are not overlapped and clearly separated from other emissions. Further, Fig. 6-8 shows various artifacts from stray light ghosts and strong lines (i.e. 184.950 nm) which saturate the ICCD. The latter is due to the provisional illumination of the spectrograph with the lamp. The spectral resolution was determined along the 77th order line for the Hg(I) lines at

313.184 nm and 313.155 nm. The 29-pm spectral separation of the lines corresponds to 4 pixel, i.e. an actual dispersion of 7.25 pm per pixel (theoretical dispersion 7.14 pm per pixel). This yields a resolving power R = λ/Δλ of 11000 at 313 nm with a line FWHM of 4 pixel. Taking into account the higher dispersion (theoretical dispersion of 3.60 pm per pixel at 160 nm and 3 pixel FWHM) in the VUV, we estimated a resolving power of 15000 for this region.

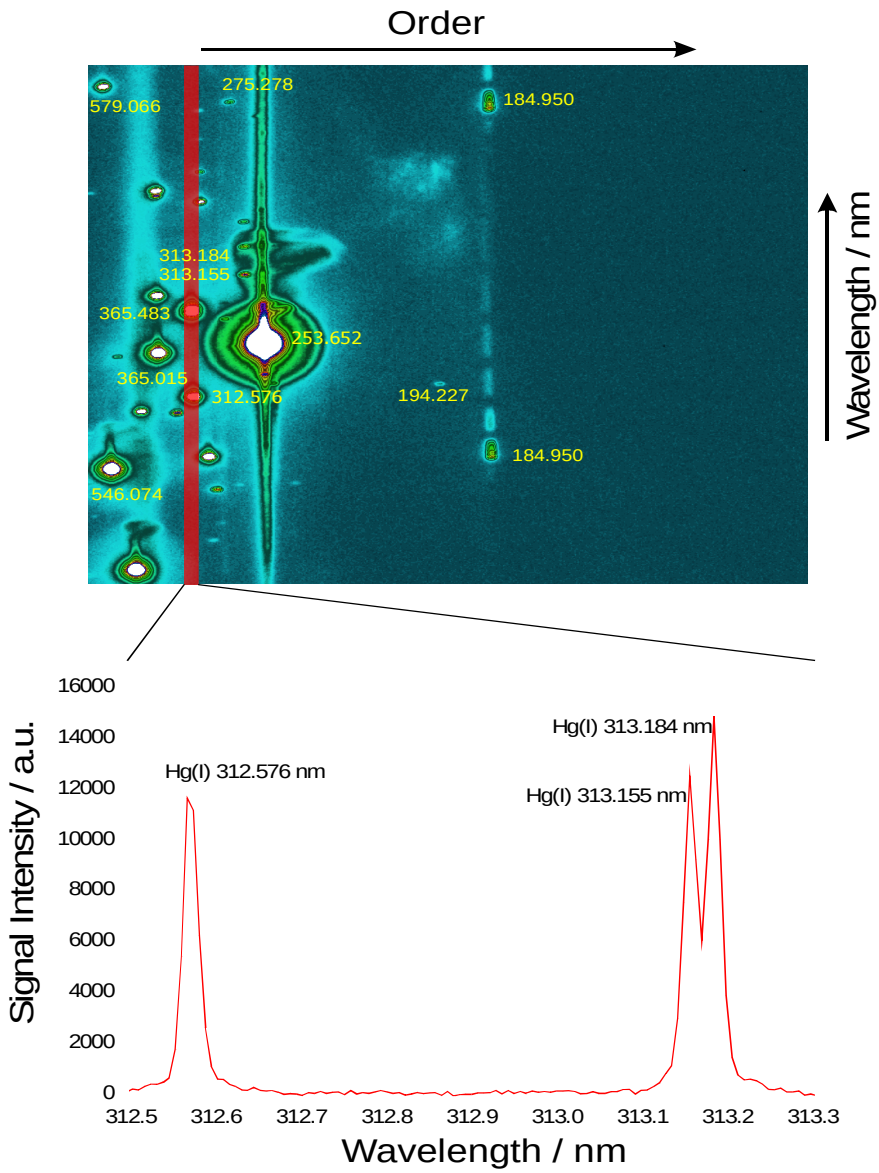

Fig. 6-8: *Echelle image from a mercury calibration lamp and a line spectrum from the 77th order to determine the spectral resolution (atmospheric conditions).*

To investigate the spatial resolution of the system, the irradiance was varied between 4 GW cm^{-2} and 22 GW cm^{-2} as well as the diameter of the final aperture in the focusing optics (see Fig 6-1). The focal spot diameter taking into account the divergence of the laser beam (through Rayleigh distance) can be calculated from [225]:

.

$$d = \frac{f \cdot d_0}{\sqrt{(z-f)^2 + z_R^2}}$$

The Z_R is the so called Rayleigh distance and can be calculated from:

$$Z_R = \frac{4\lambda}{\pi\theta^2}, \qquad (6.1.)$$

where λ is wavelength of a laser beam and Θ is beam divergence.The value d_0 is the so-called beam waist diameter and its also characteristic of the beam:

$$d_0 = \frac{4\lambda}{\pi\Theta} \text{ (for } TEM_{00}) \qquad (6.2.)$$

Assuming a gaussian profile and a divergence of 0.6 mrad at λ = 266 nm, the theoretical focal spot diameter on the sample is about 14 μm. In general, it has been observed that the crater size increases with the applied irradiance (see also [33,226,227]) and is less defined for a larger limiting aperture (see Fig. 8-10).With a small aperture and a low irradiance the beam profile approximates a top-hat profile (see Fig. 6-9), which leads to less thermally induced collateral damage (see Fig. 6-10). Unfortunately, the plasma emission signal decrease exponentially, as well (see Fig. 6-12). Generally said, lower limit of a crater diameter of this system lies at about 25 μm (Fig. 6-13). With more advanced beam shaping this could be improved to a crater size of 20 μm, however the boundary conditions of this set-up (see discussion above) of the ablation and observation optics limits the achievable minimum crater size. Note, that the optical arrangement allows easily to increase the crater size to 100-500 μm for bulk analysis.

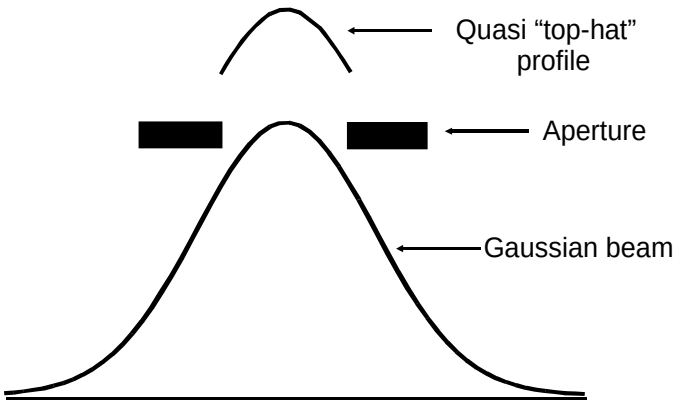

Fig. 6-9: *The modification of a Gaussian beam profile with a simple mechanical aperture.*

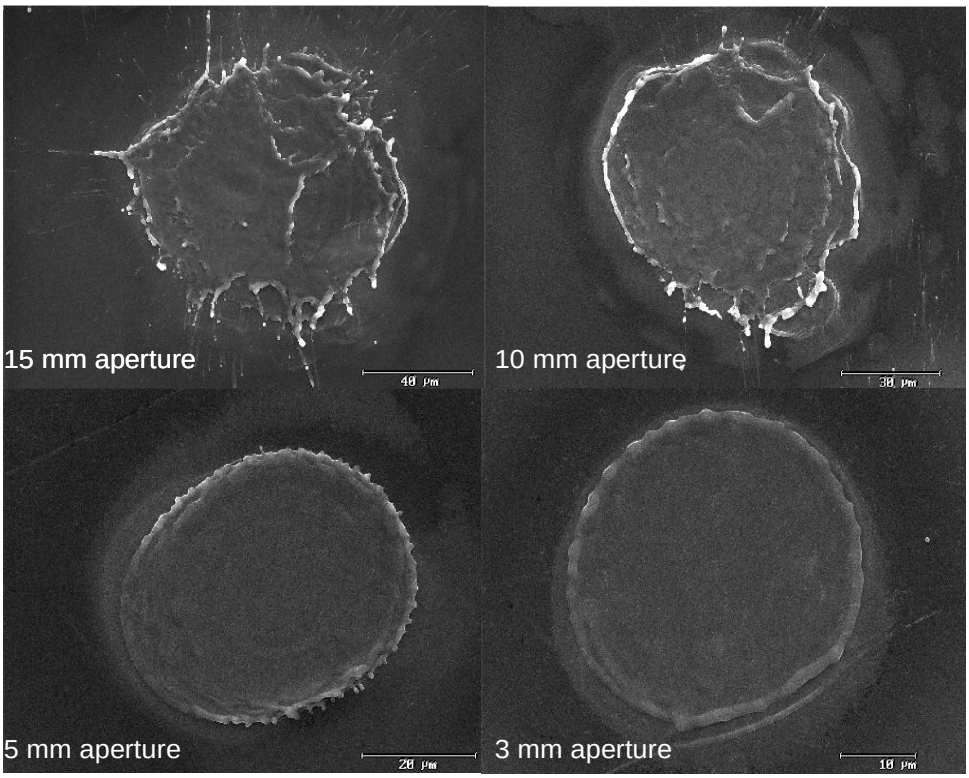

Fig. 6-10: *Craters made with the single laser pulse for the different diameters of limiting aperture (Laser: 266 nm, irradiance ≈ 10^{11} Wcm^{-2}, Substrate: Si wafer).*

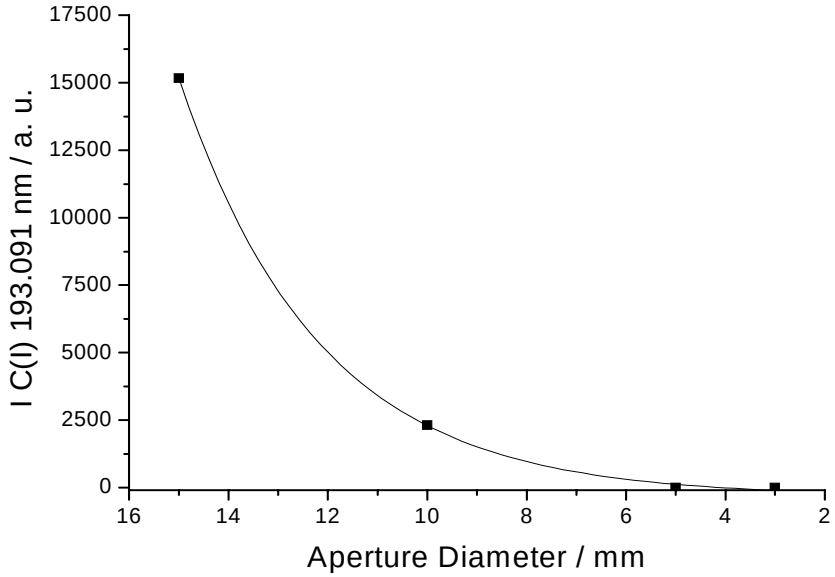

Fig. 6-11: *Intensity of C(I) 193.091 nm line vs. aperture diameter (Sample: low alloy steel SS402 (BAS) with 1.20% C).*

To evaluate the sensitivity of this set-up sulphur, phosphorus, and carbon in steel have been determined, which is a common VUV application for emission spectroscopy with LIPS and spark analyzers (see chapter 5.3). The signal-to-noise ratio for the emission lines under investigation was optimized on the way already described (see chapter 4.2) regarding the delay and integration time, respectively.

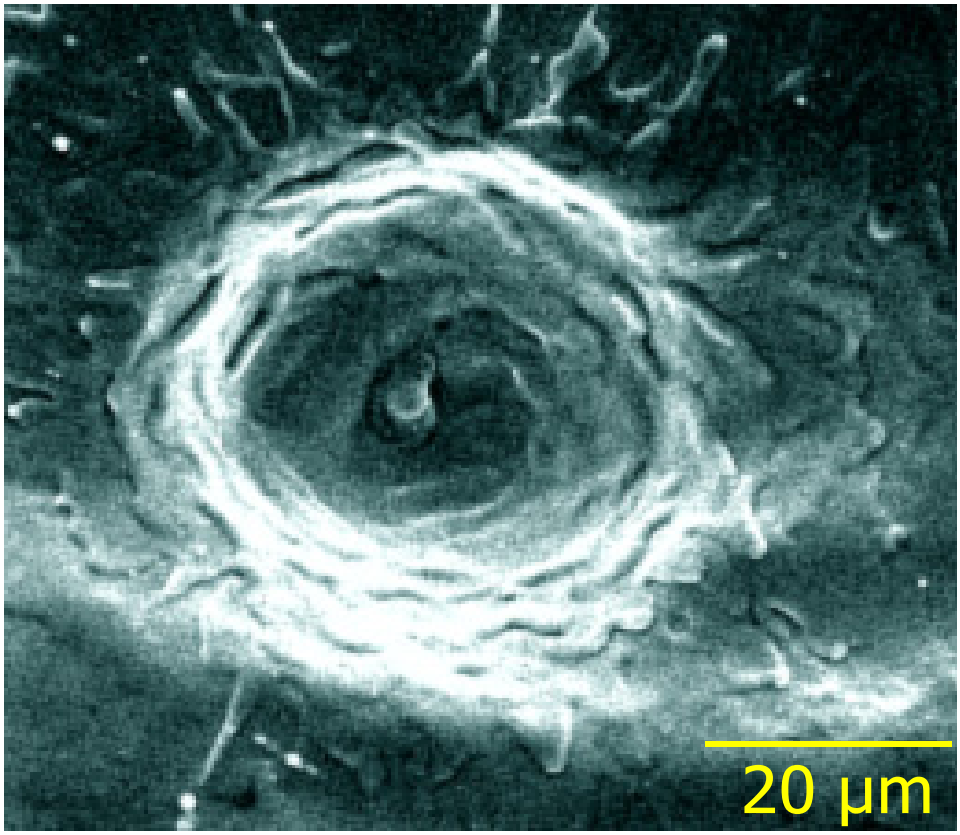

Fig. 6-12: *SEM image from a ablation crater on a polished steel sample (irradiance 4 GW cm-2).*

Concerning the former results for buffer gas optimization (see chapter 4.3.3) all measurements have been performed under the 1000 mbar of argon. Each sample was scanned for 100 laser pulses (step size 50 µm) with a delay to the plasma ignition of 1 µs and a 8 µs integration time. Figure 6-13 shows a typical echelle image from a steel sample. Due to the dynamic range of the observed lines, different color scaling was needed for different parts of the spectrum. The X-shaped structure on the image is due to presently uncompensated scattering in the spectrometer module. Figure 6-13 illustrates an obvious advantage of working in the VUV regime, which is the reduced number of lines for elements such as iron. For all calibration curves (Fig. 6-14), a good linearity was found, only in the case of carbon, saturated lines were observed at higher concentrations. Table 6-1 summarizes the determined limits of detection (LOD) calculated on the 3s-criterion of the IUPAC. The LODs are in good agreement with figures of merit reported with conventional set-ups for LIPS bulk analysis reported earlier [112,114,116,117].

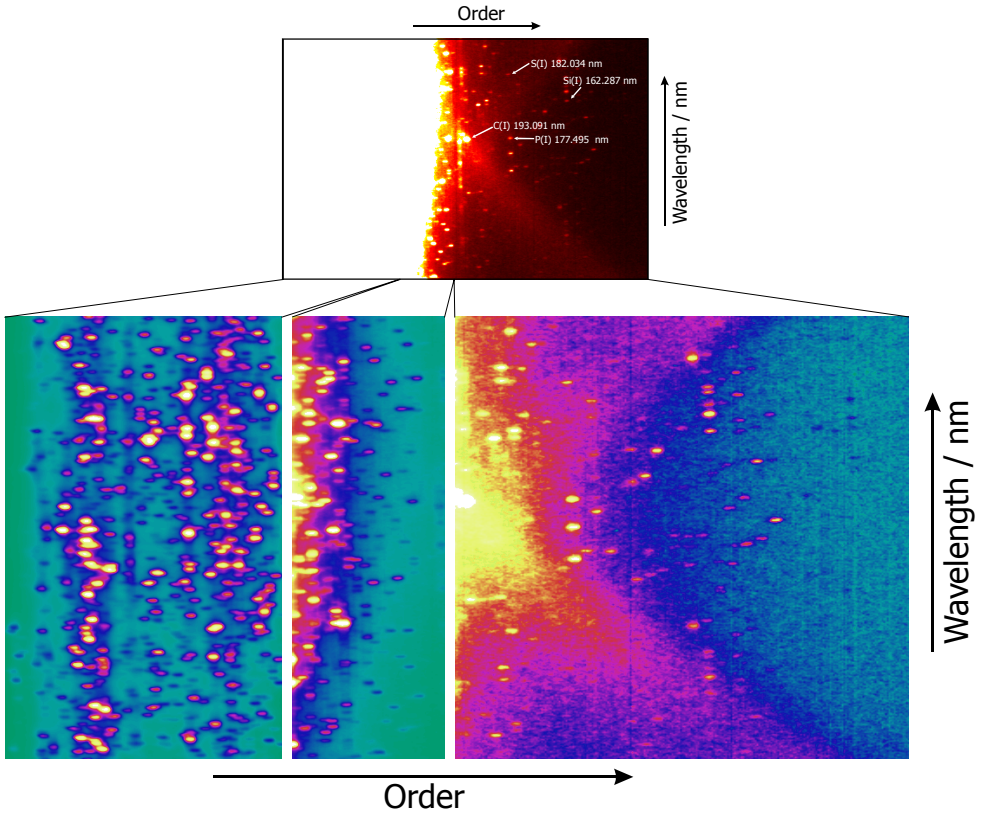

Fig. 6-13: *Echelle image from a steel sample 0.21% C, 0.008% P, and 0.011% S (buffer gas: p(Ar) =1000 mbar, delay: 1 µs, integration time: 8 µs).*

Tab. 6-1: *Limits of detection for carbon, phosphorus and sulphur in steel*

Element	Line	LOD / ppm
C	C(I) 193.091 nm	7
P	P(I) 177.495 nm	36
S	S(I) 182.034 nm	73

To demonstrate the single pulse scanning and mapping performance of the system, two mineral samples from a study on bottom ash from municipal waste incineration were investigated [222]. The fractured samples, embedded in araldite and polished, are ideal for this purpose as they are characterized through a high spatial and chemical heterogeneity. Figure 6-15 shows a scheme of a typical single pulse scan process with the system providing simultaneously the echelle images and the corresponding visual images from the long distance Schwarzschild objective. We highlighted only some of the elements found in the scanned mineral grains in Fig. 6-15. Again the visualization is complicated by the available dynamic range of the ICCD and the need to display major and minor components simultaneously. The heterogeneity of the waste input is reflected in the range of elements found, e.g. As and Co. The overall speed of scanning achieved here is 2 Hz for the complete image acquisition and movement of the xyz-stage. The rate limiting step is the complete read-out of the ICCD, with current systems 5-8 Hz should be easily possible.

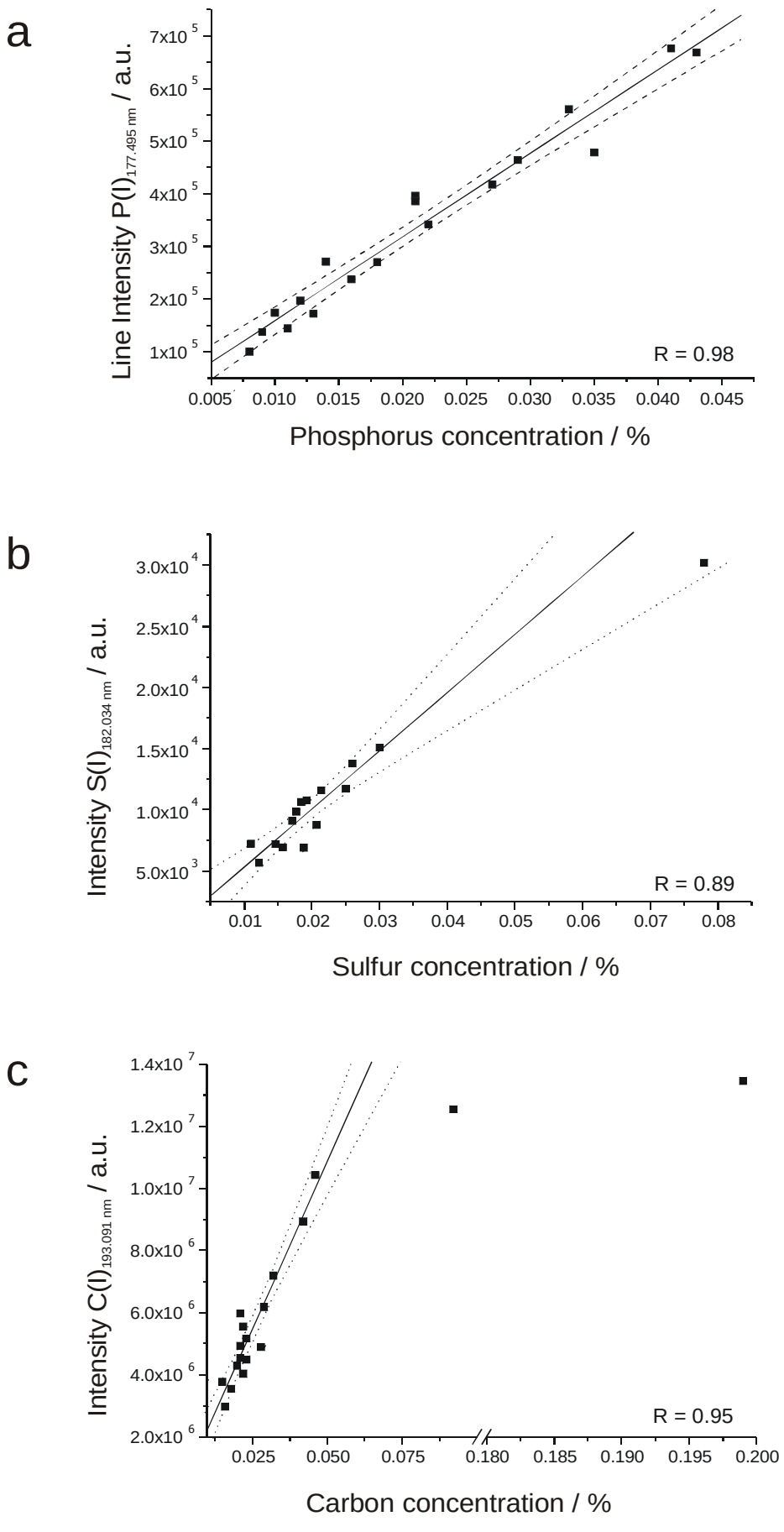

Fig. 6-14: *Calibration curves for phosphorus (a), sulfur (b), and carbon (c) in steel (n =18 samples, 100 pulses per sample, buffer gas: p(Ar) =1000 mbar, delay: 1 µs, integration time: 8 µs, dotted line: 95% confidence interval of regression) .*

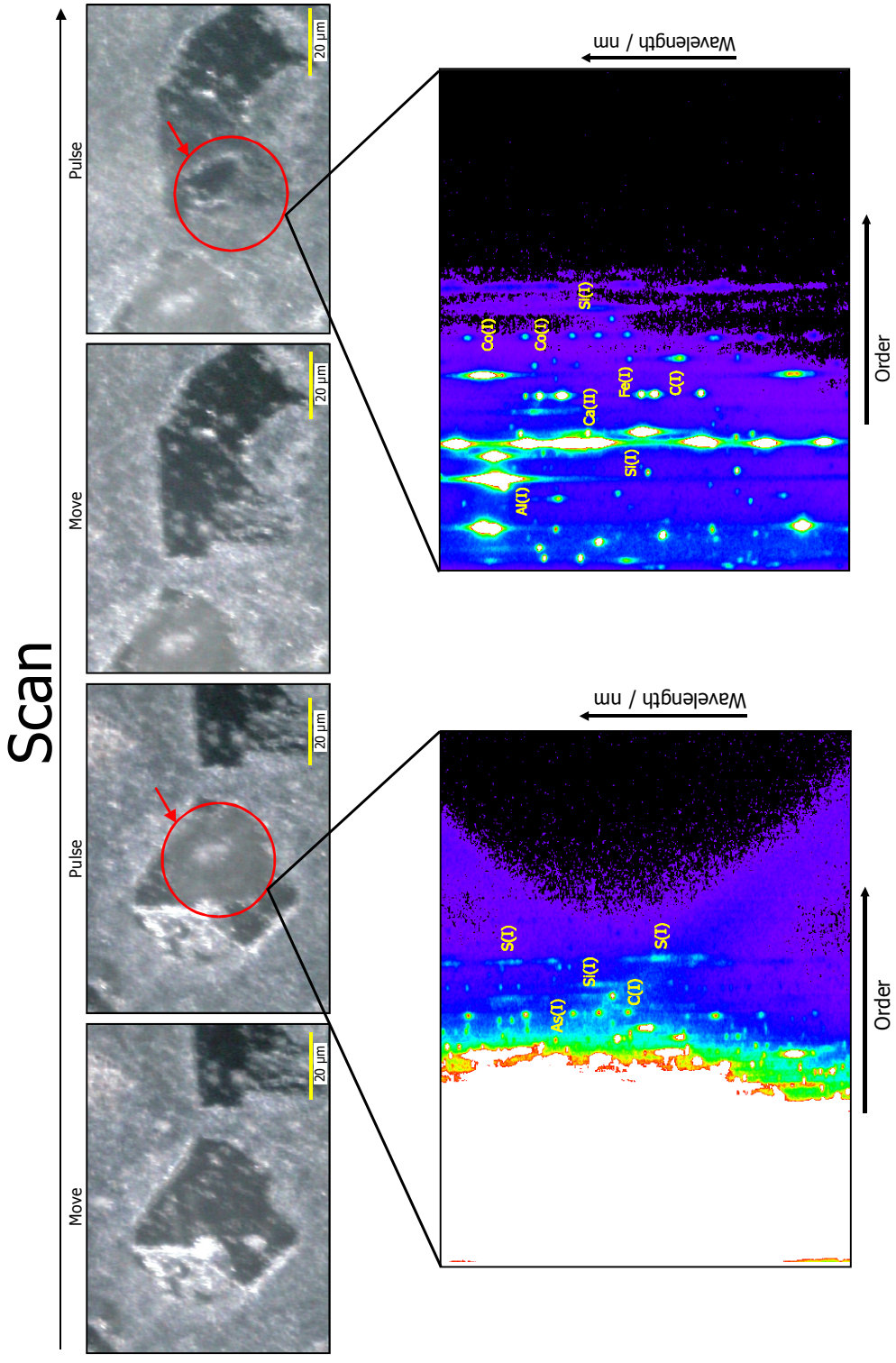

Fig. 6-15: *Schematic of a single pulse scanning of a bottom ash sample with VUV-LIPS (buffer gas: p(Ar) =1000 mbar, 7 GW cm-2, delay: 0.5 µs, integration time: 5 µs, step size 50 µm).*

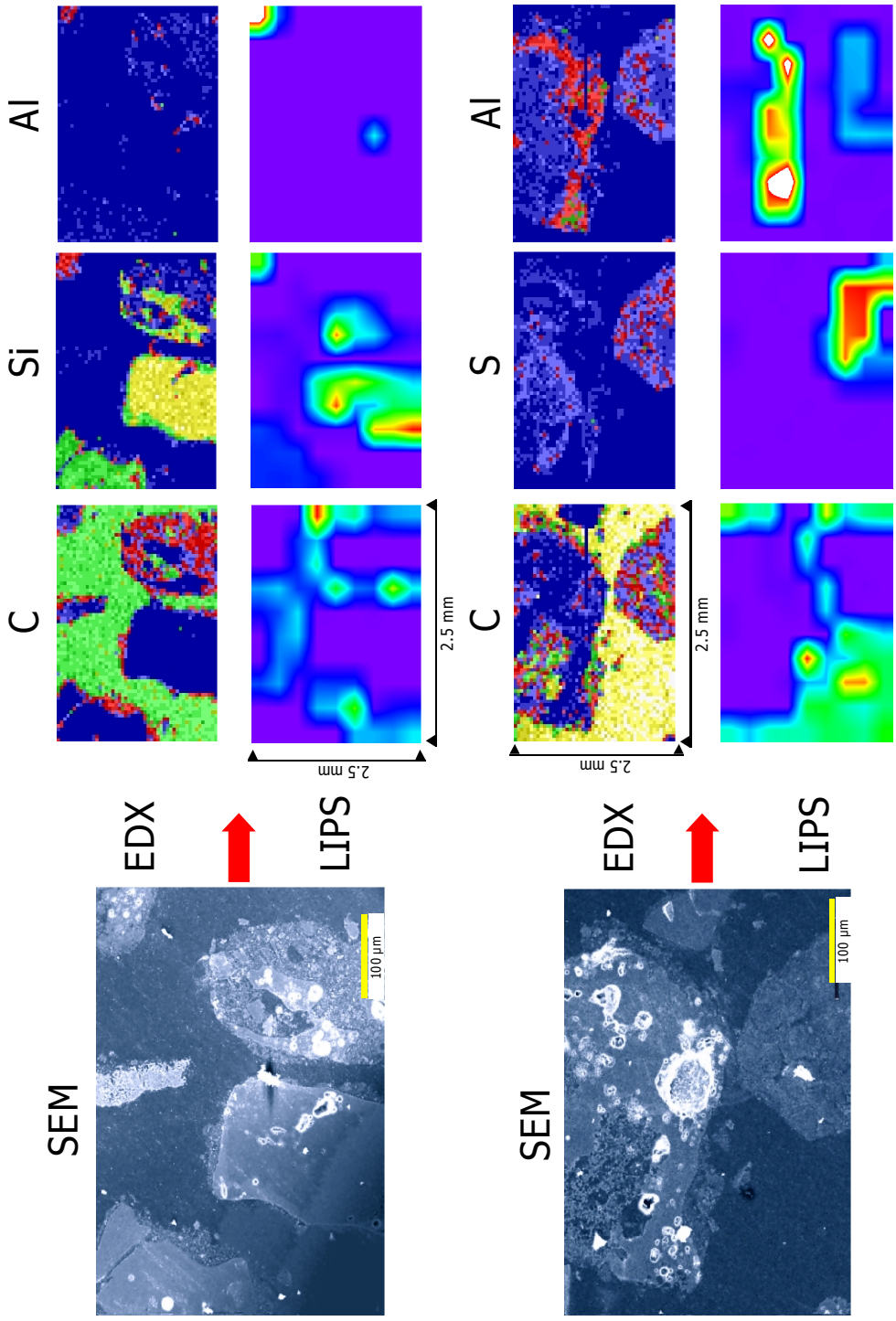

Fig. 6-16: *Comparison of an elemental mapping with LIPS and SEM/EDX (C(I) 193.091 nm, S(I) 182.034, Si(I) 162.87 nm, Al(I) 308.305 nm, sample: bottom ash particles form a municipal waste incineration, single pulse, buffer gas: p(Ar) =1000 mbar, 7 GW cm-2, delay: 0.5 µs, integration time: 5 µs, mapping area 2.5 mm ´ 2.5 mm, step size 50 µm).*

Figure 6-16 demonstrates for two different samples an elemental mapping with the VUV-lines of Si, Al, C, and S; the total raster size was 2.5 mm X 2.5 mm. Assuming a constant crater size of 25 µm, a step size of 50 µm was chosen to reduce cross-talk from adjacent craters. Despite the considerable differences in

spatial resolution, the LIPS and SEM/EDX mappings show a good agreement, all major elemental features are reproduced by the LIPS mapping. The scan time of the LIPS system was a tenth of the SEM/EDX system. However, the intrinsic sensitivity of LIPS permits only detection of major components with a single pulse mapping. We estimated a limit of detection in the order of 0.1-1% for this mode of analysis depending on the element under study.

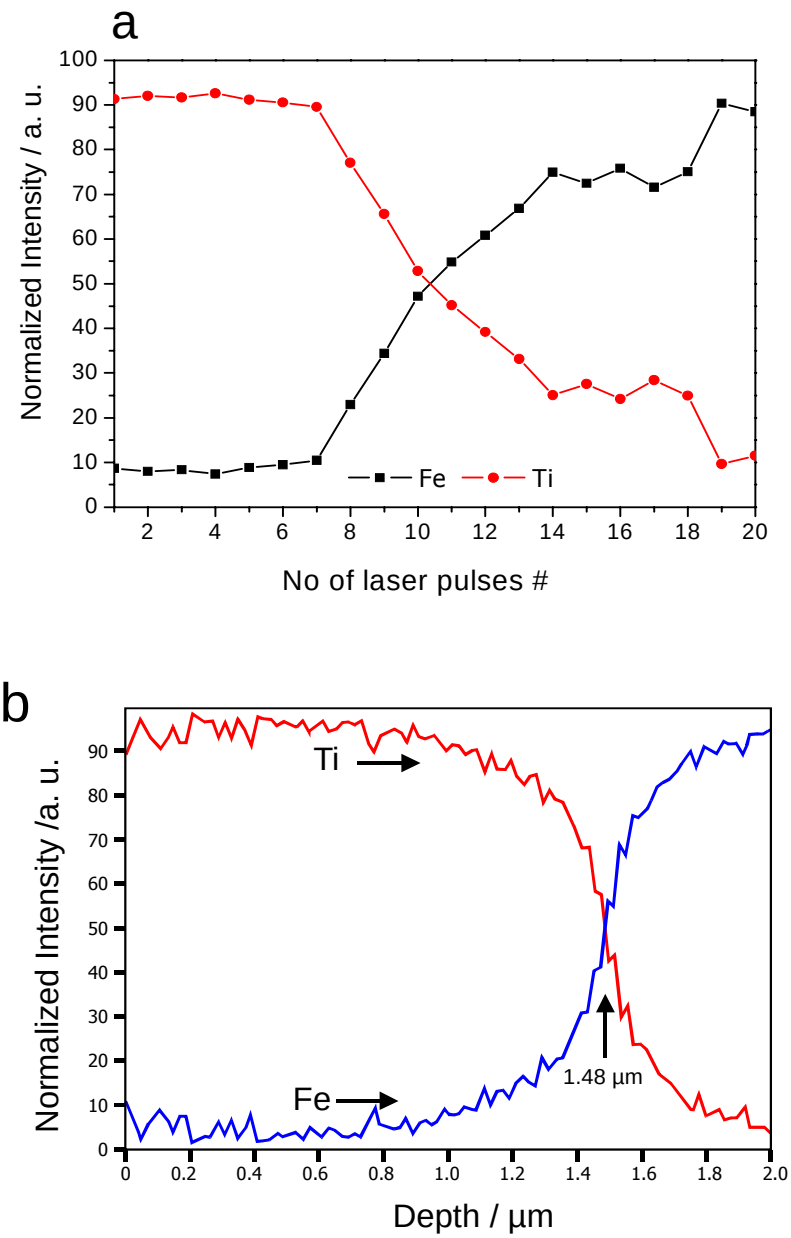

Fig. 6-17: *(a) LIPS depth profile of a steel sample coated with titanium nitride (Fe(I) 382.696 nm, Ti(I) 453.732 nm, irradiance GW cm-2, delay: 0.2 µs, integration time: 2 µs, (b) SEM/EDX analysis of a corresponding cross section of the steel sample (Fe: Ka1 at 6.403 eV, Ti Ka1 at 4.510 eV).*

To evaluate the performance for depth profiling with this system, a steel sample with a titanium nitride coating was analyzed. Figure 6-17a reveals the corresponding profiles for iron (bulk material) and titanium (coating), while Figure 6-17b shows the SEM/EDX reference analysis of the corresponding cross section. Both data sets were normalized to the total intensities of the evaluated lines. Assuming that the crossover of the depth profiles is the nominal interface, a mean ablation depth of about 150 nm per pulse can be computed, which is in good agreement with earlier studies [226]. Note, that this is rather a crude

approximation as the aspect ratio of the observation changes with increasing ablation depth and material melted and re-deposited at the crater walls will also contribute to the signal. We estimated that the real ablation depth per pulse was in the order of 500 nm per pulse and depends strongly on the spatial laser pulse profile, irradiance, and the characteristic of the ablated material, as was pointed out by several authors for laser ablation [227-229].

7 Summary

This work showed several new approaches and applications of laser-induced plasma spectroscopy (LIPS) in spectrochemical analysis of solid samples.
Using two laser pulses in LIPS experiments instead of one in order to separately control and optimize sampling, atomization and excitation process was already discussed by several authors. Either one laser is used, modified for operating in burst mode (several Q-switching within one flash lamp pumping period) or two separate lasers are used aligned perpendicular to each other. The ablation laser pulse is either preceded or followed by a laser pulse aligned parallel to the sample surface and focused a few millimeter above it. This pulse produces either a preablation plasma above the surface (in the first case) or reheats the ablation plasma (second case). Investigation of this, perpendicular, geometry within double pulse LIPS experiments was the one of the tasks in this work and results are presented in chapter 3. It has been found that timing between lasers are of essential importance. Enhancements in line intensity and improved analytical figures of merit compared to single pulse are detected in both matrices but only in preablation mode. The lines are more enhanced and calibration sensitivity is more increased for 266 nm wavelength of ablation laser than for 1064 nm. Only a moderate increase in electron temperature and number density was observed for the double pulse approach.
Chapter 4 shows results of LIPS analysis in UV-Visible spectral region. The detection system was the same as used in double pulse experiments. For the multielemental analysis of complex matrices like coal single pulse evaluation and robust statistics was applied. It has been shown that such approach can compensate for some of the variation due to the considerable heterogeneity of the material. Trimmed means improved analytical performances for some

elements. The study indicated also the problems due to the incorrect or incomplete sampling, which stems form the microanalytical nature of the method. A simple sample preparation such as drying and pressing or sampling of representative size fractions from the process stream is necessary for meaningful LIPS bulk analysis of extremely heterogeneous materials. The determined LODs in the lower ppm range and good reproducibility for samples in the form of pellets make LIPS then a good choice for assessment, i.e. monitoring and screening, of mined materials such as coal, mineral ores, and clays.

Chapters 5 and 6 are dedicated to LIPS bulk and microanalysis in VUV spectral region (< 200 nm). For that purpose two VUV-LIPS experimental set-ups were developed. The set-up for bulk analysis was based on a vacuum monochromator with a Czerny-Turner mounting and a VUV grade, closed-type photomultiplier.

Monitoring of nonmetals, such as C, S, P, and N is one of essential analytical tasks during the steel production. In this work, the feasibility of VUV-LIPS for such application was demonstrated. An optimization study of different parameters important for LIPS in the VUV were carried out. The influence of time-gating of detection, type and pressure of buffer gas, laser wavelength and pulse energy on the C(I) 193.091 nm line were studied in detail. Figures of merit were determined using a set of reference steel samples. Additionally, a set of samples from a real steel production have been measured. The achieved figures of merit are comparable with these of common spark-OES analyzers and satisfy analytical demands in modern steel industry.

Detection of bromine in thermoplasts from consumer electronic was another application of VUV-LIPS. The determination of elemental bromine by atomic emission spectroscopy is generally hampered by the high excitation energy of the emitting states, with the consequence that the atomic resonance transitions are located in the vacuum ultraviolet region. Transitions in the Vis/NIR region are several eVs above the ground state and consequently often result in a poor analytical sensitivity. This work showed the potential of LIPS in the VUV region and compared it with results from the NIR region. The LOD determined in the VUV (437 ppm) were significantly improved compared to those from the NIR region (over 1%). In addition, VUV-LIPS compares favorably with other methods for a fast determination of Br in polymers. Additionally, with an optical path purged with a buffer gas (here argon), VUV-LIPS is not only feasible in a laboratory set-up, but also for at-line identification of thermoplasts during recycling. It has been noticed that plasma chemistry of complex matrices, such as the investigated thermoplast samples, can be a serious obstacle for LIPS, as it was shown here for the intermediate formation of molecular oxygen. In general, similar effects in the UV/Vis region could be expected for example from the formation of ozone. However, we did not observe this effect for other samples analyzed in the VUV, e.g. cast iron, ceramics, and glasses.

The system for microanalysis (micro-LIPS) presented, was appropriate for quantitative and qualitative scanning and mapping of surfaces and layers. Applying appropriate beam shaping („microfocusing“) and UV ablation wavelength ($\lambda = 266$ nm) a spatial resolution in the order of 20 μm was achieved with a depth resolution of approximately 0.5 μm. Microscopic positioning and

observation of the sample was performed via a motorised stage and a new long-distance Schwarzschild objective. In addition, the system for microanalysis applied a newly developed echelle spectrograph ($\lambda/\Delta\lambda > 10\ 000$ within operating range between 150 and 300 nm) for the VUV coupled with a VUV intensified ICCD camera. The integrated, innovative approach, both in detection and the corresponding ablation set-up and estimated limits of detection in the scanning mode (0.1-1%), qualifies the system for future at-line microanalysis, e.g. steel processing or advanced surface modifications. Bioanalytical microanalysis such as fast screening of phosphorylated proteins on gels and blotting membranes are other attractive fields of application for VUV-LIPS. By simple technical upgrade of the system with an additional observation alignment it would be possible to couple it with another echelle system for the UV-Visible region and in this way to extend the number of accessible elements.

8 Appendix

8.1. List of Abbreviations

AAS - Atomic absorption spectroscopy

ABS - Acrylnitrile butadiene styrene

AES - Atomic emission spectrometry

bb - Bound-bound transition

CCD - Charge-coupled device

DCP - Direct-current plasma

DPS - Diphenylstilbene

EPMA - Electron probe microanalysis

fb - Free-bound transition

ff - Free-free transition

FWHM - Full width at half maximum of a signal

GC - Gas chromatography

GD - Glow discharge

GD-AES - Glow discharge atomic emission spectroscopy

HBCD - Hexabromocyclododecane

ICCD - Intensified charge-coupled device

ICP - Inductively-coupled plasma

ICP-AES - Inductively-coupled plasma atomic emission spectroscopy

ICP-MS - Inductively-coupled plasma mass spectrometry

INAA - Instrumentation neutron activation analysis

IR - Infrared

LA - Laser ablation

LA-ICP-MS - Laser ablation inductively-coupled plasma mass spectrometry

LIBS - Laser-induced breakdown spectroscopy

LIPS - Laser-induced plasma spectroscopy

LOD - Limit of detection

LTE - Local thermodynamic equilibrium

MCP - Microchannel plate

MIP - Microwave-induced plasma

MPI - Multiphoton ionization

MS - Mass spectrometry

Nd:YAG - Neodymium-doped yttrium aluminium garnet

NIR - Near infrared

OES - Optical emission spectroscopy

OMA - Optical multichannel analyzer

PA - Polyamide

PBB - Polybrominated biphenyle

PBDE - Polybrominated diphenyl ether

PC - Polycarbonate

PLTE - Partial local thermodynamic equilibrium

PMT - Photomultiplier tube

PPO - Polyphenylene oxide

PS - Polystyrol

PVC - Polyvinylchloride

RSD - Relative standard deviation

SB - Styrenebutadiene

SEM - Scanning electron microscope

TPB - Tetraphenylbutadiene

TPO - Thermoplastic polyester

TXRF - Total x-ray diffraction

UV - Ultraviolet

VUV - Vacuum ultraviolet

XRF - X-ray fluorescence

XRPD - X-ray powder diffraction

8.2. List of Symbols

a - Thermal diffusivity

a_0 - Bohr radius

A - Einstein coefficient

α - Absorption coefficient

$B(\nu, T)$ – Planck black body function

c - Speed of light

C - Specific heat

D - Grating dispersion

d_{laser} - Focal diameter of the laser

$\Delta\lambda_D$ - Doppler line half width (in units of wavelength)

$\Delta\lambda_S$ - Stark line half width (in units of wavelength)

$\Delta\lambda_{inst}$ - Instrumental line half width (in units of wavelength)

$\Delta\lambda_{eff}$ - Effective slit band width of monochromator

$\Delta\nu_D$ - Doppler line half width (in units of frequency)

$\Delta\nu_N$ - Natural line half width (in units of frequency)

$\Delta\nu_S$ - Stark line half width (in units of frequency)

E - Irradiance

E_H - Ionization potential of hydrogen

f_{ij} - Oscillator strength for the transition between levels i and j

$F_{\#}$ - f number

$F^N(\nu-\nu_0)$ - Natural line shape function

$F^D(\nu-\nu_0)$ - Doppler line shape function

g_i - Degeneration of the level i

h - Planck constant

I - Intensity

K - Electron-neutral inverse bremsstrahlung cross section

k - Thermal conductivity of material

k_B - Boltzmann constant

L_v - Latent heat of evaporation

λ - Wavelength

λ_L - Laser wavelength

m_e - Electron mass

n_e - Electron number density

n(p) - Ion number density of level p

ν - Photon frequency

ν_m – Momentum transfer collision frequency

ω(p) - Statistical weight of level p

p - Pressure

Q(t) - Heating rate

Q_a - Canonical partition function for species a

R - Reflectivity

ρ - Specific density of material

T - Temperature

T_e - Electron temperature

τ_a - Characteristic time for an atomic process

τ_{br} - Time required for laser induced brakdown to occur

τ_l - Duration of the laser pulse

τ_i - Natural lifetime of level i

τ_{plasma} - Characteristic time for transient plasma to change its temperature

τ_v - Characteristic time for a surface to reach the evaporate temperature

τ_{vbr} - Cime required for laser induced brakdown of vapour

v - Velocity

v_{exp} - Expansion velocity of the plasma

z_R - Rayleigh distance

8.3. List of Instruments

Lasers

He-Ne, Model 30 (LINOS Photonics, Göttingen Germany)

Nd:YAG, Surelite I (Continuum, Darmstadt, Germany)

Nd:YAG, Quanta-Ray GCR11 (Spectra-Physics, Darmstadt, Germany)

Nd:YAG, SL 280 (Spectron Laser Systems, Frankfurt, Germany)

Spectrometers

Echelle spectrograph, ESA3000 (LLA Berlin, Germany)

Spectrograph, Spectrapro 300-i (ARC, Acton, USA)

Vacuum monochromator VM-504 (ARC, Acton, USA)

Detectors

ICCD camera, DynaMight (LAVISION GmbH, Göttingen, Germany)

ICCD camera, PI-MAX (Princeton Instruments, New Jersey, USA)

Photomultiplier tube, 9635QB (Electron Tubes Limited, UK)

Oscilloscopes

Digitizing Oscilloscope, TDS 620A (Tektronix, Beaverton, USA)

Oscilloscope, 9310 AM (LeCroy, Heidelberg, Germany)

Delay - Generators

Delay generator, DG535 (Stanford Research Systems, Sunnyvale, USA)

Delay generator, 9865 (EG&G, Gaithersburg, USA)

Micro-positioning Stages

Motorized xyz-translation stage system, CTC 290 (Micos, Umkirch, Germany

Motorized xyz - translation stage system, Limes 90, HVM 60 (Owis, Staufen, Germany)

Optics, Optical Fibres, Mechanical Components

Lenses, mirrors, prisms:
Linos Photonics, Göttingen, Germany
Laser Components, Olching, Germany
Melles Griot, Bensheim, Germany
Eksma, Vilnius, Lithvania

Optical quarz fibres HCG-0550T-C01 US-10 (Laser Components, Olching, Germany)

Variable attenuator (Newport, Irwine, USA)

Vacuum Components

Oil-sealed rotary vane pump, Trivac - D25BCS (Leybold, Cologne, Germany)

Oil-free piston pump, EcoDry M20 (Leybold, Cologne, Germany)

Turbo-molecular pump, Turbovac 50 (Leybold, Cologne, Germany)

Turbo-molecular pump, Turbotronik NT10 (Leybold, Cologne, Germany)

Vacuum gauge, ITR90 (Leybold, Cologne, Germany)

Vacuum gauge, IRO90 (Leybold, Cologne, Germany)

Vacuum gauge, DVR5 (Vacuumbrand, Nertheim, Germany)

Valves, flanges, feedthroughs:
Vacom, Jena, Germany
Pfeiffer Vacuum, Asslar, Germany
VAT, Grossbrunn, Germany

Additional instruments and laboratory accesories

Laser energy detector, Powerlite C5100 (Continuum, Darmstadt, Germany)

Low pressure calibration lamps (Hg, Zn, Cd) (LOT Oriel, Darmstadt, Germany)

Analytical scale, M5 (Mettler-Toledo, Giessen, Germany)

Microwave accelerated reaction system, MWS1 (Berghof-Maassen, Eningen, Germany)

Laboratory grinder, A10 (IKA-Werke, Staufen, Germany)

Laboratory drier (Memmert, Schwabach, Germany)

8.4. List of Chemicals

All used chemicals had the „pro analysis“ purity level and were produced by Sigma-Aldrich-Fluka (Munich, Germany).

Barbituric acid ($C_4H_4O_3N_2$)
Biuret ($C_2H_5O_3N_2$)
1,1 - Carbonyldiamidazol ($C_7H_6O_{10}N_4$)
Chininsulfate ($C_{20}H_{30}O_8N_2S$)
Cyanic acid ($C_3H_3O_3N_3$)
Graphite (C)
Glycine ($C_2H_5O_2N$)
Methacrylamide (C_4H_7ON)
N,N-Methylendiacrylamide ($C_7H_{10}O_2N_2$)
Methionine ($C_5H_{11}O_2NS$)
Potassiumbromide (KBr)

Gases
Ar (purity 5.0), Messer-Griesheim, Munich, Germany
Ar (purity 4.6), Messer-Griesheim, Munich, Germany
N_2 (purity 5.0), Messer-Griesheim, Munich, Germany

8.5. Reference Analysis of Coal Samples

Tab. 7-1: *Reference analysis of coal samples (values are given in mg kg^{-1}).*

	Li	Na	Mg	Al	Si	K
HAM1	2.21	1889	706.105	144.348	0.993	235
Ham3	1.499	1106		50.547	0.783	
HAM4	1.49	959	746.605	391.502	1.368	224
Ham5	1.126	815		160.328	1.11	
Ham6	1.161	993	1279.253	28.657	1.019	225
HAM 7	3.509	703	1053.166	157.772	0.804	299
HAM 8	1.86	1382	651.956	65.392	1.215	291
HAM 9	60.197	694	655.174	7748.891	47.45	6658
HAM10	40.137	844	645.717	10107.529	33.704	4043
HAM 11	1.395	1206	776.086	112.406	0.946	245
HAM12	1.36	1271	765.718	112.905	0.979	257
HAM13	2.04	1612	664.696	115.842	1.099	184
HAM 15	1.818	1125	622.389	112.688	1.328	277
R 112	1.297	1287	834.352	76.092	1.045	213
R122	1.22	1162	660.063	136.478	1.713	358
R132	1.769	1224	528.857	80.48	2.999	580
R 146	1.424	1254	784.585	93.922	0.876	280
R155	1.33	1333	1784.225	67.96	0.901	268
R 213	1.635	1364	809.647	402.385	0.977	140
R231	1.351	1387	1787.005	377.696	0.951	279
R311	1.205	1236	1340.751	105.169	1.359	616
R323	1.499	1222		484.842	0.983	
R352	1.33	1284	1745.497	309.932	1.042	268
R431	1.282	1268		51.183	0.993	
R444	1.15	1203	748.19	101.996	0.971	249
R 456	1.17	1453	950.898	92.635	1.047	332
R722	2.577	1826	1028.794	289.293	5.891	766
R736	2.567	1808	1251.171	635.149	5.681	683
R744	3.316	2032		848.394	11.262	
R753	3.648	1906		1130.935	8.219	
R933	0.85	904	769.25	99.957	1.094	268
R942	1.122	1177	1807.398	87.503	1.801	323
R954	1.29	1114	789.388	321.131	2.659	520
R 1025	42.438	1449	679.123	5905.039	36.312	8862
R1036	19.181	1001	1069.373	1820.617	18.877	2401
R1052	30.265	1285	1337.009	2611.376	28.96	4164

Reference analysis of coal samples (extended).

	Ca	Ti	V	Cr	Mn	Fe
HAM1	11827	62	0.6	2.445	58.641	5423
Ham3	15280	25	0.331	26	78.802	7259
HAM4	12751	81	0.971	1.898	64.727	6246
Ham5	14520	70	0.857	9.62	72.768	7951
Ham6	12270	13	0.494	14.251	48.668	4720
HAM 7	6722	13	0.127	6.724	10385.486	2122380
HAM 8	10212	14	0.385	-0.824	214.704	59823
HAM 9	6467	1180	84.526	47.199	46.287	106806
HAM10	11057	1062	65.277	34.129	48.493	10750
HAM 11	11378	24	1.295	1.196	92.137	46896
HAM12	12094	11	0.503	2.926	373.854	19169
HAM13	10659	25	0.555	0.149	70.666	6259
HAM 15	9674	13	0.629	10.595	62.955	35822
R 112	12629	37	0.714	0.523	134.419	45547
R122	11172	35	0.724	1.028	108.62	5107
R132	11351	63	1.533	1.674	124.611	6096
R 146	11786	37	1.047	2.941	128.5	46929
R155	13379	62	0.664	0.904	142.63	6795
R 213	12295	61	0.496	0.213	68.797	33074
R231	13707	91	0.763	0.55	87.347	5352
R311	13416	61	0.594	1.911	60.903	5101
R323		86	0.737	22.04	71.328	5161
R352	13531	68	1.047	1.963	60.705	4412
R431		64	0.476	2.91	222.748	8084
R444	12530	44	0.571	3.531	243.188	9387
R 456	14770	49	0.749	0.363	158.75	54585
R722	10264	596	8.036	10.597	52.454	6504
R736	9707	524	9.706	12.088	50.143	7371
R744		816	12.081	14.62	57.558	9097
R753		1176	20.901	25.28	60.44	13337
R933	13091	25	0.684	1.367	297.104	11524
R942	13161	76	0.827	5.566	1158.349	35764
R954	13736	73	1.378	2.238	156.304	7790
R 1025	10636	2492	65.458	43.62	44.114	50001
R1036	10032	1325	36.986	22.29	34.902	3583
R1052	12447	1805	51.831	32.469	42.685	5172

Referencce analysis of coal samples (extended).

Analyte	Co	Ni	Cu	Zn	Ga	Sr
HAM1	0.122	0.666	0.382	1.05	2.785	124.747
Ham3	0.128	0.991	0.534	0.64	4.506	154.181
HAM4	0.573	3.735	0.187	0.95	3.22	142.463
Ham5	0.322	2.61	1.257	0.95	4.858	169.34
Ham6	0.146	1.591	1.19	0.108	3.977	118.107
HAM 7	0.06	0.583	0.7	3.129	1.052	38.264
HAM 8	0.075	0.645	0.287	0.65	2.658	115.567
HAM 9	8.537	31.551	20.183	64.744	13.481	119.576
HAM10	5.002	17.872	10.1	1.466	10.389	139.209
HAM 11	0.225	0.887	2.538	1.383	3.237	117.937
HAM12	0.1	0.458	0.197	0.86	2.774	121.397
HAM13	0.161	3.998	0.159	0.46	2.307	119.772
HAM 15	0.153	1.717	4.513	1.738	2.58	109.639
R 112	0.106	0.655	0.62	0.275	3.533	113.493
R122	0.107	0.962	2.013	1.687	2.992	104.643
R132	0.394	1.171	0.369	0.203	3.227	85.328
R 146	0.098	0.758	0.506	0.13	3.453	106.199
R155	0.124	0.849	0.447	0.133	4.748	122.869
R 213	0.129	0.536	0.863	0.222	3.784	115.099
R231	0.186	0.649	0.794	0.413	5.901	131.902
R311	0.185	4.71	1.169	1.142	4.713	117.385
R323	0.189	0.765	0.194	0.4	5.488	140.628
R352	0.141	0.787	1.065	0.328	5.389	127.357
R431	0.139	0.398	0.294	0.685	4.415	130.744
R444	0.085	0.462	0.302	0.319	3.04	115.502
R 456	0.11	0.531	0.714	0.436	4.15	129.714
R722	1.428	3.513	2.021	2.286	4.708	118.672
R736	1.838	4.479	1.156	0.473	5.302	123.201
R744	2.418	7.595	3.06	2.14	5.827	149.212
R753	3.232	9.184	4.034	1.55	7.474	146.084
R933	0.107	0.534	0.354	0.166	3.351	109.586
R942	0.232	1.822	3.416	1.12	5.027	107.519
R954	0.238	0.996	0.545	2.173	3.53	121.376
R 1025	1.081	7.73	21.629	16.766	15.205	187.277
R1036	0.867	5.178	6.494	2.23	11.09	164.038
R1052	1.193	33.376	8.547	2.072	14.986	186.994

Reference analysis of coal samples (extended).

Analyte	Ag	Cd	Ba	Tl	Pb	Bi
HAM1	1.772	0	124.179	0.002	1.168	1.208
Ham3	1.379	-0.144	160.655	0	0.126	1.296
HAM4	0.014	-0.007	138.194	0	0.883	0.581
Ham5	0.71	0.063	171.961	0.015	2.355	1.5
Ham6	0.184	-0.565	126.971	-0.002	0.003	1.052
HAM 7	-0.326	0.052	42.04	0.012	0.242	22.412
HAM 8	-0.155	-0.004	114.356	0.003	0.783	16.335
HAM 9	3.289	0.492	165.839	0.416	16.361	9.271
HAM10	0.306	0.071	165.49	0.288	10.335	3.254
HAM 11	0.623	0.078	122.849	0.004	1.667	1.595
HAM12	0.032	-0.017	117.83	0	0.274	0.562
HAM13	-0.112	-0.013	108.309	0	0.445	0.528
HAM 15	2.08	0.112	109.134	0.001	2.809	22.707
R 112	1.044	0.007	136.285	0.005	0.485	1.956
R122	3.386	0.047	132.947	0.002	1.546	6.551
R132	0.087	0.026	145.808	0.013	0.5	2.335
R 146	0.087	0.019	131.248	0.005	0.369	1.304
R155	0.497	0.071	160.044	0.004	0.367	1.184
R 213	1.523	0.034	144.035	0.015	1.039	3.355
R231	3.704	0.126	172.654	0.014	1.889	8.396
R311	0.261	-0.381	140.252	0.015	0.8	2.81
R323	0.228	-0.07	180.814	0.012	0.973	2.832
R352	2.599	0.064	163.096	0.004	1.464	2.145
R431	-0.927	0.032	158.497	0	-0.087	2.51
R444	0.055	0.037	138.415	0.002	0.21	1.561
R 456	1.544	0.041	158.291	0.002	0.542	0.996
R722	0.408	-0.377	113.935	0.075	2.881	1.809
R736	0.126	0.271	135.061	0.101	3.115	1.091
R744	0.978	11.112	160.542	0.191	5.973	3.262
R753	6.545	0.273	169.137	0.283	7.8	11.083
R933	0.119	0.024	143.437	0.001	0.207	1.124
R942	6.83	0.145	161.03	0.006	3.117	1.578
R954	0.203	0.044	149.726	0.012	0.843	3.266
R 1025	5.459	0.653	241.896	1.197	20.299	6.588
R1036	3.774	-0.245	172.81	0.12	9.962	3.095
R1052	3.981	0.657	214.35	0.226	13.537	20.965

8.6. Reference Analysis of Thermoplasts

Tab. 7-2: *Reference analysis of thermoplasts.*

Sample	Element	Concentration	Error	Rel. Error
		(mg/kg)	(mg/kg)	(%)
6804	Br	21508	1241	5.8
6810	Br	28454	2368	8.3
	Sb	1281	370	28.9
	Zn	270	71	26.3
6811	Br	18166	289	1.6
6812	Br	87816	1247	1.4
	Sb	17510	2695	15.4
6813	Sb	50627	3602	7.1
	Pb	542	214	39.5
6814	Br	254918	56803	22.3
	Sb	14628	348	2.4
6c01	Ti	5096	836	16.4
	Zn	2090	396	18.9
	Cd	452	268	59.3
6c03	Br	148008	25008	16.9
	Sb	54717	3675	6.7
	Ti	6709	1040	15.5
	Pb	1188	148	12.5
	Sn	669	56	8.4
6c05	Br	20598	2051	10
6c06	Br	18390	1563	8.5
6c08	Br	85380	8	0
	Sb	31782	1244	3.9
6c09	Sb	51282	644	1.3
	Br	433	35	8.1
6c17	Br	107391	1332	1.2
	Sb	28234	5966	21.1
	Sn	791	156	19.7
6c19	Zn	2437	625	25.6
	Cd	486	51	10.5
6c25	Cd	200	33	16.5
6c26	Br	18552	1859	10
6c28	Sb	45345	3318	7.3
7302	Sb	617	215	34.8
7303	Br	5323	43	0.8

Reference analysis of thermoplasts (extended).

7807	**Ti**	**59778**	**1374**	**2.3**
	Zn	2169	33	1.5
7808	Ti	53613	3047	5.7
	Zn	1748	221	12.6
	Sb	1441	88	6.1
7809	Ti	77379	2457	3.2
	Zn	3274	33	1
	Sb	1674	152	9.1
7810	Br	139925	3472	2.5
	Ti	31651	2164	6.8
	Sb	17950	1475	8.2
	Sn	1706	243	14.2
	Zn	244	19	7.8
7811	Ti	31676	6592	20.8
	Br	142670	23691	16.6
	Sb	17481	3281	18.8
	Sn	1265	45	3.6
	Zn	265	42	15.8
7814	Br	111519	4074	3.7
	Ti	20899	1733	8.3
	Sb	40609	662	1.6
	Sn	726	98	13.5
	Cd	458	92	20.1
7815	Br	169159	22178	13.1
	Ti	28593	2033	7.1
	Sb	16662	241	1.4
	Sn	1908	39	2
	Pb	497	72	14.5
7816	Ti	34742	559	1.6
	Br	1180	53	4.5
7817	Ti	37227	4659	12.5
	Zn	2344	911	38.9
7818	Ti	35527	1729	4.9
	Zn	1914	96	5
7819	Ti	29193	221	0.8
	Zn	1618	81	5
7820	Ti	19566	877	4.5
	Br	32568	3703	11.4

Reference analysis of thermoplasts (extended).

7305	**Zn**	**1212**	**224**	**18.5**
	Cd	519	13	2.5
7306	Zn	1326	220	16.6
7307	Br	15161	616	4.1
	Sb	48907	7981	16.3
7308	Zn	535	159	29.7
7314	Sb	54289	6760	12.5
7315	Ti	5724	1111	19.4
	Cd	2176	235	10.8
7316	Br	1209	277	22.9
	Ti	319	535	167.7
7317	Br	73386	632	0.9
	Sb	20348	1233	6.1
7319	Br	185720	2329	1.3
	Sb	29606	1632	5.5
	Sn	599	33	5.5
7320	Ti	37568	798	2.1
	Br	437	19	4.3
7706	Zn	432	117	27.1
7801	Ti	41492	468	1.1
	Zn	1389	10	0.7
7802	Ti	73274	5433	7.4
	Zn	3019	270	8.9
	Sb	1485	235	15.8
7803	Ti	48351	12354	25.6
	Zn	2109	351	16.6
7804	Ti	63348	3961	6.3
	Zn	2758	285	10.3
	Sb	1142	48	4.2
7805	Ti	51845	474	0.9
	Zn	1747	237	13.6
7806	Ti	57398	6857	11.9
	Zn	1934	434	22.4
	Sb	1048	669	63.8
7807	Ti	59778	1374	2.3
	Zn	2169	33	1.5

8.7. Reference Analysis of Clay Samples

Tab. 1-1: *Reference analysis of clay samples (values are given in mg kg^{-1}).*

Sample	S 1402	S 1200	S 1501	S 1504	S 1724
Li	38.14	38.14	38.14	38.14	38.14
Mg	2.77	2.77	2.77	2.77	2.77
Cr	2817.05	2817.05	2817.05	2817.05	2817.05
Mn	46.18	46.18	46.18	46.18	46.18
Co	7.79	7.79	7.79	7.79	7.79
Ni	32.33	32.33	32.33	32.33	32.33
Cu	29.56	29.56	29.56	29.56	29.56
Zn	0.00	0.00	0.00	0.00	0.00
Sr	179.90	179.90	179.90	179.90	179.90
Ag	20.62	20.62	20.62	20.62	20.62
Cd	7.89	7.89	7.89	7.89	7.89
Ba	165.92	165.92	165.92	165.92	165.92
Tl	19.60	19.60	19.60	19.60	19.60
Pb	107.17	107.17	107.17	107.17	107.17
Bi	0.00	0.00	0.00	0.00	0.00
Ga	95.82	95.82	95.82	95.82	95.82
Sn	23.88	23.88	23.88	23.88	23.88
Sb	10.13	10.13	10.13	10.13	10.13
Pt	1.96	1.96	1.96	1.96	1.96

9 Literature

[1] T.H. Maiman (1960), Stimulated optical emission in ruby, *Nature*, **187**, 493-494.

[2] A. E. Siegman (1986), Lasers, Mill Valley, University Science Books.

[3] F. Brech, L. Cross (1962), Optical microemission stimulated by ruby laser, *Appl. Spectrosc.*, **16**, 59.

[4] P.D. Maker, R.W. Terhune, C.M. Savage (1964). Optical third harmonic generation. Third international conference on quantum electronics, Paris, Columbia University Press, New York.

[5] E.F. Runge, R.W. Minck, F.R. Bryan (1964), Spectrochemical analysis using are pulsed laser source, *Spectrochim. Acta B*, **20**, 733.

[6] M. Young, M. Hercher, C.-Y. Yu (1966), Some characteristics of laser-induced air sparks, *J. Appl. Phys.*, **37**, 4938-4940.

[7] A. Felske, W.-D. Hagenah, K. Laqua (1972), Über einige Erfahrungen bei der Makrospektralanalyse mit Laserlichtquelen: I Durchnittsanalyse metallischer Proben, *Spectrochim. Acta Part B*, **27**, 1-16.

[8] L.J. Radziemski, T.R. Loree (1981), Laser-induced breakdown spectroscopy: time-resolved aplications, *J. Plasma Chem. Plasma Proc.*, **1**, 281-293.

[9] D.A. Cremers, L.J. Radziemski (1983), Detection of chlorine and fluorine in air by laser-induced breakdown spectrometry, *Anal. Chem*, **55**, 1252-1256.

[10] D.A. Cremers, L.J. Radziemski, T.R. Loree (1984), Spectrochemical analysis of liquids using the laser spark, *Appl. Spectrosc.*, **38**, 721-729.

[11] J.R. Wachter, D.A. Cremers (1987), Determination of uranium in solution using laser-induced breakdown spectroscopy, *Appl. Spectrosc.*, **41**, 1042-1048.

[12] (2001), First international conference on laser induced plasma spectroscopy and applications, *Spectrochim. Acta B*, **56**.

[13] http://www.uspto.gov/.

[14] G.R. Harrison (1936), Practical possibilities in spectrographic analysis, *Metals and Alloys*, **7**, 290-296.

[15] J.R. McNally, G.R. Harrison, E. Rowe (1947), A hollow cathode source applicable to spectrographic analysis for the halogens and gases, *J. Opt. Soc. Am.*, **37**, 93-98.

[16] G. Ballofet (1960), Far ultraviolet light sources and application to spectrochemical analysis, *Ann. Phys.*, **5**, 1243.-1298.

[17] J. Romand, G. Ballofet (1957), Use of sliding sparks for the spectrochemical analysis in the far ultraviolet. Possibility for the detection and determination of phosphorus in copper and in alloys of aluminum, *J. Phys. et. Radium*, **18**, 641-642.

[18] J. Romand, G. Ballofet, B. Vodar (1959), Determination of oxygen and nitrogen in titanium samples by means of a condensed spark in vacuum, *Spectrochim. Acta*, **6**, 454-460.

[19] J. Romand, G. Balloffet (1957), Spectra emitted in the far ultraviolet by sliding vacuum sparks on organic (polymer) supports, *Compt Rend.*, 244, 739-742.

[20] J. Romand, G. Ballofet, B. Vodar (1959), Emission spectroscopy in the far ultraviolet of powders containing germanium, arsenic, selenium, bromine, tin, antimony, tellurium, *J. Phys. et. Radium*, **20**, 509-512.

[21] A.N. Zaidel, V.K. Prokofjev, S.M. Raiskii, V.A. Slavnyi, E.Y. Schreider (1970). Tables of spectral lines. IFI Plenum, New York.

[22] R.L. Kelly (1959). A table of emission lines in vacuum ultraviolet for all elements. Livermore, University of California, Lawrence Radiation Laboratory.

[23] R.L. Kelly, L.J. Palumbo (1973). Atomic and ionic emission lines below 2000 Angstroms. Hydrogen through Krypton, Naval Research Laboratory, Report, NRL-7599.

[24] G.F. Kirkbright, A.F. Ward, T.S. West (1972), The determination of sulphur and phosphorus by atomic emission spectrometry with induction coupled high-frequency plasma source, *Analytica Chimica Acta*, **62**, 241-251.

[25] G.F. Kirkbright, A.F. Ward, T.S. West (1973), Atomic emission spectrometry with an induction-coupled high-frequency plasma source, *Analytica Chimica Acta*, **64**, 353-362.

[26] J. Lee, M.W. Pitchard (1981), Spectral interferences on the emission of sulfur I 180.73 nm in an inductively coupled plasma, *Spectrochim. Acta B*, **36**, 202-216.

[27] T. Hayakawa, F. Kikui, S. Ikeda (1982), The determination of I, P, B, S, As, and Sn by inductively coupled plasma emission spectrometry using lines at vacuum ultraviolet wavelengths, *Spectrochim. Acta. B*, **37**, 1069-1073.

[28] M. Taketoshi (1985), Determination of phosphorus in steels and copper metals by vacuum ultraviolet atomic emission spectrometry with inductively coupled plasma, *Spectrochim. Acta. B*, **40**, 293-300.

[29] D.D. Nygaard, D.A. Leighty (1985), Inductively coupled plasma emission lines in the vacuum ultraviolet, *Appl. Spectrosc.*, **39**, 968-976.

[30] B.R. LaFraniere, R.S. Houk, V.A. Fassel (1987), Direct detection of vacuum ultraviolet radiation through an optical orifice: analytical figures of merit for the nonmetals, metalloids, and selected metals by inductively coupled plasma atomic emission spectrometry, *Anal. Chem*, **59**, 2276-2284.

[31] J. Vilnat, J. Debras-Guedon, A. E. D. Abdellatif (1963), Excitation of atomic emission spectra of halogens in the continuous arc in a helium atmosphere, *Compt. Rend.*, 257, 3582-3584.

[32] L. Moenke-Blankenburg (1989), Laser microanalysis, *John Willey* & *Sons, New York*.

[33] D. Romero, J.J. Laserna (1997), Multielemental chemical imaging using laser induced breakdown spectrometry, *Anal. Chem.*, **69**, 2871-2876.

[34] D. Romero, J.J. Laserna (1998), Surface and tomographic distribution of carbon impurities in photonic-grade silicon using laser-induced breakdown spectrometry, *J. Anal. At. Spectrom.*, **13**, 557-560.

[35] P. Lucena, J.M. Vadillo, J.J. Laserna (1999), Mapping of platinum group metals in automotive exhaust three-way catalysts using laser-induced breakdown spectrometry, *Anal. Chem.*, **71**, 4385-4391.

[36] P. Lucena, J.M. Vaddilo, J.J. Laserna (2001), Compositional mapping of poisoning elements in automobile three-way catalytic converters by using laser-induced breakdown spectrometry, *Applied Spectrometry*, **55**, 267-272.

[37] P. Lucena, J.M. Vadillo, J.J. Laserna (2002), Spatial distribution of catalytically active elements and deactivants in diesel-engine automobile converters by laser-induced plasma spectrometry, *J. Anal. At. Spectrom.*, **17**, 548-551.

[38] C. Geertsen, A. Briand, F. Chartier, J.L. Lacour, P. Mauchein, S. Sjöström, J.M. Mermet (1994), Comparison between infrared and ultraviolet laser ablation at atmospheric pressure. Implications for solid sampling inductively coupled plasma spectrometry, *J. Anal. At. Spectrom.*, **9**, 17-22.

[39] C. Geertsen, J.L. Lacour, P. Mauchein, L. Pierrad (1996), Evaluation of laser ablation optical emission spectrometry for microanalysis in aluminium samples, *Spectrochim. Acta B*, **51**, 1403-1416.

[40] C. Fabre, M.-C. Boiron, J. Dubessy, A. Moissete (1999), Determination of ions in individual fluid inclusions by laser ablation optical emission spectroscopy: development and applications to natural fluid inclusions, *J. Anal. At. Spectrom.*, **14**, 913-922.

[41] C. Fabre, M.-C. Boiron, J. Dubessy, M. Cathelineau, D.A. Banks (2002), Palaeofluid chemistry of a single fluid event: a bulk and in-situ multi-technique analysis (LIBS, Raman Spectroscopy) of an alpine fluid (Mont-Blanc), *Chem. Geol*, **182**, 249-264.

[42] R.W. Hinton (1997), A briliant future for microanalysis?, *Analyst*, **122**, 1187-1192.

[43] F. Chan (1984). Introduction to plasma physics and controlled fusion, New York, Plenum Press.

[44] H.R. Griem (1997), Principles of plasma spectroscopy, Cambridge, University Press.

[45] H. R. Griem (1962), Stark broadening of isolated spectral lines from heavy elements in a plasma, *Phys. Rev.*, **128**, 515-23.

[46] R.H. Huddlestone, S.L. Leonard (1965), Plasma diagnostic techniques, New York, Academic Press.

[47] I.H. Hutchinson (2002), Principles of plasma diagnostic, *Cambridge University Press.*

[48] http://cfa-www.harvard.edu/amp/data/kur23/sekur.html, http://aeldata.nist.gov/nist_atomic_spectra.html Atomic spectral line database and NIST Atomic Spectroscopic Database.

[49] H.R. Griem (1964), Plasma spectroscopy, New York, McGraw-Hill.

[50] R.G. Breene (1961), The Shift and Shape of Spectral Lines, *Pergamon, London.*

[51] R.D. Bengtson, J. D. Tannich, P. Kepple (1970), Comparison between measured and theoretical Stark-broadened profiles of H6-H12 emitted from a low-density plasma, *Phys. Rev. A*, **1**, 532-533.

[52] H.R. Griem (1974), Spectral line broadening by plasmas, New York, Academic Press.

[53] J.D. Ingle, S.R. Crouch (1998). Spectrochemical Analysis, New Jersey, Prentice Hall.

[54] G. Bekefi (1976), Principles of Laser Plasmas, New York, John Willey & Sons.

[55] L.J. Radziemski, D.A. Cremers (1989), Laser-induced plasmas and application, *Marcel Dekker, INC., New York.*

[56] A.S. Epifanov (1974), Avalanche ionization induced in solid transparent dielectrics by strong laser pulses, *Sov. Phys. JETP*, **40**, 897-902.

[57] A.S. Epifanov (1976), Theory of avalanche ionisation induced in dielectrics by an electromagnetic field, *Sov. Phys. JETP*, **43**, 202-208.

[58] B.G.e.a. Gorshkov (1977), Laser-induced breakdown in alkali halides, *Sov. Phys. JETP*, **45**, 612-618.

[59] E. Yablonovich, N. Bloembergen (1971), Avalanche ionisation and the limiting diameter of filaments induced by light pulses in transparent media, *Phys. Rev. Lett.*, **29**. 102-108.

[60] B. Steverding (1974), Ignition of laser-supported detonation waves, *J. Appl. Phys.*, **45**, 3507-3511.

[61] J.F. Ready (1971), Effects of high-power laser radiation, New York, Academic Press.

[62] O.N. Krokhin (1970), Laser Handbook Vol. 2, Amsterdam, North-Holland.

[63] R.S. Adrain, J. Watson (1984), Laser microspectral analysis: A review of principles and applications, *J. Phys. D: Appl. phys*, **17**, 1915-1940.

[64] G. Weyl, A. Pirri, R. Root (1981), Laser ignition of plasma of aluminium surfaces, *AIAA J.*, **19**, 460-469.

[65] I. Ahmad, B.J. Goddard (1993), An overview of laser-induced breakdown spectroscopy, *J. Fiz. Mal.*, **14**, 43-54.

[66] R.E. Russo (1995), Laser ablation, *Appl. Spectrosc.*, **49**, A14-A28.

[67] J.C. Miller (1994), Laser ablation, Berlin, Springer Verlag.

[68] J.C. Miller, R.F. Haglund (1998), Laser ablation and deposition, San Diego, Academic Press.

[69] S. Amoruso, R. Bruzzese, N. Spinelli, R. Velotta (1999), Characterization of laser-ablation plasmas, *J.Phys.B: Mol.Opt.Phys.*, **32**, R131-R172.

[70] D.A. Skoog, F.J. Holler, T.A. Nieman (1998). Principles of instrumental analysis, Florida, Harcout Brace & Conpany.

[71] E. Voigtman (1991), Gated peak integration versus peak detection in white noise, *Appl. Spectrosc.*, **45**, 237-241.

[72] F. Leis, W. Sdorra, J.B. Ko, K. Niemax (1989), Basic investigations for laser microanalysis: 1. Optical emission spectrometry of laser-produced sample plumes, *Mikrochim. Acta*, **II**, 185-199.

[73] C.C. Garcia, M.Corral, J.M. Vadillo, J.J. Laserna (2000), Angle-resolved laser-induced breakdown spectrometry for depth profilling of coated materials, *Appl. Spectrosc.*, **54**, 1027-1031.

[74] J. Monge, C. Aragon, J.A. Aguilera (1999), Space- and time-resolved measurements of temperatures and electron densities of plasmas formed during laser ablation of metallic samples, *Appl.Phys.*, **A69**, S691-S694.

[75] R.E. Russo, S. Mao, M.C. Liu, J.H. Yoo, M. Mao (1999), Time-resolved plasma diagnostic and mass removal during single-pulse laser ablation, *Appl. Phys. A*, **69**, S887-S894.

[76] I. Schecter (1995), Direct aerosol analysis by time-resolved laser plasma spectroscopy - improvenment by single shot measurements, *Anal. Sci. Technol.*, **8**, 779-786.

[77] A. Ciucci, M.Cors, V. Palleschi, S. Rasatelli, A.Salvetti (1999), New procedure for quantitative elemental analysis by laser-induced plasma spectroscopy, *Appl. Spectrosc.*, **53**, 960-964.

[78] C. Chaleard, P. Mauchien, N. Andre, J. Uebbing, J.L. Lacour, C. Geersten (1997), Correction of matrix effects in quantitative elemental analysis with laser-ablation optical emission spectrometry, *J. Anal. At. Spectrom.*, **12.**, 183-188.

[79] G. Chen, E.S. Yeung (1988), Acoustic signal as an internal standard for quantitation in laser-generated plumes, *Anal. Chem.*, **60**, 2258-2263.

[80] A. Thorne, U. Litzen, S. Johansson (1999). Spectrophysics, Heidelberg, Springer Verlag.

[81] Hermann, C. BoulmerLeborgne, D. Hong (1998), Diagnostics of the early phase of an ultraviolet laser induced plasma by spectral line analysis considering self-absorption, *J. Appl. Phys.*, **83**, 691-696.

[82] I.B. Gornushkin, J.M. Anzano, L.A. King, B.W. Smith, N. Omenetto, J.D. Winefordner (1999), Curve of growth methodology applied to laser-induced plasma emission spectroscopy, *Spectrochim. Acta B*, **54**, 491-503.

[83] P.M. Outridge, W. Doherty, D.C. Gregoire (1996), The formation of trace element-enriched particulates during laser ablation of refractory materials, *Spectrochim. Acta B*, **51**, 1451-1462.

[84] P.M. Outridge, W. Doherty, D.C. Gregoire (1997), Ablative and transport fractionation of trace elements during laser sampling of glass and copper, *Spectrochim. Acta B*, **52**, 2093-2102.

[85] R.E. Russo, X.L. Mao, O.V. Borisov, H.C. Liu (2000), Influence of wavelength on fractionation in laser ablation ICP-MS, *J. Anal. At. Spectrom.*, **15**, 1115-1120.

[86] H.P. Longerich, D. Günther, S.E. Jackson (1996), Elemental fractionation in laser ablation inductively coupled plasma mass spectrometry, *Fresenius J. Anal. Chem.*, **355**, 538-542.

[87] J. Hermann, A.L. Thomann, C. Boulmer-Leborgne, B. Dubreuil, M.L. De Giorgi, A. Perrone, A. Luches, I.N. Mihailescu (1995), Plasma diagnostics in pulsed laser TiN layer deposition., *J. Appl. Phys.*, **77**, 2928-2936.

[88] S. H. Jeong, R. Greif, R. E. Russo (1998), Propagation of shock wave generated from excimer laser heating of aluminium targets in comparison with ideal blast wave theory, *Appl. Surf. Sci.*, **127-129**, 1029-1034.

[89] S. H. Jeong, R. Greif, R. E. Russo (1999), Shock wave and material vapour plume propagation during excimer laser ablation of aluminium samples, *J. Phys. D: Appl. Phys.*, **32**, 2578-2585.

[90] Y.I. Lee, T.L. Thiem, G.H. Kim, Y.Y. Teng, J. Sneddon (1992), Interaction of an excimer-laser beam with metals. Part III: The effect of a controlled atmosphere in laser-ablated plasma emission, *Appl. Spectrosc.*, **46**, 1597-1604.

[91] Z. Marton, A. Mechler, B. Hopp, Z. Kantor, Z. Bor (1999), Time-resolved shock wave photography above 193-nm excimer laser-ablation on graphite surface, *Appl. Phys. A*, **69**, S131-S136.

[92] R. Nyga, W. Neu (1993), Double-pulse technique for optical emission spectroscopy of ablation plasmas of samples in liquids, *Opt. Lett.*, **18**, 747-749.

[93] H. Schittenhelm, G. Callies, A. Straub, P. Berger, H. Hügel (1998), Measurements of wavelength-dependent transmission in excimer laser-induced plasma plumes and their interpretation, *J. Phys. D: Appl. Phys.*, **31**, 418-427.
[94] H. Schmidt, J. Ihlemann, B. Wolff-Rottke, K. Luther, J. Troe (1998), Ultraviolet laser ablation of polymers: spot size, pulse duration, and plume attenuation effects explained, *J. Appl. Phys.*, **83**, 5458-5468.
[95] J. Hecht (1992), Laser Guidebook, New York, McGraw-Hill.
[96] J.F. James, R.S. Sternberg (1969), The Design of Optical Spectrometers, New York, Chapman and Hall.
[97] S. Y. Lee, J. Sneddon (2000). Laser-induced Breakdown Spectroscopy, Huntington, New York, Nova Science Publishers.
[98] J.V. Sweedler (1993), Charge transfer device detectors and their applications to chemical analysis, *CRC Crit. Rev. Anal. Chem.*, **24**, 59-98.
[99] J.H. Giles, T.D. Ridder, R.H. Williams, D.A. Jones, M.B. Denton (1998), Selecting a CCD camera, *Anal. Chem.*, **70**, A663-A668.
[100] Q.S. Hanley, C.W. Earle, F.M. Pennebaker, S.P. Madden, M.B. Denton (1996), Charge-transfer devices in analytical instrumentation, *Anal. Chem.*, **68**, 661A-667A.
[101] R.E. Fields, M.B. Denton (1992), Array detectors expand atomic spectroscopy, *Laser Focus World*, **3**, 107-113.
[102] J.M. Harnly, R.E. Fields (1997), Solid-state array detectors for analytical spectrometry, *Appl. Spectrosc.*, **51**, 334A-351A.
[103] H. Okabe (1978). Photochemistry of Small Molecules, New York, John Wiley & Sons.
[104] K.Watanabe, M. Zelikoff (1953), Absorption coefficients of water vapor in the vacuum ultraviolet *J. Opt. Soc. Am.*, **43**, 753-755.
[105] K. Watanabe, A.S. Jursa (1964), ‚Absorption and photoionization cross sections of H_2O and H_2S *J. Chem. Phys.*, **41**, 1650-1653.
[106] A.N. Zaidel, E.Y. Shreider (1970). Vacuum Ultraviolet Spectroscopy, London, Ann Arbor Science Publishers.
[107] J.A. Samson, D.L. Ederer (1998). Vacuum Ultraviolet Spectroscopy I, San Diego, Academic Press.
[108] J.A. Samson, D.L. Ederer (1998). Vacuum Ultraviolet Spectroscopy II, London, Academic Press.
[109] J.V. Sweedler, K.L. Ratzlaff, M.B. Denton (1994). Charge-Transfer Devices in Spectroscopy, New York, VCH Publishers.
[110] J.F. O'Hanlon (1989). A User's Guide to Vacuum Technology, New York, John Willey & Sons.
[111] C. Carlhoff (1991), Laserinduzierte Emissionsspektroskopie für die Direktanalyse von flüssigem Stahl im Konverter, *Laser Optoelektronik*, **23**, 50-52.
[112] A. Gonzalez, M. Ortiz, J. Campos (1995), Determination of sulfur content in steel by laser-produced plasma atomic emission spectroscopy, *Appl. Spectrosc.*, **49**, 1632-1635.
[113] R. Sattmann, V. Sturm, R. Noll (1995), Laser-induced breakdown spectroscopy of steel semples using multiple Q-switched Nd:YAG laser pulses, *J. Phys. D: Appl. Phys*, **28**, 1281-1287.
[114] V. Sturm, L. Peter, R. Noll (2000), Steel analysis with laser-induced breakdown spectroscopy in the vacuum-ultraviolet, *Appl. Spectros.*, **54**, 1275-1278.
[115] M. A. Khater, P. Van Kampen, J. T. Costello, J. P. Mosnier, E. T. Kennedy (2000), Time-integrated laser-induced plasma spectroscopy in the vacuum ultraviolet for the quantitative elemental characterisation of steel alloys, *J. Phys. D: Appl.Phys.*, **33**, 2252-2262.
[116] M. Hemmerlin, R. Meiland, Falk, P. Wintjes, L. Paulard (2001), Application of vacuum ultraviolet laser-induced breakdown spectrometry for steel analysis - comparison with spark-optical emission spectrometry figures of merit, *Spectrochim Acta B*, **56**, 661-669.
[117] M.A. Khater, J.T. Costello, E.T. Kennedy (2002), Optimisation of emission characteristics of laser-produced steel plasmas in vacuum-ultraviolet: significant improvements in carbon detection limits, *Appl. Spectros.*, **56**, 970-983.
[118] D.N. Stratis, K.L. Eland, S.M. Angel (2000), Dual-pulse LIBS using a pre-ablation spark for enhanced ablation and emission, *Appl. Spectrosc.*, **54**, 1270-1274.

[119] M. Sabsabi, P. Cielo, L. St-Onge (1999). Method and apparatus for materials analysis by enhanced laser induced plasma spectroscopy. US Patent No. 1999-232722. US, National Research Council of Canada.
[120] D.N. Stratis, K.L. Eland, S.M.Angel (2000), Enhancement of aluminium, titanium, and iron in glass using pre-ablation spark dual-pulse LIBS, *Appl. Spectrosc.*, **54**, 1719-1726.
[121] D.N. Stratis, K.L.Eland, S.M. Angel (2001), Energy depedence of emission intensity and temperature in a LIBS plasma using femtosecond excitation, *Appl. Spectrosc.*, **55**, 286-291.
[122] K.L. Eland, D.N. Stratis, T. Lai, M.A. Berg, S.R. Goode, S.M. Angel (2001), Some comparisons of LIBS measurements using nanosecond and picosecond laser pulse, *Appl. Spectrosc.*, **55**, 279-285.
[123] K.L. Eland, D.N. Stratis, D.M. Gold, S.R. Goode, S.M. Angel (2001), Energy dependence of emission intensity and temperature in a LIBS plasma using femtosecond excitiation, *Appl. Spectrosc.*, **55**, 286-291.
[124] D.N. Stratis, K.L. Eland, S.M. Angel (2001), Effect of pulse delay time on a pre-ablation dual-Pulse LIBS plasma, *Appl. Spectrosc.*, **55**, 1297-1303.
[125] F. Colao, V. Lazic, R. Fantoni, S. Pershin (2002), A comparison of single and double pulse laser-induced breakdown spectroscopy of aluminium samples, *Spectrochim. Acta B*, **57**, 1167-1179.
[126] S.M. Angel, D.N. Stratis, K.L. Eland, T. Lai, M.A. Berg, D.M. Gold (2001), LIBS using dual- and ultrashort laser pulses, *Anal. Chem.*, **369**, 320-327.
[127] S. Nakamura, Y. Ito, K. Sone (1996), Determination of an iron suspension in water by laser-induced breakdown spectrometry with two sequential laser pulses, *Anal. Chem*, **68**, 2981-2986.
[128] D.A. Cremers, L.J. Radziemski, T.R. Loree (1984), Spectrochemical analysis of liquids using the laser spark, *Appl. Spectrosc.*, **38**, 721-729.
[129] C. Haisch (1998). Anwendungen der laserinduzierten Plasmaspektroskopie (LIPS) in der Prozeß- und Umweltanalyitk. Dissertation, München, Technische Universität.
[130] J. Uebbing, J. Brust, W. Sdorra, F. Leis, K. Niemax (1991), Reheating of laser-produced plasma by a second pulse laser, *Appl. Spectrosc:*, **45**, 1419-1423.
[131] L. St-Onge, M. Sabsabi, P. Cielo (1998), Analysis of solids using laser-induced plasma spectroscopy in double-pulse mode, *Spectrochim. Acta* B, **53**, 407-415.
[132] V. Detalle, R. Heon, M. Sasabi, L. St-Onge (2001), An evaluation of a comercial Echelle spectrometer with intensified charge coupled device detector for materials analysed by laser-induced plasma spectroscopy, *Spectrochim. Acta B*, **56**, 1011-1025.
[133] N. Konjevic, M. S. Dimitrijevic (1984), Experimental Stark widths and shifts for spectral lines of neutral atoms (a critical review of selected data for the period 1976 to 1982), *J.Phys. Chem. Ref. Data.*, **13**, 619-647.
[134] J. Zupan (1989). Algorithms for Chemists, New York, John Wiley & Sons.
[135] R. Wisbrun, I. Schechter, R. Niessner, H. Schröder, K.L. Kompa (1994), Detector for trace elemental analysis of solid environmental samples by laser plasma spectroscopy, *Anal. Chem.*, **66**, 2964-2975.
[136] C. Haisch, R. Niessner, O.I. Matveev, U. Panne, N. Omenetto (1996), Development of a sensor for element-specific determination of chlorine in gases by laser-induced-breakdown spectroscopy (LIBS), *Fresenius J. Anal. Chem.*, **356**, 21-26.
[137] E. Neuhauser, U. Panne, R. Niessner, G. Petrucci, P. Cavalli, N. Omenetto (1997), On-line and in-situ detection of lead in ultrafine aerosols by laser-excited atomic fluorescence spectroscopy, *Sens. Actuators*, **B 39**, 157-161.
[138] R.E. Neuhauser, U. Panne, R. Niessner, G.A. Petrucci, P. Cavalli, N. Omenetto (1997), On-line and in situ detection of lead aerosols by plasma spectroscopy and laser-excited atomic fluorescence spectroscopy, *Anal. Chim. Acta*, **346**, 37-48.
[139] R.E. Neuhauser, U. Panne; Niessner, R.; (1999), Laser-induced plasma spectroscopy (LIPS): a versatile tool for monitoring heavy metal aerosols, *Anal. Chim. Acta*, **392**, 47-54.
[140] H. Fink, U. Panne, R. Niessner (2001), Analysis of recycled thermoplasts from consumer electronics by laser-induced plasma spectroscopy, *Analytica Chimica Acta*, **440**, 17-25.
[141] R.A. Sawyer (1951). Experimental Spectroscopy, New York, Dover Publications.
[142] J.B. Ko, W. Sdorra, K. Niemax (1989), On the internal standardization in optical emission spectrometry of microplasmas produced by laser ablation, *Fresenius. J. Anal. Chem.*, **335**, 648-651.

[143] C.R. Ward (2002), Analysis and significance of mineral matter in coal seams, *Int. J. Coal Geol.*, **50**, 135-168.
[144] R.P. Gupta, T.F. Wall, L.A. Baxter (1999), Impact of Mineral Impurities in Solid fuel Combustion, *Plenum, New York*.
[145] L.L. Sloss, R.M. Davidson (2001). Rapid analysis of trace elements in coal utilisation, Kentucky, USA, IEA Publications/Theresa Wiley.
[146] P. Arikan, A. Zararzis, N. efe (1996), Determination of ash and sulfur in coal via off-line calibration of XRF, *Appl. Spectrosc. Rev.*, **31**, 167.
[147] C.S. Lim, B.D. Sowerby, D.A. Abernethy (2002), On-belt analysis of ash in coal, *Coal Preparation.*, **22**, 165.
[148] N.G. Cutmore, C.S. Lim, B.D. Sowerby (1993), Online analysis of low rank coal*, J. Coal Qual.*, **12**, 85-93.
[149] H. Lachas, R. Richaud, K.E. Jarvis, A.A. Herod, D.R. Dugwell, R. Kandiyoti (1999), Determination of 17 trace elements in coal and ash reference material by ICP-MS applied to milligram sample size, *Analyst*, **124**, 177-184.
[150] I. Rodushkin, M.D. Axelsson, E. Burman (2000), Multielement analysis of coal by ICP techniques using solution nebulization and laser ablation, *Talanta*, **51**, 743-759.
[151] E. Ikävalko, T. Laitinen, H. Revitzer (1999), Optimised method for coal digestion for trace metal determination by atomic absorption spectroscopy, *Fresenius J. Anal. Chem*, **363**, 314-318.
[152] L.J. Radziemski (2002), From LASER to LIBS, the path of technology development, *Spectrochimica Acta B*, **57**, 1109-1113.
[153] D.A. Rusak, B.C. Castle, J.D. Winefordner (1998), Recent trends and the future of laser-induced plasma spectroscopy, *Tr Anal. Chem.*, **17**.
[154] R.E. Russo, X. Mao, S.S. Mao (2002), The physics of laser ablation in microchemical analysis, *Anal. Chem.*, **74**, 70A-77A.
[155] D. Body, B.L. Chadwick (2001), Optimisation of the spectral processing in a LIBS simultanious elemental analysis system, *Spectrochim. Acta B*, **56**, 725-736.
[156] B.L. Chadwick, L. Bruce, D. Body (2002), Development and commercial evaluation of laser-induced breakdown spectroscopy chemical analysis technology in the coal power generation industry, *Appl. Spectrosc.*, **56**, 70-74.
[157] http://physics.nist.gov/cgi-bin/AtData/main_asd.
[158] P. Gans (1992). Data Fitting in the Chemical Sciences, Chichester, John Wiley & Sons.
[159] J.E. Carranza, D.W. Hahn (2002), Sampling statistic and considerations for single-shot analysis using laser-induced brakdown spectroscopy, *Spectrochim. Acta B*, **57**, 779-790.
[160] I. Schechter (1995), Direct aerosol analysis by time resolved laser plasma spectroscopy improvement by single shot measurements, *Anal. Sci.Technol.*, **8**, 779-786.
[161] D.L. Massart, L. Kaufman (1983). The Interpretation of Analytical Chemical Data by the Use of Cluster Analysis, New York, John Wiley & Sons.
[162] D.A. Spears, C.A. Booth (2002), The composition of size-fractionated pulverised coal and the trace element associations, *Fuel*, **81**, 683-690.
[163] D.J. Swaine (1985), Modern methods in bituminous coal analysis: trace elements, *CRC Crit. Rev. Anal. Chem.*, **15**, 315-46.
[164] A. Scheffer, J. Schachtschabel (1997). Lehrbuch der Bodenkunde, Stuttgart, Ferdinand Enke Verlag.
[165] J. Marshall, J. Caroll, J.S. Crington, C.L.R. Barnard (1992), *J. Anal. At. Spectrom.*, **7**, 349R.
[166] J. Marshall, J. Caroll, J.S. Crington, C.L.R. Barnard (1994), Atomic spectrometry update - industrial analysis: metals, chemicals and advanced materials., *J. Anal. At. Spectrom.*, **9**, 319R-356R.
[167] E.H. Evans, J.J. Giglio (1993), Interferences in inductively coupled plasma mass spectrometry. A review*, J. Anal. At. Spectrom.*, **8**, 1-18.
[168] R. Chuan-De, C.R. Ward (2002), Quantitative X-ray powder diffraction analysis of clay minerals in Australian coals using Rietveld methods, *Appl. Clay Sci.*, **21**, 227-240.
[169] S. Hillier (2003), Quantitative analysis of clay and other minerals in sandstones by X-ray powder diffraction, *Special publication of the International Association of Sedimentologists*, **34**, 213-251.

[170] M.A.E. Hanied Hafez (1992), Rapid chelatometric determination of bismuth, titanium and aluminum using Semixylenol Orange with visual end-point indication, *Talanta*, **39**, 1189-1194.
[171] F.E. Wagner, U. Wagner (2004) Moessbauer spectra of clays and ceramics, *Hyperfine Interactions*, **154**, 35-82.
[172] P.J. Lamothe, T.L. Fries, J.J. Consul (1986), Evaluation of a microwave-oven system for the dissolution of geologic samples, *Anal. Chem*, **58**, 1881-1886.
[173] H. Fink (2002). Anwendungen von laser- and plasmagestützten spektroskopischen Methoden in der prozess- und Umweltanalytik. München, Dissertation, Technische Universität München.
[174] D.R. Askeland (1996). Materialwissenschaften, Heidelberg, Spektrum Akademischer Verlag GmbH.
[175] M.J.P. Gerritsen, H.F. Pronk (1994). Why do we analyse during the steelmaking? An ongoing question. Forty-sixth chemists conference, Scaraborough.
[176] T.R. Dulski (1995), Steel and related materials, *Anal. Chem*, **67**, 21R-32R.
[177] R.S. Adrian, J. Watson, P.H. Richards, A. Maitland (1980), Laser microspectral analysis of steels, *Opt. Laser Technol.*, **6**, 137.143.
[178] D.A. Cramers (1987), The analysis of metals at a distance using laser-induced breakdown spectroscopy, *Appl. Spectrosc.*, **41**, 572-579.
[179] F. Leis, W. Sdorra, J.B. Ko, K. Niemax (1989), Basic investigations for laser microanalysis: I Optical emision spectroscopy of laser-produced sample plumes, *Mikrocimica Acta*, **II**, 185-199.
[180] C. Aragon, J.A. Aguilera, J. Campos (1993), Determination of carbon content in molten steel using laser-induced breakdown spectroscopy, *Appl. Spectrosc.*, **47**, 606-608.
[181] J.A. Aguilera, C. Aragon, J. Campos (1992), Determination of carbon content in steel using laser-induced breakdown spectroscopy, *Appl. Spectrosc.*, **46**, 1382-1387.
[182] W.E. Ernst, D.F. Farson, S.D. J. (1996), Determination of copper in A533b steel for the assesment of radiation embrittelmnent using laser-induced breakdown spectroscopy, *Appl. Spectrosc.*, **50**, 306-309.
[183] Y. Ishbashi (1997), Rapid analysis of steel by inductively coupled plasma atomic emission spectrometry and mass spectrometry with laser ablation solid sampling, *ISIJ Int.*, **37**, 885-891.
[184] D. Günther, S.E. Jackson, L.H. P. (1999), Laser ablation and arc/spark solid sample introduction into inductively coupled plasma mass-spectrometry with spark ablation, *Spectrochim. Acta B*, **54**, 381-409.
[185] N. Jakubowski, I. Feldman, B. Sack, D. Stuewer (1992), Analysis of conducting solids by inductively coupled plasma mass spectrometry with spark ablation, *J. Anal. At. Spectrom.*, **7**, 121-125.
[186] N. Jakubowski, I. Feldman, D. Stuewer (1995), Comparison of ICP-MS with spark ablation and GDMS for direct elemental analysis of conducting solids, *Spectrochim. Acta B*, **50**, 639-654.
[187] A.G. Coedo, M.T. Dorado, B. Fernandez (1995), Spark ablation as sampling device for inductively coupled mass spectrometric analysis of low alloyed steels, *J. Anal. At. Spectrom.*, **10**, 859-863.
[188] R. Maibusch, H.M. Kuss, A.G. Coedo, M.T. Dorado, I. Padilla (1999), Spark ablation inductively -coupled plasma-mass spectrometric analysis of minor and trace elements in low and high alloy steel using single calibration curve, *J. Anal. At. Spectrom.*, **14**, 839-846.
[189] J. Sneddon, G. Mitchell (1987), Direct determination of metal in solids samples by plasma ES with sample introduction by laser ablation, *Int. Lab.*, **4**, 18-26.
[190] L. Hiddemann, J. Uebbing, A. Ciocan, O. Dessenne, K. Niemax (1993), Simultanious multi-element analysis of solid samples by laser ablation-microwave-induced plasma optical emission spectrometry, *Anal. Chimica. Acta.*, **283**, 152-159.
[191] M. Gagean, J.M. Mermet (1997), Comparison of ultraviolet laser ablation and spark ablation of metals and alloys for analysis by axially viewed inductively coupled plasma atomic emission spectrometry, *J. Anal. At. Spectrom.*, **12**, 189-193.
[192] W.B. Cho, Y.A. Woo, H.J. Kim, W.K. Kang (1997), Comparison between direct-curent and radio-frequency gas-jet-boosted glow discharge atomic emission spectrometry for the analysis of steel, *Appl. Spectrosc.*, **51**, 1060-1066.

[193] C. Aragon, J.A. Aguilera, F. Penalba (1999), Improvements in quantitative analysis of steel composition by laser-induced breakdown spectroscopy at atmospheric pressure using an infrared Nd:YAG laser, *Appl. Spectrosc.*, **53**, 1259-1267.

[194] W. Sdorra, K. Niemax (1992), Basic investigations of laser microanalysis: III Application of different buffer gases for laser-produced sample plumes, *Mikrochim. Acta*, **107**, 319-327.

[195] K. Niemax (2001), Laser-ablation - reflections on a very complex technique for laser sampling, *Anal. Bioanal. Chem.*, **370**, 332-340.

[196] W. Sdorra, J. Brust, K. Niemax (1992), Basic investigations for laser microanalysis: IV The dependence on the laser wavelenght in laser ablation, *Mikrochim. Acta*, **108**, 1-10.

[197] R. Russo, E., X. Mao, S. Mao Samuel (2002), The physics of laser ablation in microchemical analysis, *Anal. Chem.*, **74**, 70A-77A.

[198] R.E. Russo, X. Mao, H. Liu, J. Gonzalez, S.S. Mao (2002), Laser ablation in analytical chemistry - a review, *Talanta*, **57**, 425-451.

[199] E. Thienmann, W. Dropmann, J. Flock, B.J. Schlothmann, D. Thierig, V. Tröbs, H.J. Wachtendonk (1995), Spektrometrische Stickstoffbestimung in Stählen, *Stahl und Eisen*, **115**, 115.

[200] E. Thienmann, J. Bewerunge, J. Flock, R. Hussmann, B.J. Schlothmann, V. Tröbs, H. Unger (1997), New findings in the spectrometric determination of steel nitrogen level, *Steel Research*, **68**, 301-308.

[201] M. Hemmerlin, L. Paulard, G. Schotter (2003), Determination of ultra-low carbon and nitrogen contents in steel: combustion versus electrical spark source optical emission spectrometry for steel making process control, *J. Anal. At. Spectrom.*, **18**, 282-286.

[202] K. Brodersen, B. Danzer, W. Miekisch, M. Wolf (1996), Identification and quantification of brominated flame retardants in electronic components, *GIT Fachz. Lab.*, **40**, 1132-1134,1136-1137.

[203] M. Hemmerlin, J.M. Mermet (1996), Determination of elements in polymers by laser ablation inductively coupled plasma atomic emission spectrometry: effect of the laser beam wavelength, energy and masking on the ablation threshold and efficiency, *Spectrochim. Acta B*, **51**, 579-589.

[204] M. Hemmerlin, J.M. Mermet, M. Bertucci, P. Zydowicz (1997), Determination of additives in PVC material by UV laser ablation inductively coupled plasma atomic emission spectrometry, *Spectrochim. Acta B*, **52**, 421-430.

[205] H. Fink, U. Panne, R. Niessner (2002), Process analysis of recycled thermoplasts from consumer electronics by laser-induced plasma spectroscopy, *Anal. Chem.*, **74**, 4334-4342.

[206] H. Fink, U. Panne und R. Niessner (2001), Analysis of recycled thermoplasts from consumer electronics by laser-induced plasma spectroscopy, *Anal. Chim. Acta*, **440**, 17-25.

[207] A. Sjoedin, H. Carlsson, S. Thuresson, S. Sjoelin, A. Bergman, C. Oestman (2001), Flame retardants in indoor air at an electronics recycling plant and at other work environments, *Environ. Sci. Technol.*, **35**, 448 -454.

[208] T. Hyötyläinen, K. Hartonen (2002), Determination of brominated flame retardants in environmental samples, *Tr Anal. Chem.*, **21**, 13-30.

[209] D.R. Anderson, C.W. McLeod, T.A. Smith (1994), Rapid survey of polymeric materials by laser-induced plasma emission spectrometry, *J. Anal. Atom. Spectrom.*, **9**, 67-72.

[210] R. Sattmann, I. Monch, H. Krause, R. Noll, S. Couris, A. Hatziapostolou, A. Mavromanolakis, C. Fotakis, E. Larrauri, R. Miguel (1998), Laser-induced breakdown spectroscopy for polymer identification, *Appl. Spectrosc.*, **52**, 456-461.

[211] J.M. Anzano, I.B. Gornushkin, B.W. Smith, J.D. Winefordner (2000), Laser-induced plasma spectroscopy for plastic identification, *Polym. Eng. Sc.*,**40**, 2423-2429.

[212] E.D. Lancaster, K.L. McNesby, R.G. Daniel, A.W. Miziolek (1999), Spectroscopic analysis of fire suppressants and refrigerants by laser-induced breakdown spectroscopy, *Appl. Opt.*, **38**, 1476-1480.

[213] M. Tran, Q. Sun, B.W. Smith, J.D. Winefordner (2001), Determination of F, Cl and Br in solid organic compounds by laser-induced plasma spectroscopy, *Appl: Spectrosc.*, **55**, 739-744.

[214] M. Stepputat, R. Noll (2002), On-line detection of heavy metals and brominated flame retardants in technical polymers with laser-induced breakdown spectrometry, *Appl. Opt.*, **42**, 6210-6220.

[215] H. Fink, U. Panne, M. Theisen, R. Niessner, T. Probst, X. Lin (2000), Determination of metal additives and bromine in recycled thermoplasts from electronic waste by TXRF analysis, *Fresenius J. Anal. Chem*, **368**, 235-239.

[216] Y. Lida (1990), Effects of atmosphere on laser vaporization and excitation processes of solid samples, *Spectrochim. Acta B*, **45**, 1353-1367.

[217] R.L. Shriner (1998). The Systematic Identification of Organic Compounds, New York, John Wiley.

[218] I.B. Gornushkin, A. Ruiz-Medina, J.M. Anzano, B.W. Smith, J.J. Winefordner (2000), Indentification of practiculate materials by correlation analysis using a microscopic laser induced breakdown spectrometer, *J. Anal. At. Spectrom.*, **15**, 581-586.

[219] B. Morris, B.E. Forch, A.W. Miziolek (1990), A novel detector for gas chromatography based on UV laser-produced microplasmas, *Appl. Spectrosc.*, **44**, 1040.

[220] E. Tongoni, V. Palleschi, M. Corsi, G. Cristoforetti (2002), Quantitative micro-analysis by laser-induced breakdown spectroscopy: a rewiew of the experimental approaches, *Spectrochim. Acta B*, **57**, 1115-1130.

[221] R. Noll, H. Bette, A. Brysch, M. Kraushaar, I. Monch, L. Peter, V. Sturm (2001), Laser-induced breakdown spectrometry - applications for production control and quality assurance in the steel industry, *Spectrochim. Acta B*, **56**, 637-649.

[222] C. Speiser, T. Baumann, R. Niessner (2001), Characterization of municipal solid waste incineration (MSWI) bottom ash by scanning electron microscopy and quantitative energy dispersive x-ray microanalysis (SEM/EDX)*, Fresenius J. Anal. Chem*, **370**, 752-759.

[223] J.A. Samson (1967). Techniques of Vacuum Ultraviolet Spectroscopy, New York, John Wiley & Sons.

[224] C.H. S. Florek, M. Okruss, H. Becker-Ross (2001), A new, versatile echelle spectrometer relevant to laser-induced plasma applications, *Spectrochim. Acta B*, **56**, 1027-1034.

[225] D.C. O'Shea (1985). Elements of Modern Optical Design, New York, John Willey & Sons.

[226] J.M. Vadillo, J.J. Laserna (1997), Depth resolved analysis of multilayered samples by laser induced breakdown spectrometry, *J. Anal. At. Spectrom.*, **12**, 859-862.

[227] M.P. Mateo, J.M. Vadillo, J.J. Laserna (2001), Irradiance-dependent depth profiling of layered materials using laser-induced plasma spectrometry, *J. Anal. At. Spectrom.*, **16**, 1317-1321.

[228] A. Plotnikov, C. Vogt, K. Wetzig (2002), An approach to the reconstruction of true concentration profile from transient signal in spatially resolved analysis by means of laser ablation ICP MS, *J. Anal. At. Spectrom.*, **17**, 1114-1120.

[229] L.J. St-Onge (2002), A mathematical framework for modeling the compositional depth profiles obtained by pulsed laser ablation, *J. Anal. At. Spectrom.*, **17**, 1083-1089.

[230] J. M. Vadillo, J. J. Laserna (2004), Laser-induced plasma spectrometry: truly a surface analytical tool, *Spectrochim. Acta B***, 59**, 147-161.